

Doctoral thesis / Dissertation

for the doctoral degree / zur Erlangung des Doktorgrads

Doctor rerum naturalium (Dr. rer. nat.)

Potential of Remote Sensing in Modeling Long-Term
Crop Yields

*Potenzial der Fernerkundung für die Modellierung
Langfristiger Ernteerträge*



Submitted by

Maninder Singh Dhillon

From Ghattian Wali Jattan, Punjab, India

Würzburg, 2023

Submitted on:

Stamp Graduate School

Members of thesis committee

Chairperson

1. Reviewer and Examiner: Prof. Dr. Tobias Ullmann

2. Reviewer and Examiner: Prof. Dr. Ingolf Steffan-Dewenter

3. Examiner: Prof. Dr. Andrea Holzschuh

Additional Examiners: Prof. Dr. Andreas Nüchter

Mentor: Dr. Thorsten Dahms

.....

Day of thesis defense:

**Dedicated to my mother
Harpreet Kaur**

Table of Contents

POTENTIAL OF REMOTE SENSING IN MODELING LONG-TERM CROP YIELDS.....	1
List of Figures.....	3
List of Tables.....	10
List of Symbols and Abbreviations	11
Summary.....	15
Zusammenfassung	17
CHAPTER 1	21
GENERAL INTRODUCTION.....	21
1.1. Historical Background of Agriculture: A Journey from Neolithic Period to Modern Age.....	22
1.2. Agriculture: Challenges and Solutions	24
1.3. The Impact of Crop Yield Predictions on Sustainable Agriculture.....	29
1.4. Potential Methods in Science for Accurate Crop Yield Predictions.....	31
1.5. Objectives and Structure of the Thesis.....	39
1.6. Thesis in Brief	41
CHAPTER 2	47
SPATIOTEMPORAL FUSION MODELLING USING STARFM: EXAMPLES OF LANDSAT 8 AND SENTINEL-2 NDVI IN BAVARIA, GERMANY.....	47
Abstract	48
2.1. Introduction.....	49
2.2. Materials and Methods	51
2.3. Results	61
2.4. Discussion.....	73
2.5. Conclusions	78
CHAPTER 3	81
EVALUATION OF MODIS, LANDSAT 8, AND SENTINEL-2 DATA FOR ACCURATE CROP YIELD PREDICTIONS: A CASE STUDY USING STARFM NDVI IN BAVARIA, GERMANY	81
Abstract	82
3.1. Introduction.....	83
3.2. Materials and Methods	86
3.3 Results	100
3.4. Discussion.....	115
3.5. Conclusions	123
CHAPTER 4	125
IMPACT OF STARFM ON CROP YIELD PREDICTIONS: FUSING MODIS WITH LANDSAT 5, 7, AND 8 NDVIS IN BAVARIA, GERMANY.....	125
Abstract	126
4.1. Introduction.....	127
4.2. Materials and Methods	130
4.3. Results	141
4.4. Discussion.....	154
4.5. Conclusions	160
CHAPTER 5	163

Table of Contents

INTEGRATING RANDOM FOREST AND CROP MODELLING IMPROVES THE CROP YIELD PREDICTION OF WINTER WHEAT AND OIL SEED RAPE	163
Abstract	164
5.1. Introduction	165
5.2. Materials and Methods.....	168
5.3. Results.....	176
5.4. Discussion	189
5.5. Conclusions.....	192
CHAPTER 6	195
POTENTIAL AND CHALLENGES OF SATELLITE REMOTE SENSING IN ANALYSING THE RELATIONSHIP BETWEEN LAND USE DIVERSITY AND CROP BIOMASS IN BAVARIA, GERMANY	195
Abstract	196
6.1. Introduction	197
6.2. Materials and Methods.....	200
6.3. Results.....	208
6.4. Discussion	217
6.5. Conclusions.....	221
CHAPTER 7	223
GENERAL DISCUSSION, OUTLOOK, AND CONCLUSION	223
7.1. Importance of RS in Crop Yield Predictions	224
7.2. Role of the Synthetic NDVI RS Data in Crop Yield Predictions	225
7.3. Comparison of Crop Yield Prediction Models.....	230
7.4. Influence of Climate Elements in Crop Yield Predictions	231
7.5. Spatial Analysis of Yield Variation in Bavaria	232
7.6. Potentials and Limitations of the Research	233
7.7. Broader Implications of this Research: Outlook of the Study.....	235
7.8. Conclusions.....	236
APPENDICES.....	240
Appendix 1: Figures and Tables	240
Appendix 2: Author Contributions.....	253
REFERENCES	261
ACKNOWLEDGEMENTS.....	283
AFFIDAVIT	279
CV.....	280

List of Figures

Figure 1.1. The diagram shows the (a) world population in 2020, (b) the UN population projection until 2100, (c) world crop yields in 2020, (d) change in world's crop yields from 1961 to 2020 (e) global hunger map 2021, and (f) number of undernourished people worldwide from 2005 to 2020.....	25
Figure 1.2. Global monthly mean temperature graph from 1851 to 2020.....	27
Figure 1.3. The flowchart shows the impact of climate change on agriculture. Several symbols, which were used to generate the infographic, were adopted or modified according to courtesy of the Integration and Application Network, University of Maryland Center for Environmental Science	28
Figure 1.4. A flow diagram showing crop cycle used by different methods to predict crop yields. Method 1 uses crop growth models, method 2 uses machine or deep learning algorithms, method3 integrates unmanned aerial vehicles (UAVs or drones) with crop growth modelling, method 4 integrates satellite remote sensing with crop growth modelling, and method 5 couples' remote sensing, crop growth modelling, and machine or deep learning to accurately predict crop yields.....	32
Figure 1.5. Flowchart shows an example of the spatio-temporal data fusion combining different satellite data together to fill cloud and shadow gaps of high spatial resolution sensor. The example shows a fusion of the cloudy Landsat NDVI time series with the MODIS dataset in Bavaria. The synthetic cloud and shadow free NDVI data generated was 30 m with a temporal frequency of 8-days.....	35
Figure 1.6. Flowchart of the chapter-wise overview of the dissertation.....	46
Figure 2.1. Flowchart of data used and processed to generate the synthetic NDVI time series using STARFM.	52
Figure 2.2. The cloud-free scenes are available for (a) Landsat and (b) Sentinel-2. Nine cloud-free scenes were collected for the Landsat data, and thirteen were collected for the Sentinel-2 data.	53
Figure 2.3. The LC map of Bavaria is obtained by combining multiple inputs of Landcover maps such as Amtliche Topographisch-Kartographische Informationssystem (ATKIS), Integrated Administration Control System (IACS) Corine LC, into one map.....	54
Figure 2.4. The average spatial correlations between the reference Landsat and Sentinel-2 NDVI with synthetic (a) L-MOD09Q1, (b) S-MOD09Q1, (c) L-MOD98GQ, (d) S-MOD09GQ, (e) L-MCD43A4, (f) S-MCD43A4 (g) L-MOD13Q1, and (h) S-MOD13Q1, NDVI time series for 2019 respectively.	63
Figure 2.5. The day of the year (DOY) based comparison of correlation coefficients between synthetic NDVI time series and the reference NDVI values obtained from (a) Landsat and (b) Sentinel-2 with different MODIS products.	64

List of Figures

Figure 2.6. The statistical comparison shows R^2 and RMSE values of different NDVI STARFM products obtained using (a,c) Landsat (L) and (b,d) Sentinel-2 (S) with varying products of MODIS, respectively.....	65
Figure 2.7. The scatter plots compare the accuracies of reference Landsat and Sentinel-2 products with synthetic (a) L-MCD43A4, (b) S-MCD43A4, (c) L-MOD98GQ, (d) S-MOD09GQ, (e) L-MOD09Q1, (f) S-MOD09Q1, (g) L-MOD13Q1, and (h) S-MOD13Q1 products, respectively.	66
Figure 2.8. Image-wise comparison of STARFM and real-time NDVI values from (a) MOD13Q1, (b) Landsat, (c) L-MOD13Q1, (d) Landsat minus L-MOD13Q1 (difference) (e) Sentinel-2, (f) S-MOD13Q1, and (g) Sentinel-2 minus S-MOD13Q1 (difference), on DOY 193 (12th July 2019).	71
Figure 2.9. The line and bar plots show the DOY-based and inter-quartile-range based comparison of STARFM generated NDVI values with their respective high-resolution input (Landsat (L) or Sentinel-2 (S)) and low-resolution input (a,b) MOD09Q1 (c,d) MOD09GQ, (e,f) MCD43A4, (g,h) MOD13Q1 respectively.	73
Figure 3.1. The conceptual framework of the study is divided into two parts: Part 1 states the data fusion for 2019 to investigate the synthetic NDVI time series product (this section is already completed in our previous study (Dhillon et al., 2022)), and Part 2 estimates and validates the crop yield for Bavaria by inputting the fused L-MOD13Q1 time series.....	88
Figure 3.2. An overview of the study region.	90
Figure 3.3. The cloud-free scenes are available for Landsat (in red box) and Sentinel-2 (in blue box) during the seasons of OSR and WW.	94
Figure 3.4. Field-wise comparison of STARFM and real-time NDVI values of (a) MOD13Q1, (b) Landsat 8, (c) L-MOD13Q1, (d) Sentinel-2, and (e) S-MOD13Q1 on DOY 145 (25th May 2019) on WW fields.	102
Figure 3.5. The (a) line and (b) bar plots show the DOY-based and interquartile-range-based comparison of STARFM-generated NDVI values with their respective high-resolution input (Landsat (L) or Sentinel-2 (S)) and low-resolution input MOD13Q1, respectively.	103
Figure 3.6. The scatter plots (a)-(l) compare the accuracies of LUE and WOFOST modelled yields (inputting the 8- and 16-day MOD13Q1, L-MOD13Q1 and S-MOD13Q1) with the referenced yield of WW.	106
Figure 3.7. The scatter plots (a)-(l) compare the accuracies of LUE and WOFOST modelled yields (inputting the 8- and 16-day MOD13Q1, L-MOD13Q1 and S-MOD13Q1) with the referenced yield of OSR.	107
Figure 3.8. The violin plots compare the crop yields of referenced (at 95% confidence interval) and modelled yields obtained from multi-source data (MOD13Q1, L-MOD13Q1, and S-MOD13Q1) at 8- and 16-days of temporal scales of (a,b) WW and (b,d) OSR using the (a,c) LUE and (b,d) WOFOST models in 2019.	108

Figure 3.9. The box plots compare the accuracies (a,c) R^2 , and (b,d) RMSE of referenced (at 95% confidence interval) and modelled yields obtained from multi-source data: MOD13Q1, L-MOD13Q1, and S-MOD13Q1, at temporal scales of 8- and 16-days.	109
Figure 3.10. Spatial distribution of referenced yields and the predicted yields for WW using MOD13Q1 (8- and 16-days), L-MOD13Q1 (8- and 16-days), and S-MOD13Q1 (8- and 16-days) with LUE and WOFOST models for the state of Bavaria.	110
Figure 3.11. The dot plots show the region-wise distribution of referenced yields and modelled yields obtained from multi-source data (MOD13Q1 (8- and 16-days), L-MOD13Q1 (8- and 16-days), and S-MOD13Q1 (8- and 16-days)) for WW using (a) LUE, (b) WOFOST, in 2019.	111
Figure 3.12. Spatial distribution of referenced yields and the predicted yield for OSR using MOD13Q1 (8- and 16-days), L-MOD13Q1 (8- and 16-days), and S-MOD13Q1 (8- and 16-days) with LUE and WOFOST models for the state of Bavaria.	111
Figure 3.13. The dot plots show the region-wise distribution of referenced yields and modelled yields obtained from multi-source data (MOD13Q1 (8- and 16-days), L-MOD13Q1 (8- and 16-days), and S-MOD13Q1 (8- and 16-days)) for OSR using (a) LUE, (b) WOFOST, in 2019.	112
Figure 3.14. The box plots show the comparison of accuracies (a,c) R^2 values and (b,d) RMSE values.	113
Figure 3.15. The dot plots show the comparison of accuracies (a) R^2 values, (b) RMSE, (c) RRMSE and (d) ME values obtained from the referenced yields (at 95% confidence interval) for LUE (dark blue) and WOFOST (dark pink) models.	114
Figure 3.16. The box plots compare the accuracies for (a) R^2 and (b) RRMSE of referenced (at 95% confidence interval) and modelled yields obtained from multi-source data using LUE and WOFOST models in 2019.	114
Figure 3.17. Visualization of field level biomass of L-MOD13Q1 and S-MOD13Q1 with 8-days, 16-days, and the difference (16-days – 8-days) obtained using the LUE model for (a) WW and (b) OSR.	115
Figure 4.1. The conceptual framework of the study is divided into three parts.	131
Figure 4.2. Overview of the study region.	133
Figure 4.3. The scatter plots (a–s) compare the accuracies of Landsat (referenced NDVI) with L-MOD13Q1 (synthetic NDVI) for 2001 to 2019.	144
Figure 4.4. The correlation plots between the total number of Landsat scenes per year (N) and (a) R^2 values and (b) RMSE values obtained during the accuracy assessment of referenced and synthetic NDVI products from 2001 to 2019.	144
Figure 4.5. The day of the year (DOY)-based comparison of correlation coefficients between (a) R^2 values and (b) RMSE values obtained during the accuracy assessment of referenced and synthetic NDVI products from 2001 to 2019.	144

List of Figures

Figure 4.6. The dot plots compare the accuracies (a) R^2 , (b) RMSE, and (c) ME of referenced data (at 95% confidence intervals) and modelled yields obtained from multi-source data: MOD13Q1 and L-MOD13Q1 in 2019. 145

Figure 4.7. The scatter plots compare the accuracies of modelled and referenced yields (at 95% confidence interval) of (a) WW and (b) OSR for 19 years together (i.e., from 2001 to 2019)..... 146

Figure 4.8. The scatter plots correlating the modelled yield and regional mean elevation for (a) WW and (b) OSR. The dashed line represents the regression line..... 147

Figure 4.9. The bar plots show the yearly comparison of accuracies (a) R^2 values and (b) RMSE values obtained from the referenced yields 148

Figure 4.10. Spatial distribution of mean referenced yield (2001-2019) and the year-wise predicted yield for WW from 2001 to 2019 using the LUE model for the state of Bavaria. 149

Figure 4.11. Spatial distribution of mean referenced yield (2001-2019) and the year-wise predicted yield for OSR from 2001 to 2019 using the LUE model for the state of Bavaria. 150

Figure 4.12. The dot plots show the district-wise distribution of modelled yield for (a) WW, (b) OSR, from 2001 to 2019..... 151

Figure 4.13. The line plots compare the accuracies with the mean yield percent difference (as calculated in Equation (4.9)) for WW and OSR for 19 years (i.e., from 2001 to 2019)..... 151

Figure 4.14. The bar plots compare the yearly (a) R^2 and (b) RMSE values, of estimated OSR yield (orange), WW yield (green) and synthetic NDVI (purple) from 2001 to 2019. The units of RMSE values of both WW and OSR yields are dt/ha..... 152

Figure 4.15. The correlation plots between R^2 of Synthetic NDVI time series and R^2 of modelled yield time series for (a) WW (green), and (b) OSR (orange), from 2001 to 2019. 152

Figure 4.16. The side-by-side visualisation of synthetic NDVI products obtained on June 18th of 2005, 2013 and 2019 (left) with the WW biomass obtained from the LUE modelled for the years of 2005, 2013 and 2019 (right). 153

Figure 5.1. Conceptual framework of the study that explains the methodology of four random forest (RF1, RF2, RF3 and RF4) models with different input requirements to predict crop yield for winter wheat (WW) and oil seed rape (OSR). 169

Figure 5.2. Overview of the study region with spatial information of Winter Wheat (WW) and Oil Seed Rape (OSR) fields (left)..... 171

Figure 5.3. Scatter plots of the validation of WW and OSR modeled yield using RF1 model with referenced yield..... 177

Figure 5.4. Scatter and bar plots of the validation of WW and OSR modeled yield with referenced yield and the variable importance using the RF2 model, respectively..... 178

Figure 5.5. Scatter plots of the validation of WW and OSR modeled yield using RF3 model with referenced yield..... 180

Figure 5.6. Bar plots of the variable importance of WW and OSR after validation of the modeled yield with referenced yield using the RF3 model.....	181
Figure 5.7. Scatter plots of the validation of WW and OSR modeled yield using LUE model with referenced yield.	182
Figure 5.8. Scatter plots of the validation of WW and OSR modeled yield using RF4 model with referenced yield.	184
Figure 5.9. Bar plots of the variable importance of WW and OSR after validation of the modeled yield with referenced yield using the RF4 model.....	185
Figure 5.10. Bar plots for the overall accuracy assessment of WW and OSR with four RF (RF1, RF2, RF3, RF4) and one LUE model with different input variables (shown in the legend at right). (a) R ² , (b) RMSE, (c) ME, and (d) RRMSE for WW and (e) R ² , (f) RMSE, (g) ME, and (h) RRMSE for OSR using different models with various inputs, respectively.....	186
Figure 5.11. Box plots show the comparison of the accuracy assessment of three satellite inputs (S-MOD13Q1 (10 m), L-MOD13Q1 (30 m) and MOD13Q1 (250 m)) used in four models (RF1, RF3, LUE and RF4) for yield prediction of WW (green) and OSR (orange). (a) R ² (b) RMSE (c) ME and (d) RRMSE.....	187
Figure 5.12. Spatial distribution of referenced yield and predicted yield for WW using RF1, RF2, RF3, LUE and RF4 models by inputting S-MOD13Q1 (10 m) for the state of Bavaria in 2019. The white color represents no data available. (a) Referenced Yield (b) RF4 (c) LUE, (d) RF3, (e) RF2, and (f) RF1.....	188
Figure 5.13. Spatial distribution of referenced yield and predicted yield for OSR using RF1, RF2, RF3, LUE and RF4 models by inputting S-MOD13Q1 (10 m) for the state of Bavaria in 2019. The white color represents no data available. (a) Referenced Yield (b) RF4 (c) LUE, (d) RF3, (e) RF2, and (f) RF1.....	189
Figure 6.1. The conceptual framework of the study is divided into three parts	201
Figure 6.2. Overview of the study region of Bavaria.....	202
Figure 6.3. The cloud-free scenes are available for Landsat during the seasons of OSR and WW in 2019.....	204
Figure 6.4. The scatter plots compare the accuracies of modelled and referenced yields for 21 quadrants using (a) real MOD13Q1 and (b) synthetic L-MOD13Q1 for OSR in 2019.	209
Figure 6.5. Spatial distribution of Shannon Diversity Index in Bavaria with 11 window sizes of 150, 250, 350, 450, 850, 950, 1050, 1350, 1750, 2150 and 2650 m.	210
Figure 6.6. The box plots show the distribution of Shannon Diversity Index values of mean (a,b), standard deviation (c,d), and range (e,f) at different window sizes (150, 250, 350, 450, 850, 950, 1050, 1350, 1750, 2150 and 2650 m) of both WW (a,c,e) and OSR (b,d,f), respectively.....	211
Figure 6.7. The correlation plots (a)-(k) show the relationship between the mean of Shannon Diversity Index and mean of the LUE modelled biomass on every field at	

List of Figures

different window sizes (150, 250, 350, 450, 850, 950, 1050, 1350, 1750, 2150 and 2650 m) for WW. 213

Figure 6.8. The correlation plots (a)-(k) show the relationship between the mean of Shannon Diversity Index and mean of the LUE modelled biomass on every field at different window sizes (150, 250, 350, 450, 850, 950, 1050, 1350, 1750, 2150 and 2650 m) for OSR. 214

Figure 6.9. The line plots show the correlation coefficient between (the mean, standard deviation, and range of) Shannon Diversity Index and the LUE modelled biomass on every field at different window sizes (150, 250, 350, 450, 850, 950, 1050, 1350, 1750, 2150 and 2650 m) for (a) WW and (b) OSR. SD is for standard deviation. 214

Figure 6.10. Spatial distribution of difference in landscape metrics between 2018 and 2019 in Bavaria at 750 m. 215

Figure 6.11. The box plots show the distribution of difference in landscape metrics between 2018 to 2019 values of mean (a), standard deviation (b), and range (c) at different window sizes (150, 250, 350, 450, 850, 950, 1050, 1350, 1750, 2150 and 2650 m) for OSR. 216

Figure 6.12. The correlation plots (a)-(k) show the relationship between the mean of difference in landscape metrics (i.e., 2019 minus 2018) and mean of the LUE modelled biomass on every field at different window sizes (150, 250, 350, 450, 850, 950, 1050, 1350, 1750, 2150 and 2650 m) for OSR. 217

Figure 6.13. The line plot shows the correlation coefficient between (the mean, standard deviation, and range of) the difference in landscape metrics and the LUE modelled biomass on every field at different window sizes (150, 250, 350, 450, 850, 950, 1050, 1350, 1750, 2150 and 2650 m) for OSR. SD is for standard deviation. 217

Figure 7.1. An overview stating the importance of satellite RS on predicting accurate crop yield predictions by providing certain field level benefits to farmers. 225

Figure A1. Detailed map of administrative regions of Bavaria. 240

Figure A2: Flowchart of the WOFOST model. 241

Figure A3. The digital elevation map of Bavaria. 242

Figure A4. The scatter plots (a)-(s) compare the accuracies of modelled and referenced yields of WW for 2001 to 2019. 244

Figure A5. The scatter plots (a)-(s) compare the accuracies of modelled and referenced yields of OSR for 2001 to 2019. The values of the statistical parameters such as R^2 , RMSE (dt/ha), and ME (dt/ha) are displayed at the top of each plot. 246

Figure A6. The regional scale average yield percent difference between the referenced and the modelled yield from 2001 to 2019 (a) WW, (b) OSR. 246

Figure A7. The correlation plots (a)-(k) show the relationship between the range of Shannon Diversity Index and range of the LUE modelled biomass on every field at different window sizes (150, 250, 350, 450, 850, 950, 1050, 1350, 1750, 2150 and 2650 m) for WW. 247

Figure A8. The correlation plots (a)-(k) show the relationship between the range of Shannon Diversity Index and range of the LUE modelled biomass on every field at different window sizes (150, 250, 350, 450, 850, 950, 1050, 1350, 1750, 2150 and 2650 m) for OSR. **248**

Figure A9. The correlation plots (a)-(k) show the relationship between the standard deviation of Shannon Diversity Index and standard deviation of the LUE modelled biomass on every field at different window sizes (150, 250, 350, 450, 850, 950, 1050, 1350, 1750, 2150 and 2650 m) for WW..... **249**

Figure A10. The correlation plots (a)-(k) show the relationship between the standard deviation of Shannon Diversity Index and standard deviation of the LUE modelled biomass on every field at different window sizes (150, 250, 350, 450, 850, 950, 1050, 1350, 1750, 2150 and 2650 m) for OSR..... **250**

Figure A11. The correlation plots (a)-(k) show the relationship between the standard deviation of difference in landscape metrics (i.e., 2019 minus 2018) and standard deviation of the LUE modelled biomass on every field at different window sizes (150, 250, 350, 450, 850, 950, 1050, 1350, 1750, 2150 and 2650 m) for OSR. **251**

Figure A12. The correlation plots (a)-(k) show the relationship between the range of difference in landscape metrics (i.e., 2019 minus 2018) and range of the LUE modelled biomass on every field at different window sizes (150, 250, 350, 450, 850, 950, 1050, 1350, 1750, 2150 and 2650 m) for OSR..... **252**

List of Tables

Table 2.1. A summary of the collected datasets.....	55
Table 2.2. The DOY-based statistical analysis (R^2 and mean RMSE) between the synthetic NDVI (for four different MODIS products) and reference Landsat (L) NDVI	68
Table 2.3. The DOY-based statistical analysis (R^2 and mean RMSE) between the synthetic NDVI (for four different MODIS products) and reference Sentinel-2 (S) NDVI	69
Table 3.1. A summary of the collected datasets for crop modelling of winter wheat’s (WW) and oil seed rape’s (OSR) in 2019.....	91
Table 3.2. The DOY-based statistical analysis (R^2 and mean RMSE) between the synthetic NDVI (for MOD13Q1 MODIS product) and reference Landsat (L) and Sentinel-2 (S) NDVI.....	95
Table 3.3. A summary of equations used to calculate LAI from NDVI satellite products for WW and OSR. These equations are derived from the growth stage of a crop till the flowering stage. The LAI product is used as an input to the WOFOST model.....	96
Table 3.4. Description of model calibration values taken from the related literature for the WOFOST and LUE models. Plus, the climate thresholds used to calculate the climate stress indexes used in the design of a model.	99
Table 4.1. A summary of the collected datasets for fusion modelling and winter wheat’s (WW) and oil seed rape’s (OSR) crop modelling.	134
Table 4.2. A summary of the collected cloud and shadow free Landsat 5, Landsat 7 and Landsat 8 datasets available every year with their day of the years (DOYs) between start- and end of the seasons of WW and OSR from 2001 to 2019.	137
Table 5.1. Summary of collected datasets for Winter Wheat (WW) and Oil Seed Rape (OSR) crop modelling.....	172
Table 5.2. Input requirements of different Random Forest (RF) models (RF1, RF2, RF3 and RF4) implemented using the package ‘randomForest’ in the software R. CV represents to climate variables.....	175
Table 6.1. A summary of the collected datasets for the study.....	203
Table 6.2. The DOY-based statistical analysis (R^2 and mean RMSE) between the synthetic NDVI (for MOD13Q1 MODIS product) and reference Landsat (L) NDVI in Bavaria.....	204
Table A1. A summary of linear regression equations used to calculate crop yield from biomass obtained from different satellite products (MOD13Q1, Landsat (L)-MOD13Q1 and Sentinel-2 (S)-MOD13Q1) for WW and OSR using LUE and WOFOST models. The yield obtained is in dt/ha.	252

List of Symbols and Abbreviations

List of Important Symbols Used

- A_i - first observation (unit depends on the variable being observed)
 α - significance level (unitless)
 A_m - gross assimilation rate (unit of carbon dioxide uptake per unit of time)
 B_i - second observation (unit depends on the variable being observed)
 C_e - conversion efficiency (unitless)
dt/ha - deciton per hectare (unit of biomass production)
 E - evapotranspiration (unit of water loss per unit of time)
 E_p - evaporation (unit of water loss per unit of time)
 ϵ - actual light use efficiency (unit of biomass produced per unit of absorbed light)
 ϵ_0 - optimal light use efficiency (unit of biomass produced per unit of absorbed light)
 H_0 - null hypothesis (no relationship)
 H_1 - alternative hypothesis (relationship exists)
 $\text{kg ha}^{-1} \text{ yr}^{-1}$ - kilogram per hectare per year (unit of biomass production)
kdf - diffusion coefficient (unit of area per unit of time)
m - meter (unit of length)
 N - number of Landsat scenes per year (unitless)
 n - total number of observations (unitless)
 O_i - observed value
 O' - observed mean
 P - precipitation
 P_i - predicted value
 P' - predicted mean
 R - correlation coefficient (unitless)
 R_a - extra-terrestrial radiation (unit of energy per unit of time per unit of area)
RH - relative humidity (unit of percentage)
RO - runoff (unit of water flow per unit of time)
 R_s - solar radiation (unit of energy per unit of time per unit of area)
 R^2 - regression coefficient (unitless)
 T_{\min} - minimum temperature (unit of temperature)
 $T_{\min \max}$ - maximum of minimum temperature (unit of temperature)
 $T_{\min \min'}$ - temperature stress (unitless)
 T_{\max} - maximum temperature (unit of temperature)
VPD min - minimum VPD (unit of vapor pressure deficit)
VPD max - maximum VPD (unit of vapor pressure deficit)
 Z_r - maximum root depth (unit of length)
 ρ_{NIR} - reflectance in the near-infrared band
 ρ_{Red} - reflectance in the red band
 ΔG - growth rate (unit of biomass production per unit of time)
 ξ - scattering coefficient

List of Important Abbreviations Used

AA - Amino Acid
APAR - Absorbed Photosynthetically Active Radiation
ATKIS - Amtliches Topographisch-Kartographisches Informationssystem
BRDF - Bidirectional Reflectance Distribution Function
CART - Classification and Regression Tree
CASA - Carnegie Ames Stanford Approach
CGMs - Crop Growth Models
CV - Climate Variables
DOY - Day of Year
DL - Deep Learning
ECMWF - European Centre for Medium-Range Weather Forecasts
EOS - End of Season
ERA - European Research Area
EROS - Earth Resources Observation and Science Center
ESTARFM - Enhanced Spatial and Temporal Adaptive Reflectance Fusion Model
EVI - Enhanced Vegetation Index
FAO - Food and Agriculture Organization
FSDAF - Flexible Spatiotemporal Data Fusion
FPAR - Fraction of Photosynthetically Active Radiation
HLS - Harmonized Landsat Sentinel
IACS - Integrated Administration and Control System
IPCC - Intergovernmental Panel on Climate Change
ISTARFM - Improved Spatial and Temporal Adaptive Reflectance Fusion Model
LC - Land Cover
LEDAPS - Landsat Ecosystem Disturbance Adaptive Processing System
LAI - Leaf Area Index
LP DAAC - Land Processes Distributed Active Archive Center
LRM - Linear Regression Model
LUE - Light Use Efficiency
MASI - Multi-Spectral Imagery
ME - Mean Error
ML - Machine Learning
MODIS - Moderate Resolution Imaging Spectroradiometer
MSI - Multi-Spectral Imagery
NBAR - Nadir Bidirectional Reflectance
NDBI - Normalized Difference Built-up Index
NDVI - Normalized Difference Vegetation Index
NDWI - Normalized Difference Water Index
NDYI - Normalized Difference Yellow Index
NIR - Near Infrared
NPP - Net Primary Productivity
OSR - Oil Seed Rape
OOB - Out-of-Bag
PAR - Photosynthetically Active Radiation

RF – Random Forest
RMSE - Root Mean Square Error
RRMSE - Relative Root Mean Square Error
RS - Remote Sensing
RVM - Relevance Vector Machine
SAR - Synthetic Aperture Radar
SD - Standard Deviation
SDGs - Sustainable Development Goals
SPOT - Satellite Pour l'Observation de la Terre
SOS – Start of Season
SPSTFM - Spectral and Spatial Temporal Fusion Model
SSFIT - Single-Site Data Fusion with Incomplete Data and Temporal Correlation
STAARCH - Spatial and Temporal Adaptive Algorithm for Mapping Reflectance Change
STM - Spatiotemporal-Metrics
STAIR - Spatial-Temporal Airborne Image Registration
STDFA - Space-Time Downscaling Factor Analysis
SWAP - Soil Water Atmosphere Plant model
SWIR - Shortwave Infrared
SUCROS - Simple and Universal Crop growth Simulator
TAW - Total Available Water
TM - Thematic Mapper
UAVs - Unmanned Aerial Vehicles
UTM - Universal Transverse Mercator
VI - Vegetation Index
VPD - Vapor Pressure Deficit
WW – Winter Wheat
WOFOST - World Food Studies

Summary

Accurate crop monitoring in response to climate change at a regional or field scale plays a significant role in developing agricultural policies, improving food security, forecasting, and analysing global trade trends. Climate change is expected to significantly impact agriculture, with shifts in temperature, precipitation patterns, and extreme weather events negatively affecting crop yields, soil fertility, water availability, biodiversity, and crop growing conditions. Remote sensing (RS) can provide valuable information combined with crop growth models (CGMs) for yield assessment by monitoring crop development, detecting crop changes, and assessing the impact of climate change on crop yields. This dissertation aims to investigate the potential of RS data on modelling long-term crop yields of winter wheat (WW) and oil seed rape (OSR) for the Free State of Bavaria (70,550 km²), Germany. The first chapter of the dissertation describes the reasons favouring the importance of accurate crop yield predictions for achieving sustainability in agriculture. Chapter second explores the accuracy assessment of the synthetic RS data by fusing NDVIs of two high spatial resolution data (high pair) (Landsat (30 m, 16-days; L) and Sentinel-2 (10 m, 5–6 days; S), with four low spatial resolution data (low pair) (MOD13Q1 (250 m, 16-days), MCD43A4 (500 m, one day), MOD09GQ (250 m, one-day), and MOD09Q1 (250 m, 8-days)) using the spatial and temporal adaptive reflectance fusion model (STARFM), which fills regions' cloud or shadow gaps without losing spatial information. The chapter finds that both L-MOD13Q1 ($R^2 = 0.62$, RMSE = 0.11) and S-MOD13Q1 ($R^2 = 0.68$, RMSE = 0.13) are more suitable for agricultural monitoring than the other synthetic products fused. Chapter third explores the ability of the synthetic spatiotemporal datasets (obtained in chapter 2) to accurately map and monitor crop yields of WW and OSR at a regional scale. The chapter investigates and discusses the optimal spatial (10 m, 30 m, or 250 m), temporal (8 or 16-day) and CGMs (World Food Studies (WOFOST), and the semi-empiric light use efficiency approach (LUE)) for accurate crop yield estimations of both crop types. Chapter third observes that the observations of high temporal resolution (8-day) products of both S-MOD13Q1 and L-MOD13Q1 play a significant role in accurately measuring the yield of WW and OSR. The chapter investigates that the simple light use efficiency (LUE) model ($R^2 = 0.77$ and relative RMSE (RRMSE) = 8.17%) that required

Summary

fewer input parameters to simulate crop yield is highly accurate, reliable, and more precise than the complex WOFOST model ($R^2 = 0.66$ and $RRMSE = 11.35\%$) with higher input parameters. Chapter four researches the relationship of spatiotemporal fusion modelling using STRAFM on crop yield prediction for WW and OSR using the LUE model for Bavaria from 2001 to 2019. The chapter states the high positive correlation coefficient ($R = 0.81$ and $R = 0.77$ between the yearly R^2 of synthetic accuracy and modelled yield accuracy for WW and OSR from 2001 to 2019, respectively. The chapter analyses the impact of climate variables on crop yield predictions by observing an increase in R^2 (0.79 (WW)/0.86 (OSR)) and a decrease in RMSE (4.51/2.57 dt/ha) when the climate effect is included in the model. The fifth chapter suggests that the coupling of the LUE model to the random forest (RF) model can further reduce the relative root mean square error (RRMSE) from -8% (WW) and -1.6% (OSR) and increase the R^2 by 14.3% (for both WW and OSR), compared to results just relying on LUE. The same chapter concludes that satellite-based crop biomass, solar radiation, and temperature are the most influential variables in the yield prediction of both crop types. Chapter six attempts to discuss both pros and cons of RS technology while analysing the impact of land use diversity on crop-modelled biomass of WW and OSR. The chapter finds that the modelled biomass of both crops is positively impacted by land use diversity to the radius of 450 (Shannon Diversity Index ~ 0.75) and 1050 m (~ 0.75), respectively. The chapter also discusses the future implications by stating that including some dependent factors (such as the management practices used, soil health, pest management, and pollinators) could improve the relationship of RS-modelled crop yields with biodiversity. Lastly, chapter seven discusses testing the scope of new sensors such as unmanned aerial vehicles, hyperspectral sensors, or Sentinel-1 SAR in RS for achieving accurate crop yield predictions for precision farming. In addition, the chapter highlights the significance of artificial intelligence (AI) or deep learning (DL) in obtaining higher crop yield accuracies.

Zusammenfassung

Die genaue Überwachung von Nutzpflanzen als Reaktion auf den Klimawandel auf regionaler oder feldbezogener Ebene spielt eine wichtige Rolle bei der Entwicklung von Agrarpolitiken, der Verbesserung der Ernährungssicherheit, der Erstellung von Prognosen und der Analyse von Trends im Welthandel. Es wird erwartet, dass sich der Klimawandel erheblich auf die Landwirtschaft auswirken wird, da sich Verschiebungen bei den Temperaturen, Niederschlagsmustern und extremen Wetterereignissen negativ auf die Ernteerträge, die Bodenfruchtbarkeit, die Wasserverfügbarkeit, die Artenvielfalt und die Anbaubedingungen auswirken werden. Die Fernerkundung (RS) kann in Kombination mit Wachstumsmodellen (CGM) wertvolle Informationen für die Ertragsbewertung liefern, indem sie die Entwicklung von Pflanzen überwacht, Veränderungen bei den Pflanzen erkennt und die Auswirkungen des Klimawandels auf die Ernteerträge bewertet. Ziel dieser Dissertation ist es, das Potenzial von RS-Daten für die Modellierung langfristiger Ernteerträge von Winterweizen (WW) und Ölraps (OSR) für den Freistaat Bayern (70.550 km²), Deutschland, zu untersuchen. Das erste Kapitel der Dissertation beschreibt die Gründe, die für die Bedeutung genauer Ernteertragsvorhersagen für die Nachhaltigkeit in der Landwirtschaft sprechen. Das zweite Kapitel befasst sich mit der Bewertung der Genauigkeit der synthetischen RS-Daten durch die Fusion der NDVIs von zwei Daten mit hoher räumlicher Auflösung (hohes Paar) (Landsat (30 m, 16 Tage; L) und Sentinel-2 (10 m, 5-6 Tage; S) mit vier Daten mit geringer räumlicher Auflösung (niedriges Paar) (MOD13Q1 (250 m, 16 Tage), MCD43A4 (500 m, ein Tag), MOD09GQ (250 m, ein Tag) und MOD09Q1 (250 m, 8 Tage)) unter Verwendung des räumlich und zeitlich adaptiven Reflexionsfusionsmodells (STARFM), das Wolken- oder Schattenlücken in Regionen füllt, ohne räumliche Informationen zu verlieren. In diesem Kapitel wird festgestellt, dass sowohl L-MOD13Q1 ($R^2 = 0,62$, RMSE = 0,11) als auch S-MOD13Q1 ($R^2 = 0,68$, RMSE = 0,13) für die Überwachung der Landwirtschaft besser geeignet sind als die anderen fusionierten synthetischen Produkte. Im dritten Kapitel wird untersucht, inwieweit die (in Kapitel 2 gewonnenen) synthetischen raum-zeitlichen Datensätze geeignet sind, die Ernteerträge von WW und OSR auf regionaler Ebene genau zu kartieren und zu überwachen. Das Kapitel untersucht und diskutiert die optimalen räumlichen (10 m, 30 m oder 250 m),

Zusammenfassung

zeitlichen (8 oder 16 Tage) und CGMs (World Food Studies (WOFOST) und den semi-empirischen Ansatz der Lichtnutzungseffizienz (LUE)) für genaue Ertragsschätzungen beider Kulturarten. Im dritten Kapitel wird festgestellt, dass die Beobachtung von Produkten mit hoher zeitlicher Auflösung (8 Tage) sowohl des S-MOD13Q1 als auch des L-MOD13Q1 eine wichtige Rolle bei der genauen Messung des Ertrags von WW und OSR spielt. In diesem Kapitel wird untersucht, dass das einfache Modell der Lichtnutzungseffizienz (LUE) ($R^2 = 0,77$ und relativer RMSE (RRMSE) = 8,17 %), das weniger Eingabeparameter zur Simulation des Ernteertrags benötigt, sehr genau, zuverlässig und präziser ist als das komplexe WOFOST-Modell ($R^2 = 0,66$ und RRMSE = 11,35 %) mit höheren Eingabeparametern. In Kapitel vier wird der Zusammenhang zwischen der raum-zeitlichen Fusionsmodellierung mit STRAFM und der Ertragsvorhersage für WW und OSR mit dem LUE-Modell für Bayern von 2001 bis 2019 untersucht. Das Kapitel stellt den hohen positiven Korrelationskoeffizienten ($R = 0,81$ und $R = 0,77$ zwischen dem jährlichen R^2 der synthetischen Genauigkeit und der modellierten Ertragsgenauigkeit für WW bzw. OSR von 2001 bis 2019 fest. In diesem Kapitel werden die Auswirkungen der Klimavariablen auf die Ertragsvorhersagen analysiert, wobei ein Anstieg des R^2 (0,79 (WW)/0,86 (OSR)) und eine Verringerung des RMSE (4,51/2,57 dt/ha) festgestellt werden, wenn der Klimaeffekt in das Modell einbezogen wird. Das fünfte Kapitel deutet darauf hin, dass die Kopplung des LUE-Modells mit dem Random-Forest-Modell (RF) den relativen mittleren quadratischen Fehler (RRMSE) von -8 % (WW) und -1,6 % (OSR) weiter reduzieren und das R^2 um 14,3 % (sowohl für WW als auch für OSR) erhöhen kann, verglichen mit Ergebnissen, die nur auf LUE beruhen. Das gleiche Kapitel kommt zu dem Schluss, dass die satellitengestützte Pflanzenbiomasse, die Sonneneinstrahlung und die Temperatur die einflussreichsten Variablen bei der Ertragsvorhersage für beide Kulturarten sind. In Kapitel sechs wird versucht, sowohl die Vor- als auch die Nachteile der RS-Technologie zu erörtern, indem die Auswirkungen der unterschiedlichen Landnutzung auf die modellierte Biomasse von WW und OSR analysiert werden. In diesem Kapitel wird festgestellt, dass die modellierte Biomasse beider Kulturen durch die Landnutzungsvielfalt bis zu einem Radius von 450 (Shannon Diversity Index $\sim 0,75$)

bzw. 1050 m (~0,75) positiv beeinflusst wird. In diesem Kapitel werden auch künftige Auswirkungen erörtert, indem festgestellt wird, dass die Einbeziehung einiger abhängiger Faktoren (wie die angewandten Bewirtschaftungsmethoden, die Bodengesundheit, die Schädlingsbekämpfung und die Bestäuber) die Beziehung zwischen den mit RS modellierten Ernteerträgen und der biologischen Vielfalt verbessern könnte. Im siebten Kapitel schließlich wird die Erprobung neuer Sensoren wie unbemannte Luftfahrzeuge, hyperspektrale Sensoren oder Sentinel-1 SAR in der RS erörtert, um genaue Ertragsvorhersagen für die Präzisionslandwirtschaft zu erreichen. Darüber hinaus wird in diesem Kapitel die Bedeutung der künstlichen Intelligenz (KI) oder des Deep Learning (DL) für die Erzielung einer höheren Genauigkeit der Ernteerträge hervorgehoben.

Chapter 1

General Introduction

1.1. Historical Background of Agriculture: A Journey from Neolithic Period to Modern Age

Agriculture today still plays a crucial role in human society, although it has changed significantly due to technological advancements and shifts in international economic systems. As soon as people learnt how to cultivate crops and domesticate animals to feed their basic requirements, it became an essential aspect of human civilization. The origins of agriculture can be traced back to the Neolithic period, around 10,000 BCE when humans ceased being nomadic, began to settle in one place and cultivate crops (Cauvin, 2000; Pringle, 1998; Vasey, 1992). In the Fertile Crescent, a region encompassing parts of present-day Iraq, Syria, and Turkey, people began cultivating wheat, barley, and other crops and domesticating animals such as sheep and goats (Vigne, Peters, & Helmer, 2005). The transition from a hunter-gatherer lifestyle to a more settled, agricultural one signified a profound change in human society. Agriculture eventually extended to other continents, including the Americas, China, and India. In China, rice cultivation became an essential part of the economy, while in the Americas, crops like maize, potatoes, and beans were cultivated (Butzer, 1992; Harlan, 1975). Early agricultural practices were rudimentary and involved simple tools like digging sticks and hoes (Hurt, 1987). Farmers used canal systems and irrigation in ancient Egypt to grow crops in the desert. Farmers frequently practiced slash-and-burn agriculture, removing woods by burning them and using the newly cleared ground for cropping. Farmers relied on rainwater for irrigation. These unsustainable methods frequently caused soil erosion and nutrient loss. But, to support the expanding human population, more sophisticated agricultural techniques emerged over time. In ancient Egypt, farmers employed irrigation and canal systems to raise crops in the desert. (Noaman & El Quosy, 2017). Crop rotation was employed by farmers in ancient Greece to increase soil fertility, while dung was utilized as a fertilizer in Rome (White, 1970). The three-field method, which rotated crops among three fields to maintain soil fertility, was established throughout the Middle Ages as agriculture continued to advance (Butzer, 1992). Ploughs and draft animals were also used more frequently, enabling farmers to

cultivate larger tracts of land. In the Renaissance, which lasted from the 14th to the 17th century, agricultural methods kept getting better (Brown, 1989; Miskimin, 1975, 1977). In order to cultivate new crops and create new equipment like the seed drill and the hoe that would increase agricultural production, the Dutch created a system of polders, or reclaimed land from the sea (Grigg, 1980). The 18th and 19th centuries saw the Agricultural Revolution, which spurred fast agricultural development (Gorlinski, 2012).

The era was fuelled by new technologies like the steam engine, which allowed for the mechanization of agriculture and the development of new crop varieties and fertilizers. The enclosure movement was one of the critical development of the Agricultural Revolution, where the large landowners enclosed their land and converted it to commercial agriculture (Bryer, 2004). The movement significantly impacted the development of agriculture in England, as it facilitated the growth of larger, more productive farms and paved the way for the modernization of agriculture (Timmer, 1988). However, it also had social and environmental consequences, including the displacement of rural communities and the loss of biodiversity and natural habitats. During the mid-20th century, from the 1940s to the 1970s, the rapid growth of the population and high demand for food led to the rise of the Green Revolution that took place (F. Wu & Butz, 2004). It was a period of significant agricultural advancements and technological innovations that increased agricultural productivity, especially in developing countries. The development and adoption of high-yielding crop varieties, chemical fertilizers, and improved irrigation systems characterized the Green Revolution. However, it also brought environmental threats, including the depletion of soil nutrients, the loss of biodiversity, and the displacement of small farmers, as it focused on large-scale and industrialized agriculture (Cleaver, 1972; Du Pisani, 2006). Today, significant investments in research and innovations helped to bring the era of modern agriculture characterized by large-scale commercial farming and the use of advanced technologies like genetically modified crops, precision agriculture, and automation (Altman & Hasegawa, 2011). These new agricultural technologies have been used to develop more sustainable, efficient, and resilient practices, including developing new crop varieties that are more resistant to pests, drought, and disease, as well as improving irrigation and fertilizer use efficiency (Koohafkan & Altieri, 2011). Even

though the rise of modern agriculture brought some positive advancements, due to an increase in the global population, agricultural land faces numerous challenges ranging from climate change and soil degradation to water scarcity, loss of biodiversity, food security, rural poverty, and health risks.

1.2. Agriculture: Challenges and Solutions

Agriculture is a fundamental aspect of human civilization and is crucial in ensuring food security for the world's growing population (Thrupp, 2000). According to the United Nations (UN), the current global population as of February 2023 is approximately 7.97 billion people. The UN projects that the world's population will continue to grow and is expected to reach 9.7 billion by 2050 (Laurance & Engert, 2022) (Figure 1.1a,b). The increase in the world's population is directly proportional to the increase in demand for food. The period from 1961 to 2020 has witnessed a significant increase in global crop yields. According to data from the Food and Agriculture Organization of the United Nations (FAO), global cereal yields increased from an average of 1.23 tonnes per hectare in 1961 to 3.89 tonnes per hectare in 2020, representing an increase of over 215% (Figure 1.1c,d). The population growth will likely put pressure on food systems and supply chains, which will make ensuring food security for everyone more challenging. It could also exacerbate social inequalities and increase poverty and hunger, as the global hunger index score for 2021 was 20.0, considered "serious", and represents an increase from the previous year's score of 18.2 (Index, 2022) (Figure 1.1e). The 2021 report showed that 2020 was particularly challenging for global food security, with the COVID-19 pandemic exacerbating food insecurity and malnutrition. The report also highlighted the impact of climate change on food security, with extreme weather events such as droughts and floods becoming more frequent and severe. According to the report, 9.9% of the world's population, or around 768 million people, were undernourished in 2020 (Figure 1.1f). The report also showed that nearly one in five children under five were stunted, meaning they have a low height due to malnutrition. In addition, the report highlighted the growing problem of obesity and overweight, particularly in middle and high-income countries.

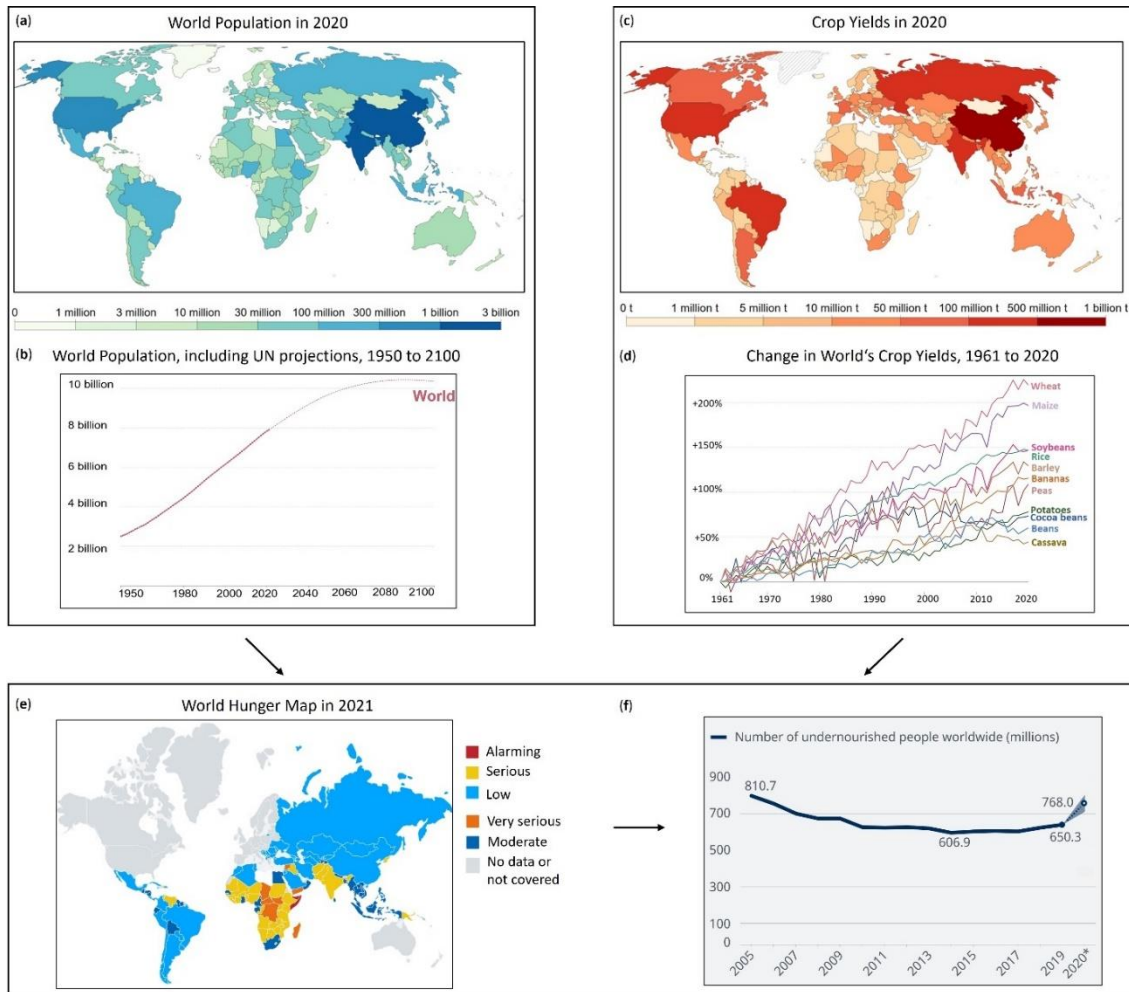


Figure 1.1. The diagram shows the (a) world population in 2020, (b) the UN population projection until 2100 (<https://population.un.org/wpp/Download/>, accessed on 20 March 2023), (c) world crop yields in 2020, (d) change in world's crop yields from 1961 to 2020 (<http://www.fao.org/faostat/en/#data>, accessed on 20 March 2023), (e) global hunger map 2021, and (f) number of undernourished people worldwide from 2005 to 2020 (<https://www.dw.com/en/pandemic-climate-change-and-conflict-fuel-sharp-rise-in-global-hunger/a-59488549>, accessed on 20 March 2023). The crop yield charts are prepared by (Ritchie, Roser, & Pablo, 2022).

Chapter 1

As the population continues to rise, there is a growing demand for food, fuel, and other agricultural products, which has led to the expansion of agricultural lands and intensified agricultural practices. This expansion and intensification of agriculture has led to the destruction and fragmentation of natural habitats, severely impacting biodiversity (Pellegrini & Fernández, 2018; Raven & Wagner, 2021). The loss and degradation of natural habitats due to agricultural expansion have resulted in a decline in the populations of many plant and animal species. These species are either directly affected by habitat destruction or indirectly affected by changes in ecosystem dynamics, such as soil degradation and water availability (Maitima et al., 2009; Potts et al., 2010). Additionally, the intensification of agricultural practices, such as chemical fertilizers, pesticides, and genetically modified crops, can significantly impact biodiversity (Y. Liu, Pan, & Li, 2015). For example, pesticides can kill non-target species, such as beneficial insects and birds, while fertilizers can lead to nutrient imbalances in the soil, affecting plant growth and nutrient uptake. Moreover, monoculture farming practices, where only one crop is grown on a large land area, can lead to a loss of plant diversity, affecting the composition of plant communities and ecosystem functioning (Tilman, 2001). The loss of plant diversity can also impact food availability and habitat availability for wildlife species.

As a crucial driver of climate change, agriculture is responsible for around one-quarter of the world's greenhouse gas emissions (Arcipowska, Mangan, Lyu, & Waite). Moreover, climate change is expected to significantly impact agriculture, with shifts in temperature, precipitation patterns, and extreme weather events negatively affecting crop yields, soil fertility, water availability, and crop growing conditions. Higher temperatures can reduce yields and alter the timing of planting and harvesting (Howden et al., 2007; Olesen et al., 2011). The global monthly mean temperature has been steadily increasing since the mid-19th century, according to data from the National Oceanic and Atmospheric Administration (NOAA). From 1851 to 2020, the mean temperature increased by about 1.5°C, with the rate of increase accelerating in recent decades (Figure 1.2). At the same time, changes in precipitation trends can lead to droughts, floods, and other extreme weather events that can damage crops. Climate change can also affect soil fertility, as extreme climatic events can alter the nutrient

content and structure of the soil, which can impact a crop's ability to absorb water and nutrients from it, leading to reduced yields (Rosenzweig, Iglesias, Yang, Epstein, & Chivian, 2001).

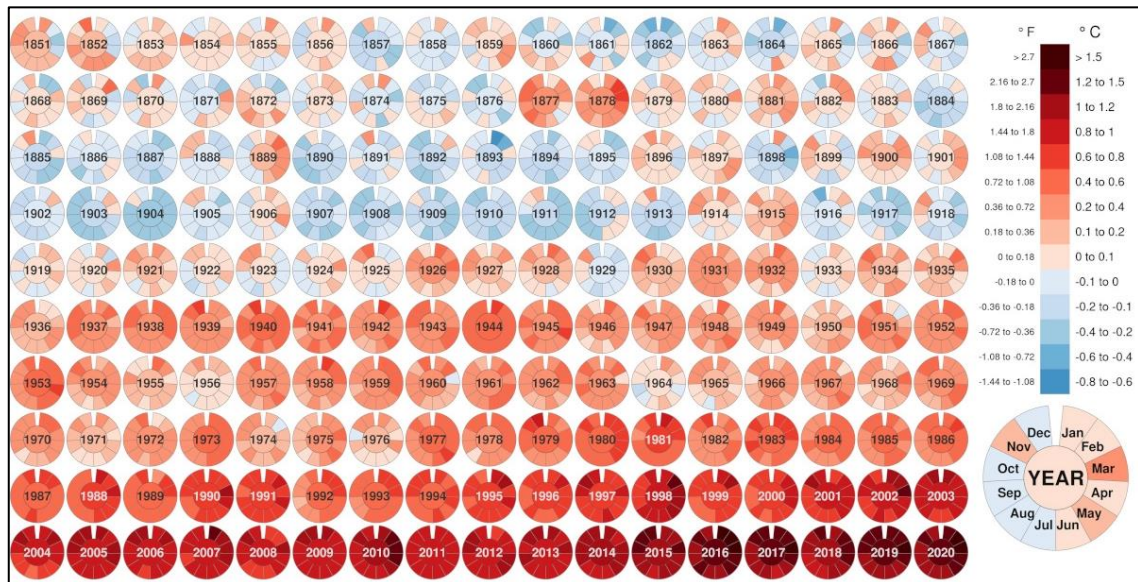


Figure 1.2. Global monthly mean temperature graph from 1851 to 2020 (<https://www.visualcapitalist.com/global-temperature-graph-1851-2020/>, accessed on 20 March 2023).

Additionally, changes in precipitation and evaporation rates can reduce the water available for irrigation, leading to water scarcity and lower crop yields (Howden et al., 2007). Moreover, climate change can affect the prevalence of pests and diseases that affect crops (Figure 1.3). Warmer temperatures can increase the survival rates of pests, while changes in rainfall patterns can alter the distribution of pests and their natural enemies (Skendžić, Zovko, Živković, Lešić, & Lemić, 2021).

Another significant challenge of agriculture is its impact on human health. Using chemical fertilizers and pesticides can lead to food contamination and health hazards, particularly in developing countries, where regulations are often lax (Levy, 2006). In addition, agriculture significantly impacts society, particularly regarding food security and rural poverty. The rise in demand for agricultural products has led to a concentration of wealth and power in the hands of a few giant agribusiness corporations, leaving small farmers and rural communities at a disadvantage (Figure 1.3).

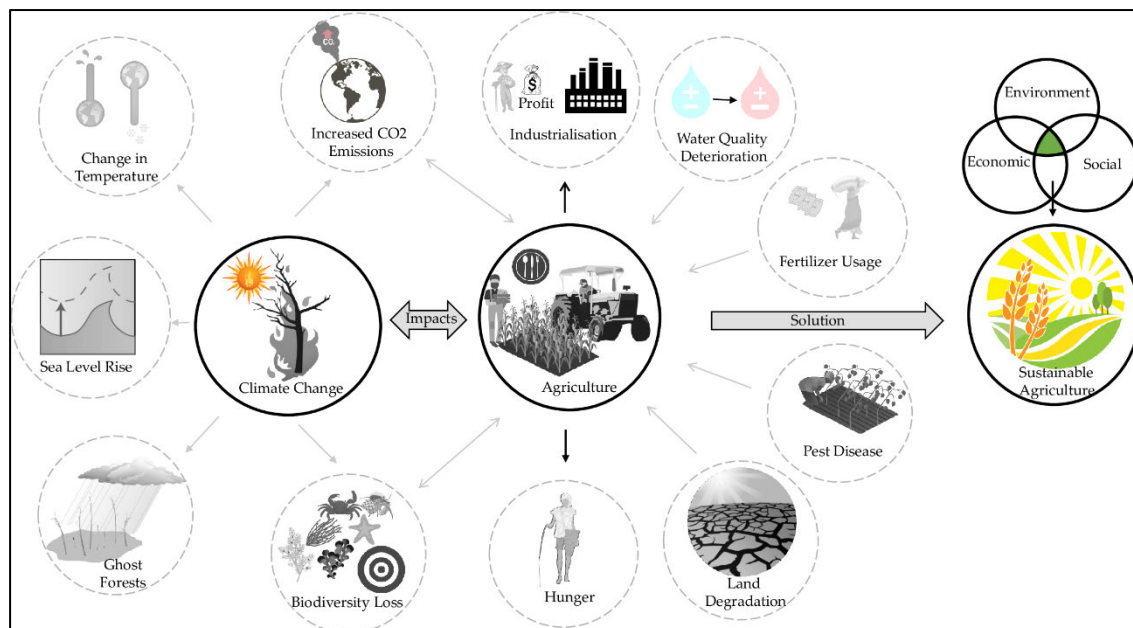


Figure 1.3. The flowchart shows the impact of climate change on agriculture. Several symbols, which were used to generate the infographic, were adopted or modified according to courtesy of the Integration and Application Network, University of Maryland Center for Environmental Science (<https://ian.umces.edu/symbols/>, accessed on 20 March 2023).

Despite all these challenges, sustainable agricultural practices help regain our lost resources by improving soil health, promoting biodiversity, and conserving water and other natural resources vital for maintaining healthy ecosystems (Basiago, 1995; McNeely & Scherr, 2003). Achieving sustainability in agriculture is a multifaceted approach that addresses agriculture's economic, social, and environmental dimensions (Figure 1.3). Sustainability in agriculture can be achieved in various ways. For example, (i) investing in agroecology that promotes the use of ecological principles and methods to manage agricultural ecosystems, (ii) reducing the use of agrochemicals, promoting integrated pest management, and using sustainable land-use practices such as conservation agriculture and agroforestry, and (iii), enhancing strategies to improve soil health include reducing tillage, using cover crops, and promoting soil organic matter (Altieri & Toledo, 2005; Kassam & Kassam, 2020). Moreover, sustainable agriculture must also ensure that food is available, accessible, and nutritious for all people.

1.3. The Impact of Crop Yield Predictions on Sustainable Agriculture

Agriculture is a crucial sector for human well-being and economic development, but it also poses significant challenges to the environment, human health, and social welfare. Addressing these challenges will require a collective effort by governments, civil society, and the private sector to promote sustainable agricultural practices that protect the environment, ensure food security, and promote social and economic justice. The FAO is a specialized agency of the United Nations that works to achieve agricultural sustainability by promoting sustainable agriculture, fisheries, and forestry practices. FAO provides technical assistance, policy guidance, and capacity building to member countries to help them achieve their sustainable development goals (SDGs) that are essential in promoting sustainable agriculture (Bebbington & Unerman, 2018; Bexell & Jönsson, 2017). The SDGs provide a framework for action to address the challenges facing agriculture and promote ecological agriculture practices. The SDGs relevant to agriculture include SDG 2 (Zero Hunger), which aims to end hunger and promote food security, and SDG 15 (Life on Land), which aims to "restore, protect, and promote sustainable use of terrestrial ecosystems, and reverse land degradation and biodiversity loss". The SDGs guide policymakers, farmers, and other stakeholders to develop and implement sustainable agriculture practices. They also provide a platform for collaboration between different sectors and stakeholders to promote sustainable agriculture and achieve food security. Additionally, sound investments in research and innovation can help identify and develop new agricultural technologies and practices that are more sustainable, efficient, and resilient.

Crop yield predictions have emerged as critical in promoting sustainable agriculture, providing farmers with vital information about the potential yields of their crops and allowing them to make better decisions about the resources required to maximize yields (Sivakumar, Gomme, & Baier, 2000). By accurately estimating crop yields, farmers can optimize their use of inputs such as water, fertilizers, and pesticides, reducing the environmental impact of agriculture, which, in turn, helps to conserve natural resources and preserve the health of surrounding ecosystems. Additionally,

Chapter 1

yield predictions can help farmers to identify potential issues before they become significant problems, such as pest infestations or disease outbreaks, allowing them to take action to mitigate their impact (Pinter Jr et al., 2003).

Yield predictions can also be essential in promoting economic growth and improving farmers' livelihoods. Farmers can plan their harvests and negotiate better prices for their produce by providing accurate yield estimations, which, in turn, help to increase their income and improve their standard of living, making it easier for them to invest in sustainable farming practices (Dasgupta, Saha, Venkatasubbu, & Ramasubramanian, 2020; de Sousa et al., 2021). Yield predictions support farmers in identifying which crops are most suitable for their region or climate, enabling them to diversify their crops and reduce their reliance on a single crop which can be vulnerable to fluctuations in weather patterns or market demand (Dasgupta et al., 2020).

Moreover, researchers can create new methods and technology to increase crop output with the use of precise crop yield projections. This can involve creating crops that can withstand droughts, enhancing irrigation systems, and creating fertilizers and insecticides that are more effective. By predicting crop yields, policymakers can allocate resources like land, water, and fertilizers in an efficient manner (Boelens & Vos, 2012). Agricultural yield forecasts can also influence market and trade policy decisions. Accurate forecasts can assist decision-makers in anticipating supply and demand mismatches and in taking actions to control prices and guarantee a reliable supply of food. Accurate crop output forecasts can assist policymakers in adjusting to changing conditions as climate change continues to affect agriculture (Bryan, Deressa, Gbetibouo, & Ringler, 2009). Policymakers can take action to reduce the negative effects of climate change on food production by having a better grasp of how crops will fare under various climate scenarios (G. C. Nelson et al., 2010). As such, efforts to develop and refine crop yield prediction methods are essential for promoting sustainable agriculture and ensuring the long-term health of our planet.

1.4. Potential Methods in Science for Accurate Crop Yield Predictions

Accurate crop monitoring in response to climate change at a regional or field scale plays a significant role in developing agricultural policies, improving food security, forecasting, and analysing global trade trends (Jeong et al., 2016). It is essential to investigate the potentials and challenges of new and old methods, and data which have massive potential in achieving accurate crop yield predictions with the increasing pace of technological growth due to advances in computing power, artificial intelligence, and other vital areas (Figure 1.4). For example, many studies in the last two decades have started to examine the relationship between plants and their growing environment and propose crop models to simulate the crop growth status (Boogaard, De Wit, Te Roller, & Van Diepen, 2011; Brisson et al., 2003; Franko, Puhlmann, Kuka, Böhme, & Merbach, 2007; Jones et al., 2003; Keating et al., 2003; Nendel et al., 2011; Steduto, Hsiao, Raes, & Fereres, 2009; Stöckle, Donatelli, & Nelson, 2003). Since then, crop models have advanced in monitoring crop growth from the qualitative to the quantitative level and modified from the simulation of the growth process at a plant level to the field and regional level. Crop modelling uses mathematical equations to simulate crop growth and development under different scenarios, taking temperature, precipitation, soil conditions, and crop management practices into consideration (Kasampalis et al., 2018). Farmers can make informed decisions about crop management using crop yield models, such as determining the optimal planting time, fertilization rates, and irrigation scheduling, which can help maximize crop yields while minimizing resource use (Figure 1.4).

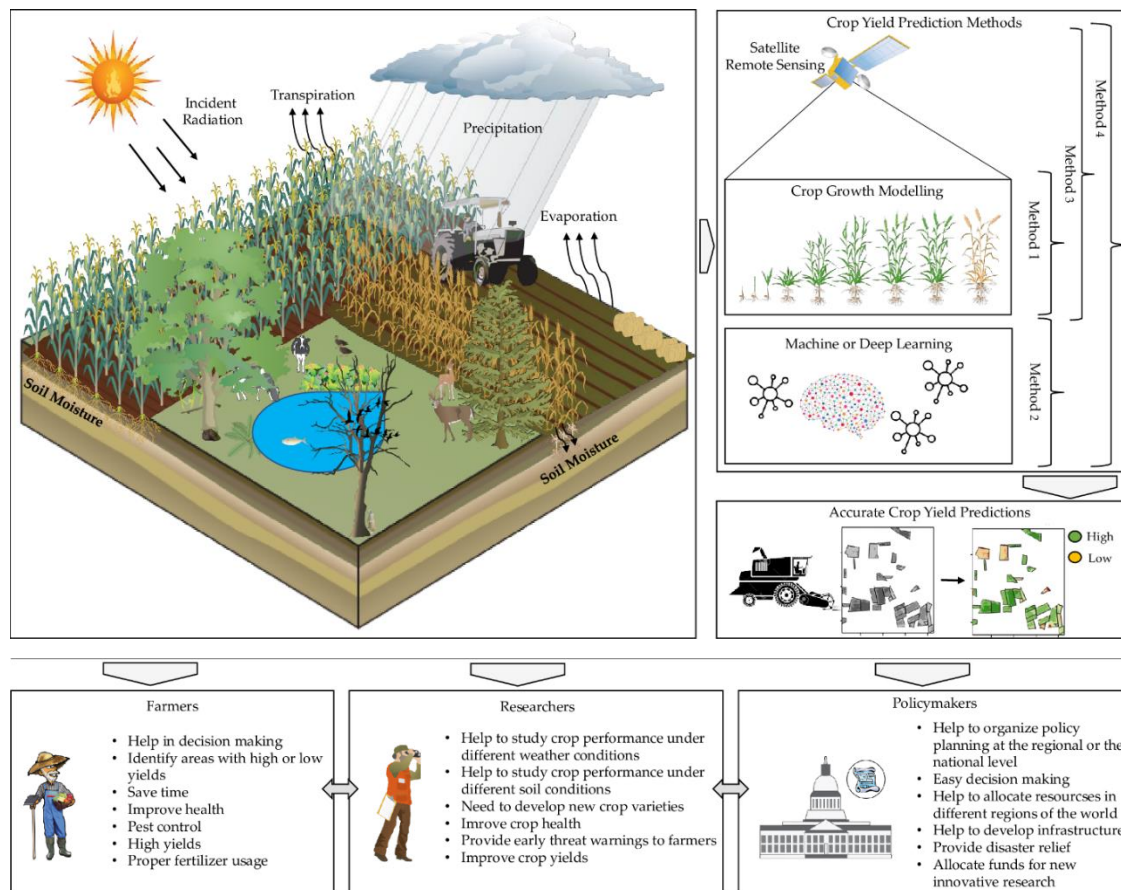


Figure 1.4. A flow diagram showing crop cycle used by different methods to predict crop yields. Method 1 uses crop growth models, method 2 uses machine or deep learning algorithms, method 3 integrates satellite remote sensing with crop growth modelling, and method 4 couples’ remote sensing, crop growth modelling, and machine or deep learning to accurately predict crop yields. Several symbols, which were used to generate the infographic, were adopted or modified according to courtesy of the Integration and Application Network, University of Maryland Center for Environmental Science (<https://ian.umces.edu/symbols/>, accessed on 20 March 2023).

Moreover, crop models can predict the potential impact of climate change on crop production, providing farmers with insights into how they can adapt their practices to cope with changing conditions. Over time, many crop growth models (CGMs) such as World Food Studies (WOFOST), Agricultural Production Systems Simulator (APSIM), AquaCrop, Cropping Systems Simulation Model (CropSyst), Light Use Efficiency (LUE) have been refined and updated to simulate better crop growth status and yield (Boogaard et al., 2011; Dhillon et al., 2020; Jin et al., 2018; Kasampalis et al., 2018; Keating et al., 2003; J. L. Monteith, 1972; John Lennox Monteith, 1977; Steduto et al., 2009; Stöckle et al., 2003). However, when crop yields are examined at field scales, CGMs need to account for the spatial variation by providing the spatial distribution of climate variables (temperature, precipitation, soil moisture) and biophysical parameters (leaf

area index (LAI), biomass, fraction of absorbed photosynthetic active radiation (FPAR)) (Hansen & Jones, 2000). The unavailability of spatial information in crop modelling causes uncertainties that affect the whole model's physiological growth simulation process and lead to more significant errors in crop yield estimation (J. Huang et al., 2019; Jin et al., 2018).

As an alternative, Remote Sensing (RS), the emerging technology revolutionizing agriculture, have a vast potential to provide both spatial and temporal information about a crop to CGMs (J. Huang et al., 2019). RS involves using sensors and imaging devices mounted on aircraft, drones, and satellites to collect information about crops and their environment (Figure 1.4). Coupling CGMs and RS provides farmers with valuable information on crop health, yield prediction, and environmental conditions, allowing them to make more informed decisions about crop management (Dhillon et al., 2020; Kasampalis et al., 2018; Mirschel, Schultz, Wenkel, Wieland, & Poluektov, 2004; Murthy, 2004; Zhuo et al., 2022). For example, they can detect changes in plant growth patterns and colour, indicating the presence of pests and diseases. This can help farmers to take action to prevent or mitigate damage to their crops before it becomes widespread.

Moreover, RS can help farmers to optimize resource use, such as water and fertilizers. Farmers can adjust their irrigation and fertilization practices to reduce waste and increase yields by providing information about soil moisture and nutrient levels. RS can also help farmers to identify specific areas of their fields that require water or fertilizers, enabling them to apply resources more efficiently. Another significant benefit of RS is its ability to provide farmers with real-time information about weather conditions, enabling them to make informed decisions about planting, harvesting, and other critical activities. It can also help farmers track their crops' growth and development over time, providing insights into long-term trends and enabling them to make more informed decisions about crop rotations and other practices (Patnaik, Sen, & Mahmoud, 2020).

RS technology has advanced significantly, improving our ability to observe and understand our planet. It provides access to vast amounts of data, but selecting the most

Chapter 1

appropriate dataset for a particular application requires careful consideration as each dataset has its own unique advantages and limitations. For instance, commercial datasets such as DigitalGlobe (0.30 to 1.5 m, days to weeks) and Planet (3 to 5 m, daily) offer higher spatial and temporal resolution and are used for various applications, including disaster response, urban planning, and infrastructure, but they come at a cost (Cadamuro, 2020; Jackson, 2020). On the other hand, openly accessible optical datasets such as Landsat (30 m, 16-days) and Sentinel-2 (10 m, 5-6 days) are widely used for monitoring land cover (LC) and land use changes, vegetation dynamics, and environmental monitoring (Lasaponara et al., 2022). However, they are affected by the presence of clouds which can reduce the quality of the imagery. In addition, MODIS (Moderate Resolution Imaging Spectroradiometer) is a key instrument aboard two NASA Earth Observing System satellites that have been in operation since 2000. With a temporal resolution of one to 16-days and a spatial resolution of 250 to 1000 m, MODIS data are freely accessible. The datasets have been used to track changes in vegetation, climate change, and LC and land use (Jabal, Khayyun, & Alwan, 2022; Kumar & Arya, 2021). However, the disadvantage of having low spatial resolution makes it less suitable for detailed analysis.

Because the optical data can suffer from significant gaps in the data record due to cloud and shadow cover that can cause uncertainties in the retrieved set of parameters (Dhillon et al., 2022; Whitcraft, Vermote, Becker-Reshef, & Justice, 2015; Wiseman, McNairn, Homayouni, & Shang, 2014), the spatiotemporal data fusion can help fill the data gaps in the RS data (Figure 1.5). Combining data from multiple sensors with different spatial and temporal resolutions makes it possible to obtain a more complete picture of the area of interest. For example, some sensors may have a higher spatial resolution but a lower temporal resolution, while others may have the reverse. Fusing the data from these sensors makes it possible to fill gaps in the data. Spatio-temporal data fusion can help to reduce the noise and errors in the data caused by the different sources. Integrating data from multiple sources can reduce errors caused by atmospheric conditions, sensor calibration, and other factors, which can lead to more accurate and reliable data. Importantly, the data fusion methods can help improve the accuracy of crop yield predictions by providing a complete and more accurate picture

of the crop health and growth conditions (Dhillon et al., 2022; Dhillon et al., 2020; Li et al., 2021). Combining data from multiple sources makes it possible to monitor crop growth and health better and identify areas that may be impacted by data gaps.

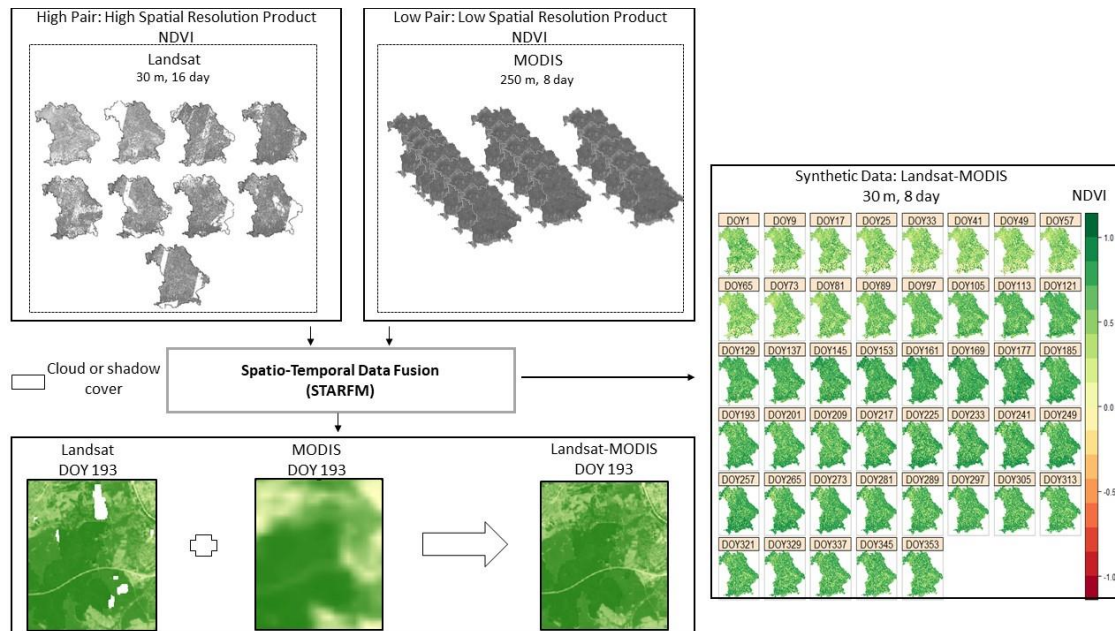


Figure 1.5. Flowchart shows an example of the spatio-temporal data fusion combining different satellite data together to fill cloud and shadow gaps of high spatial resolution sensor. The example shows a fusion of the cloudy Landsat NDVI time series with the MODIS dataset in Bavaria. The synthetic cloud and shadow free NDVI data generated was 30 m with a temporal frequency of 8-days.

Since 2006, many spatiotemporal fusion models have been developed. An important initiative in fusion modelling was started by (F. Gao, Masek, Schwaller, & Hall, 2006), who created the spatial and temporal adaptive reflectance fusion model (STARFM) to blend data from MODIS and Landsat surface reflectance. Since then, STARFM has been one of the most widely used algorithms in literature for detecting vegetation change over large areas (Cui, Zhang, & Luo, 2018; Lee, Cheon, & Eo, 2019; Xie et al., 2016; L. Zhu, Radeloff, & Ives, 2017). Despite the development of several spatiotemporal models, including Enhanced STARFM (ESTARFM) and Improved STARFM (ISTARFM), STARFM has been demonstrated to be superior to other spatiotemporal fusion algorithms in terms of accuracy and consistency. (Emelyanova, McVicar, Van Niel, Li, & Van Dijk, 2013; F. Gao et al., 2006; Hilker et al., 2009; B. Huang & Song, 2012; Luo, Guan, & Peng, 2018; M. Wu, Niu, Wang, Wu, & Wang, 2012; X. Zhu, Chen, Gao, Chen, & Masek, 2010; X. Zhu et al., 2016). As a result, it remains a favoured choice among researchers and practitioners in RS applications. While STARFM is

Chapter 1

recognized for its ability to fuse Landsat and MODIS images, its effectiveness for fusing Sentinel-2 and MODIS images in heterogeneous landscapes is not yet established. Furthermore, the potential of synthetic data generated through STARFM for predicting crop yield using crop modelling techniques remains unexplored.

Another critical data that has a high impact on the accuracy of crop yield estimations is the climate data. Climate data is crucial in accurate crop yield predictions (Hoogenboom, 2000). Climate, including temperature, precipitation, humidity, and sunlight, significantly impact crop growth and development and can affect various stages of the crop cycle, from planting to harvest. Accurate climate data, such as historical weather patterns and long-term climate projections, can be used as inputs to CGMs to estimate the impact of climate on crop yield (Kephe, Ayisi, & Petja, 2021). For example, if there is a drought or excessive rainfall during a growing season, it can have a significant impact on crop growth, leading to lower yields. Climate data can also be used to integrate with CGMs by taking account of historical climate patterns, along with other factors such as soil characteristics and crop management practices, to forecast crop yield for future seasons. These models can help farmers and agricultural experts make more informed decisions about planting schedules, irrigation, and fertilization, among other things (Shelia et al., 2019).

Crop yield prediction at local, regional, and global scales has been conducted based on both RS and climate data (Schwalbert et al., 2020). Temperature, evaporation, transpiration, solar radiation, and precipitation, as well as normalized difference vegetation index (NDVI) and LAI, are generally considered the primary climatic and satellite-based input variables used in CGMs (Kern et al., 2018; Shammi & Meng, 2021). Previous studies have performed a sensitivity analysis to evaluate the impact of climate parameters on crop yield predictions (N. Kim et al., 2019; J. Wang, Li, Lu, & Fang, 2013b). However, there is still a gap in research regarding the impact of climate factors on crop yields modelled using synthetic remote sensing data. Additionally, it is necessary to investigate the annual impact of climate variables on crop yields predicted through remote sensing-based crop modelling. In addition, studies have used machine, or deep learning (ML/DL) approaches to investigate the impact of individual climate elements in crop predictions (Dhillon, Dahms, Kuebert-Flock, et al., 2023).

ML and DL have a significant role in accurate crop yield predictions. By analysing large amounts of data, these techniques can help identify patterns and relationships between different variables that affect crop yield, such as weather patterns, soil quality, and fertilizer application. One common approach in using ML for crop yield prediction is to create predictive models that consider historical crop yield data and data on weather conditions, soil composition, and other factors that affect crop growth. These models can then predict crop yield for future growing seasons. They can process and analyse large amounts of data from various sources, such as satellite imagery and sensor data, to identify patterns and relationships that may not be immediately apparent to the human eye. It can help farmers and agricultural experts make more informed decisions about crop management practices, such as when to plant and harvest crops and apply fertilizers and pesticides. Numerous ML algorithms (such as linear regression, decision tree, and random forest (RF)) were applied to the RS data for various applications like flood mapping and detection and prediction of agronomic variables (Basso & Liu, 2019; Haque, Abdelgawad, Yanambaka, & Yelamarthi, 2020; Khaki & Wang, 2019; Khaki, Wang, & Archontoulis, 2020). Most ML applications have been focused on its utility as a classification tool, with limited studies exploring its regression capabilities for predicting crop yields (Fukuda et al., 2013; Mutanga, Adam, & Cho, 2012; Vincenzi et al., 2011). However, some studies found that the ML approaches could overfit data, making it unstable for crop yield estimation (Breiman, 2001; Segal, 2004). Even though CGMs have a reasonable prediction accuracy, they are not readily applicable due to the data calibration requirements, long runtimes, and data storage constraints (Drummond, Sudduth, Joshi, Birrell, & Kitchen, 2003; Puntel et al., 2016; Shahhosseini, Martinez-Feria, Hu, & Archontoulis, 2019). Moreover, their specified designs restrict them to considering only limited climate parameters, whereas the other essential climate elements were neglected, which might benefit from further increasing the prediction accuracy. Therefore, coupling ML models with CGMs, combining high-resolution satellite data and climate data could be tested by training an ML algorithm with the output of a crop model so that the ML model can have the potential of overfitting issues within the range of training data (Dhillon, Dahms, Kuebert-Flock, et al., 2023).

Chapter 1

Although the research on coupling synthetic RS with CGMs for crop yield estimations has made significant strides in recent years, several areas still require further investigation. Addressing these research gaps is essential for developing a more comprehensive understanding of the potential synthetic remote sensing in accurately predicting crop yields and informing evidence-based practices and policies.

In recent years, the availability of satellite data has significantly increased, and new technologies have emerged, presenting the opportunity to generate and analyse a vast amount of data with varying spatial, temporal, and spectral resolutions. Despite this progress, the potential of STARFM generating cloud and shadow-free high spatial resolution NDVI time series by replacing Landsat with Sentinel-2 still needs to be studied, as STARFM is not only restricted to MODIS and Landsat data. In addition, many studies have used STARFM for homogeneous landscapes; however, the accuracy assessment of the fusion model for heterogeneous landscapes by inputting it with a detailed and comprehensive LC map for different land use classes is still not assessed. Moreover, there is still a need to investigate the essential prerequisites for effectively predicting crop yields using newly generated synthetic data, particularly regarding their appropriate spatial (10 m or 30 m or 250 m) or temporal (8-or 16-day) resolutions. Also, research on the influence of climate variables on crop yields predicted through RS-based crop modelling using synthetic data is still insufficient.

Even though many studies coupled CGMs and synthetic RS data and achieved significant results in crop yield predictions (Dhillon et al., 2020; Kasampalis et al., 2018; Mirschel et al., 2004; Murthy, 2004; Zhuo et al., 2022), to adequately justify their models' reliability, stability, and preciseness, very few studies have consistently tested their methodologies for yield prediction for two decades. Moreover, there is a need to explore the impact of fused NDVI time series on the accuracy of yield predictions over longer time periods. Also, an investigation is needed to determine the annual impact of climate factors on crop yields. Previous literature found that ML models positively affect the accuracy of crop yields (De'ath & Fabricius, 2000); however, coupling ML with CGMs to increase the accuracy of crop yield predictions using the synthetic RS data still needs to be inspected. As RS plays a crucial role in correlating changes in LC and land use change with biodiversity, providing an effective means to monitor and manage

ecosystems. Therefore, there is still needed to explore the potential and challenges of satellite RS as a potent tool for examining land use patterns and tracking alterations over time in assessing the effect of land use diversity on crop yields or biomass.

1.5. Objectives and Structure of the Thesis

This dissertation aimed to investigate the potential of synthetic RS data on modelling long-term crop yields of WW and OSR from 2001 to 2019 for the Free State of Bavaria (which covers one-fifth of the area of Germany). This study has important implications for farmers, policymakers, and researchers who rely on accurate crop yield predictions to plan and decide to achieve higher crop yields with sustainable agriculture. The study used the STARFM to generate the cloud and shadow-free synthetic RS time series for crop yield predictions of Bavaria at the regional level. The crop yield predictions of Bavaria were validated using Bayerisches Landesamt für Statistik (LfStat) data with a 95% confidence interval. The study investigated the relationship between the STARFM-generated RS data and modelled crop yields of WW and OSR. In addition, the study investigated the best spatial (10 m, 30 m, or 250 m) and temporal (8-or 16-day) resolution from the synthetic or non-synthetic RS products for crop yield modelling. The study also compared two widely used models, LUE and WOFOST and analysed their performance based on their simplicity, reliability, and preciseness.

Moreover, the study found the importance of climate variables in crop yield modelling by performing sensitivity analysis by running the model with and without the climate stress factors. Intending to increase the accuracy of crop yield predictions, the study coupled the output of the LUE model with the RF model for both crop types. The study analysed the variable importance to find the essential crop variables impacting the accuracy of crop yields in Bavaria. Lastly, the study discussed the potential and challenges of RS data in establishing a relationship between the land use diversity and modelled biomass of WW and OSR. In brief, the study answers the following research questions.

- (i) As previous studies used the STARFM to fuse MODIS and Landsat data, what would be the potential of the STARFM on fusing Sentinel-2 with

MODIS? Moreover, due to the availability of multiple historical records and increasing resolutions of globally available satellite products, which is the most accurate fusion combination of the RS dataset for six different LC classes such as agriculture, forest, grassland, semi-natural, urban, and water? To analyse this, the study compares the accuracies of the Sentinel-2 and Landsat-based fusion products with different MODIS datasets in 2019, respectively.

- (ii) Determining the optimal synthetic RS product for the agricultural land use class, what would be the difference in accuracy assessments of both fused and non-fused NDVI time series in crop yield predictions? Moreover, what are the optimal spatial and temporal resolutions for the accurate crop yield estimations on comparing six different RS products (real: MOD13Q1 (250 m, 8- and 16-days), and synthetic: L-MOD13Q1 (30 m, 8- and 16-days), and S-MOD13Q1 (10 m, 8- and 16-days)) with two widely used CGMs (WOFOST and LUE), for WW and OSR? As the thesis used two different CGMs for crop yield modelling, which is the suitable CGM between WOFOST and LUE based on their simplicity, reliability, and preciseness? As climate change significantly impacts the world's crop production, how climate variables in crop modelling with different synthetic inputs would influence the crop yield prediction accuracy?
- (iii) Also, many studies analysed the performance of synthetic RS time series in crop modelling for a short time; what would be the impact of STARFM-based synthetic data on the accuracy of crop yields of WW and OSR from 2001 to 2019? Furthermore, it is important to investigate the regional variations in modelled crop yields in Bavaria and how the diverse range of topography in the region may impact the predicted yields. This is done by correlating the regional mean elevation with the regional crop yields.
- (iv) Both LUE and RF have their advantages and disadvantages in crop yield predictions. Comparing the accuracy of crop yield predictions, how will the coupling of LUE with RF using synthetic RS data for WW and OSR differ in

terms of accuracy compared to using LUE alone? Moreover, which are the suitable crop yield predictors (NDVI or climate variables or NDVI plus climate variables) used to generate accurate crop predictions using the RF? Also, which are the important climate variables impacting crop yield estimations of WW and OSR?

- (v) Because the diversity of land use patterns in agricultural landscapes has positively impacted agriculture, ecological sustainability, and resilience to climate change, it is essential to find the potential of the RS-based crop yields and their relationship with biodiversity. Therefore, what is the impact of land use diversity on the satellite-modelled biomass of OSR and WW in 2019? Moreover, what is the impact of arable land use between 2018 and 2019 on the biomass of OSR?

Answering these questions would help to improve the understanding of the potential of synthetic RS data in crop yield predictions and the impact of various factors such as land use diversity and climate variables on the accuracy of these predictions. It could also help to identify the most suitable crop yield predictors and fusion combinations of RS data for accurate yield estimations. Furthermore, investigating the regional variations in modelled crop yields and their relationship with topography could provide insights into the potential impact of topography on crop yields. Finally, understanding the relationship between satellite-modelled biomass and biodiversity could provide insights into the potential of remote sensing data in promoting ecological sustainability and resilience to climate change. Undeniably, the answer to these questions can save time and computation power for future crop yield prediction and precision farming studies.

1.6. Thesis in Brief

The detailed chapter-wise overview of this thesis is shown in Figure 1.6. The thesis presents the research led within the LandKlif project (<https://www.bayklif.de/en>, accessed on 1 March 2019), which aims to disentangle the combined effects of climate and land use on biodiversity, ecosystem functions and related ecosystem services and to develop viable management strategies for adaptation to climate change. Agricultural

Chapter 1

ecosystems provide benefits to human society through crop yields, and RS technology facilitates the gathering of data on various environmental and land use factors. This technology can predict crop yields using crop models and promote sustainable agriculture through its relation to biodiversity. Thus, the aim of this thesis is to explore the potential of RS data for modelling the long-term crop yields of WW (*Triticum aestivum*) and OSR (*Brassica napus*) in the Free State of Bavaria, Germany, which spans an area of 70,550 km², from 2001 to 2019. Bavaria plays an essential role in the agricultural economy of Germany, contributing significantly to the country's food production and exports. The agricultural sector in Bavaria is diverse and includes livestock farming, crop production, fruit and vegetable cultivation, forestry, and fishing. WW has a high yield potential, making it an attractive crop for farmers in Bavaria looking to maximize their production and profits. OSR is a significant source of edible oil for cooking and food preparation. Both are major crops with high economic value for animal feed, biodiesel production, pollination, biodiversity, and human consumption in the European Union (Alarcón-Segura, Grass, Breustedt, Rohlf, & Tschardt, 2022; Eurostat, 2019). For this dissertation, the modelled crop yields are validated at regional levels using the district level Bayerisches Landesamt für Statistik (LfStat) data of Bavaria for WW and OSR. The detailed overview of the dissertation chapters is as follows.

Chapter 2 (time frame: 2019) finds the potential of STARFM generating cloud and shadow-free high spatial resolution NDVI time series by replacing Landsat with Sentinel-2, which still needs to be studied, as STARFM is not only restricted to MODIS and Landsat data. The chapter explores the accuracy assessment of synthetic RS data for six LC classes, such as agriculture, forest, grassland, water, urban, and natural-seminatural. The chapter fuses NDVIs of two high spatial resolution data (high pair) (Landsat (30 m, 16-days; L) and Sentinel-2 (10 m, 5–6 days; S), with four low spatial resolution data (low pair) (MOD13Q1 (250 m, 16-days), MCD43A4 (500 m, one day), MOD09GQ (250 m, one-day), and MOD09Q1 (250 m, 8-days)) using STARFM, which fills regions' cloud and shadow gaps without losing spatial information. The results of the chapter try to create new possibilities for generating accurate datasets for earth observation. Moreover, the aim of this chapter is to reduce the pre-processing time required for future research to identify the optimal RS data for monitoring a specific LC

class (such as agriculture, forest, grassland, etc.). This process is typically time-consuming and requires significant computational power.

Chapter 3 (2019) uses chapter 2's best synthetic NDVI (L-MOD13Q1 (30 m, 8- and 16-days) and S-MOD13Q1 (10 m, 8- and 16-days)) and real (MOD13Q1 (250 m, 8- and 16-days)) outputs for the agricultural LC class and combines to CGMs for crop yield estimations of WW and OSR in 2019. The chapter aims to minimize future research efforts by identifying and recommending the most suited synthetic or non-synthetic satellite inputs for accurate crop yield predictions by discovering the best spatial (10 m, 30 m, or 250 m) and temporal (8-or 16-day) resolutions on a regional scale. The chapter also compares the performance of LUE and WOFOST models in crop yield predictions. The study performs sensitivity analysis using synthetic or non-synthetic data to analyse the impact of climate elements on modelled crop yields. The study recommends testing the methodology for longer time series to analyse the consistency, and reliability of the synthetic RS data.

Chapter 4 (2001-2019) is based on the outlook of chapter 3 by investigating the relationship of spatiotemporal fusion modelling using STARFM (fusing Landsat and MOD13Q1) on crop yield predictions of WW and OSR using the LUE model for longer time series from 2001 to 2019. The study correlates the regional mean elevation with modelled crop yields of WW and OSR at regional level. The LUE model inputs the spatial and temporal resolution data that was proven to be the best for accurate crop modelling in the previous chapter. The study also performed the sensitivity analysis to analyse the impact of climate variables on yearly crop yield predictions from 2001 to 2019. The chapter visualises the yearly crop yield distribution in Bavaria at regional scale and correlates the crop yields with regional mean elevation of Bavaria. The outlook of this chapter states that the spatiotemporal modelling with CGMs would not be limited to one geographical region; therefore, the study recommends testing the methodology globally to obtain food security and maintain biodiversity.

Chapter 5 (2019) finds whether a coupling approach (Light Use Efficiency (LUE) + Random Forest (RF)) would result in better and more accurate yield predictions compared to results provided with other models not using or only using the LUE. For

Chapter 1

this study, different RF models (RF1 (input: NDVI), RF2 (input: climate variables), RF3 (input: Normalized Difference Vegetation Index (NDVI) + climate variables), RF4 (input: LUE generated biomass + climate variables), and one semi-empiric LUE model were designed with different input requirements to find the best predictors of crop monitoring. This chapter discusses the individual strengths of both ML and CGMs and recommends overcoming their challenges for accurate yield predictions by integrating them. This chapter also finds that climate elements have a higher impact on yield predictions. This study discusses the simplicity and reliability by concluding that the design needs to be implemented for different periods, locations, and crop types to improve the global yield estimation for developing agricultural policies, improving food security, forecasting, and analysing global trade trends.

Chapter 6 (2019) broadens the aim of this dissertation by finding the potentials and challenges of RS in analysing the relationship between land use diversity and modelled biomass. The chapter finds the impact of arable land use between 2018 and 2019 on the OSR's biomass. Results of the study discuss the challenges of RS for excluding some dependent factors (such as the specific crops being grown, the management practices used, soil health, biotic and abiotic stressors, pest management, pollinators, and the local environmental conditions) that might be impactful on positively affecting the accuracy of the analysis. The study concluded that including these factors for future analysis might ensure the reliability and applicability of the findings for researchers, policymakers, and practitioners in agriculture and food security.

Chapter 7 discusses the key findings of the above chapters from 2 to 6 for predicting crop yields of WW and OSR in Bavaria. The discussion covers the strengths and limitations of the synthetic RS by establishing its relationship with crop yield prediction accuracies. In addition, this thesis discusses the significance of potential methods such as suitable CGMs and ML in crop yield modelling. Moreover, this dissertation briefly discusses the role of climate variables in yield predictions of WW and OSR. As the crop yield estimations are performed at the regional scale of Bavaria, a concise discussion on spatial analysis of crop yield variation in Bavaria is reviewed. The study discusses the potential and limitations of the research by highlighting the outline and suggesting future implications, for example, including more sensors for data fusion, integration of

deep learning methods with CGMs for crop yield modelling, and integration of UAVs and satellite RS for precision agriculture. Lastly, the study briefly discusses the challenges of the RS technology while correlating modelled crop yields to the land use diversity and landscape metrics in Bavaria.

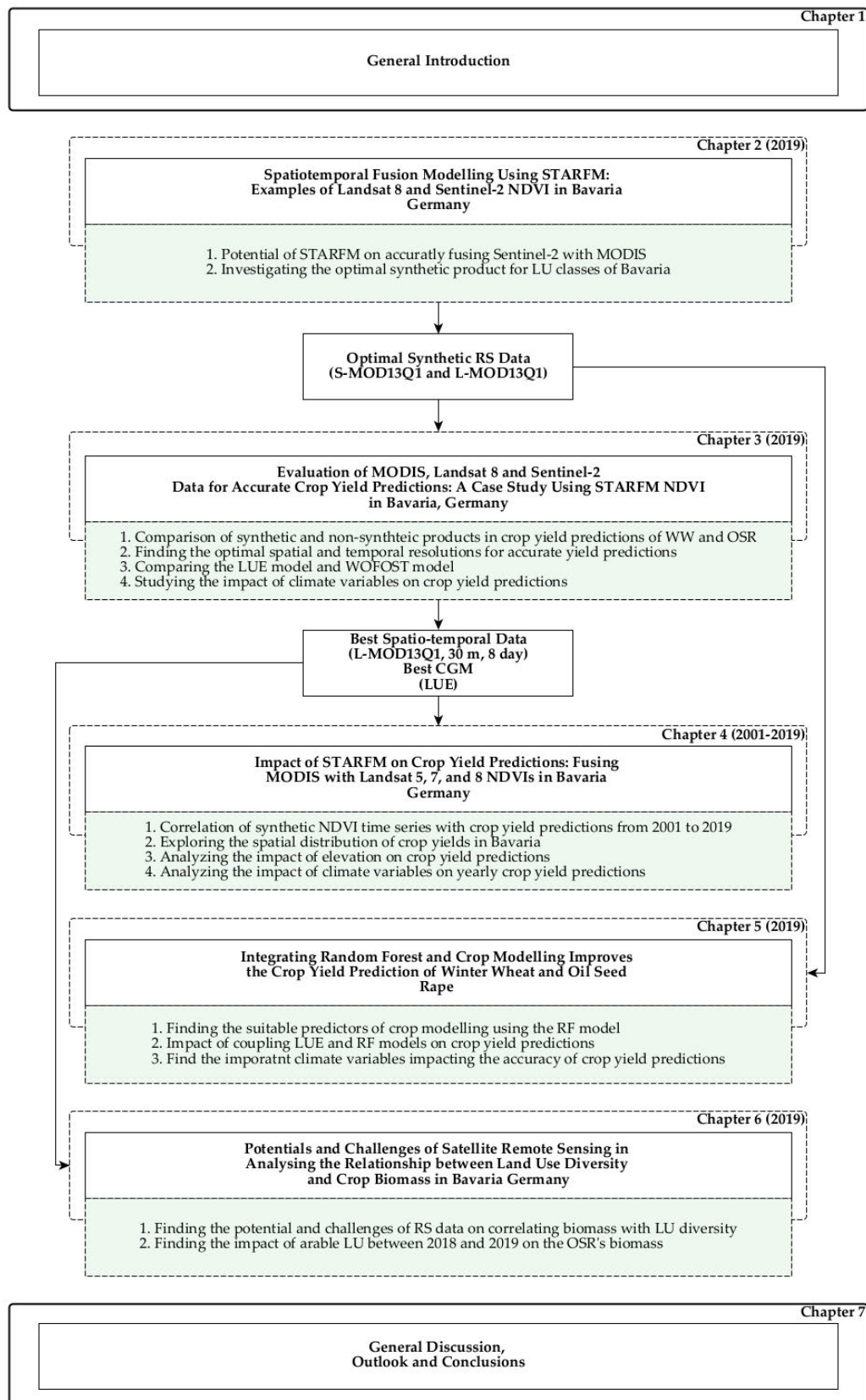


Figure 1.6. Flowchart of the chapter-wise overview of the dissertation. The thesis consists of seven chapters starting with a general introduction (Chapter 1) and ending with a general discussion (Chapter 7). RS stands for remote sensing and CGM stands for crop growth model. The chapter objectives displayed in light green color.

Chapter 2

This chapter is a verbatim reproduction (except the figure and table numbers) of the paper:

Spatiotemporal Fusion Modelling Using STARFM: Examples of Landsat 8 and Sentinel-2 NDVI in Bavaria, Germany

Dhillon, M. S., Dahms, T., Kübert-Flock, C., Steffan-Dewenter, I., Zhang, J., & Ullmann, T. (2022). Spatiotemporal Fusion Modelling Using STARFM: Examples of Landsat 8 and Sentinel-2 NDVI in Bavaria. *Remote Sensing*, 14(3), 677.

Published in MDPI Remote Sensing

Abstract

The increasing availability and variety of global satellite products provide a new level of data with different spatial, temporal, and spectral resolutions; however, identifying the most suited resolution for a specific application consumes increasingly more time and computation effort. The region's cloud coverage additionally influences the choice of the best trade-off between spatial and temporal resolution, and different pixel sizes of remote sensing (RS) data may hinder the accurate monitoring of different land cover (LC) classes such as agriculture, forest, grassland, water, urban, and natural-seminatural. To investigate the importance of RS data for these LC classes, the present study fuses NDVIs of two high spatial resolution data (high pair) (Landsat (30 m, 16-days; L) and Sentinel-2 (10 m, 5–6 days; S), with four low spatial resolution data (low pair) (MOD13Q1 (250 m, 16-days), MCD43A4 (500 m, one day), MOD09GQ (250 m, one-day), and MOD09Q1 (250 m, 8-day)) using the spatial and temporal adaptive reflectance fusion model (STARFM), which fills regions' cloud or shadow gaps without losing spatial information. These eight synthetic NDVI STARFM products (2: high pair multiply 4: low pair) offer a spatial resolution of 10 or 30 m and temporal resolution of 1, 8, or 16-days for the entire state of Bavaria (Germany) in 2019. Due to their higher revisit frequency and more cloud and shadow-free scenes ($S = 13$, $L = 9$), Sentinel-2 (overall $R^2 = 0.71$, and $RMSE = 0.11$) synthetic NDVI products provide more accurate results than Landsat (overall $R^2 = 0.61$, and $RMSE = 0.13$). Likewise, for the agriculture class, synthetic products obtained using Sentinel-2 resulted in higher accuracy than Landsat except for L-MOD13Q1 ($R^2 = 0.62$, $RMSE = 0.11$), resulting in similar accuracy preciseness as S-MOD13Q1 ($R^2 = 0.68$, $RMSE = 0.13$). Similarly, comparing L-MOD13Q1 ($R^2 = 0.60$, $RMSE = 0.05$) and S-MOD13Q1 ($R^2 = 0.52$, $RMSE = 0.09$) for the forest class, the former resulted in higher accuracy and precision than the latter. Conclusively, both L-MOD13Q1 and S-MOD13Q1 are suitable for agricultural and forest monitoring; however, the spatial resolution of 30 m and low storage capacity makes L-MOD13Q1 more prominent and faster than that of S-MOD13Q1 with the 10-m spatial resolution.

2.1. Introduction

Over the past five decades, satellite remote sensing (RS) has become one of the most efficient tools for surveying the Earth at local, regional, and global spatial scales (Dubovik et al., 2021b). Availability of multiple historical records and increasing resolutions of globally available satellite products provide a new level of data with different spatial, temporal, and spectral resolutions, creating new possibilities for generating accurate datasets for earth observation (Dhillon et al., 2020). However, the pre-process to find out the best scale for monitoring any specific land cover (LC) class (such as agriculture, forest, grassland, etc.) is very time-consuming and needs high computation power. Most of the freely available high spatial resolution products, such as Landsat (30 m) and Sentinel-2 (10 m), hinder the accurate and timely-dense monitoring of LC classes because of their significant data gaps due to cloud and shadow coverage (Gevaert & García-Haro, 2015; David P. Roy et al., 2008). A possible solution to fill those observation gaps could be resolved by the process of multi-sensor data fusion, where a high spatial resolution product (high pair) is synchronized with a coarse/low spatial resolution satellite product (low pair) with high revisit frequency (Gevaert & García-Haro, 2015). The Moderate Resolution Imaging Spectroradiometer (MODIS) is the most suitable low pair imagery, which has provided multi-spectral RS for monitoring different land use classes with a daily or weekly revisit since 2001 (Arai, Shimabukuro, Pereira, & Vijaykumar, 2011; Bhandari, Phinn, & Gill, 2012). Due to its high temporal availability, spatial and temporal filtering methods could eliminate cloud-contaminated pixels with high accuracy (Darlane, Khoramian, & Santi, 2017; C. Dong & Menzel, 2016; Parajka & Blöschl, 2008); however, the effectiveness for fine-scale environmental applications is relatively low and limited by the spatial resolution of 250 to 1000 m (Gevaert & García-Haro, 2015). In addition, the availability of multiple MODIS products with different spatial and temporal characteristics complicates the decision-making to choose the best suitable low pair MODIS imagery for data fusion.

Since 2006, many spatiotemporal fusion models have been developed. An important initiative in fusion modelling was started by (F. Gao et al., 2006), who created the spatial and temporal adaptive reflectance fusion model (STARFM) to blend data

from MODIS and Landsat surface reflectance. Since then, STARFM is one of the most widely used algorithms in literature for detecting vegetation change over large areas (Cui et al., 2018; Lee et al., 2019; Xie et al., 2016; L. Zhu et al., 2017). However, its unsuitability for heterogeneous landscapes and its ability to fuse Landsat and MODIS data encouraged the development of design and usage of later fusion algorithms (Belgiu & Stein, 2019; J. Zhang, 2010).

Unlike STARFM, most of the available fusion algorithms need special permissions for their use. Due to its public availability of code and simplicity of design, the benchmark of improvement in many spatiotemporal algorithms, such as enhanced STARFM (ESTARFM) (X. Zhu et al., 2010), Flexible Spatiotemporal Data Fusion method (FSDAF) (Olexa & Lawrence, 2014), the spatial and temporal data fusion approach (STDFA) (M. Wu et al., 2012), the spatial and temporal adaptive algorithm for mapping reflectance change (STAARCH) (Hilker et al., 2009), the sparse representation-based spatiotemporal reflectance fusion model (SPSTFM) (B. Huang & Song, 2012), and the satellite data integration (STAIR) (Luo et al., 2018), was based on the functioning of STARFM (Emelyanova et al., 2013; X. Zhu, Cai, Tian, & Williams, 2018). Most spatiotemporal fusion models focus on the fusion of Landsat and MODIS data, and very few studies have tried to research and deeply compare other RS data (Htitiou, Boudhar, & Benabdelouahab, 2021; Olexa & Lawrence, 2014). As Normalized Difference Vegetation Index (NDVI) is the most widely acknowledged indicator in many RS applications, many fusion algorithms are designed for blending different reflectance bands than focusing on NDVI, which can be similarly effective and much faster (X. Chen et al., 2018; Jarihani et al., 2014; Liao, Wang, Pritchard, Liu, & Shang, 2017; Rao, Zhu, Chen, & Wang, 2015). For example, a Spatiotemporal fusion method to Simultaneously generate Full length normalized difference vegetation Index Time series (SSFIT) yields in better accuracy and efficiency as compared to some typical spatiotemporal fusion models (Qiu, Zhou, Chen, & Chen, 2021).

Thus, the present study tries to overcome the limitation of the most easily accessible fusion algorithm: STARFM. The study checks the algorithm's potential by replacing Landsat with Sentinel-2, as STARFM is not only restricted to MODIS and Landsat data.

Among the wide range of available MODIS datasets, the study makes use of four different MODIS products with different spatial and temporal resolutions such as MOD13Q1 (16-day, 250 m), MCD43A4 (1-day, 500 m), MOD09GQ (8-day, 250 m), and MOD09Q1 (1-day, 250 m). Concerning the suitability of STARFM for homogeneous landscapes, the study compares the accuracy of synthetic products for six LC classes (agriculture, forest, grassland, semi-natural, urban, and water) using a detailed and comprehensive LC map of Bavaria (Germany). In brief, the present study compares the output of 8 (2 (high pair: Landsat and Sentinel-2) \times 4 (low pair: MODIS)) different NDVI STARFM products on six LC classes in 2019 for the entire state of Bavaria.

2.2. Materials and Methods

The general workflow of the study is shown in Figure 2.1. Different combinations of low spatial resolution (low pair) data (MOD13Q1 (16-day, 250 m), MCD43A4 (1-day, 500 m), MOD09GQ (8-day, 250 m), and MOD09Q1 (1-day, 250 m)) and high spatial resolution (high pair) data (Landsat 8 (16-day, 30 m) and Sentinel-2 (5–6-day, 10 m)) are used as an input to STARFM. The fusion process generates eight synthetic NDVI products for Bavaria in 2019. Before data fusion, the input satellite data is preprocessed by removing the clouds and shadows using quality assurance (QA) data (Figure 2.2). The NDVI of the real satellite data is calculated, and then the gaps by cloud and shadow removal were filled by linear interpolation in the following steps. In the last stages of preprocessing, the input data is reprojected, resampled, and masked using the LC map of Bavaria for 2019. The correlation analysis and accuracy assessment of 8 synthetic NDVI products are done separately for every LC class (agriculture, urban, forest, grassland, water, and natural-seminatural). The high and low pair data sets are downloaded and preprocessed in Google Earth Engine (GEE), and the fusion analysis is done in R (version 4.0.3) using RStudio at the University of Wuerzburg, Germany.

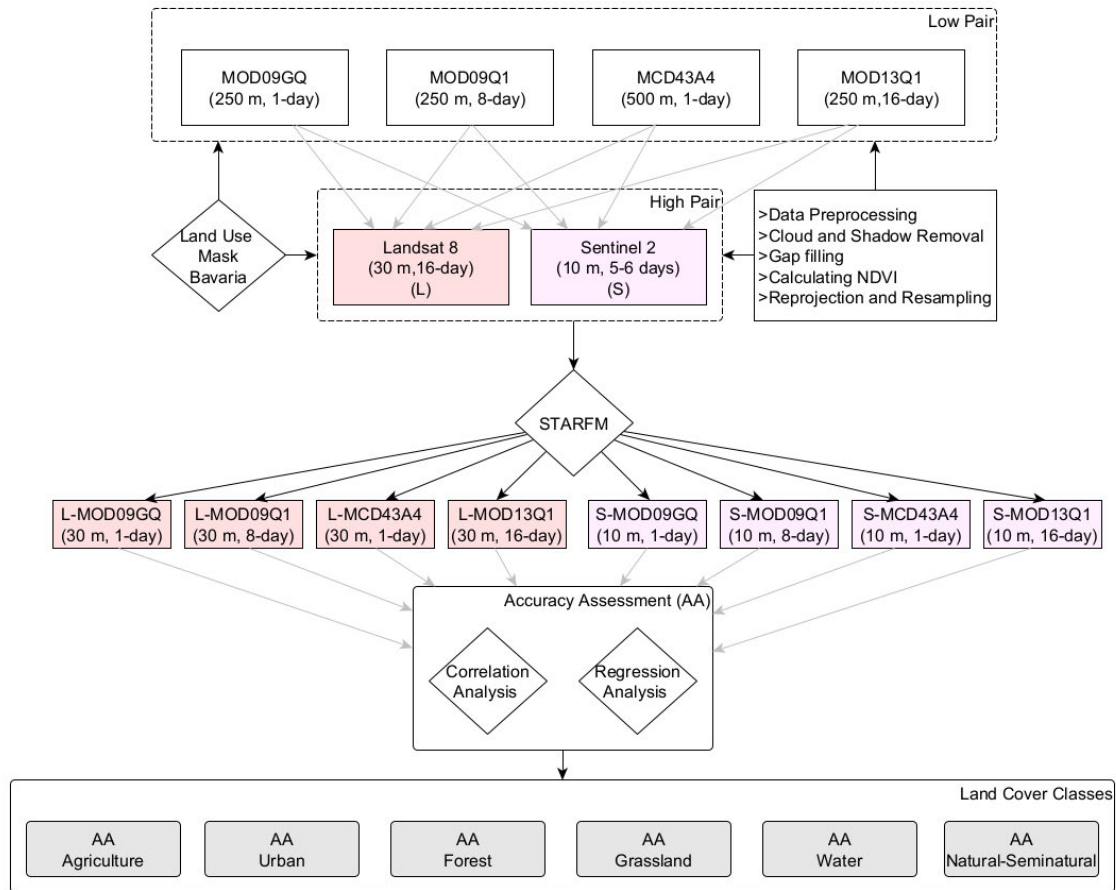


Figure 2.1. Flowchart of data used and processed to generate the synthetic NDVI time series using STARFM; STARFM = Spatial and Temporal Adaptive Reflectance Fusion Model; NDVI = Normalized Difference Vegetation Index; L-MOD09GQ = Landsat-MOD09GQ; L-MOD09Q1 = Landsat-MOD09Q1; L-MCD43A4 = Landsat-MCD43A4; L-MOD13Q1 = Landsat-MOD13Q1; S-MOD09GQ = Sentinel-2-MOD09GQ; S-MOD09Q1 = Sentinel-2-MOD09Q1; S-MCD43A4 = Sentinel-2-MCD43A4; S-MOD13Q1 = Sentinel-2-MOD13Q1; AA = Accuracy Assessment.

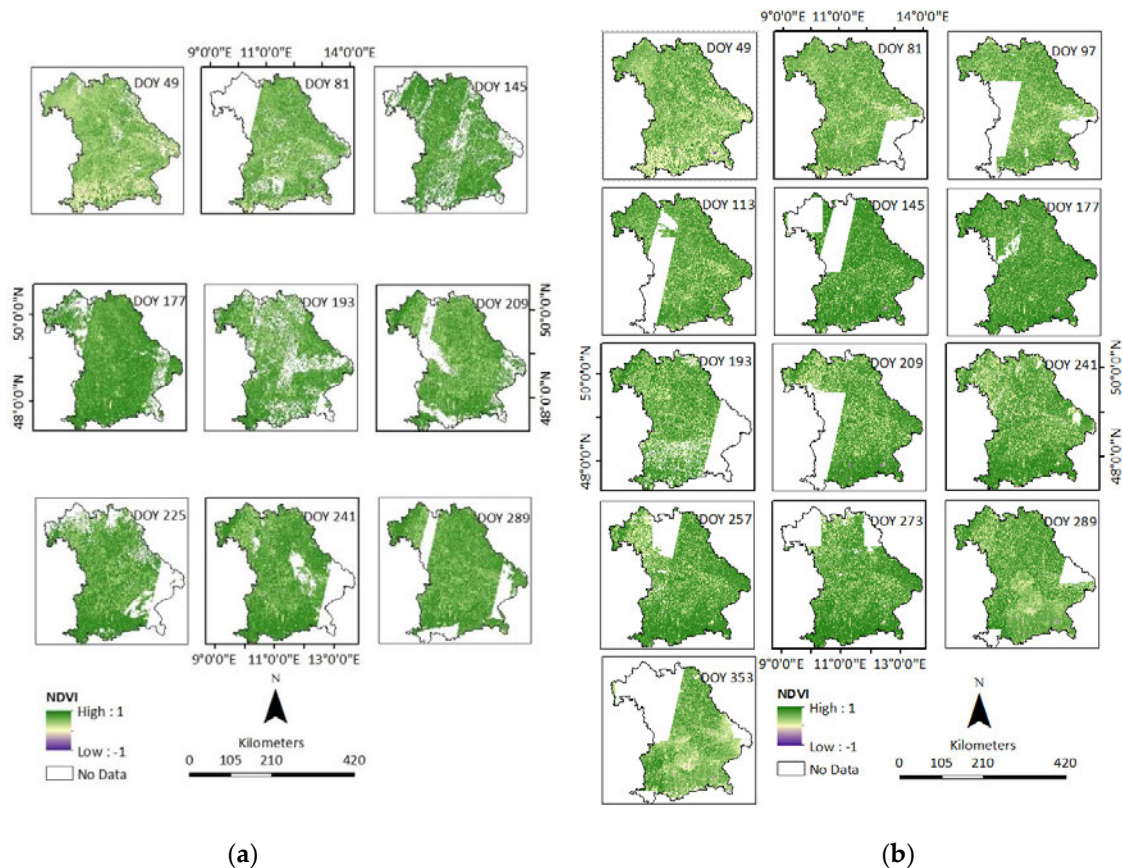


Figure 2.2. The cloud-free scenes are available for (a) Landsat and (b) Sentinel-2. Nine cloud-free scenes were collected for the Landsat data, and thirteen were collected for the Sentinel-2 data. The maps show the NDVI values from -1 to 1 for the entire Bavaria during 2019.

2.2.1. Study Area

The study area of Bavaria is located between 47°N and 50.5°N, and between 9°E and 14° E, in the southeastern part of Germany (Figure 2.3). The topography strongly influences the region's climate, with higher elevations in the south (northern edge of the Alps) and east (Bavarian Forest and Fichtel Mountains). The mean annual temperature ranges from -3.3 to 11 °C, but in most of the territory, the mean annual temperature ranges between 8 and 10 °C (Kloos, Yuan, Castelli, & Menzel, 2021). The mean annual precipitation sums range from 515 to 3184 mm, with wetter conditions in the southern part of Bavaria. In 2019, the landcover was highly dominated by forest (36.91%) and agriculture (31.67%) (based on LC map of Bavaria, 2019). The agricultural areas are mainly found in the northwest and southwest of Bavaria, while forest cover dominates towards the Alps and in the east of Bavaria. The other landcover classes like grassland, urban, natural-semi natural, and water cover, 19.16%, 8.97%, 1.84%, and 1.44%, respectively (based on LC map of Bavaria, 2019). Open grasslands and larger water

areas are primarily localized in the Alpine region and Alpine foothills. Bavaria is divided into 96 counties, with Munich and Nuremberg constituting the most significant metropolitan areas.

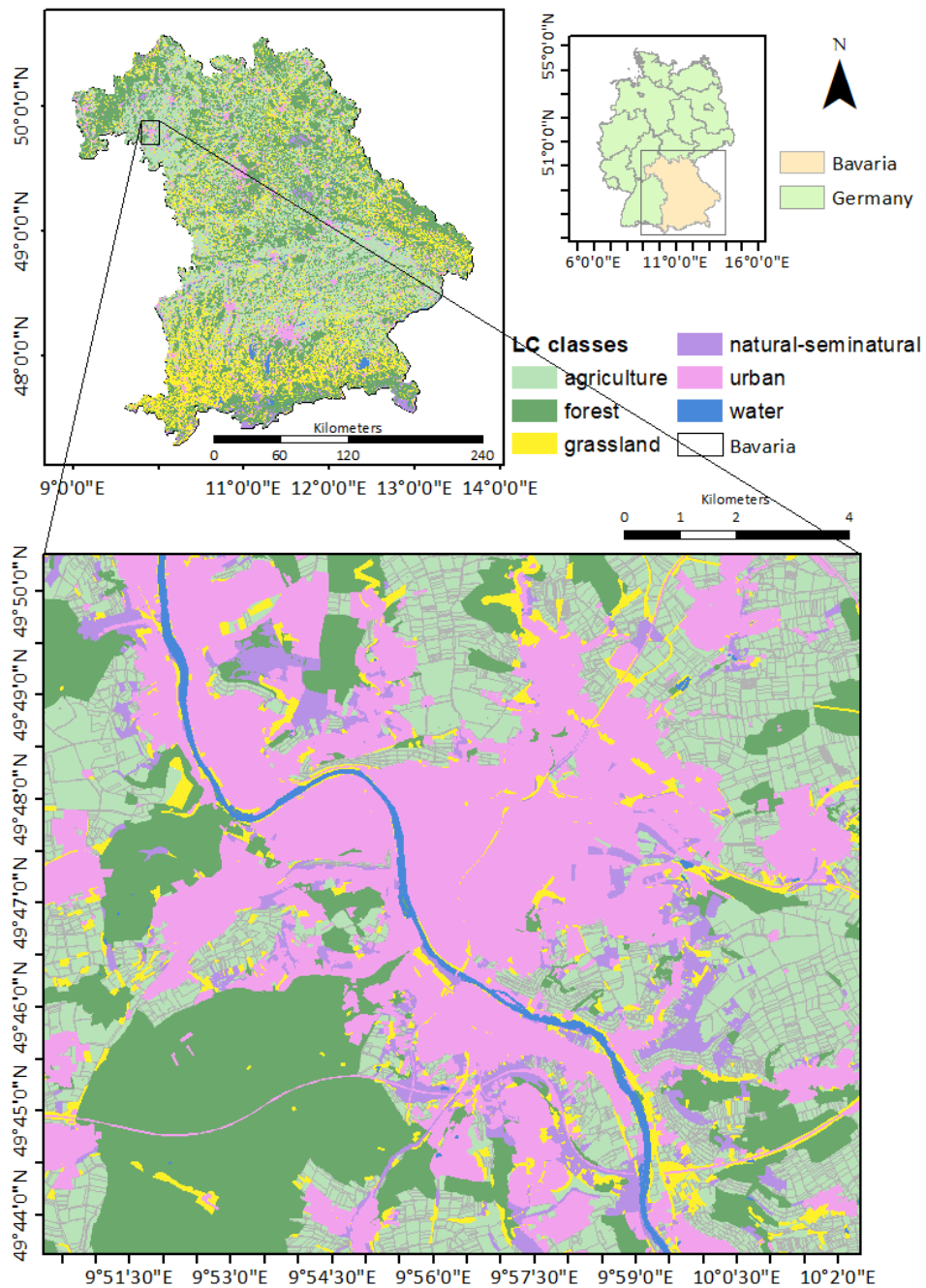


Figure 2.3. The LC map of Bavaria is obtained by combining multiple inputs of Landcover maps such as Amtliche Topographisch-Kartographische Informationssystem (ATKIS), Integrated Administration Control System (IACS) Corine LC, into one map. Agriculture (peach green) dominates mainly in the northwest and southeast of Bavaria, while forest and grassland classes (dark green and yellow, respectively) dominate in the northeast and south. The enlargement shows the urban area of the city Würzburg.

2.2.2. Data

The study collected different satellite data with different spatial and temporal resolutions. A brief description of the data used in the present study with their spatial and temporal resolutions and references are shown in Table 2.1.

Table 2.1. A summary of the collected datasets. The satellite data used are Sentinel-2, Landsat 8, and Moderate Resolution Imaging Spectroradiometer (MODIS) MOD09Q1, MOD09GQ, MCD43A4, MOD13Q1; the Land Cover (LC) data is based covers six land use classes of Bavaria: agriculture, forest, urban, water, natural-semi natural, and grassland.

	Data	Product Name	Resolution Spatial-Temporal	References
Satellite data	Sentinel	Sentinel-2	10 m 5–6 days	www.copernicus.eu
	Landsat	Landsat 8	30 m 16-days	www.usgs.gov
		MOD09GQ	250 m 1-day	www.lpdaac.usgs.gov
	MODIS	MOD09Q1	250 m 8-days	www.lpdaac.usgs.gov
		MCD43A4	500 m 1-day	www.lpdaac.usgs.gov
		MOD13Q1	250 m 16-days	www.lpdaac.usgs.gov
Vector data	Land Cover (LC) LC Map of Bavaria	2019	www.landklif.biozentrum.uni-wuerzburg.de (accessed on 21 June 2021)	

2.2.2.1. Satellite Data

High Spatial Resolution NDVI Products: High Pairs

For the spatio-temporal analysis, the study uses freely accessible spatially high-resolution products from Landsat 8 Land Surface Reflectance Code (LASRC) and Sentinel-2 Copernicus program. The LASRC Tier 1 has a spatial resolution of 30 m on a Universal Transverse Mercator (UTM) projection and provides seven spectral bands (coastal/aerosol, blue, green, red, near-infrared (NIR), shortwave infrared (SWIR) 1, SWIR 2). The data is atmospherically corrected using LASRC. The given quality assessment band “pixel_qa,” generated using the C function of mask (CFMask) algorithm, removes snow (using the Bit 4 of pixel_qa), clouds (Bit 5), and cloud-shadows (Bit 3) via the snow, shadow, and cloud masks. After preprocessing, the available snow-free, cloud-free, and shadow-free Landsat images were acquired in 2019 for the state of Bavaria at the following day-of-year (DOY), date respectively: 49 (18 February), 81 (22 March), 145 (25 May), 177 (26 June), 193 (12 July), 209 (28 July), 225 (13 August), 241 (29 August), and 289 (16 October) (Figure 2.2).

The study also uses Sentinel-2 data that allows for multi-spectral imaging with 12 spectral bands in 10–20 m spatial resolution, with global coverage and a five-day revisit frequency. The surface reflectance data of Sentinel-2 is downloaded from the Copernicus Open Access Hub and processed using the Google Earth Engine (accessed on 02 August 2021) (Gorelick et al., 2017). The data was computed by sen2cor, where the cloud-free images are produced using three quality assessment (QA) bands with QA60 bitmask band containing cloud mask information. The data of Sentinel-2 is acquired at the following DOY, date respectively: 49 (18 February), 81 (22 March), 97 (07 April), 113 (23 April), 145 (25 May), 177 (26 June), 193 (12 July), 209 (28 July), 241 (29 August), 257 (14 September), 273 (30 September), 289 (16 October), and 353 (19 December) (Figure 2.2).

Low Spatial Resolution NDVI Products: Low Pairs

Additionally, the study uses four different MODIS NDVI products, namely MOD09Q1, MOD09GQ, MCD43A4, and MOD13Q1, with different spatial and temporal resolutions. MODIS MCD43A4 version (V) 6 Nadir Bidirectional reflectance Distribution Function (BRDF)-Adjusted Reflectance (NBAR) dataset that is produced daily using 16-days of Terra and Aqua MODIS data at 500 m spatial resolution. Both the cloud cover and the noise are removed from the quality index included in the product. The cloud gaps in the MODIS data are filled using linear interpolation.

The MOD13Q1 V6 product provides an NDVI value per pixel basis with 250 m spatial and 16-day temporal resolution. Based on the quality information (QA), pixels with the constraints were masked out. MOD13Q1 is a composed product, assigning the pixel value with the minor rules and best viewing geometry to the first date of a 16-days' time frame. Linear interpolation of all NDVI values was performed by taking the day of acquisition (doa) science data set and the QA into account (Kuebert, 2018a). The 16-day data of MOD13Q1 is acquired at the following DOY, date respectively: 1 (1 January), 17 (17 January), 33 (02 February), 49 (18 February), 65 (06 March), 81 (22 March), 97 (07 April), 113 (23 April), 129 (09 May), 145 (25 May), 161 (10 June), 177 (26 June), 193 (12 July), 209 (28 July), 225 (13 August), 241 (29 August), 257 (14 September),

273 (30 September), 289 (16 October), 305 (01 November), 321 (17 November), 337 (03 December), and 353 (19 December).

MOD09GQ V6 surface reflectance product provides an estimate of the surface spectral reflectance as it would be measured at ground level in the absence of atmospheric scattering. It provided bands 1 (red) and 2 (NIR) at a 250 m resolution in a daily gridded L2G product in the sinusoidal projection, including quality control (QC) and five observation layers. NDVI of the product is calculated by using the available surface reflectance bands.

MOD09Q1 V6 estimated the surface reflectance of bands 1 (red) and 2 (NIR) at 250 m resolution and corrected for atmospheric conditions for 8-days' time frame. Along with the two-reflectance bands, the quality layer removes clouds and shadows. The 8-day data of MOD09Q1 DOYs, and dates are acquired with an interval of 8-days starting from 1 (1 January) to 353 (19 December) with a total of 45 scenes.

2.2.2.2. LC Map of Bavaria 2019

The LC map of Bavaria is generated by combining Amtliche Topographisch-Kartographische Informationssystem (ATKIS), Integrated Administration Control System (IACS), and Corine LC (100m) at ArcGIS pro 2.2.0 (Figure 2.3). The ATKIS data describes the topographical objects of the landscape in vector format, generated by the official surveying system in Germany, and IACS generates all agricultural plots in European Union (EU) countries by allowing farmers to graphically indicate their agricultural areas. Combining ATKIS, IACS, and Corine LC aims to create an updated LC map of the entire Bavaria for 2019. The features of each dataset are reclassified into pre-defined land use (sub) classes, such as, agriculture (annual crops, perennial crops, and annual crop/managed grassland), forest (deciduous, coniferous, and mixed forest), grassland (managed and permanently managed grassland), urban (settlements and traffic), water, and natural-seminatural (small woody features, wetland, unmanaged grassland, and succession area). Layers with the same land use from different sources are combined into one layer. Selection of every LC class is based on the priority of data sources, for instance, agriculture: IACS > ATKIS, forest: ATKIS, grassland: IACS >

ATKIS; urban: ATKIS, water: ATKIS, natural-semiatural: Corine LC > IACS > ATKIS. However, if there are conflicts among the data sources or if there are holes in the area (i.e., no information from both IACS and ATKIS), the gap is filled with Corine LC. This study uses the LC map to mask the high and low pair data fusion inputs into six LC classes before using them for the fusion process.

2.2.3. Method

The STARFM is used to fuse both Landsat and Sentinel-2 with four different MODIS data sets to configure the best spatial, temporal time series with high spatial and temporal resolution. Before applying the fusion algorithm, a single band of NDVI from every time step has been generated from the reflectance bands of the Landsat, Sentinel-2, and MODIS data. Before the data fusion, the MODIS daily NDVI dataset is reprojected and resampled to Landsat and Sentinel-2 imageries using bilinear interpolation. The fused model is based on the principle that low- and high-resolution products have the same NDVI values, which are biased by a constant error due to their differences in data processing, acquisition time, bandwidth, and geolocation errors. The algorithm states that if a high-low spatial resolution image pair is available on the same DOY, this constant error can be calculated for each pixel in the image. After that, these errors can be applied to the available MODIS dataset of a prediction date to obtain a prediction image with the exact spatial resolution of Landsat, or Sentinel-2 respectively. According to (F. Gao et al., 2006), this is done in four steps: (i) The MODIS time series is reprojected and resampled to the available corresponding high spatial resolution imagery. (ii) Next, a moving window is applied to the high spatial resolution image to identify the similar neighboring pixels. (iii) After that, the weight of Wijk is assigned to each similar neighbor. (iv) Lastly, the NDVI of the central pixel is calculated.

After obtaining the STARFM time series, the study validates the received synthetic product by dropping a single available high spatial resolution NDVI image during the fusion process and comparing both actual (the dropped high spatial resolution NDVI) and synthetic (STARFM NDVI) images of the same time zone (Dhillon et al., 2020). The STARFM performs the fusion process using Equation (2.1) for Landsat (L) and Sentinel-2 (S):

$$\begin{aligned}
& L(\text{or } S) \left(\frac{x_w}{2}, \frac{y_w}{2}, t_0 \right) \\
&= \sum_{i=1}^w \sum_{j=1}^w \sum_{k=1}^n W_{ijk} \\
& * (M(x_i, y_j, t_0) + L(\text{or } S)(x_i, y_j, t_k) - M(x_i, y_j, t_k)),
\end{aligned} \tag{2.1}$$

where w is the size of the moving window, $L(\text{or } S)(x_{w/2}, y_{w/2}, t_0)$ is the central pixel of the moving window for the Landsat (Sentinel-2) image prediction at a time t_0 , and $x_{w/2}, y_{w/2}$ is the central pixel within the moving window, the spatial weighting function $W_{i,j,k}$ determines how much each neighboring pixel x_i, y_j in w contributes to the estimated reflectance of the central pixel. (x_i, y_j, t_0) is the MODIS reflectance at the window location (x_i, y_j) observed at t_0 , while $L(S)(x_i, y_j, t_k)$ and $M(x_i, y_j, t_k)$ are the corresponding Landsat (Sentinel-2) and MODIS pixel values observed at the base date t_k (F. Gao et al., 2006). The n counts for the total number of input pairs of $L(S)(x_i, y_j, t_k)$ and $M(x_i, y_j, t_k)$, and each pair is supposedly acquired on the same date. The size of the moving window is taken as 1500 m by 1500 m, which is three times the size of the MODIS (MCD43A4) pixel (500 m), six times that of the MODIS (MOD13Q1, MOD09Q1, and MOD09GQ) pixel (250 m), 50 times that of the Landsat pixel (30 m) and 150 times that of the Sentinel-2 pixel (Atamanyuk et al., 2019). The windows minimize the effect of pixel outliers and are therefore used for predicting changes using the spatially and spectrally weighted mean difference of pixels within the window area (F. Gao et al., 2006; Hilker et al., 2009).

2.2.3.1. Correlations between Reference and Synthetic NDVI Time Series

The first step of the present study is a correlation analysis between STARFM NDVI and the pre-processed Landsat and Sentinel-2 images to determine when and where the synthetic NDVI product differs from the real-time satellite imagery. NDVI is one of the most widely used vegetation indices in RS and is defined as follows (Equation 2.2) (Rouse, Haas, Schell, Deering, & Harlan, 1974; Tucker, 1979):

$$\text{NDVI} = \frac{\rho_{\text{NIR}} - \rho_{\text{Red}}}{\rho_{\text{NIR}} + \rho_{\text{Red}}} \quad (2.2)$$

where ρ_{NIR} is the reflectance in the near-infrared band and ρ_{Red} is the reflectance in the red band. The correlation coefficient is calculated using the Equation (2.3), where R is the coefficient of correlation. R values lie between -1 (strong negative correlation between two variables) to 1 (strong positive correlation between two variables). Strong correlations would signify the best performing location and time for regions in Bavaria on eight different synthetic output results.

2.2.3.2. Regression Analysis between Reference and Synthetic NDVI Time Series

The STARFM NDVI data are validated with the pre-processed, cloud and shadow-free Landsat and Sentinel-2 images acquired during the study period. From the predicted NDVI (STARFM NDVI) and observed NDVI (Landsat/Sentinel-2 NDVI), the coefficient of determination (R^2) (Equation (2.4)) and root mean square error (RMSE) (Equation (2.5)) are calculated. In the last steps, the final NDVI STARFM and the pre-processed Landsat and Sentinel-2 products are masked with Bavarian LC (e.g., agriculture, forest, water, urban, grasslands, natural-seminatural), and the regression analysis between them is carried out for each LC class.

$$R = \frac{n(\sum O_i * P_i) - (\sum O_i)(\sum P_i)}{\sqrt{((n \sum O_i^2) - (\sum O_i)^2)((n \sum P_i^2) - (\sum P_i)^2)}}, \quad (2.3)$$

$$R^2 = \frac{((\sum P_i - P') (O_i - O'))^2}{(\sum P_i - P')^2 (\sum O_i - O')^2}, \quad (2.4)$$

$$\text{RMSE} = \sqrt{\frac{1}{n} \sum_{i=1}^n (O_i - P_i)^2}, \quad (2.5)$$

where P_i is the predicted value, O_i is the observed value, P' is the predicted mean, O' is the observed mean value, and n is the total number of observations. To check the significance of the fusion products, the probability value (p-value) is calculated using a Linear Regression Model (LRM) with the null hypotheses (H_0) that there is no relationship between the measured and synthetic NDVI values and an H_1 that the relationship exists. To perform this test, a significance level (also called alpha (α)) is set

to 0.05. A p-value of less than 0.05 shows that a model is significant, and it rejects the H_0 that there is no relationship.

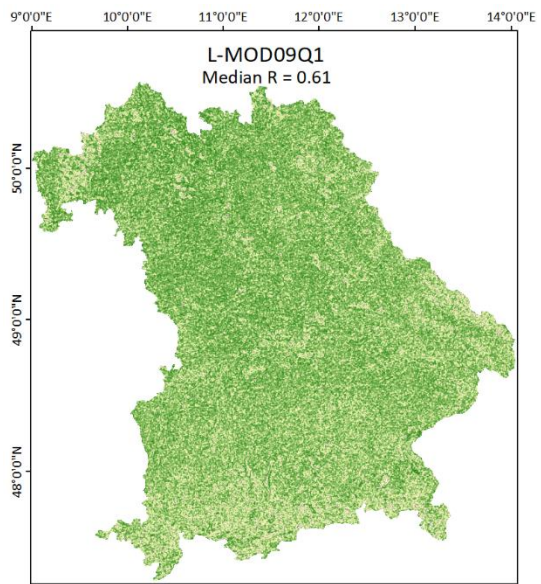
2.3. Results

2.3.1. Correlations between Reference and Synthetic NDVI Time Series of Landsat and Sentinel-2

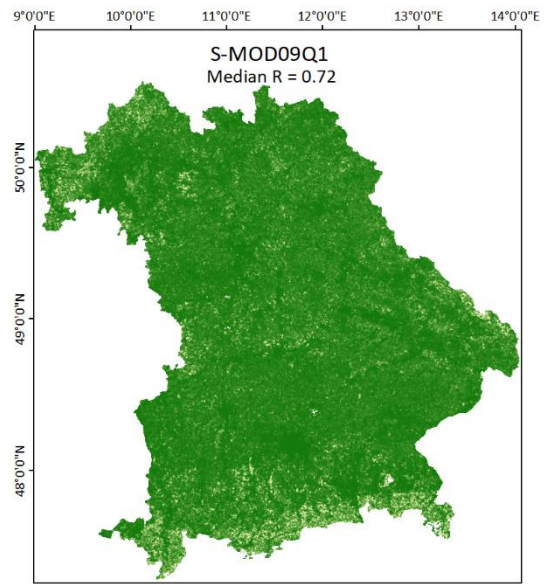
The reference and synthetic relationships show dependency on many factors, as visualised in Figure 2.4 by the yearly mean correlations between actual and synthetic NDVI products of Landsat and Sentinel-2 after individually fusing with multiple MODIS products. The factors show the impact of high temporal frequency and more cloud-free scenes of the high pair product on the quality of the fusion process. For example, the NDVI products L-MOD09Q1 and L-MOD09GQ result in lower positive correlation coefficients than S-MOD09Q1 and S-MOD09GQ. Almost all MODIS products show higher correlations when combined with Sentinel-2 than with Landsat, except the synthetic product L-MOD13Q1, which showed similar positive correlations as S-MOD13Q1.

Comparing the synthetic products based on their respective MODIS product used in the fusion process, L-MOD13Q1 and S-MOD13Q1 have shown the median correlation coefficient (refers to R^2 in Equation (3)) of 0.81 and 0.87, respectively (Figure 2.4). The S-MCD43A4 positively correlated slightly better than L-MCD43A4 with a median correlation of 0.81 and 0.76, respectively. L-MOD09GQ and L-MOD09Q1 both resulted in a median of less than 0.70; however, the values of S-MOD09GQ and S-MOD09Q1 lie between 0.70 to 0.75. This considerable variation in these two products could be due to the high temporal frequency and availability of cloud-free scenes of Sentinel-2 than Landsat.

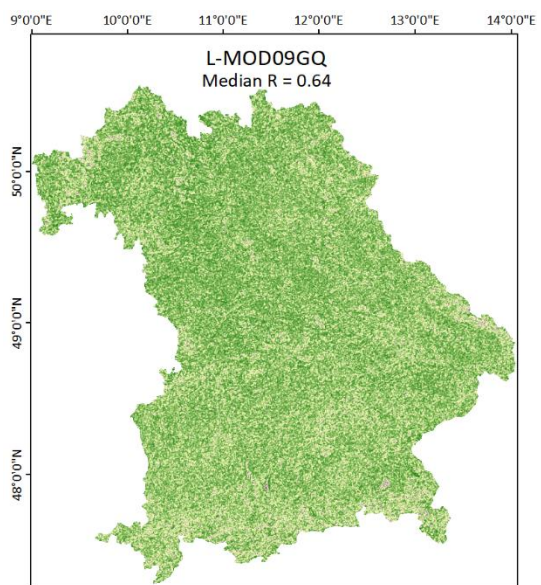
Chapter 2



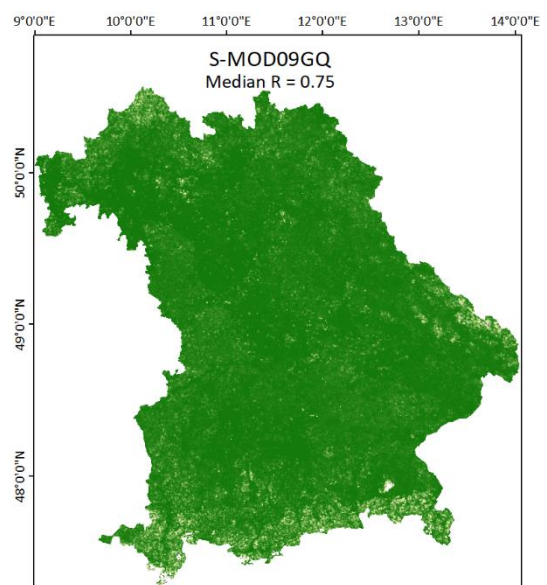
(a)



(b)



(c)



(d)

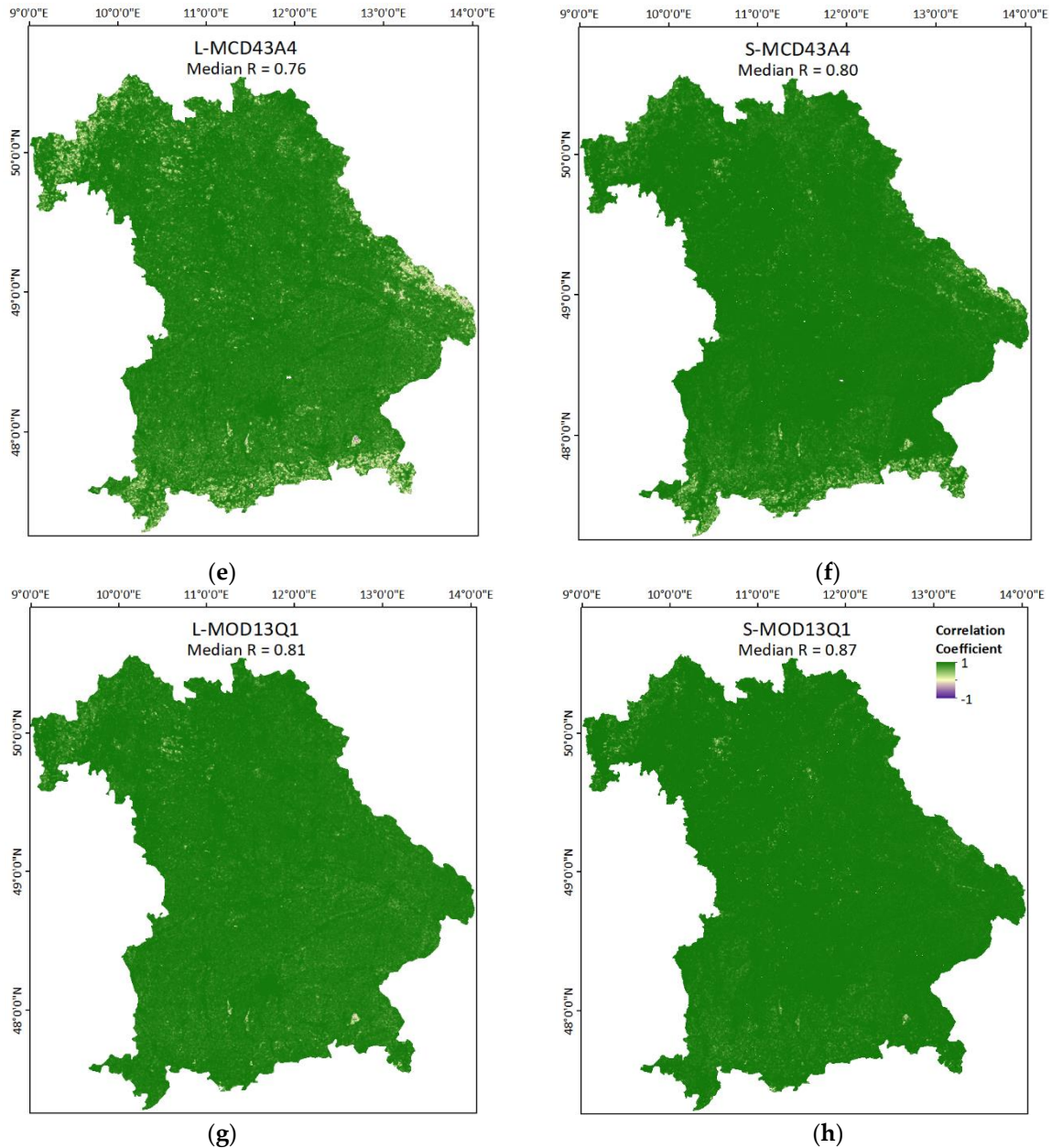


Figure 2.4. The average spatial correlations between the reference Landsat and Sentinel-2 NDVI with synthetic (a) L-MOD09Q1, (b) S-MOD09Q1, (c) L-MOD98GQ, (d) S-MOD09GQ, (e) L-MCD43A4, (f) S-MCD43A4 (g) L-MOD13Q1, and (h) S-MOD13Q1, NDVI time series for 2019 respectively. The average correlation is calculated by taking the mean of dropped scenes used for calculating the accuracy assessment of the eight synthetic NDVI products. The legend of the spatial correlations (High: 1 (Green) to Low: -1 (Purple)) is provided at the top right of figure (h). The median correlation coefficient (R) is given at the top of each figure. The correlation coefficient refers to R (see Equation (2.3)).

On comparing the fusion products based on the available DOYs, the DOY 209 showed the highest correlation with Landsat and Sentinel-2 synthetic products (Figure 2.5). For the maximum values, Sentinel-2 based fusion showed a high correlation for DOYs 49 and 289; however, for the DOYs from 183 to 241, Landsat shows higher

correlation values than Sentinel-2. This suggests that the STARFM performs better for Landsat when the number of consecutive cloud-free scenes is higher.

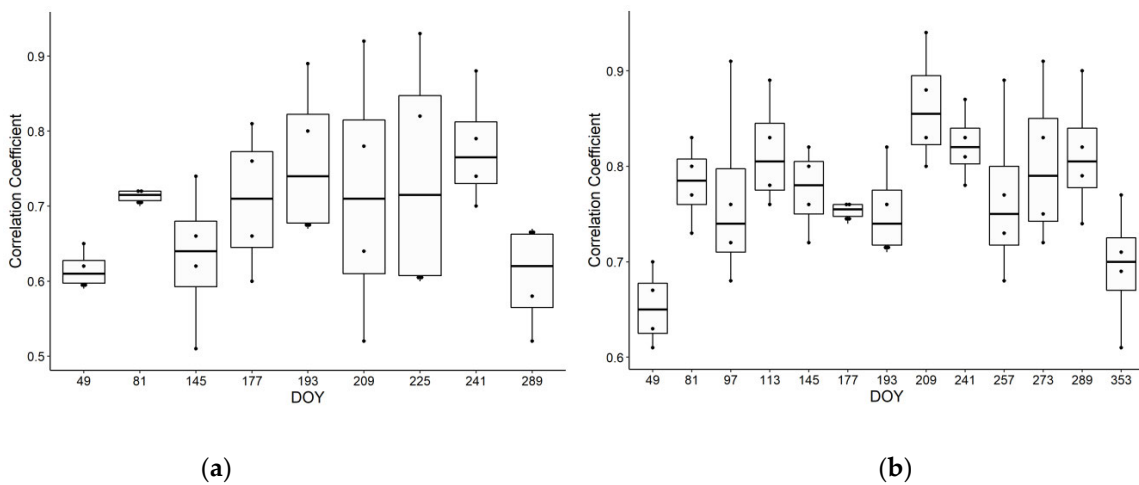


Figure 2.5. The day of the year (DOY) based comparison of correlation coefficients between synthetic NDVI time series and the reference NDVI values obtained from (a) Landsat and (b) Sentinel-2 with different MODIS products. The correlation coefficient refers to R (see Equation (2.3)).

2.3.2. Statistical Analysis between Reference and Synthetic NDVI Time Series of Landsat and Sentinel-2

For eight different synthetic products, the STARFM performed significantly for every synthetic output (having a p -value < 0.05); this rejects the H_0 of the linear regression model that there is no correlation between the reference and synthetic NDVI. After generating the scatter plots, all synthetic products' R^2 , and RMSE values are analysed. The histograms compare different MODIS products when fused with Landsat and Sentinel-2 on a DOY-basis (Figure 2.6). Both L-MOD13Q1 and S-MOD13Q1 result in high R^2 (0.74 and 0.76) and low RMSE (< 0.11) compared to L- and S-MCD43A4, L- and S-MOD09GQ, and L- and S-MOD09Q1. For L-MCD43A4, L-MOD09GQ, and L-MOD09Q1, the R^2 (0.69, 0.56, 0.45) and RMSE (0.12, 0.14, 0.15) values vary in an order of higher accuracy. However, for Sentinel-2, this trend is more accurate and homogenous with R^2 and RMSE of 0.71 and 0.11 (S-MCD43A4), 0.68 and 0.12 (S-MOD09GQ), 0.67 and 0.12 (S-MOD09Q1).

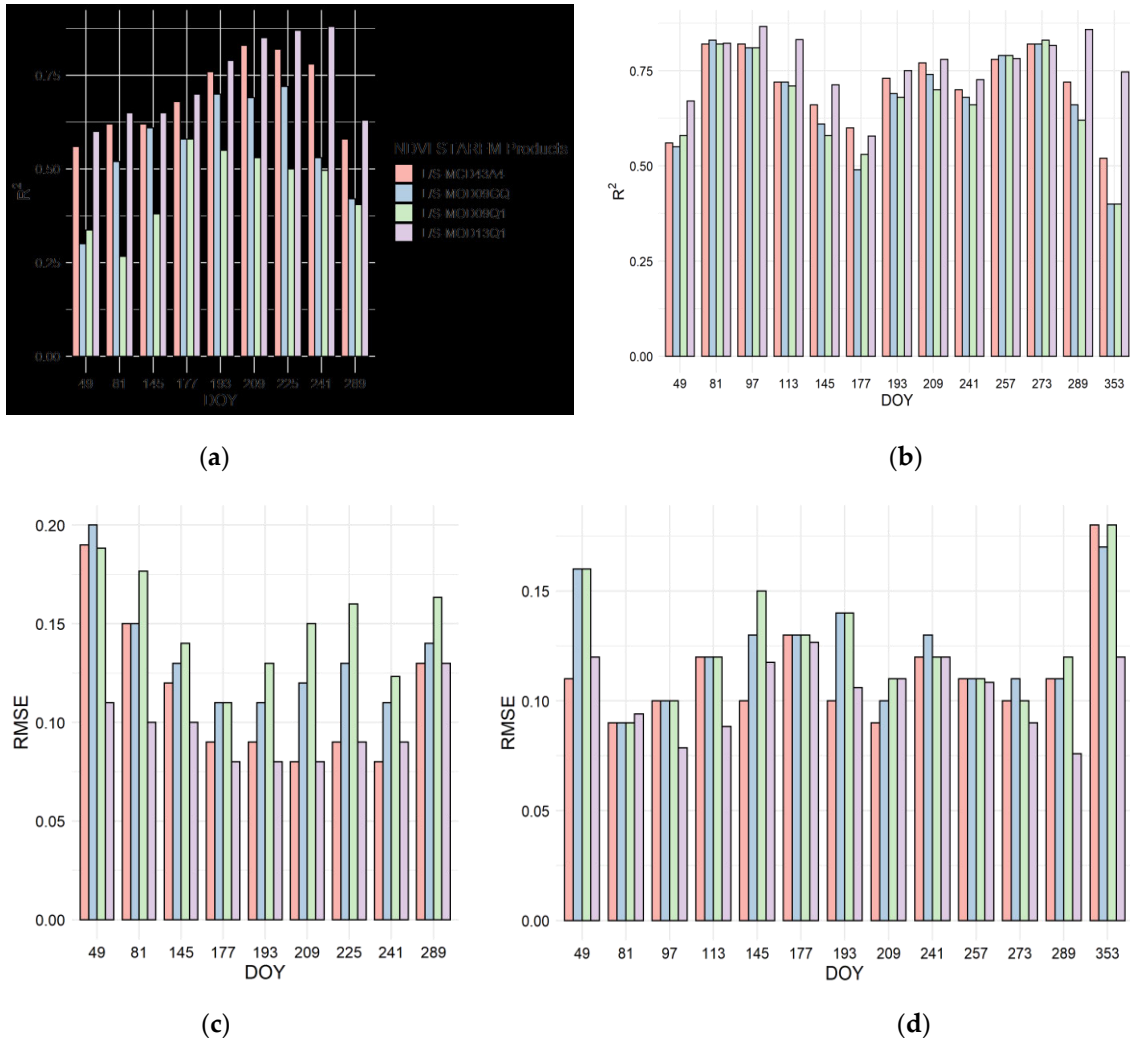


Figure 2.6. The statistical comparison shows R^2 and RMSE values of different NDVI STARFM products obtained using (a,c) Landsat (L) and (b,d) Sentinel-2 (S) with varying products of MODIS, respectively. Different colors show the R^2 and RMSE values with four different MODIS products: MCD43A4 (orange), MOD09GQ (blue), MOD09Q1 (green), and MOD13Q1 (purple).

Compared on a DOY-basis, the synthetic L-MOD13Q1 and S-MCD13Q1 show the top edge in almost all the DOYs. The L-MOD13Q1 and L-MCD43A4 result in closer R^2 and RMSE; however, S-MCD43A4, S-MOD09GQ, S-MOD09Q1 result in similar accuracies. The vast contrast in the accuracies of Landsat and Sentinel-2 is seen in DOYs 49 and 289 with the synthetic product of L- and S-MOD13Q1 with an R^2 of 0.62, 0.76, and RMSE of 0.12, 0.10, respectively. On comparing the accuracies of Landsat and Sentinel-2 for all fused pairs, synthetic products generated with Sentinel-2 resulted more accurately and precisely than Landsat, respectively (Figure 2.7).

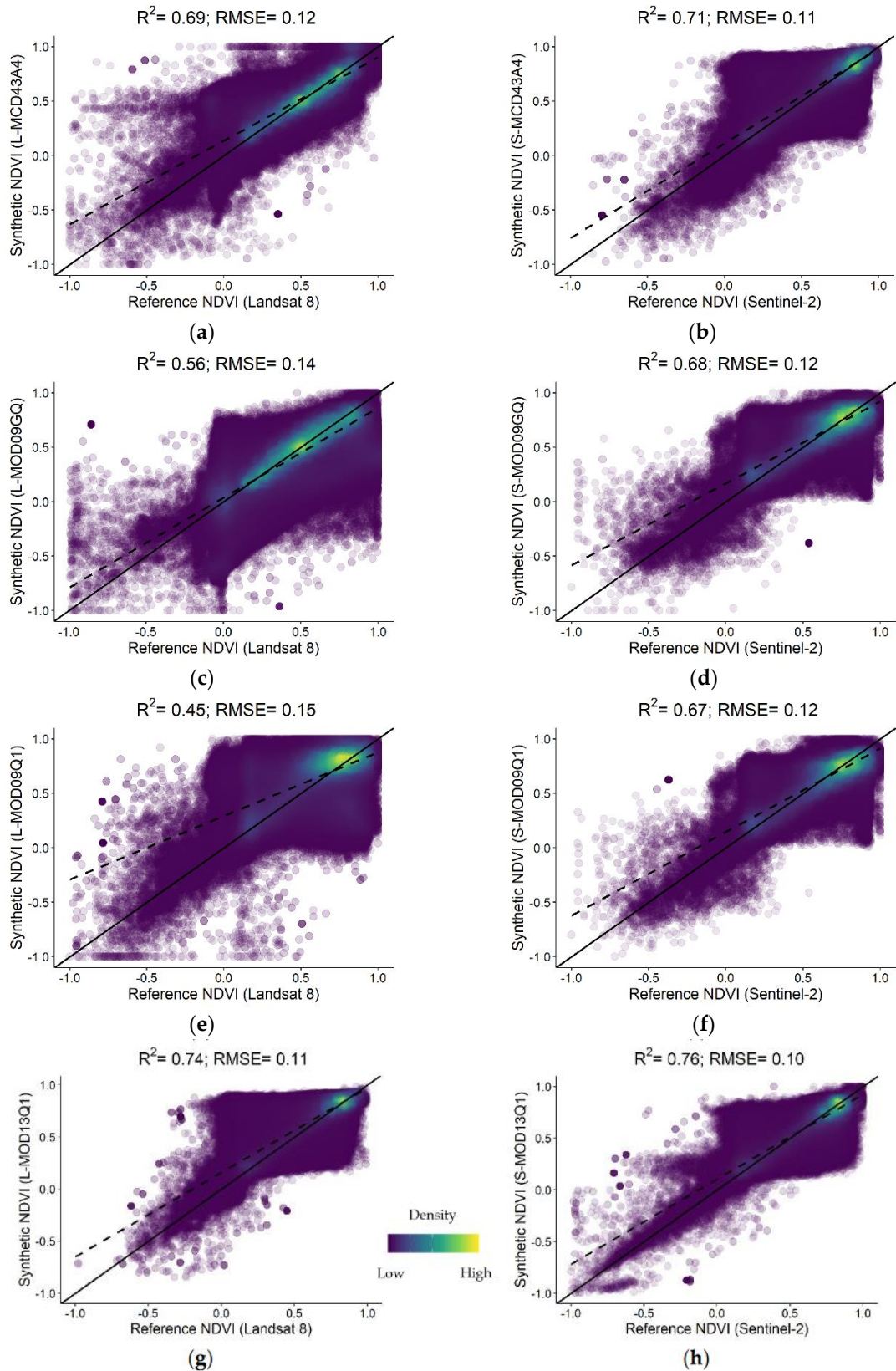


Figure 2.7. The scatter plots compare the accuracies of reference Landsat and Sentinel-2 products with synthetic (a) L-MCD43A4, (b) S-MCD43A4, (c) L-MOD98GQ, (d) S-MOD09GQ, (e) L-MOD09Q1, (f) S-MOD09Q1, (g) L-MOD13Q1, and (h) S-MOD13Q1 products, respectively. The values of the statistical parameters, such as R^2 and RMSE are displayed at the top of each plot. Every plot contains

a solid 1:1 line that is used to visualise the correlation of pixels between the reference and synthetic NDVI values.

2.3.3. Statistical Analysis between Reference and Synthetic NDVI Time Series of Landsat and Sentinel-2 Based on Land Use Classes

Tables 2.2 and 2.3 show the accuracy and precision of eight different synthetic products categorized on LC classes such as agriculture, forest, grassland, seminatural-natural, urban, and water at different DOYs. The urban and water classes resulted in the higher R^2 and lower RMSE with Landsat and Sentinel-2 than other land use classes. Both classes within S-MCD43A4, S-MOD09GQ, and S-MOD09Q1 resulted in higher mean R^2 values more than 0.75 and lower mean RMSE of ~ 0.08 (urban) and ~ 0.12 (water), respectively. Both with L-MOD13Q1 and S-MOD13Q1, the class of agriculture resulted with high R^2 (0.62, 0.68) and low RMSE (0.11, 0.13) compared to other STARFM products. In addition, the mean R^2 and RMSE for agriculture in S-MCD43A4, S-MOD09GQ, and S-MOD09Q1 are nearly similar with values 0.66 and 0.14, respectively. The forest class in L-MOD13Q1 showed the higher accuracy ($R^2 = 0.60$, RMSE = 0.05) than S-MOD13Q1 ($R^2 = 0.52$, RMSE = 0.09). MOD09GQ and MOD09Q1 performed better with Sentinel-2 than Landsat. Even though the water class resulted in high R^2 with both high-resolution products, the RMSE of the same is quite high (>0.10) with all MODIS products. On the contrary, the forest class resulted in very low RMSE (~ 0.08) despite having rather low R^2 values.

Table 2.2. The DOY-based statistical analysis (R² and mean RMSE) between the synthetic NDVI (for four different MODIS products) and reference Landsat (L) NDVI in Bavaria for every LC class such as agriculture (31.67%), urban (8.97%), water (1.44%), forest (35.91%), seminatural-natural (1.84%) and grassland (19.16%), in 2019. The percentage represents the number of pixels in each LC class from the total number of pixels (n = 7,83,48,322). A legend table of R² values are shown at top right of the table. The mean RMSE values are shown in white color.

NDVI Product	LC Class	DOY											Mean R ²	Mean RMSE	R ²
		49	81	145	177	193	209	225	241	289					
L-MOD13Q1	Agriculture	0.41	0.49	0.66	0.65	0.62	0.79	0.81	0.64	0.48	0.62	0.11	0.62	0.11	0.00-0.25
	Urban	0.35	0.46	0.67	0.81	0.85	0.85	0.85	0.86	0.71	0.71	0.07	0.71	0.07	0.26-0.50
	Water	0.44	0.55	0.64	0.72	0.79	0.71	0.74	0.83	0.74	0.68	0.13	0.68	0.13	0.51-0.75
	Forest	0.49	0.53	0.60	0.46	0.67	0.69	0.72	0.69	0.50	0.60	0.05	0.60	0.05	0.76-1.00
	Seminatural-natural	0.59	0.64	0.72	0.64	0.81	0.81	0.81	0.81	0.35	0.69	0.07	0.69	0.07	
L-MCD43A4	Grassland	0.30	0.35	0.35	0.45	0.66	0.68	0.68	0.58	0.50	0.51	0.11	0.51	0.11	
	Agriculture	0.21	0.45	0.46	0.62	0.64	0.74	0.74	0.61	0.48	0.55	0.11	0.55	0.11	
	Urban	0.14	0.18	0.62	0.77	0.86	0.81	0.85	0.81	0.79	0.65	0.07	0.65	0.07	
	Water	0.48	0.50	0.67	0.59	0.79	0.74	0.74	0.74	0.79	0.67	0.13	0.67	0.13	
	Forest	0.45	0.36	0.31	0.40	0.64	0.56	0.50	0.45	0.45	0.46	0.06	0.46	0.06	
L-MOD09GQ	Seminatural-natural	0.14	0.32	0.58	0.48	0.76	0.71	0.77	0.71	0.64	0.57	0.07	0.57	0.07	
	Grassland	0.28	0.18	0.13	0.34	0.64	0.67	0.64	0.53	0.32	0.41	0.11	0.41	0.11	
	Agriculture	0.18	0.22	0.46	0.26	0.59	0.61	0.64	0.58	0.36	0.43	0.13	0.43	0.13	
	Urban	0.12	0.17	0.56	0.55	0.69	0.61	0.67	0.74	0.72	0.54	0.10	0.54	0.10	
	Water	0.38	0.48	0.59	0.55	0.64	0.62	0.55	0.69	0.71	0.58	0.18	0.58	0.18	
L-MOD09Q1	Forest	0.45	0.37	0.22	0.17	0.32	0.27	0.23	0.31	0.14	0.28	0.09	0.28	0.09	
	Seminatural-natural	0.20	0.46	0.61	0.56	0.59	0.59	0.67	0.49	0.48	0.52	0.10	0.52	0.10	
	Grassland	0.22	0.15	0.14	0.25	0.52	0.52	0.52	0.46	0.25	0.34	0.12	0.34	0.12	
	Agriculture	0.24	0.23	0.38	0.32	0.45	0.56	0.41	0.53	0.30	0.38	0.15	0.38	0.15	
	Urban	0.14	0.16	0.50	0.52	0.45	0.52	0.44	0.64	0.67	0.45	0.13	0.45	0.13	
L-MOD09Q1	Water	0.42	0.41	0.59	0.46	0.49	0.41	0.45	0.69	0.67	0.51	0.21	0.51	0.21	
	Forest	0.45	0.32	0.17	0.29	0.23	0.25	0.23	0.30	0.45	0.30	0.10	0.30	0.10	
	Seminatural-natural	0.24	0.46	0.49	0.46	0.36	0.37	0.53	0.58	0.45	0.44	0.12	0.44	0.12	
	Grassland	0.20	0.42	0.59	0.32	0.45	0.38	0.40	0.46	0.18	0.38	0.12	0.38	0.12	

Table 2.3. The DOY-based statistical analysis (R^2 and mean RMSE) between the synthetic NDVI (for four different MODIS products) and reference Sentinel-2 (S) NDVI in Bavaria for every LC class such as agriculture (31.67%), urban (8.97%), water (1.44%), forest (35.91%), seminatural-natural (1.84%) and grassland (19.16%), in 2019. The percentage represents the number of pixels in each LC class from the total number of pixels ($n = 70,51,34,896$). A color legend follows the same trend as in Table 2.2.

NDVI Product	LC Class	DOY																Mean R^2	Mean RMSE
		49	81	97	113	145	177	193	209	241	257	273	289	353					
S-MOD13Q1	Agriculture	0.49	0.74	0.85	0.76	0.50	0.60	0.66	0.85	0.74	0.69	0.74	0.71	0.46	0.68	0.13			
	Urban	0.45	0.71	0.85	0.88	0.86	0.86	0.79	0.90	0.90	0.90	0.92	0.86	0.76	0.82	0.08			
	Water	0.53	0.62	0.72	0.77	0.79	0.86	0.81	0.86	0.86	0.85	0.88	0.86	0.79	0.79	0.11			
	Forest	0.67	0.85	0.79	0.94	0.40	0.53	0.18	0.66	0.29	0.42	0.42	0.34	0.23	0.52	0.09			
	Seminatural-natural	0.55	0.71	0.90	0.86	0.83	0.81	0.67	0.86	0.72	0.77	0.86	0.79	0.56	0.76	0.11			
	Grassland	0.18	0.37	0.69	0.66	0.45	0.22	0.44	0.74	0.58	0.64	0.72	0.61	0.35	0.51	0.11			
S-MCD43A4	Agriculture	0.49	0.74	0.85	0.71	0.46	0.60	0.59	0.85	0.74	0.69	0.74	0.69	0.44	0.66	0.14			
	Urban	0.69	0.61	0.85	0.85	0.86	0.86	0.79	0.90	0.88	0.89	0.90	0.85	0.76	0.82	0.08			
	Water	0.38	0.48	0.71	0.74	0.76	0.86	0.81	0.85	0.85	0.83	0.88	0.83	0.76	0.75	0.12			
	Forest	0.42	0.76	0.74	0.45	0.28	0.53	0.15	0.62	0.28	0.42	0.41	0.30	0.14	0.42	0.11			
	Seminatural-natural	0.64	0.67	0.74	0.66	0.64	0.76	0.53	0.83	0.69	0.76	0.85	0.76	0.52	0.69	0.10			
	Grassland	0.64	0.53	0.62	0.53	0.35	0.20	0.44	0.72	0.56	0.64	0.72	0.59	0.34	0.53	0.11			
S-MOD09GQ	Agriculture	0.71	0.76	0.83	0.71	0.49	0.40	0.61	0.83	0.72	0.69	0.74	0.69	0.44	0.66	0.14			
	Urban	0.42	0.61	0.85	0.85	0.86	0.85	0.79	0.88	0.88	0.88	0.90	0.85	0.74	0.80	0.09			
	Water	0.42	0.53	0.72	0.72	0.76	0.83	0.83	0.83	0.86	0.85	0.88	0.85	0.76	0.76	0.12			
	Forest	0.37	0.77	0.74	0.46	0.23	0.36	0.18	0.42	0.26	0.41	0.40	0.28	0.14	0.39	0.11			
	Seminatural-natural	0.86	0.77	0.71	0.64	0.66	0.72	0.67	0.77	0.69	0.76	0.83	0.72	0.50	0.72	0.10			
	Grassland	0.67	0.53	0.61	0.55	0.36	0.20	0.42	0.66	0.53	0.64	0.71	0.56	0.31	0.52	0.11			
S-MOD09Q1	Agriculture	0.64	0.76	0.83	0.69	0.46	0.40	0.62	0.79	0.72	0.69	0.74	0.69	0.45	0.65	0.14			
	Urban	0.69	0.64	0.85	0.85	0.83	0.85	0.81	0.85	0.88	0.88	0.90	0.83	0.64	0.81	0.08			
	Water	0.36	0.50	0.72	0.74	0.76	0.85	0.79	0.74	0.85	0.83	0.88	0.85	0.76	0.74	0.12			
	Forest	0.45	0.77	0.74	0.42	0.20	0.48	0.16	0.35	0.26	0.42	0.42	0.27	0.14	0.39	0.11			
	Seminatural-natural	0.69	0.76	0.72	0.64	0.61	0.76	0.52	0.71	0.67	0.74	0.85	0.72	0.49	0.68	0.11			
	Grassland	0.66	0.50	0.61	0.55	0.34	0.24	0.44	0.62	0.53	0.64	0.74	0.58	0.32	0.52	0.13			

2.3.4. Visualization of Resulted Synthetic Products Obtained from Different MODIS Imageries

The spatial visualisation of the products MOD13Q1, Landsat, L-MOD13Q1, Landsat minus L-MOD13Q1, Sentinel-2, S-MOD13Q1, Sentinel-2 minus S-MOD13Q1 at DOY 193 is shown in Figure 2.8a–g, respectively. Figure 2.8d,g show the slight overestimation and underestimation of NDVI values with the synthetic product (L- and S-MOD13Q1) is subtracted from its respective reference high-resolution products (Landsat or Sentinel-2). Figure 2.8h shows the spatial location of 10,000 random points that compares eight synthetic products with their respective low pair (MODIS) and high pair (Landsat or Sentinel-2) products by considering the mean values at different DOYs (Figure 2.9). Figure 2.9a–h shows the line plot comparison of eight synthetic products along with their interquartile comparison of NDVI values.

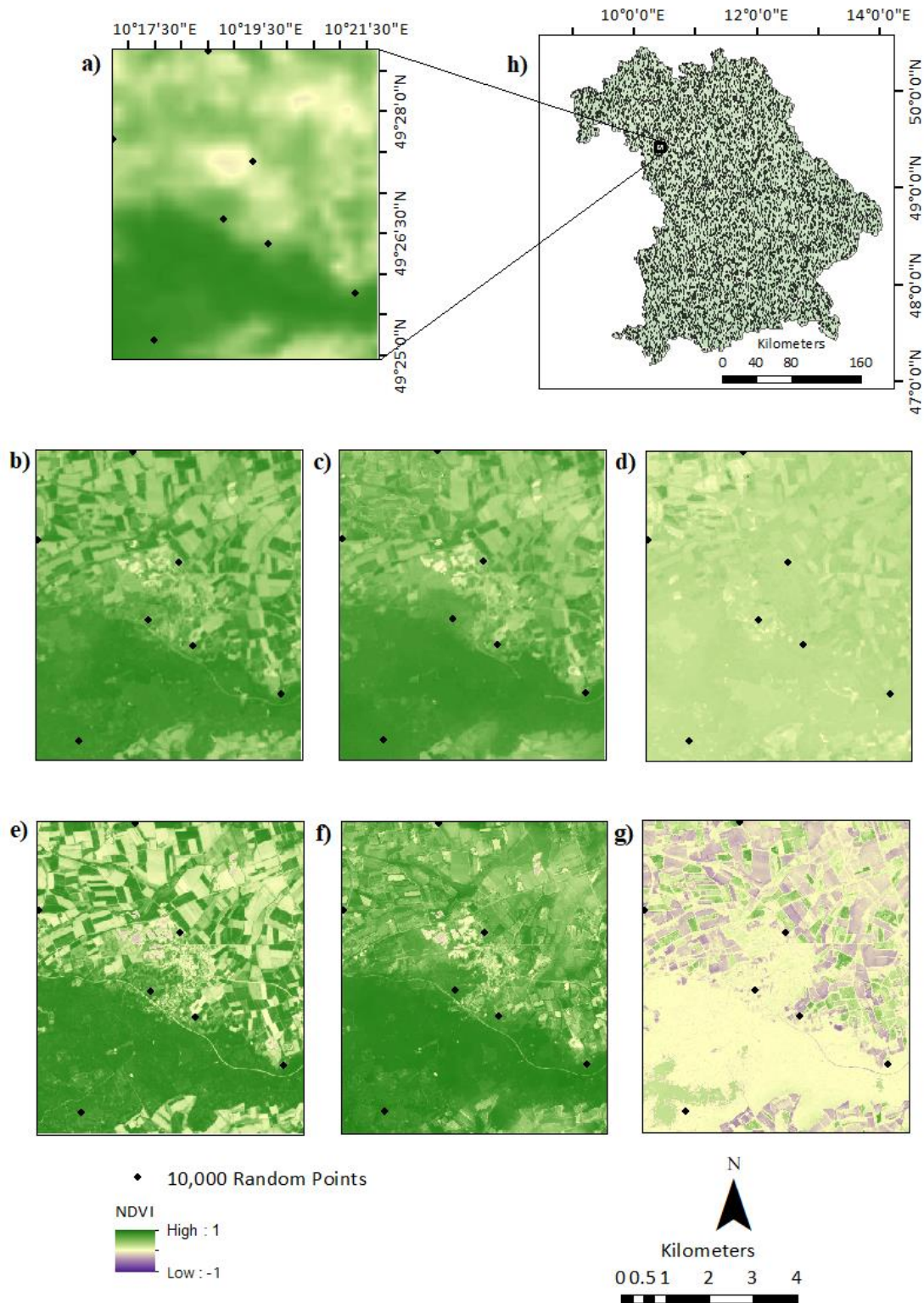
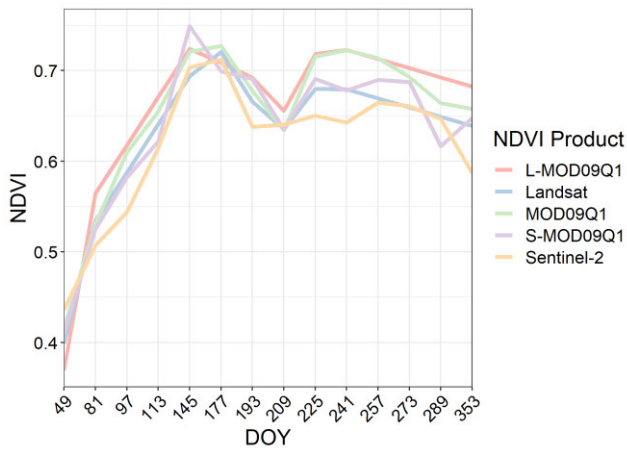
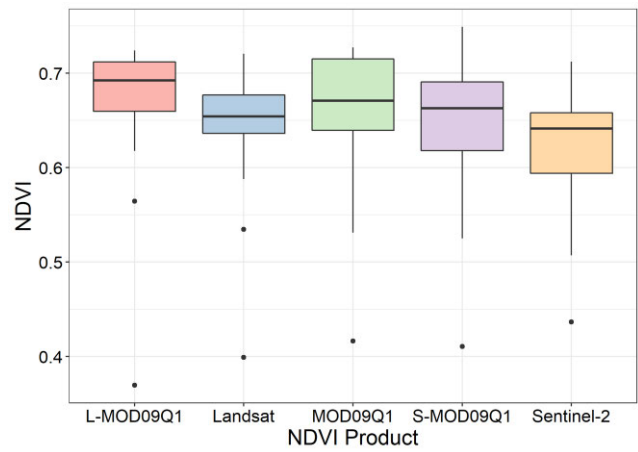


Figure 2.8. Image-wise comparison of STARFM and real-time NDVI values from (a) MOD13Q1, (b) Landsat, (c) L-MOD13Q1, (d) Landsat minus L-MOD13Q1 (difference) (e) Sentinel-2, (f) S-MOD13Q1, and (g) Sentinel-2 minus S-MOD13Q1 (difference), on DOY 193 (12th July 2019). The figure (h) shows the spatial location of 10,000 random points in Bavaria used to draw line and bar plots in Figure 2.9 for comparing the mean NDVI values on DOYs basis for the eight different synthetic NDVI products.

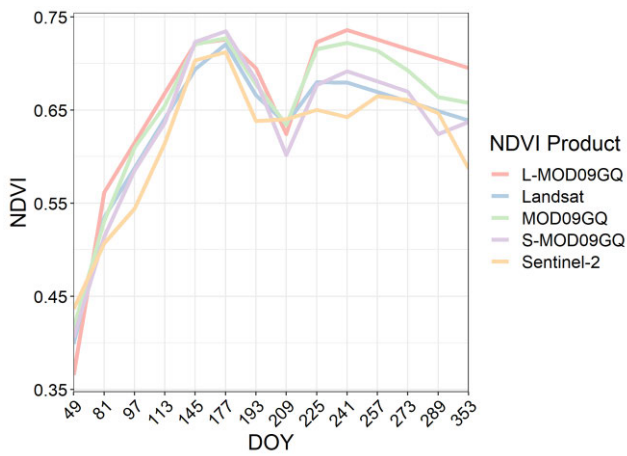
Chapter 2



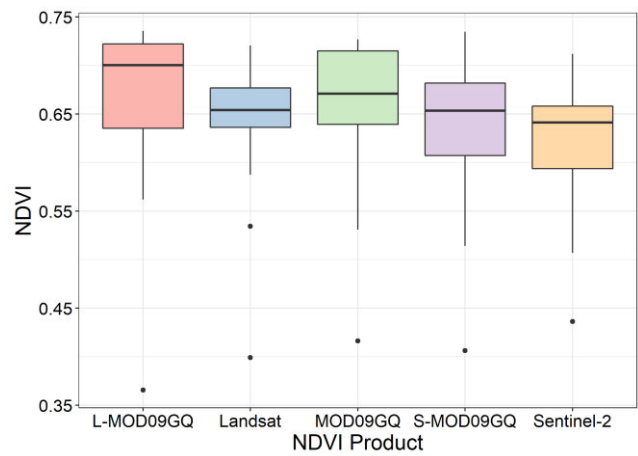
(a)



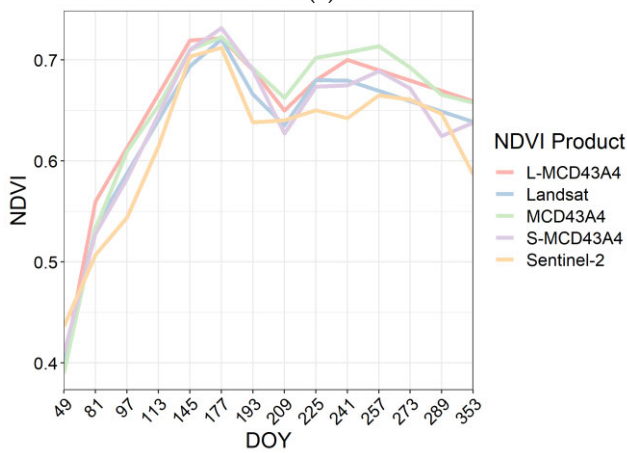
(b)



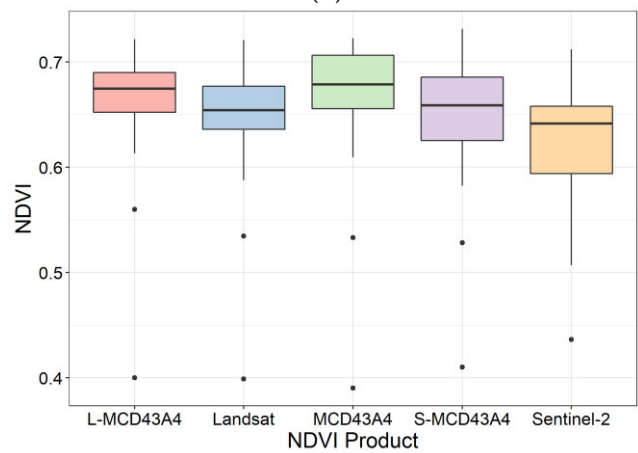
(c)



(d)



(e)



(f)

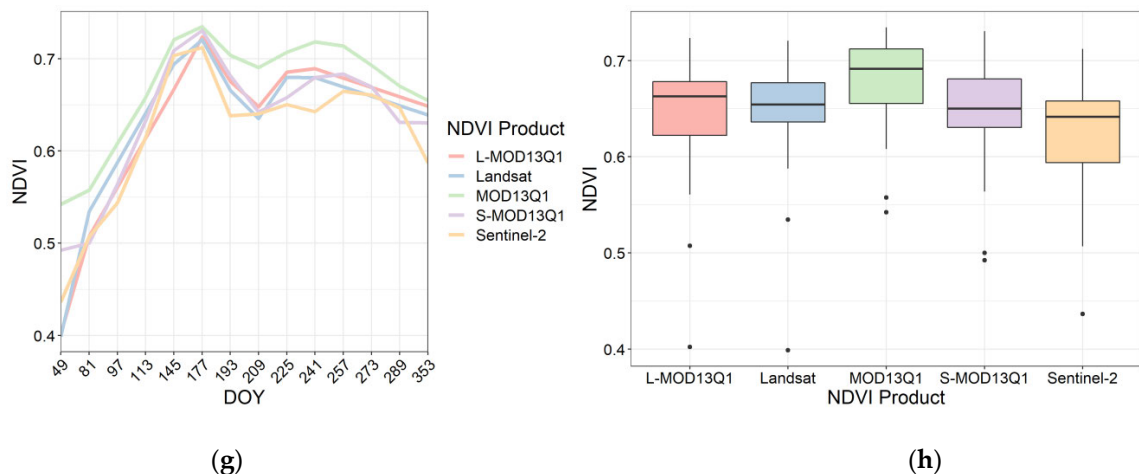


Figure 2.9. The line and bar plots show the DOY-based and inter-quartile-range based comparison of STARFM generated NDVI values with their respective high-resolution input (Landsat (L) or Sentinel-2 (S)) and low-resolution input (a,b) MOD09Q1 (c,d) MOD09GQ, (e,f) MCD43A4, (g,h) MOD13Q1 respectively. The comparison is based on the mean values extracted for 10,000 random points (whose spatial location is shown in Figure 2.8 (h)) taken for entire Bavaria.

Both L-MOD13Q1 and S-MOD13Q1 show a slight overestimation and underestimation of NDVI values compared to the reference Landsat and Sentinel-2 NDVI values at different DOYs. The median NDVI values of L-MOD13Q1 and S-MOD12Q1 lie close to their respective high pair product. However, the difference in median values of synthetic products from their high pair products increases from L- and S-MCD43A4, L- and S-MOD09GQ, and L- and S-MOD09Q1, respectively. The mean NDVI values (Figure 2.9a,c) and median (Figure 2.9b,d) of L-MOD09GQ and L-MOD09Q1 lie close to their low pair MOD09GQ and MOD09Q1 products than the Landsat. However, the products S-MOD09GQ and S-MOD09Q1 lie closer to Sentinel-2. This might be the reason that the accuracies of S-MOD09GQ and S-MOD09Q1 resulted higher than that of L-MOD09GQ and L-MOD09Q1.

2.4. Discussion

2.4.1 Quality Assessment of Data Fusion

The study investigates the capability of the STARFM (F. Gao et al., 2006) over the Bavarian state of Germany to generate the synthetic NDVI time series of 2019 by testing different high (Landsat (L) (16-day, 30 m) and Sentinel-2 (S) (10 m, 5–6 day)) and low

(MOD13Q1 (16-day, 250 m), MCD43A4 (1-day, 500 m), MOD09GQ (1-day, 250 m), and MOD09Q1 (8-day, 250 m)) spatial resolution products. NDVI is considered the most effective and widely acknowledged vegetation index among other vegetation indices. Various studies with spatiotemporal data fusion have used NDVI as their primary input for different applications such as phenology analysis (Bhandari et al., 2012; Htitiou et al., 2019; Qiu et al., 2021), yield and drought monitoring (Benabdelouahab et al., 2019; Dhillon et al., 2020; Htitiou et al., 2019), forest mapping (Hilker et al., 2009; Xin, Olofsson, Zhu, Tan, & Woodcock, 2013), and biophysical parameter estimation (Anderson et al., 2011; F. Gao, Anderson, Kustas, & Wang, 2012; Lebrini et al., 2020; Singh, 2011). However, many spatiotemporal fusion algorithms are based on reflectance fusion, which needs more computation power than the NDVI fusion.

The study uses the strategy “index-then-blend” (IB), which generates the NDVI from both high pair and low pair images before they are blended for the data fusion (X. Chen et al., 2018). On the contrary, many studies first blend the reflectance of the individual MODIS and Landsat data sets and then generate the NDVI using the “blend-then-index” (BI) approach (T. Dong, Liu, Qian, Zhao, et al., 2016; J. J. Walker, K. M. De Beurs, R. H. Wynne, & F. Gao, 2012). Ref. (X. Chen et al., 2018) has conducted a theoretical and experimental analysis that states if the predicted NDVI values are lower than the input Landsat values, IB performs better and vice versa. Among 10,000 randomly selected points in the entire Bavaria, some predicted higher NDVI values, and the remaining plots predicted lower; therefore, both BI and IB errors are expected to be small (X. Chen et al., 2018). Additionally, the IB approach has less computation cost than BI, as it blends only one band: the NDVI. Therefore, the present study decided to perform the IB approach’s fusion analysis.

Many studies have started using the combined use of Landsat and Sentinel-2 for RS applications (Moon, Richardson, & Friedl, 2021; Pahlevan, Chittimalli, Balasubramanian, & Vellucci, 2019; Quintano, Fernández-Manso, & Fernández-Manso, 2018; Y. Zhang et al., 2021). The 16-day temporal resolution of Landsat is not fine enough to monitor a variety of landscape changes. The recent launch of new satellite missions such as Landsat 9, Sentinel-2A, or Sentinel-2B can ensure a much higher temporal

1. 2. 3. 4. 5. 6. 7. 8. 9. 10. 11. 12. 13. 14. 15. 16. 17. 18. 19. 20. 21. 22. 23. 24. 25. 26. 27. 28. 29. 30. 31. 32. 33. 34. 35. 36. 37. 38. 39. 40. 41. 42. 43. 44. 45. 46. 47. 48. 49. 50. 51. 52. 53. 54. 55. 56. 57. 58. 59. 60. 61. 62. 63. 64. 65. 66. 67. 68. 69. 70. 71. 72. 73. 74. 75. 76. 77. 78. 79. 80. 81. 82. 83. 84. 85. 86. 87. 88. 89. 90. 91. 92. 93. 94. 95. 96. 97. 98. 99. 100.

1. 2. 3. 4. 5. 6. 7. 8. 9. 10. 11. 12. 13. 14. 15. 16. 17. 18. 19. 20. 21. 22. 23. 24. 25. 26. 27. 28. 29. 30. 31. 32. 33. 34. 35. 36. 37. 38. 39. 40. 41. 42. 43. 44. 45. 46. 47. 48. 49. 50. 51. 52. 53. 54. 55. 56. 57. 58. 59. 60. 61. 62. 63. 64. 65. 66. 67. 68. 69. 70. 71. 72. 73. 74. 75. 76. 77. 78. 79. 80. 81. 82. 83. 84. 85. 86. 87. 88. 89. 90. 91. 92. 93. 94. 95. 96. 97. 98. 99. 100.

cover, the synthetic product obtained using different MODIS outputs is not as accurate as Sentinel-2 (5–6 days) (Gevaert & García-Haro, 2015; David P. Roy et al., 2008). For example, the availability of 13 cloud-free scenes of Sentinel-2 in 2019 result in higher accuracy of S-MOD09GQ ($R^2 = 0.68$, RMSE = 0.12) and S-MOD09Q1 ($R^2 = 0.65$, RMSE = 0.13), as compared to L-MOD09GQ ($R^2 = 0.56$, RMSE = 0.13) and L-MOD09Q1 ($R^2 = 0.45$, RMSE = 0.15), with nine partially available cloud-free scenes of Landsat. Similarly, the spatial correlation of the obtained synthetic product is higher when Sentinel-2 data is used as an input with MODIS products than Landsat, respectively. However, Sentinel-2 shows higher accuracy, its spatial resolution of 10 m consumes more storage and increases the computing load.

Among the MODIS products, MCD13Q1 and MCD43A4 showed higher accuracy and higher positive spatial correlation with both Landsat and Sentinel-2. However, with a frequency of one day, MCD43A4 with 500 m spatial resolution makes the data storage heavier with more run-time than MCD13Q1 with 250 m spatial and 16-days revisit. Moreover, MCD13Q1 is a high-quality product employed in more than 1700 peer-reviewed research articles (Google Scholar), and its fewer cloud contaminated pixels resulted in higher accuracy in data fusion (Didan, Munoz, Solano, & Huete, 2015; Robinson et al., 2017; Solano, Didan, Jacobson, & Huete). In addition, comparing the better product between MCD13Q1 and MCD43A4 also depends on the requirement. The required product will be selected accordingly if the need is to generate a time series with a daily or 16-day frequency. On the other hand, L- and S-MOD09GQ and L- and S-MOD09Q1 result in higher accuracy with Sentinel-2 than Landsat. This justifies that high pair product plays a significant role in the accuracy assessment of any synthetic product. Moreover, L-MOD09GQ and L-MOD09Q1 showed a weak spatial correlation with their reference Landsat images. Contrarily, the opposite was true for S-MOD09GQ and S-MOD09Q1. The obtained R^2 and RMSE of these synthetic products obtained through the STARFM are comparable to those obtained by other studies (Emelyanova et al., 2013; B.-C. Gao, 1996; F. Gao et al., 2006). Comparing the accuracy, storage, and processing time required between L- and S-MOD09GQ and L- and S-MOD09Q1, the former is not only more accurate, but it also needs less storage and lower computation

power due to its 8-day temporal resolution. However, high cloud coverage and gaps put them on the least accurate NDVI synthetic products list.

2.4.2. Quality Assessment of Data Fusion based on Different Land Use Classes

To evaluate the suitability of the STARFM for homogenous landscapes, this study individually runs the algorithm for six different land use classes: agriculture, forest, urban, water, grassland, and seminatural-natural. The spatial correlation of other classes greatly influences the used high pair product. The data fusion results of the study indicate that the STARFM can successfully fuse MODIS with both Landsat and Sentinel-2 (Gevaert & García-Haro, 2015; Thorsten, Christopher, Babu, Marco, & Erik). On average, synthetic time series with Sentinel-2 showed more positive correlations than Landsat. However, comparing accuracy assessments based on different low pair products used, each class varied differently. Almost every synthetic product is accurate and precise for the water and urban classes with a high to low variation from L- and S-MOD13Q1, L- and S-MCD43A4 L- and S-MOD09GQ, and L- and S-MOD09Q1. This might be because the values of these classes remain similar throughout the year; however, for agriculture, synthetic products obtained using Sentinel-2 resulted in higher accuracy than Landsat. This could be because the chances of mixed pixels are lesser for agricultural fields with lower spatial resolution. Exceptionally, L-MOD13Q1 resulted in similar accuracy and preciseness as S-MOD13Q1 for the agriculture class. This justifies that both products are suitable for the application of agricultural monitoring. The only difference separating them is their computation power and data storage. S-MOD13Q1 needs high processing power and time with high storage capacity due to its 10-m spatial resolution. Similarly, comparing L-MOD13Q1 and S-MOD13Q1 for the forest class, the former resulted in higher accuracy than the latter. Therefore, this proves that both L-MOD13Q1 and S-MOD13Q1 are suitable for agricultural and forest monitoring; however, L-MOD13Q1 has the upper hand due to its fast and easy processing with less storage requirement. Besides that, the present study compares the synthetic NDVI products generated from the STARFM, where NDVI is mostly

correlation and accuracy. For example, the availability of 13 cloud-free scenes of Sentinel-2 (5–6 days) in 2019, result in higher accuracy of S-MOD09GQ ($R^2 = 0.68$, RMSE = 0.12) and S-MOD09Q1 ($R^2 = 0.65$, RMSE = 0.12), as compared to L-MOD09GQ ($R^2 = 0.56$, RMSE = 0.14) and L-MOD09Q1 ($R^2 = 0.45$, RMSE = 0.15), with 9 partially available cloud-free scenes of Landsat (16-days). Conclusively, it also states that the synthetic products obtained using Sentinel-2 are more accurate than products obtained using Landsat. Therefore, Sentinel-2 could be used as an input high pair product for the STARFM. The study also compares the synthetic NDVI products based on their respective low pair input used in the blending process. This resulted that L- and S-MOD13Q1 ($R^2 = 0.74/0.76$, RMSE = 0.11/0.10) showed higher spatial correlation than L- and S-MCD43A4 ($R^2 = 0.69/0.71$, RMSE = 0.12/0.11), L- and S-MOD98GQ, L- and S-MOD09Q1. This concludes that the MOD13Q1 is the best suitable low pair product because of its higher quality. Moreover, due to its temporal resolution of 16-days, the fusion process takes less computation time to produce the synthetic RS product, even at a large scale.

On comparing the synthetic NDVI products on different land use classes, the urban and water classes resulted in the higher R^2 (>0.75) and lower RMSE (0.08, and 0.12, respectively) with both Landsat and Sentinel-2 than the other land use classes. For agricultural and forest classes, both L-MOD13Q1 and S-MOD13Q1 showed higher accuracy than the other products. With both L-MOD13Q1 and S-MOD13Q1, the class of agriculture resulted with an R^2 of 0.62, and 0.68 and RMSE of 0.11, and 0.13, and the forest class with an R^2 of 0.60, and 0.52 and RMSE of 0.05, and 0.09, respectively. Conclusively, both L-MOD13Q1 and S-MOD13Q1 are suitable for agricultural and forest monitoring; however, the spatial resolution of 30 m and low storage capacity makes L-MOD13Q1 more prominent and faster than that of S-MOD13Q1 with the 10-m spatial resolution. From an application perspective, both products (L-MOD13Q1 and S-MOD13Q1) could be further tested for the RS application of crop yield estimation.

Chapter 3

This chapter is a verbatim reproduction (except the figure and table numbers) of the paper:

Evaluation of MODIS, Landsat 8, and Sentinel-2 Data for Accurate Crop Yield Predictions: A Case Study Using STARFM NDVI in Bavaria, Germany

Dhillon, M. S., Kübert-Flock, C., Dahms, T., Rummler, T., Arnault, J., Steffan-Dewenter, I., & Ullmann, T. (2023). Evaluation of MODIS, Landsat 8 and Sentinel-2 Data for Accurate Crop Yield Predictions: A Case Study Using STARFM NDVI in Bavaria, Germany. *Remote Sensing*, 15(7), 1830.

Published by MDPI Remote Sensing

• $\mathbb{Y} \cdot \mu \cdot$

' « " ± | μ | ± a d1 α-αY-1/4α±S 1 αμ· 1/4° © a-2Yα° ¶ α-α-α 3 μ²S, |·¶ α±S « " μ³S S " 1-23° " ± · 2 © ± " ° α a2 μ a « ° ¶ « ¶ 3 μ² 1 S " S a μ a 32 " ± α · 2 a " ± μ a " α ± " ° " 1 " - 2 © S α α ° α S © μ ± · ¶ 3 α α · " ° 32 μ α ± S ¶ 3 | · μ μ ¶ 2 , · ± ± ¶ fi 2° " 1 " μ · « " αY-1/4² © « " ¶ ¶ 1/4 « " · ¶ ¶ α · 2 " ° 32 μ S α α ¶ · ¶ · 2 α | | , μ a " 1/4° α³ α ± S ° 2 ± α² μ² , μ³ α ± " · 2 ± α © S 2 μ μ a ± α α ¶ ¶ α " μ ° α ± ¶ , ± S " μ " 3 2 μ S ' « ¶ ¶ , S 1/4 α ° " S · 2 ¶ 332 μ © , μ μ ¶ α μ « " © μ ¶ ± " ¶ ° α ± a | μ² 3 1/4 S ¶ ¶ 1/4 S " ± · © ± a « " 23 · α ¶ 3 α α " ° ° 2 μ ° α ± S " ° 32 μ α 2 μ S α ¶ μ μ ¶ 2 , · ± ± ¶ 2 ± α μ a ± α α ¶ ¶ α " ' « " | , μ ± · ¶ , S 1/4 " » 3 2 μ S α ± S S ¶ | , ¶ ¶ S « " ¶ αY-1/4 2 © © , μ S © μ ± · ¶ 1/4 « " · ¶ Ž α ± S ¶ α Ž ž " , S ° α ± S S α ¶ α ± S & ± · ± " & ž " , S ° α ± S S α ¶ α ± S · ° 2 μ α ž " , S ° α ± S S α ¶ ! ,) fi 3 μ² S, |·¶ | 2° Y ± " S ¶ 3 α μ a " 1/4 · 2 · ° 2 ° S " 1/4, ¶ S | μ² 3 a μ² ° « ° 2 S " ¶ " / ž ¶ * 2 μ S 1 22 S & , S ¶ ¶ * " 1 " & α ± S « " ¶ " ° 3 μ ¶ Ž a « (¶ " © | ± ± | 1/4 α³ 3 μ² α | « Ž (" © μ ° ± " μ ° « " α * * α ± S 2 " ¶ " S μ³ " & % 1/4 S © μ | α ¶ ¶ ± ° α 1 α α © © μ « " 1/4 α μ 1 2 μ * * α ± S " & % « " ¶ 1/4 « " · ¶ 3 μ² S, |·¶ « a « ¶ 3 α α α ± S " ° 32 μ α μ ¶ 2 , · ± ± μ ¶ , " S ± « a « μ 1/4 S α | | , μ α | · ¶ , ¶ ± a Ž (" α ± S * " 1 " & ' « " 2 Y ¶ μ a ± α ¶ 2 © a « " ° 32 μ α μ ¶ 2 , · ± ± S α 1/4 3 μ² S, |·¶ 2 © Y² « & ž " , S α ± S Ž ž " , S 3 α 1/4 S α ¶ ± α α α · μ² " ± α | | , μ a " 1/4 " α ¶ , μ ± a « " 1/4 S 2 © * * α ± S " & % 1 2 μ " » α ° 3 " Ž α ± S & ž " , S μ ¶ , " S ± α ± % α ± S % ž & α ± S S « α © μ * * % α ± S α ± S % ž & α ± S S « α © μ " & % , ¶ ± a « " Ž (" ° 2 S " μ ¶ 3 " · 1 " 1/4 α ° α μ 1/4 © μ « " α ± S S α 1/4 3 μ² S, |·¶ « " ¶ ° 3 " Ž (" ° 2 S " % α ± S μ " α " ° % ž & % ž & μ ' , μ S © ° " μ ± 3 , · 3 α μ α " " μ ¶ · 2 ¶ ° , α " | μ² 3 1/4 S α ± S ° α ¶ « a « 1/4 α | | , μ a " μ " α Y " α ± S ° 2 μ 3 μ | ¶ " « α ± « " | 2° 3 " » * " 1 " & ° 2 S " % α ± S % ž & ° α « a « μ ± 3 , · 3 α μ α " " μ ¶ " 2 ± | , ¶ 1 " 1/4 Y² « & ž " , S α ± S Ž ž " , S ± | 2° Y ± α · ± ° α « Ž (" ° " μ ° 2 μ 3 μ² ° ± " ± © μ 3 μ S | · ± a | μ² 3 1/4 S ¶ 2 ± α μ a ± α α ¶ ¶ α " « α ± « " S α 1/4 3 μ² S, |·¶ « 2° " 1 " μ Ž ž " , S ° α ¶ α S 1 α ± · α a 2 , ¶ © μ a " ± μ a ± a α ± S " » 3 2 μ ± a « " 2 ± a " μ 1/4 S · ° " ¶ μ ¶ S , " · 2 « " α 1 α-αY-1/4² © Ž α ± S ¶ α S α α ¶ ± | " ° α α ° α α ° , ° μ ¶ 2 , · ± ± 2 © ° fi α S S α ± ± « ¶ ¶ , S 1/4 μ | 2° ° " ± S " « " © μ « " μ , ¶ 2 © ¶ © ± S ± a ¶ © μ ° 3 " ° " ± · ± a α ± S 1 α S α ± a « " 2 ± a " μ | μ² 3 1/4 S · ° " ¶ μ ¶ ± S © μ ± · μ a ± α ¶ 2 © « " ° 2 μ S

fi.μ²S, |.²±

~ μ²³ ¼ S ¶ ³ ¼ α ¶ a ± ⊕ α ±. μ² ± . « ° ² μ S ¶ α μ ¶, , μ S " 1 " ²³ ° ±. «²º " 1 " μ . « " |²º ¥ ± " S " ⊕ |. ¶ ² ⊕ | -º α " | « α ± a " ± | μ ¶ ¶ ± a ² ¥ α ³ ²³ , - α ² ± α ± S S " a μ S α ² ± ² ⊕ ¶ ² - α ± S ° α " μ μ ¶², μ ¶ ¶ μ ¶, μ ¶ ¶ ° α ± ° " . «² S ¶ . « α ³ μ ¶¹ - S " α .º " ¼ α ± S α | |, μ α " α ¶ ¶ ¶ ¶ " ±. ² ⊕ | μ²³ ³ μ² S, |.² ± α ± S |² ± . μ ¥, . " .²º α S ¶ ± | μ ¶ ¶ ± a . « " ¶, ¶ α ± α ¥ - ¼ ¶ ⊕ α μ ¶, , μ ¶ ⊕ ² S ³ μ² S, |.² ± 1 " ff " L² ± a " . α " 1 " μ . « " ³ α ¶. ⊕ ° ¼ α ¶ ¶ . « " a μ² ° . « ± ³, ¥ - ¼ α¹ α - α ¥ " ¶ α " - " S α α α ± S . « " ° " μ ± ± | " ² ⊕ ± " ° . " | « ± ² a - ¶ ¶ « ¶ ¶ ³ μ ¶¹ - S " S . « " ³ ² . " ± . α . ² a " ± " μ α " α ± S " » ³ ² μ α ± " ° " 1 " - ² ⊕ S α α ° - « S - ⊕ μ ± . ¶³ α - α " . " ° ³ ² μ α " α ± S ¶³ " | . μ ¶ μ ¶², .² ± ¶ ¶ , « - ² ± " . α " « - ² ± " . α " ~ ° " ¼ ± ²¹ α " . α " Ž, ² " . α " + - «, " . α " fi²º " 1 " μ . « " ⊕ ± S α ° " ± . α " μ ¶, μ ¶ " ± . ¶ ² ⊕ ± " ° ¼ a " ± " μ α " S ¶ ¼ « " . - | S α α - " . « " μ ²³ .º α " ¶³ α - α ² μ . " ° ³ ² μ α " μ ¶², .² ± ¶ ¶ ± α | |, μ α " ¼ μ S - | . ± a | μ²³ ¼ S ¶ ¶ - ± " S . ² ¥ " » ³ ² μ S , « - ² ± , α α ° ¶ | ¥ μ 1 ² | ® " . α " « - ² ± " . α " « - ² ± " . α " α α ° ¶ | , " ¥ μ 1 ² | ® " . α "

! ² " ± ¶, μ ¶ . « " α | |, μ α " ° ² ± - ² μ ± a ² ⊕ | μ²³ ¼ S ¶ ¶ ° α ± ¼ ¶, S - ¶ ¶ ± . « " ³ α ¶. ° ² S " | α S " ¶ ¶ « α " ¶ μ S . ² " » α ° ± " . « " μ - α ² ± ¶ ¶ « - ² ¥ . ° " ± ³ - α ± . ¶ α ± S . « " μ a μ² ° ± a " ± 1 - μ² ± ° " ±. α ± S ³ μ² ³ ² ¶ ¶ S | μ²³ ° ² S " ¶ . ² ¶ ¶ ° , - α " . « " | μ²³ a μ² ° . « ¶ α , ¶ ° ² ² a α α S " . α " ° μ ¶ ¶ ± " . α " 1 μ α ± ® " . α " L² ± " ¶ " . α " | " α ± a " . α " ! " ± S " " . α " & " S, . ² " . α " & ý | ® " " . α " & ± | " . « " ± | μ²³ ° ² S " ¶ ¶ « α " α S¹ α ± | " S ± ° ² ± - ² μ ± a | μ²³ a μ² ° . « ¶ ¶ ° . « " ' , α - α - 1 " . ² . « " ' , α ± . - α - 1 " " 1 " - α ± S « α " ¥ " ± ° ² S - ⊕ S ¶ ¶ ° . « " ¶ ¶ ° , - α ² ± ² ⊕ . « " a μ² ° . « ³ μ² | " ¶ ¶ α α ³ - α ± . " 1 " - . ² . « " ⊕ S ² μ μ a - ² ± α " 1 " - " 1 " μ . -º " | μ²³ a μ² ° . « ° ² S " ¶ ¶ / ž ¶ ¶ | « ¶ ¶ * ² μ S 1 ² ² S & , S - ¶ ¶ * " 1 " & " a μ ¶, , μ ¶ # μ² S, |.² ± & ¶ . " ° ¶ & ° , - α ² μ . # & ž " ' , α " μ²³ " μ²³ ± a & ¶ . " ° ¶ & ° , - α ² ± ž ² S " " μ²³ & ¶ . α ± S Ž - a . (¶ " ⊕ | - ± | ¼ Ž (" « α " ¥ " ± μ ⊕ ± S α ± S , ³ S α " S . ² ¶ ¶ ° , - α " ¥ " μ | μ²³ a μ² ° . « ¶ α , ¶ α ± S ¼ S ¶ ° ² ² a α α S " . α " « - ² ± " . α " L ± " . α " | α ¶ α ³ α - ¶ ¶ " . α " | " α ± a " . α " L Ž ž ² ± . " - « L² « ± Ž " ± ± ² » ž ² ± . " - « & " S, . ² " . α " & ý | ® " " . α " fi²º " 1 " μ ° « " ± | μ²³ ¼ S ¶ ¶ α μ " » α ° ± " S α ⊕ S ¶ ¶ α " ¶ " / ž ¶ ± " S . ² α | |², ± . ⊕ μ . « " ¶³ α - α ¹ α μ α ² ± ¥ ¼ μ²¹ - S ± a . « " ¶³ α - α S - ¶ . μ ¥, .² ± ² ⊕ | -º α " 1 α μ α ¥ " ¶ " . " ° ³ " μ α , μ

$^3 \mu |^{-3} \rightarrow \alpha \cdot \mu \pm \mu^2 \rightarrow ^2 \mu$, μ $\pm \mu^2 \mu^3 \ll \mu^4 | \alpha^{-3} \mu \mu^0 \dots \mu \mu^1 \mu^2 \mu^3 \mu^4 \mu^5 \mu^6 \mu^7 \mu^8 \mu^9 \mu^{10} \mu^{11} \mu^{12} \mu^{13} \mu^{14} \mu^{15} \mu^{16} \mu^{17} \mu^{18} \mu^{19} \mu^{20} \mu^{21} \mu^{22} \mu^{23} \mu^{24} \mu^{25} \mu^{26} \mu^{27} \mu^{28} \mu^{29} \mu^{30} \mu^{31} \mu^{32} \mu^{33} \mu^{34} \mu^{35} \mu^{36} \mu^{37} \mu^{38} \mu^{39} \mu^{40} \mu^{41} \mu^{42} \mu^{43} \mu^{44} \mu^{45} \mu^{46} \mu^{47} \mu^{48} \mu^{49} \mu^{50} \mu^{51} \mu^{52} \mu^{53} \mu^{54} \mu^{55} \mu^{56} \mu^{57} \mu^{58} \mu^{59} \mu^{60} \mu^{61} \mu^{62} \mu^{63} \mu^{64} \mu^{65} \mu^{66} \mu^{67} \mu^{68} \mu^{69} \mu^{70} \mu^{71} \mu^{72} \mu^{73} \mu^{74} \mu^{75} \mu^{76} \mu^{77} \mu^{78} \mu^{79} \mu^{80} \mu^{81} \mu^{82} \mu^{83} \mu^{84} \mu^{85} \mu^{86} \mu^{87} \mu^{88} \mu^{89} \mu^{90} \mu^{91} \mu^{92} \mu^{93} \mu^{94} \mu^{95} \mu^{96} \mu^{97} \mu^{98} \mu^{99} \mu^{100}$

$\mu \pm \mu^2 \mu^3 \mu^4 \mu^5 \mu^6 \mu^7 \mu^8 \mu^9 \mu^{10} \mu^{11} \mu^{12} \mu^{13} \mu^{14} \mu^{15} \mu^{16} \mu^{17} \mu^{18} \mu^{19} \mu^{20} \mu^{21} \mu^{22} \mu^{23} \mu^{24} \mu^{25} \mu^{26} \mu^{27} \mu^{28} \mu^{29} \mu^{30} \mu^{31} \mu^{32} \mu^{33} \mu^{34} \mu^{35} \mu^{36} \mu^{37} \mu^{38} \mu^{39} \mu^{40} \mu^{41} \mu^{42} \mu^{43} \mu^{44} \mu^{45} \mu^{46} \mu^{47} \mu^{48} \mu^{49} \mu^{50} \mu^{51} \mu^{52} \mu^{53} \mu^{54} \mu^{55} \mu^{56} \mu^{57} \mu^{58} \mu^{59} \mu^{60} \mu^{61} \mu^{62} \mu^{63} \mu^{64} \mu^{65} \mu^{66} \mu^{67} \mu^{68} \mu^{69} \mu^{70} \mu^{71} \mu^{72} \mu^{73} \mu^{74} \mu^{75} \mu^{76} \mu^{77} \mu^{78} \mu^{79} \mu^{80} \mu^{81} \mu^{82} \mu^{83} \mu^{84} \mu^{85} \mu^{86} \mu^{87} \mu^{88} \mu^{89} \mu^{90} \mu^{91} \mu^{92} \mu^{93} \mu^{94} \mu^{95} \mu^{96} \mu^{97} \mu^{98} \mu^{99} \mu^{100}$

$^2 \mu \mu^3 \mu^4 \mu^5 \mu^6 \mu^7 \mu^8 \mu^9 \mu^{10} \mu^{11} \mu^{12} \mu^{13} \mu^{14} \mu^{15} \mu^{16} \mu^{17} \mu^{18} \mu^{19} \mu^{20} \mu^{21} \mu^{22} \mu^{23} \mu^{24} \mu^{25} \mu^{26} \mu^{27} \mu^{28} \mu^{29} \mu^{30} \mu^{31} \mu^{32} \mu^{33} \mu^{34} \mu^{35} \mu^{36} \mu^{37} \mu^{38} \mu^{39} \mu^{40} \mu^{41} \mu^{42} \mu^{43} \mu^{44} \mu^{45} \mu^{46} \mu^{47} \mu^{48} \mu^{49} \mu^{50} \mu^{51} \mu^{52} \mu^{53} \mu^{54} \mu^{55} \mu^{56} \mu^{57} \mu^{58} \mu^{59} \mu^{60} \mu^{61} \mu^{62} \mu^{63} \mu^{64} \mu^{65} \mu^{66} \mu^{67} \mu^{68} \mu^{69} \mu^{70} \mu^{71} \mu^{72} \mu^{73} \mu^{74} \mu^{75} \mu^{76} \mu^{77} \mu^{78} \mu^{79} \mu^{80} \mu^{81} \mu^{82} \mu^{83} \mu^{84} \mu^{85} \mu^{86} \mu^{87} \mu^{88} \mu^{89} \mu^{90} \mu^{91} \mu^{92} \mu^{93} \mu^{94} \mu^{95} \mu^{96} \mu^{97} \mu^{98} \mu^{99} \mu^{100}$

20

Therefore, filling the data gaps in the RS input data is more realistic before implementing the synergistic approach (where CGMs are linked with the RS data) for crop monitoring.

To fill the observation gaps in the RS data, spatial-temporal data fusion, where a high spatial resolution product is synchronised with a coarse or low-resolution product, is considered the most effective solution recommended by many studies on detecting vegetation changes (Cui et al., 2018; Lee et al., 2019; Xie et al., 2016; L. Zhu et al., 2017). The Spatial and Temporal Adaptive Reflectance Fusion Model (STARFM), which blends the coarse spatial resolution of MODIS and high spatial resolution of Landsat data, was the first initiative in fusion modelling. Since then, many spatiotemporal models have been developed with a successful validation of new synthetic data (Emelyanova et al., 2013; F. Gao et al., 2006; Hilker et al., 2009; B. Huang & Song, 2012; Luo et al., 2018; M. Wu et al., 2012; X. Zhu et al., 2010; X. Zhu et al., 2016). Moreover, generating new-resolution synthetic products provides geoscience applications with multi-spatial and multi-temporal resolution data. It then outputs different spatial and temporal data of the ground objects (Dhillon et al., 2022; Dhillon et al., 2020). However, the potential of newly generated synthetic data obtained from fusion modelling in crop yield predictions using crop modelling still needs to be explored. Inputting RS data with high spatial and temporal resolution could be further used to improve the time series simulation of crop models and increase the models' simulation accuracy. In addition, the high spatial resolution of RS data could be used to reduce the problem of mixed pixels and then increase the accuracy of different spatial properties at the field scale (Jin et al., 2018).

In the current study, the STARFM-based synthetic NDVI time series for the application of agriculture is selected from (Dhillon et al., 2022; Dhillon et al., 2020), where the fusion of MOD13Q1 (20 m, 16 days) is individually achieved with Landsat (30 m, 16 days; L) and Sentinel-2 (10 m, 5–6 days; S). Therefore, intending to investigate the importance of synthetic and real NDVI products with a different spatial and temporal resolutions, this research paper compares other output products which

calculate the crop yield of winter wheat (WW) and oil seed rape (OSR) for Bavaria in 2019. The crop yield output of six different RS products (real: MOD13Q1 (250 m, 8 and 16 days); synthetic: L-MOD13Q1 (30 m, 8 and 16 days) and S-MOD13Q1 (10 m, 8 and 16 days)) with two widely used CGMs (WOFOST and LUE), for the respective crops, is tested. Eventually, for accurate crop yield modelling of WW and OSR in 2019, this study answers three research questions:

1. What is the best suitable spatial resolution (10 m, 30 m, or 250 m)?
2. What is the best suitable temporal resolution (8- or 16-days)?
3. Which is the best suitable CGM (LUE or WOFOST)?

Investigating RS products' optimal spatial and temporal resolutions for accurate crop yield predictions using CGMs requires heavy pre-processing of multiple synthetic and non-synthetic remote sensing datasets. Therefore, knowing the suitable data inputs for crop modelling would save time and computation power for future crop yield prediction and precision farming studies.

3.2. Materials and Methods

The general workflow of the study is shown in Figure 3.1. The flow diagram is divided into 1) Data fusion and 2) Crop yield modelling for 2019. The first part was a testing phase that investigated the suitable synthetic NDVI product (which were L-MOD13Q1 and S-MDO13Q1) for the agricultural land cover (LC) class of Bavaria for the year 2019 (completed in the preceding work (Dhillon et al., 2022)). The "index-then-blend" (IB) technique is used in the previous study to first produce the NDVI from the high pair (Landsat or Sentinel-2) and low pair (MOD13Q1) images before blending them for the data fusion (X. Chen et al., 2018). The IB technique combines only one band, the NDVI. Therefore, it was faster and less expensive to compute. In the second section, the selected output NDVI time series of part 1 (two real: MOD13Q1 (250 m, 8- and 16-days), and four synthetic: L-MOD13Q1 (30 m, 8- and 16-days), and S-MOD13Q1 (10 m, 8- and 16-days)) and the climate elements were used as an input to the LUE and WOFOST models estimating the crop yield of WW and OSR 2019 in Bavaria. The satellite NDVI and the climate data were selected for the respective start and end of the season for WW

and OSR for 2019. Both inputs are masked for WW and OSR using the InVeKos data (source: www.ec.europa.eu/info/index_en, accessed on 21 June 2021).

In the last steps, Bavaria's obtained crop yield is validated using the Bayerisches Landesamt für Statistik (LfStat) data at the regional level (with a 95% confidence interval). The satellite data sets were downloaded and preprocessed in Google Earth Engine (GEE), and the fusion analysis was done in R (version 4.0.3) using RStudio.

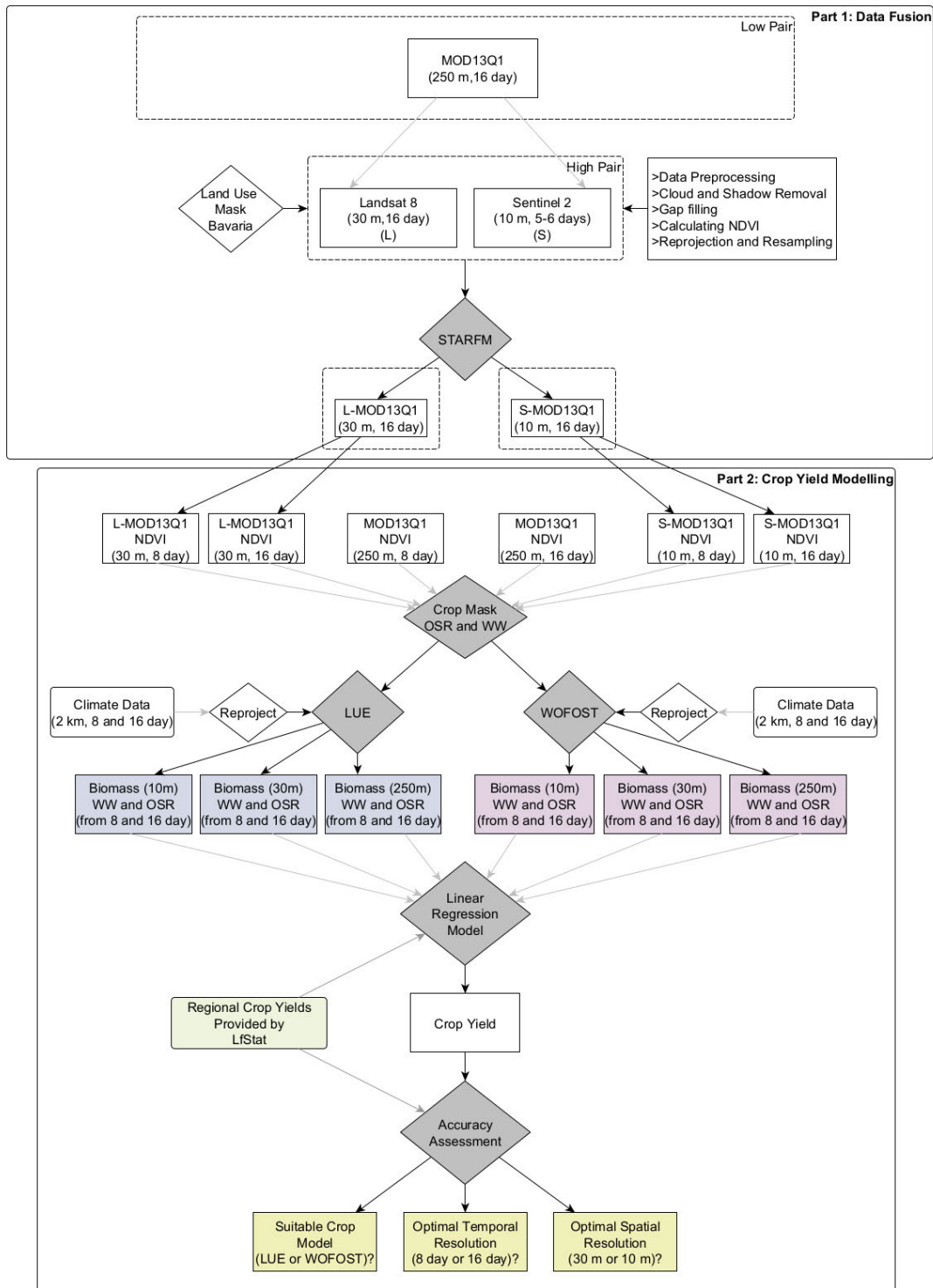


Figure 3.1. The conceptual framework of the study is divided into two parts: Part 1 states the data fusion for 2019 to investigate the synthetic NDVI time series product (this section is already completed in our previous study (Dhillon et al., 2022)), and Part 2 estimates and validates the crop yield for Bavaria by inputting the fused L-MOD13Q1 time series and climate elements to a semi-empiric Light Use Efficiency (LUE) model; STARFM = Spatial and Temporal Adaptive Reflectance Fusion Model; NDVI = Normalized Difference Vegetation Index; L-MOD09GQ = Landsat-MOD09GQ; L-MOD09Q1 = Landsat-MOD09Q1; L-MCD43A4 = Landsat-MCD43A4; L-MOD13Q1 = Landsat-MOD13Q1; S-MOD09GQ = Sentinel-2-MOD09GQ; S-MOD09Q1 = Sentinel-2-MOD09Q1; S-MCD43A4 = Sentinel-2-MCD43A4; S-MOD13Q1 = Sentinel-2-MOD13Q1; LfStat = the Bayerisches Landesamt für Statistik (LfStat).

3.2.1. Study Area

The federal state of Bavaria is located between 47°N and 50.5°N and between 9°E and 14°E in the southeastern part of Germany (Figure 3.2). The topography mainly influences the region's climate, with higher elevations in the south (northern edge of the Alps) and east (Bavarian Forest and Fichtel Mountains). The mean annual temperature ranges from -3.3 to 11°C, but in most of the territory, the temperature ranges between 8 and 10°C (Dhillon et al., 2022). The mean annual precipitation sums range from approximately 500 to above 3100 mm, with wetter conditions in the southern part of Bavaria. In 2019, the LC was highly dominated by forest (36.91%) and agriculture (31.67%) (based on the LC map of Bavaria, 2019). The agricultural areas are mainly found in the northwest and southwest of Bavaria, while forest cover dominates towards the Alps and the east. The other LC classes include grassland, urban, natural-semi, and water cover approx. 19.16%, 8.97%, 1.84%, and 1.44% for the territory (estimates based on the LC map of Bavaria, 2019) (Dhillon et al., 2022). With an area of approx. 70,500 km² Bavaria covers almost one-fifth of Germany. The federal state is divided into 96 counties with 71 rural districts (so-called "Landkreise") and 25 city districts (so-called "Kreisfreie Städte"). A brief description of the regions of Bavaria is shown in Figure A1.

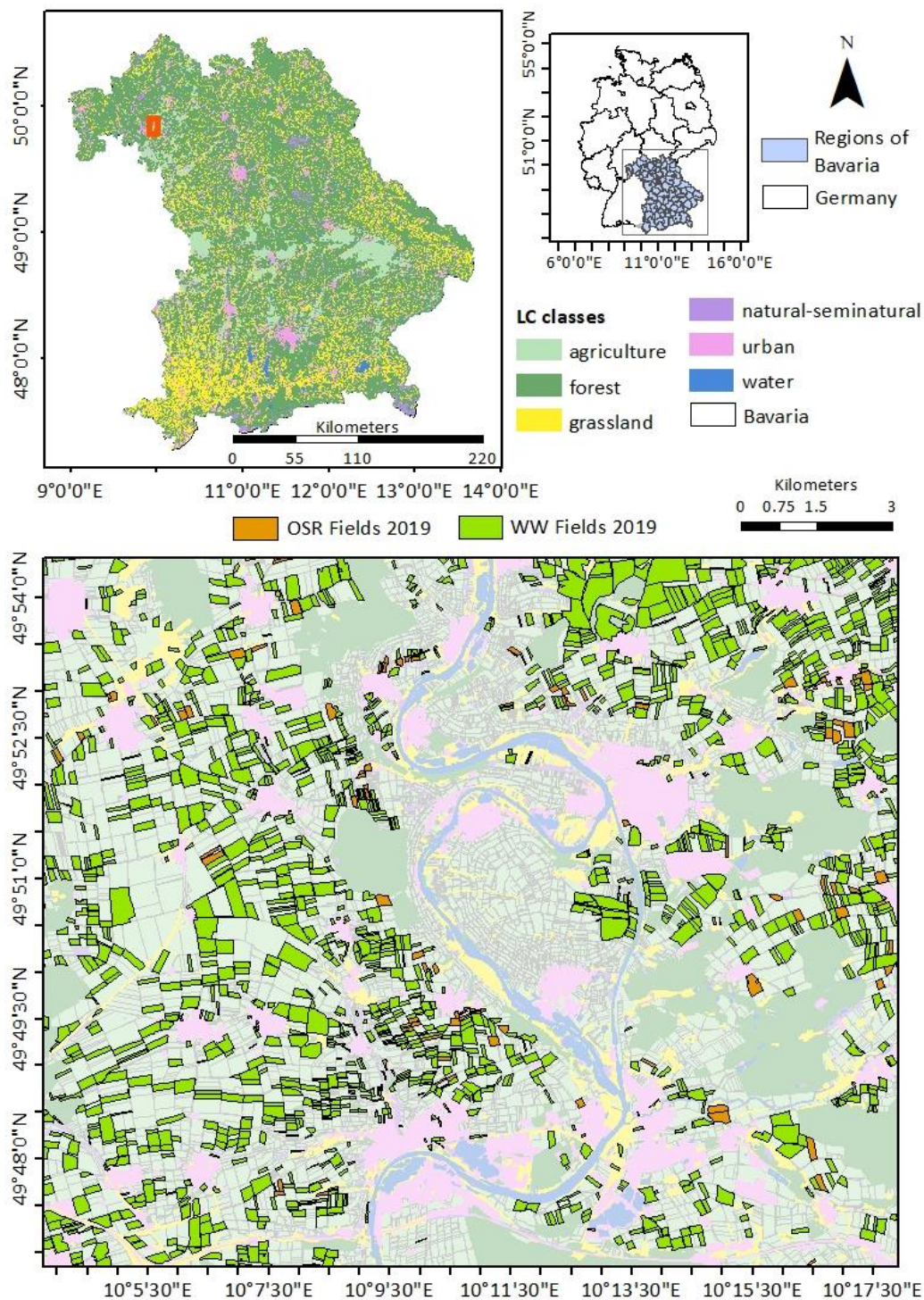


Figure 3.2. An overview of the study region. The LC map of Bavaria is obtained by combining multiple inputs of Landcover maps such as Amtliche Topographisch-Kartographische Informationssystem, Integrated Administration Control System (provides the crop field information), and Corine LC, into one map. Agriculture (peach green) dominates mainly in the northwest and southeast of Bavaria, while forest and grassland classes (dark green and yellow, respectively) dominate in the northeast and south. The LC map is overlaid by the district map of Bavaria. The enlargement (displayed with a dark red box on top right map) shows the urban area of the town Volkach, with the oil seed rape (OSR) fields (dark orange) and the winter wheat (WW) fields (dark green) in 2019. Brief description of the regions of Bavaria is shown in Figure A1.

3.2.2. Data

This study investigated relevant satellite data, with different spatial and temporal resolutions used to predict the crop yields of Bavaria on a regional level. Several climate parameters were inputted into the crop models along with the satellite data. Further, the updated InVeKos data of 2019 (https://ec.europa.eu/info/index_en) are used to obtain the reference field information of WW and OSR for every district of Bavaria. Table 3.1 briefly describes the used data and indicates the spatial and temporal resolutions.

Table 3.1. A summary of the collected datasets for crop modelling of winter wheat's (WW) and oil seed rape's (OSR) in 2019. The satellite data used for crop yield modelling are synthetic L-MOD13Q1, S-MOD13Q1 and real Moderate Resolution Imaging Spectroradiometer (MODIS) MOD13Q1; the climate parameters are minimum temperature (°C) (Tmin), maximum temperature (°C) (Tmax), dewpoint temperature (°C) (Tdew), solar radiation ($\text{MJm}^{-2}\text{day}^{-1}$) (Rs), sunshine duration (hours) (N), evaporation (mm) (Ep), Transpiration (mm) (Tp), Run off (mm) (Roff) and, precipitation (mm) (P); InVeKos data provides the fields of WW and OSR for Bavaria for 2019; the Bayerisches Landesamt für Statistik (LfStat) data provides the crop yield information (dt/ha) of WW and OSR at district level of Bavaria 2019.

| Data | Product Name | Resolution (Spatial-Temporal) | References |
|----------------|--|-------------------------------|--|
| Climate data | Tmin, Tmax, Tdew, Rs, N, Ep, Tp, Roff, P | 2000 m, 8- and 16-days | https://www.uni-augsburg.de/de/fakultaet/fai/geo/ (accessed on 21 June 2021) |
| | L-MOD13Q1 | 30 m, 8- and 16-days | (Dhillon et al., 2022) |
| Satellite data | S-MOD13Q1 | 10 m, 8- and 16-days | (Dhillon et al., 2022) |
| | MODIS (MOD13Q1) | 250 m, 8- and 16-days | www.lpdaac.usgs.gov (accessed on 21 June 2021) |
| Vector data | InVeKos | 2019 | www.ec.europa.eu/info/index_en (assessed on 21 June 2021) |
| | LfStat | 2019 | https://www.statistikdaten.bayern.de/geneis/online/ (accessed on 21 June 2021) |

3.2.2.1. Satellite Data

The study employed freely available two spatially high-resolution products obtained from the Sentinel-2 Copernicus program and Landsat 8 Land Surface Reflectance Code (LASRC). The LASRC Tier 1 offers seven spectral bands (coastal/aerosol, blue, green, red, near-infrared (NIR), shortwave infrared (SWIR) 1, SWIR 2) with a spatial resolution of 30 m on a Universal Transverse Mercator (UTM) projection. Using the snow, shadow, and cloud masks, the created C function of the mask (CFMask) method removed snow (Bit 4), clouds (Bit 5), and cloud shadows (Bit 3)

using the “pixel_qa” band. After preprocessing, the available snow-free, cloud-free, and shadow-free Landsat images were acquired in 2019 for the state of Bavaria on the following day-of-year (DOY), respectively: 49 (18 February), 81 (22 March), 145 (25 May), and 177 (26 June) (Figure 3.3).

Moreover, the study also used Sentinel-2 data, which enabled global coverage, five-day return frequency, and multi-spectral imaging with 12 spectral bands at spatial resolutions of 10–20 m. Sentinel-2's surface reflectance data were processed using the Google Earth Engine after being acquired from the Copernicus Open Access Hub (accessed on 02 August 2021) (Gorelick et al., 2017). The data was computed using *sen2cor*, which used three quality assessment (QA) bands to create cloud-free images with a QA60 bitmask band containing cloud mask information. After preprocessing, the available Sentinel-2 images were acquired in 2019 for the state of Bavaria at the following DOY, respectively: 49 (18 February), 81 (22 March), 97 (7 April), 113 (23 April), 145 (25 May), and 177 (26 June) (Figure 3.3).

For data fusion, the coarse resolution MOD13Q1 V6 product was used in the study to generate L-MOD13Q1 and S-MOD13Q1 by fusing it with the preprocessed Landsat and Sentinel-2 data. The MOD13Q1 provided an NDVI value per pixel with 250 m spatial and 16-day temporal resolution. In the composed product of MOD13Q1, the NDVI value of a pixel value is assigned with the minor rules and best viewing geometry to the first date of a 16-days' time frame. Pixels with constraints (e.g., shadows, clouds) were masked using the quality information (QA) provided along with the NDVI band. Considering the day of acquisition and the QA, the linear interpolation of all NDVI values was performed on the product (Kuebert, 2018b) to generate a time series without gaps.

The present study used the synthetic L-MOD13Q1 (30 m, 16-days) and S-MOD13Q1 (10 m, 16-days) NDVI time series generated by (Dhillon et al., 2022) as input to the two CGMs obtaining crop yields. Both synthetic products (16-days), L-MOD13Q1 and S-MOD13Q1, were generated using the STARFM and the 8-day products were further developed by applying the linear interpolation approach on 16-day products. The 8- and 16-day time series for RS products were obtained for DOYs from the stem elongation

phases till the flowering stages of both WW and OSR. For OSR, the start of the season was on the 15th of February, and the end of the season was 20th of April 2019 (Zamani-Noor & Feistkorn, 2022). Moreover, for WW, the start and end of the season period lay between the 15th of April and to 30th of June 2019 (Harfenmeister, Itzerott, Weltzien, & Spengler, 2021). In addition, the MOD13Q1 (i.e., just the MODIS NDVI time series without image fusion) was also chosen as an input to the CGMs to allow a comparison between the synthetic and the real RS time series for crop yield estimation. Based on our previous study, the accuracy assessments of STARFM-generated L-MOD13Q1 and S-MOD13Q1 NDVI products (further used as input for the two CGMs) with the real Landsat and Sentinel-2 NDVI for the agricultural LC class are shown in Table 3.2 (Dhillon et al., 2022). Our previous study briefly discusses the accuracy assessment of different spatial, temporal products (Dhillon et al., 2022). However, the present study also evaluated synthetic NDVI products' performance by comparing them with the real NDVI products of Landsat, Sentinel-2 and MOD13Q1. The study compared the mean NDVI values for all RS products used by taking 10,000 random points in Bavaria.

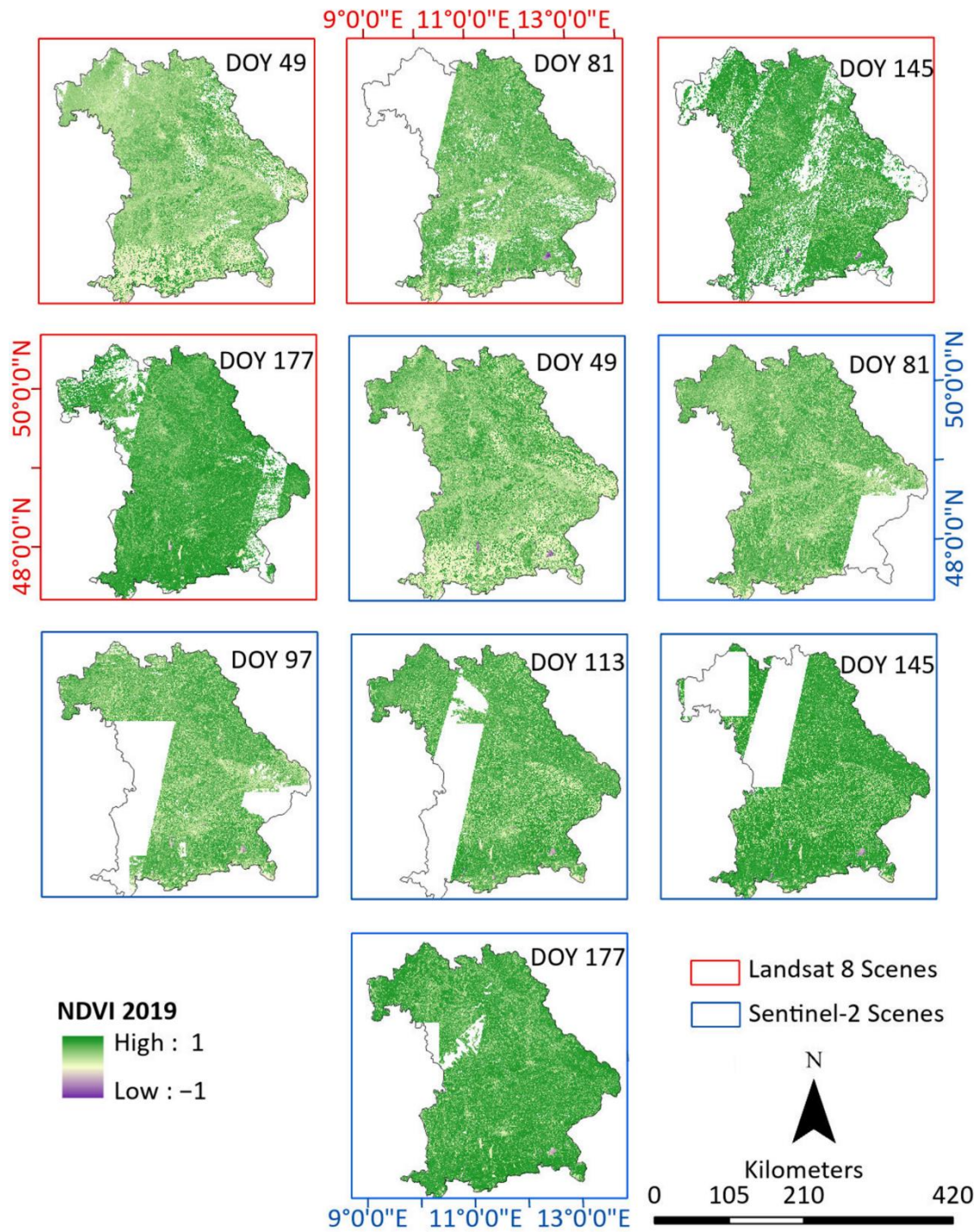


Figure 3.3. The cloud-free scenes are available for Landsat (in red box) and Sentinel-2 (in blue box) during the seasons of OSR and WW. Four cloud-free scenes were collected for the Landsat data, and six were collected for the Sentinel-2 data. The maps show the NDVI values from -1 to 1 for the entire Bavaria during 2019.

$\tilde{Z} \otimes \alpha$

' « " ° ¼ μ ¶ | « ¶ Z ± S ¶ ¶ ° . © μ & α ¶ ¶ ° Z & α ¶ ¶ . « " | μ²³ ¼ ¶ S¹ α- S α- ± S α α
 3 μ²¹ S ± a . « " | μ²³ ¼ ¶ S ± © μ α- ± ± 2 © | μ²³ | α- a² μ ¶ ¶ ± | , S ± a * * ± S " & % ±
 ° α¹ μ α² ± α S ¶ ¶ ¶ . " " ± ¶ ¶ , μ " ° ° ° ¶ ¶ ¶ ° S α- ± ± ¼ μ ¶ S " a " ± ¶ ¶ ¶
 & α ¶ ¶ ¶ ¶ ° 2 S " α | ¶ ¶ ¶ S² ± L_± " ' « " Z & α S α α ° " μ , ¶ S .² 1 α- S α- " .
 « " Z (~ ° 2 S " S ¼ ¶ S ¶ ° 2 © * * ± S " & % ' « " 1 α- S α- ± μ ¶ ¶ ¶ ¶ ° " μ , ¶ S .² | « " | ©
 . « " ° 2 S " ¶ ¶ ¶ | , μ ¶ ¼ | ± ± ¶ ¶ " ± | ¼ ± S ¶ ¶ α- ± ± ¼ ± a " ± " μ ± a . « " ¼ ¶ S μ ¶ ¶ ¶ ± . « " μ^a ± ± ' « " 1 α- S α- ± ° ¶ ¶ ° ¶ S .² . « " μ μ α μ ¶ ¶ ± S . « " | - ¼ S ¶ ¶ ¶ ¶ ° " μ " » | , S S
 1 - a , μ " .

3.2.3. Method

* " 1 " &

' « " * " 1 " & ° 2 S " ¶ ¶ ¶ α 3 μ ¶ ¶ ¶ ¶ ¶ S ° " | « ± ¶ ¶ ¶ ° 2 S " . « α S " ¶ ¶ μ ¶ ¶ | μ²³
 3 μ α ° " . μ ¶ ¶ | « ¶ | μ²³ ¶ ° ¶ ¶ ¶ ± S ¼ ¶ S ¶ ¼ |² ± ¶ S " μ ± a | μ²³ a " ± " . 3 μ²³ μ ¶ ¶ ± S
 | - ° α - | ± S ° ± α a " ° " ± . 3 μ α ° " . μ ¶ ¶) ± , - " ± * 2 ©) ± | " , " ± % α³³² S .

' « " ¶ ± ± © ± . 3 μ ¶ ¶ ¶ ¶ ¶ μ ¶ " ¶ ¶ ¶ ° α- ± ± . μ ± ¶ ± μ α- ± ± μ ¶ ± μ α- ± ±
 3 « ± ± 2 a - | α S " 1 " 23 ° " ± . ± S S μ ¼ ° α . " μ © μ α- ± ± | μ²³ ¶ ° ¶ ¶ ¶ ' « " ° 2 S " ¶ ¶ ¶ ¶
 | μ²³ ¶ ° ¶ ¶ ¶ ¶ | α © ± | . ± ± 2 © ¶ ° μ μ S α- ± ± . " ° 3 " μ , μ ± S S α- ¼ | μ²³
 | « μ α | . μ ¶ ¶ ¶ ¶ Z : ¶ ¶ α 1 - α ¶ ¶ α " 1 μ α ¶ " ± . « " * " 1 " & ° 2 S " .² ± α - ¼ ¶ S ¼ α ° -
 a μ² ° . « 3 μ ¶ ¶ ¶ ¶ ¶ ' « " ° 2 S " ¶ ¶ ¶ , α " ¶ ¶ . « " S α- ¼ | μ²³ a μ² ° . « μ α " . « " a μ ¶ ¶ " " ¶
 ¶ ¶ ° α- ± ± μ α " . « α S " 3 " ± S ¶ ¶ 2 ± . « " Z : ¶ ± S ± |² ° ± a μ S α- ± ± ¶ ± S α- ± ± Z : ¶ ¶
 ± " ¶ ¶ " ± . α- 3 μ α ° " . μ © μ . « " | α | , α- ± ± 2 © . « " 3 2 . " ± . α- . μ ± ¶ ± μ α- ± ± ± . « " ° 2 S " -
 ' « " ± 3 , . " S Z : ¶ ¶ | α | , α " S ¶ ¶ α © ± | . ± ± 2 © ! .) ¶ © μ * * ± S " & % ' α ¶ " .

' α ¶ " : ¶ ¶ ° μ ¼ ¶ ° , α- ± ± ¶ , ¶ S .² | α | , α " Z : ¶ ¶ ° ! .) ¶ ¶ " - " 3 μ S , | ¶ © μ * * ± S " &
 ' « " ¶ " , α- ± ± ¶ μ ¶ S ¶ ° . « " a μ² ° . « ¶ α " 2 © α | μ²³ . - . « " ° μ ± a ¶ α " ' « " Z : ¶ ¶ μ S , | - ¶
 , ¶ S ¶ ± ± 3 , .² . « " * " 1 " & ° 2 S " -

| " μ ²³ ¼ " | ~ , α- ± ± | % | % © μ ± ¶ ¶ |
|-----------------------|-------------------------------|---|----------------------------------|
| * * | LAI = -16.606 + 20.612 * NDVI | | fi ± ½ - * ¶ ¶ ° " μ , ± Z " ± ½ |
| " & | LAI = -0.393 + 4.769 * NDVI | | * " - . α |

' « " S α- ¼ a μ ¶ ¶ ¶ ¶ ¶ ¶ ¶ ° α- ± ± μ α " 2 © . « " | μ²³ ¶ | α | , α " S ¶ ¼ . « " S α- ¼ a μ ¶ ¶ ¶ S
 μ S α- ± ± ± S . « " 3 « 2 . 2 ¶ ¼ . « " - | « μ α | . μ ¶ ¶ ¶ ¶ 2 © α | « " α © ± S - © μ " μ | α | , α " ¶ . « " .
 .² . α | μ ¶ ¶ ¶ ¼ μ ¶ ¶ ¶ " fi " 3 μ S , | S & ° " ¶ ¶ . ± ± ¶ ¶ 2 © . « " " fi " 3 μ S , | S μ ¶ , ¶ S

actual Light Use Efficiency (g C M J^{-1}), $T_{\text{min}_{\text{min}}}$ is the minimum of the minimum temperature ($^{\circ}\text{C}$) index, VPD is the vapour pressure deficit (kPa) index, and K_s is the soil moisture stress index. The temperature and vapour pressure indexes are calculated using the minimum and maximum values for the study region. The total aboveground biomass calculated by the LUE model is equivalent to the net primary productivity (NPP) ($\text{kg ha}^{-1} \text{yr}^{-1}$). A brief explanation of the model with a flow diagram is described in our previous study (Dhillon et al., 2020). The specific model is not only selected for its performance but also its high processing speed and low requirement of input parameters compared to the other CGMs. The linear regression equations used to calculate crop yields of WW and OSR for different satellite biomass products using LUE are shown in Table A1.

Both models (LUE and WOFOST) were calibrated by using values shown in Table 4. This study used a minimum lethal temperature of -2°C for WW and OSR (Habekotté, 1997; Hodgson, 1978; Single, 1985). In the other studies, the optimal minimum values of temperature of WW and OSR at growth stages were 10°C and 12°C , respectively (Habekotté, 1997; Hodgson, 1978; Single, 1985). For the Vapor Pressure Deficit (VPD), the present study followed (Russell & Wilson, 1994), which analysed the environmental impact on leaf gas exchange of WW with minimum and maximum values of 1.5 and 4.0 kPa, respectively. The value for optimal light use efficiency is used as 3 gC/MJ (Djumaniyazova et al., 2010).

Table 3.4. Description of model calibration values taken from the related literature for the WOFOST and LUE models. Plus, the climate thresholds used to calculate the climate stress indexes used in the design of a model.

| Parameter | Description | Model(s) | Value | Units | Reference |
|--------------|--------------------------------|------------|----------|------------------|--|
| ξ | Scattering coefficient | WOFOST | 0.2 | - | (Van Diepen et al., 1989) |
| kdf | Diffusion coefficient | WOFOST | 0.72 | - | (Goudriaan, 1977) |
| Am | Gross assimilation rate | WOFOST | 4 | g/m ² | (C. J. T. Spitters & Kramer, 1986) |
| Ce | Conversion coefficient | WOFOST | 0.0399 | - | (Slattery & Ort, 2015) |
| ϵ_0 | Light use efficiency | WOFOST&LUE | 3 | gC/MJ | (Djumaniyazova et al., 2010) |
| Tmin min | Minimum of minimum temperature | WOFOST&LUE | -2 | °C | (Single, 1985) |
| Tmin max | Maximum of minimum temperature | WOFOST&LUE | 12 | °C | (Russell & Wilson, 1994) |
| VPD min | Minimum VPD | LUE | 1.3- 1.5 | k Pa | (Ray, Gesch, Sinclair, & Allen, 2002; Q. Xue, Weiss, Arkebauer, & Baenziger, 2004) |
| VPD max | Maximum VPD | LUE | 3.6-4 | k Pa | (Ray et al., 2002; Q. Xue et al., 2004) |
| Zr | Maximum root depth | WOFOST&LUE | 1.5-1.8 | m | (Allen, Pereira, Raes, & Smith, 1998) |
| P | Average fraction of TAW | WOFOST&LUE | 0.55 | - | (Allen et al., 1998) |

3.2.3.3. Sensitivity Analysis

This study performed a sensitivity analysis of the LUE and WOFOST models for both WW and OSR in Bavaria in 2019. The values of climate variables were optimised in the design of every model. During the analysis, the impact of climate stress factors was nullified, and the biomass calculation replaced the actual Light Use Efficiency (ϵ) values with the optimal (ϵ_0) values.

3.2.3.4. Statistical Analysis

Both the referenced and the modelled (LUE and WOFOST) crop yield of WW and OSR were validated using LfStat crop yield (with a 95% confidence interval) for 2019, respectively. The quality (R^2) and the precision (root mean square error (RMSE)) of the obtained results were calculated using a linear regression model (LRM), which aimed to establish a linear relationship between the referenced (independent variable) and modelled yields (dependent variable) of WW and OSR at different spatial (10, 30, and

250 m) and temporal (8- and 16-days) scales. The statistical parameters used to validate and compare the accuracies of the LUE and WOFOST modelled yields with the referenced yield are R^2 (Equation (3.5)), Mean Error (ME) (Equation (3.6)), RMSE (Equation (3.7)), and relative RMSE (RRMSE) (Equation (3.8)). To compare the yield outputs of both models, the study considered RRMSE < 15% as good agreement, 15-30% as moderate agreement, and > 30% as poor agreement (Yang, Yang, Liu, & Hoogenboom, 2014). The lower the value of ME, RMSE and RRMSE, the better the model performed.

$$R^2 = \frac{((\sum P_i - P') (O_i - O'))^2}{(\sum P_i - P')^2 (\sum O_i - O')^2} \quad (3.5)$$

$$ME = \frac{1}{n} \sum_{i=1}^n (O_i - P_i)^2 \quad (3.6)$$

$$RMSE = \sqrt{ME}, \quad (3.7)$$

$$RRMSE (\%) = \frac{RMSE}{\frac{1}{n} \sum_{i=1}^n O_i} * 100, \quad (3.8)$$

where P_i is the predicted value, O_i is the observed value, P' is the predicted mean, O' is the observed mean value, n is the total number of observations, referenced yield_y is the LfStat yield of every district in 2019, and modelled yield_y is the LUE-generated yield of every district in 2019. The significance of the obtained results was obtained by observing the probability value (p-value) which was calculated using the LRM with a H_0 that there is no correlation between the referenced and the modelled or synthetic values and an H_1 that the correlation exists. The test was performed at a significance (or alpha (α)) of 0.05. A p-value lower than 0.05 indicates that the model is significant and rejects the H_0 that there is no correlation.

3.3 Results

3.1. Evaluation of Real (MOD13Q1, Landsat, and Sentinel-2) and Synthetic (L-MOD13Q1 and S-MOD13Q1) Satellite NDVI Products

The spatial visualisation of the products MOD13Q1, Landsat, L-MOD13Q1, Sentinel-2, and S-MOD13Q1 at DOY 145 is shown in Figure 3.4, respectively. Both

synthetic products, L-MOD13Q1 and S-MOD13Q1, had shown higher dependency on their high-resolution products (Landsat and Sentinel-2) than MOD13Q1. Figure 3.4f shows the spatial location of 10,000 random points that compares real and synthetic NDVI products with their respective low pair (MOD13Q1) and high pair (Landsat or Sentinel-2) products by considering the mean values at different DOYs (Figure 3.5). Figure 3.5a,b show the line and box plot comparison of real and synthetic products and their interquartile comparison of NDVI values.

Both synthetic products underestimated the NDVI values compared to their actual NDVI products between DOYs 81 and 145 (Figure 3.5a). From DOYs 145 to 177, Landsat, L-MOD13Q1, Sentinel-2, and S-MOD13Q1 achieved a mean NDVI of approx.. 0.71. The median NDVI values of L-MOD13Q1 and S-MOD12Q1 lie close to their respective high pair product (Figure 3.5b).

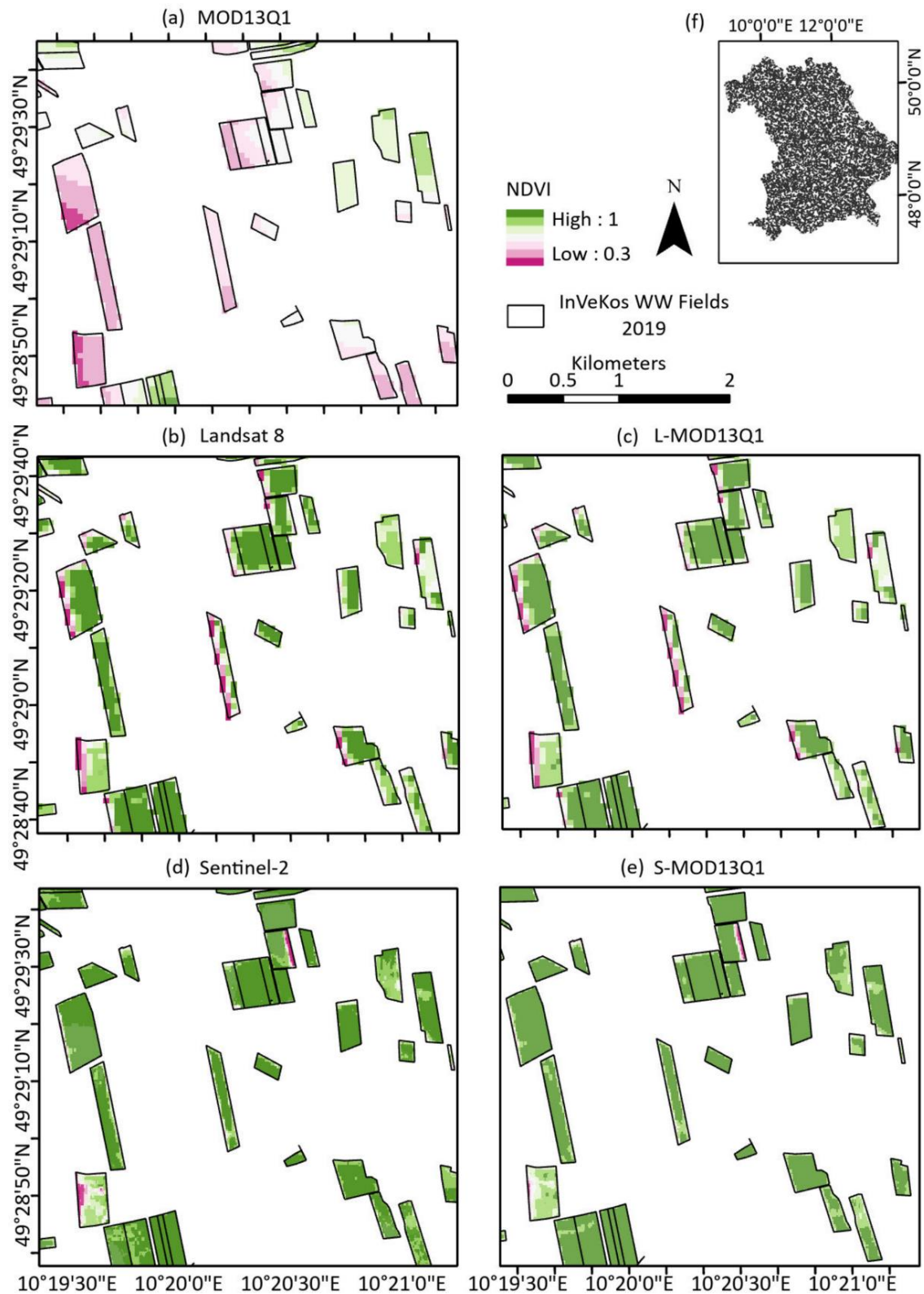


Figure 3.4. Field-wise comparison of STARFM and real-time NDVI values of (a) MOD13Q1, (b) Landsat 8, (c) L-MOD13Q1, (d) Sentinel-2, and (e) S-MOD13Q1 on DOY 145 (25th May 2019) on WW fields. The image in (f) shows the spatial location of 10,000 random points in Bavaria used to draw line and bar plots in Figure 5 for comparing the mean NDVI values on a DOY basis for the real and synthetic NDVI products.

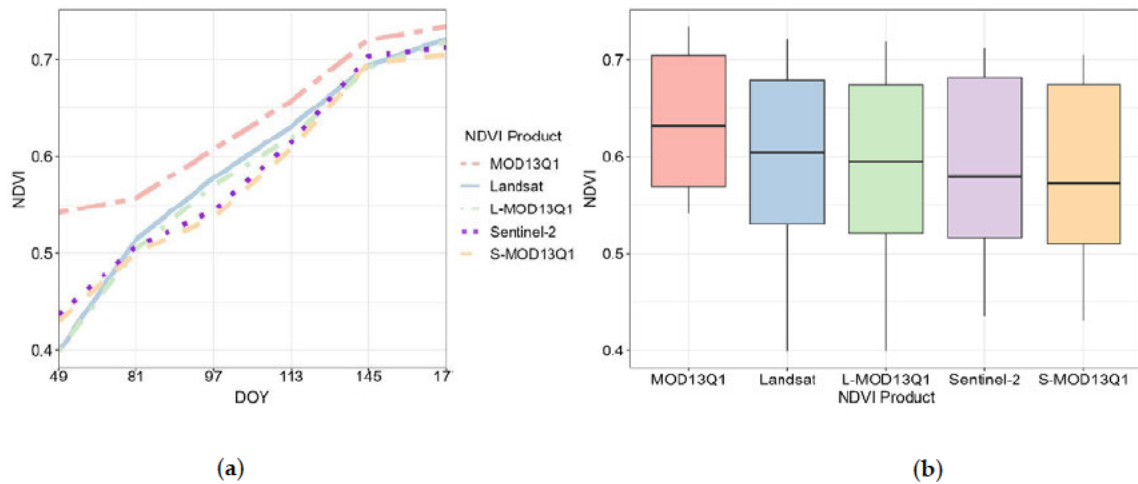


Figure 3.5. The (a) line and (b) bar plots show the DOY-based and interquartile-range-based comparison of STARFM-generated NDVI values with their respective high-resolution input (Landsat (L) or Sentinel-2 (S)) and low-resolution input MOD13Q1, respectively. The comparison is based on the mean values extracted for 10,000 random points (whose spatial location is shown in Figure 3.4f) taken for the entire Bavaria.

3.3.2. Statistical Analysis of Crop Yields Obtained from LUE and WOFOST Models for WW and OSR Using Multisource Data in 2019

Both 8- and 16-day NDVI inputs, such as L-MOD13Q1 and S-MOD13Q1 and MOD13Q1, performed significantly for WW and OSR with LUE and WOFOST models (p -value < 0.05); this rejects the H_0 of the LRM that there is no relationship between the modelled and measured crop yield (Figure 3.6, 3.7). The R^2 values obtained from the S-MOD13Q1 NDVI (8-and 16-days) products have a higher accuracy compared to the L-MOD13Q1(8-and 16-days) and MOD13Q1 (8-and 16-days). Based on the R^2 of the different spatial resolutions of the NDVI products for WW, the models' in descending order is LUE (S-MOD13Q1, 8-days, 10 m), LUE (S-MOD13Q1, 16-days, 10 m), LUE (L-MOD13Q1, 8-days, 30 m), LUE (L-MOD13Q1, 16-day, 30 m), WOFOST (S-MOD13Q1, 8-day, 10 m), WOFOST (L-MOD13Q1, 8-days, 10 m), LUE (MOD13Q1, 8-days, 250 m), WOFOST (S-MOD13Q1, 16-days, 10 m), WOFOST (MOD13Q1, 8-days, 250 m), WOFOST (MOD13Q1, 16-days, 250 m), WOFOST (L-MOD13Q1, 16-days, 30 m), and LUE (MOD13Q1, 16-days, 250 m), with R^2 values of 0.85, 0.85, 0.82, 0.78, 0.78, 0.75, 0.73, 0.73, 0.69, 0.65, 0.64 and 0.52, respectively. In general, the predicted values by both models with different satellite inputs follow a similar pattern, and none of the models

can claim to outclass the others. However, the ME and RMSE values give a complete picture of the model comparisons (8-and 16-day products) and performances (i.e., their quality and precision) with every satellite input. The ME and RMSE of WW from the WOFOST (MOD13Q1 8-day) is slightly lower than the WOFOST (L-MOD13Q1-16-day and S-MOD13Q1 16-day); moreover, the RMSE of the WOFOST (S-MOD13Q1 and L-MOD13Q1 (8-day)) is lower than the WOFOST (MOD13Q1 16-day). The overall results of LUE inputting L-MOD13Q1, S-MOD13Q1, and MOD13Q1 8 to 16-days NDVIs range from 5.46-6.32 dt/ha (RMSE), 5.01-5.40 dt/ha and 6.52-9.33 dt/ha.

Like WW, the R^2 of the different spatial resolutions of NDVI satellite products for OSR in descending order are LUE (S-MOD13Q1, 8-day, 10 m), LUE (L-MOD13Q1, 8-day, 30 m), LUE (S-MOD13Q1, 16-day, 10 m), LUE (L-MOD13Q1, 16-day, 30 m), LUE (MOD13Q1, 8-day, 250 m), WOFOST (S-MOD13Q1, 8-day, 10 m), WOFOST (L-MOD13Q1, 8-day, 10 m), LUE (MOD13Q1, 16-day, 250 m), WOFOST (S-MOD13Q1, 16-day, 10 m), WOFOST (L-MOD13Q1, 16-day, 30 m), WOFOST (MOD13Q1, 8-day, 250 m), and WOFOST (MOD13Q1, 16-day, 250 m), and, with R^2 values of 0.82, 0.80, 0.80, 0.78, 0.67, 0.64, 0.63, 0.63, 0.63, 0.62, 0.62 and 0.60, respectively. It showed that the LUE model is more accurate at different spatial scales than the WOFOST model. Moreover, the model resulted in higher accuracy for the 8-day products of S-MOD13Q1 and L-MOD13Q1 compared to their 16-day products. The overall results of LUE inputting L-MOD13Q1, S-MOD13Q1, and MOD13Q1 8 to 16-days NDVIs range from 2.23 to 2.36 dt/ha (RMSE), 2.11 to 2.39 dt/ha and 3.02 to 3.40 dt/ha.

For the LUE model for WW, both 8-day products of S-MOD13Q1 (median yield = 71.68 dt/ha) and L-MOD13Q1 (74.65 dt/ha) obtained their yield close to the referenced yield (72.30 dt/ha) (Figure 3.8). For the LUE model of OSR, the 8-day and 16-day S-MOD13Q1 and L-MOD13Q1 had resulted in similar predictions, respectively, where the 8-days (median yield ~33 dt/ha) show the median yield closer to the referenced yield (33.50 dt/ha) than the 16-days (~34 dt/ha) (Figure 3.8).

Figures 3.9a,b displayed that the fused products obtained higher R^2 and lower RMSE values (L- and S-MOD13Q1: R^2 = 0.72, 0.76 and RMSE = 4.91, 4.49 dt/ha) than the non-fused products (MOD13Q1: R^2 = 0.63 and RMSE = 5.85 dt/ha) for both WW and

OSR. Analysing the different temporal resolutions of 8- and 16-day products with LUE and WOFOST models, the 8-day products (median $R^2 = 0.77$, RMSE= 6.14 dt/ha) resulted in higher R^2 and lower RMSE than the 16-day products (median $R^2 = 0.69$, RMSE= 8.0 dt/ha) (Figure 3.9c,d).

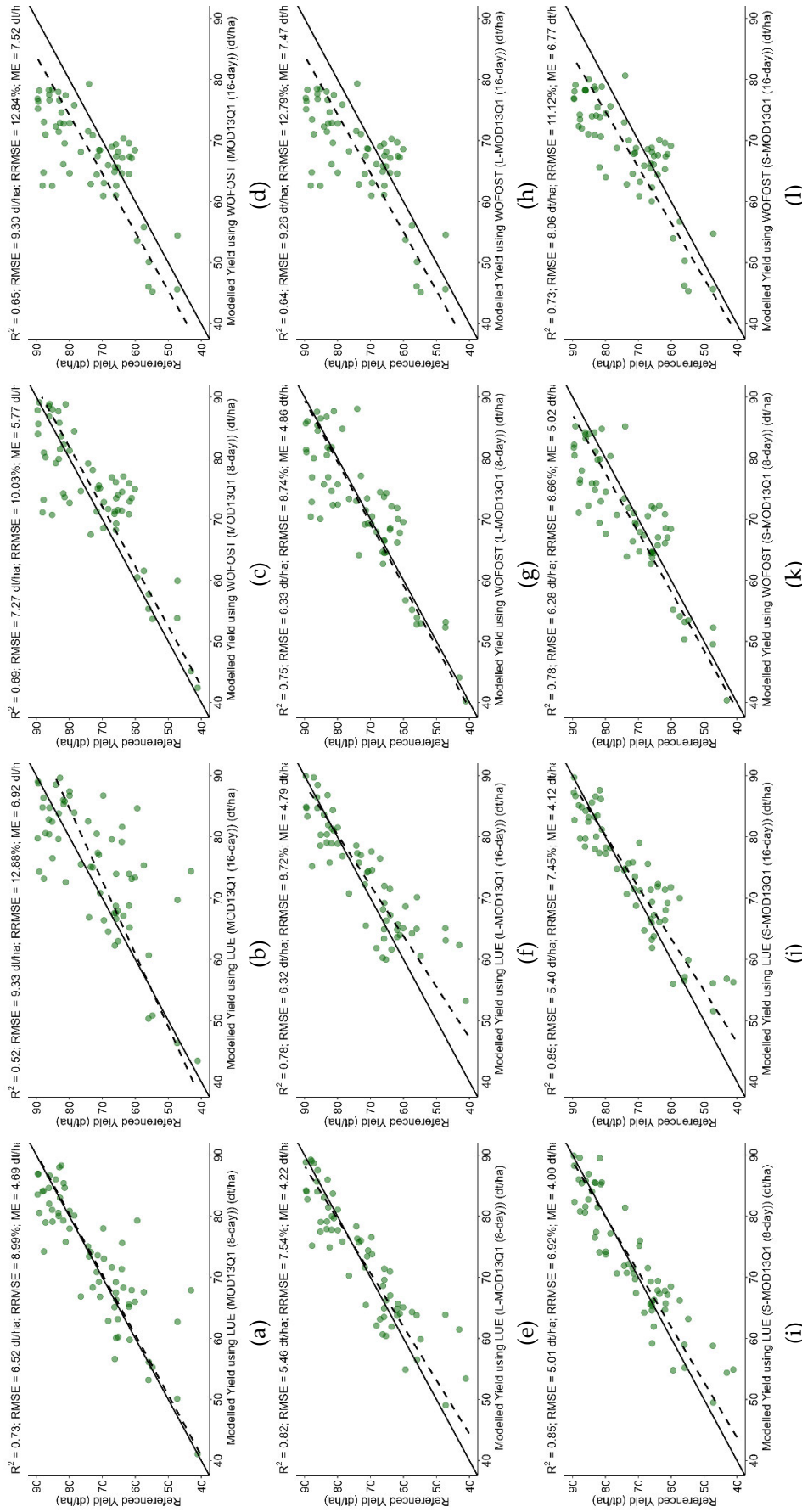


Figure 3.6. The scatter plots (a)-(l) compare the accuracies of LUE and WOFOST modelled yields (inputting the 8- and 16-day MOD13Q1, L-MOD13Q1 and S-MOD13Q1) with the referenced yield of WW. The green dots represent WW. Every plot contains a solid line to visualise the correlation of pixels between the referenced and modelled yield values.

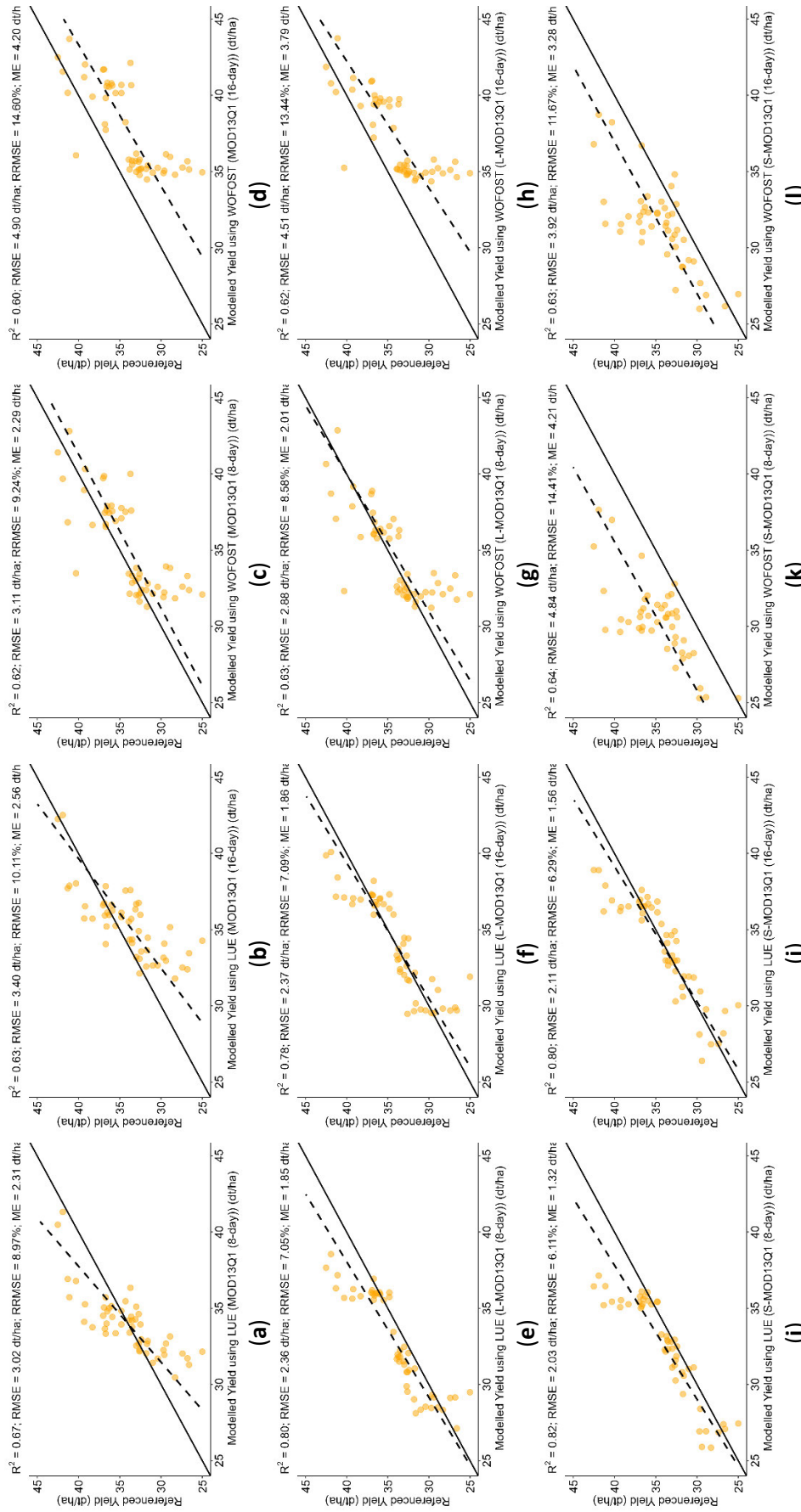


Figure 3.7. The scatter plots (a)-(l) compare the accuracies of LUE and WOFOST modelled yields (inputting the 8- and 16-day MOD13Q1, L-MOD13Q1 and S-MOD13Q1) with the referenced yield of OSR. The orange dots represent OSR. Every plot contains a solid line to visualise the correlation of pixels between the referenced and modelled yield values.

Chapter 3

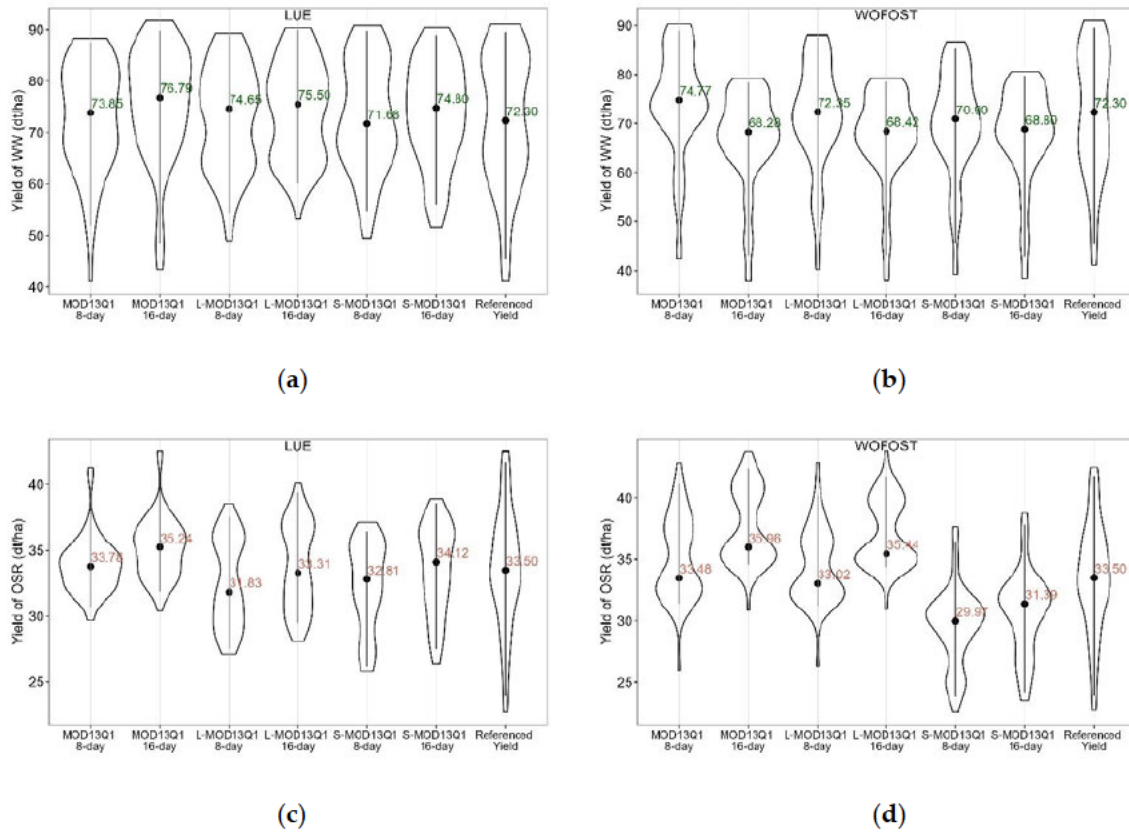


Figure 3.8. The violin plots compare the crop yields of referenced (at 95% confidence interval) and modelled yields obtained from multi-source data (MOD13Q1, L-MOD13Q1, and S-MOD13Q1) at 8- and 16-days of temporal scales of (a,b) WW and (b,d) OSR using the (a,c) LUE and (b,d) WOFOST models in 2019. The green-coloured text represents WW and the orange-coloured text represents OSR. The text values represent the median yield values of every product.

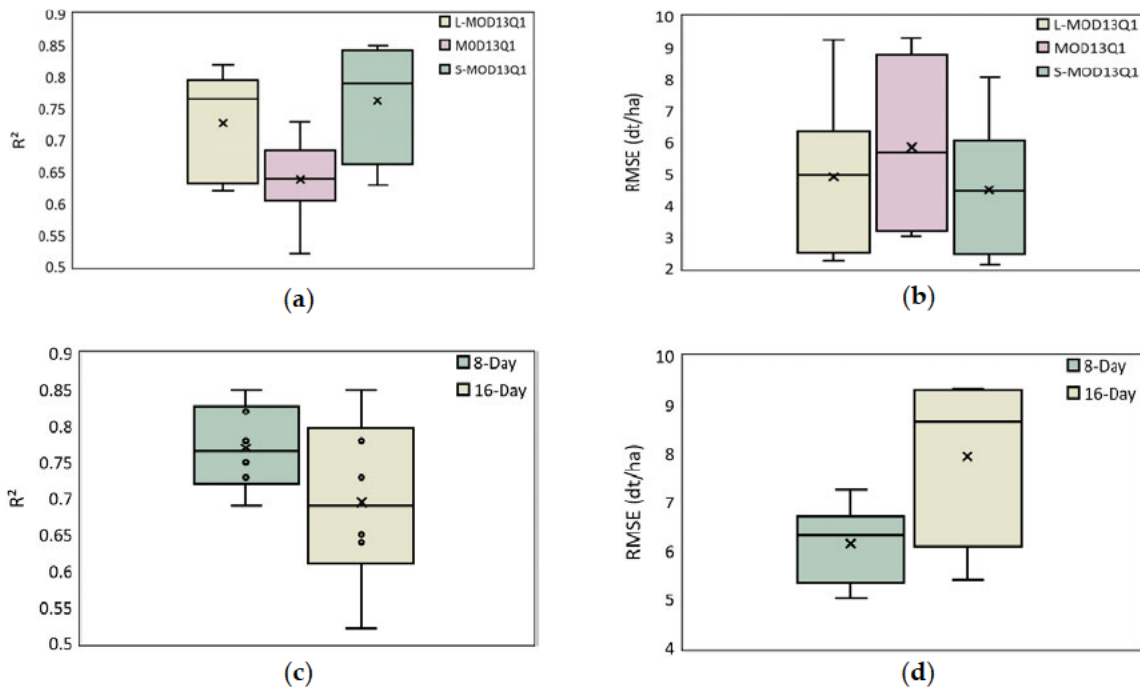


Figure 3.9. The box plots compare the accuracies (a,c) R^2 , and (b,d) RMSE of referenced (at 95% confidence interval) and modelled yields obtained from multi-source data: MOD13Q1, L-MOD13Q1, and S-MOD13Q1, at temporal scales of 8- and 16-days.

3.3.3. Spatial Analysis of Crop Yields Obtained from LUE and WOFOST Models for WW and OSR Using Multisource Data in 2019

The spatial comparison of crop yield at the regional level from the referenced and modelled yield with multi-source data was displayed for both WW and OSR (Figure 3.10-13). For WW, the LUE model showed consistency in yield prediction for regions such as, Straubing Bogen, Bad Kissingen, Landsberg am Lech, Dillingen a.d. Donau, Fresing, Würzburg, Neuburg-Schrobenhausen, Fürth, Neustadt a.d. Aisch, Bad Windsheim, Rhön-Grabfeld, Oberallgäu, Regensburg, Aschaffenburg, and Ansbach, for all satellite inputs. However, the WOFOST model showed stability for regions such as Freising, Tirschenreuth, Neustadt a.d.Waldnaab, Kitzingen, Fürth, Schweinfurt, Weißenburg-Gunzenhausen, Neustadt a.d.Aisch-Bad Windsheim, and Kulmbach. The S-MOD13Q1 8-day showed higher spatial accuracy than other remote sensing inputs used in both models. The S-MOD13Q1 8-day product with LUE predicted a higher yield of more than 85 dt/ha for regions such as Altötting, Passau, Straubing-Bogen, Deggendorf, Fürstenfeldbruck, Donau-Ries, Ebersberg, and Unterallgäu, like the referenced yield (Figure 3.11a). However, when inputted into the WOFOST model, the exact product underestimated the yield for all regions (except Fürstenfeldbruck and Unterallgäu) (Figure 3.11b).

Similarly, for the OSR, both models showed consistency in yield prediction in the regions such as, Ebersberg, Eichstätt, Lichtenfels, Würzburg, Roth, Schweinfurt, Dingolfing-Landau, Neustadt a.d. Waldnaab, Pfaffenhofen a.d.Ilm, Kelheim, and Mühldorf a.Inn, for all satellite inputs (Figure 3.12). The WOFOST model had overestimated the crop yields with MOD13Q1 (8- and 16-days) for nearly 18 regions (>40 dt/ha) as compared to the referenced yield (Figure 3.13a,b). The L-MOD13Q1 8-day resulted in an overestimation of crop yields compared to the L-MOD13Q1 8-day product with both LUE and WOFOST models.

Chapter 3

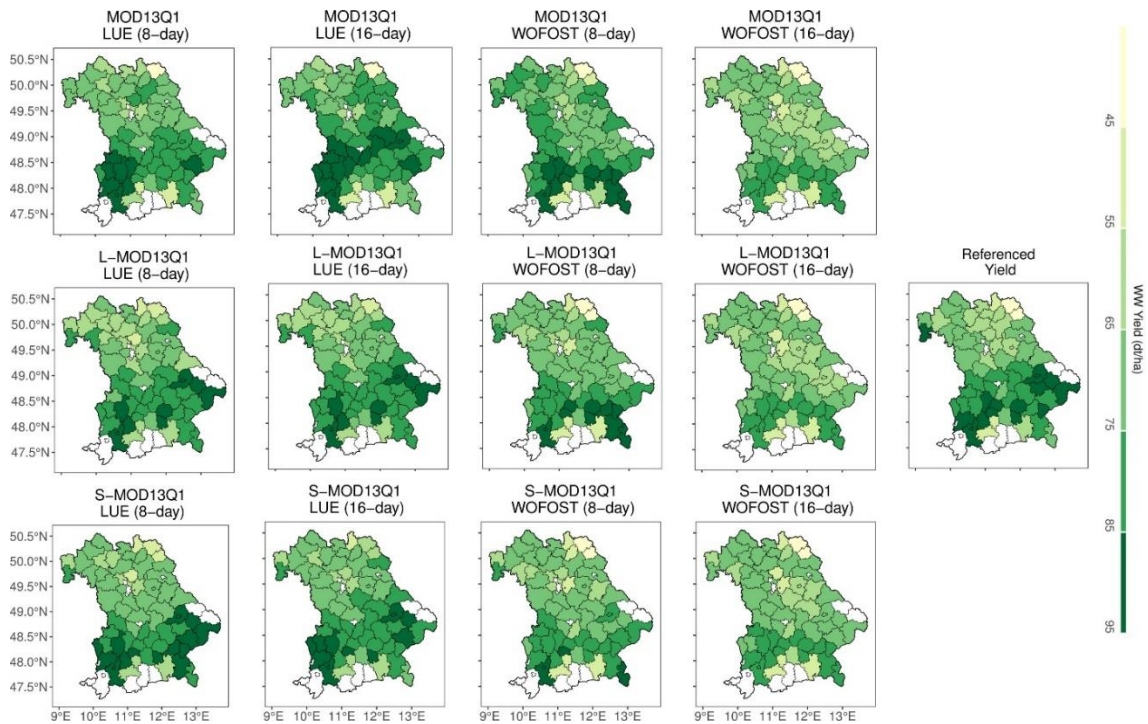
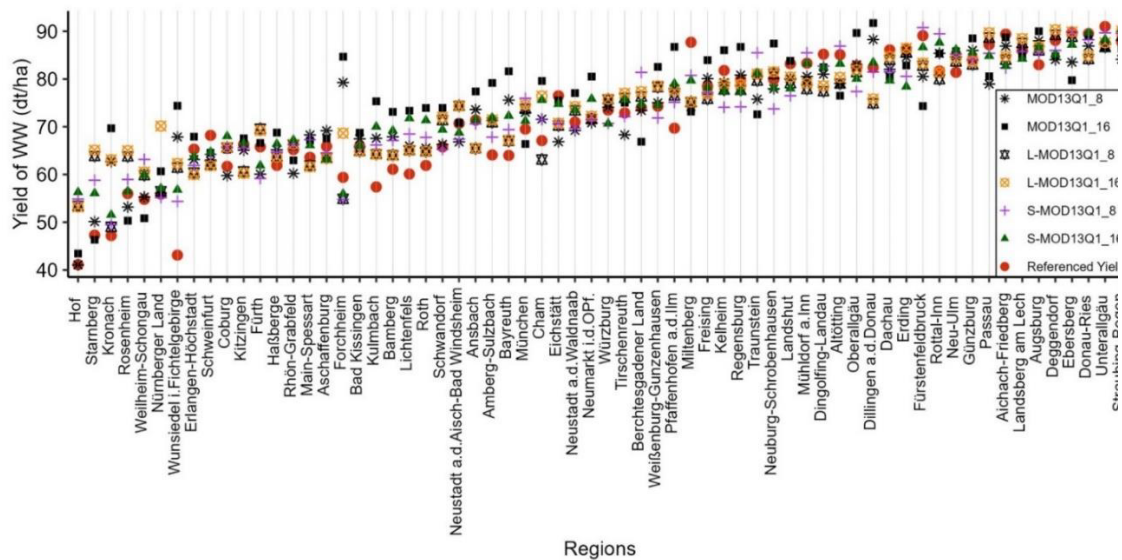
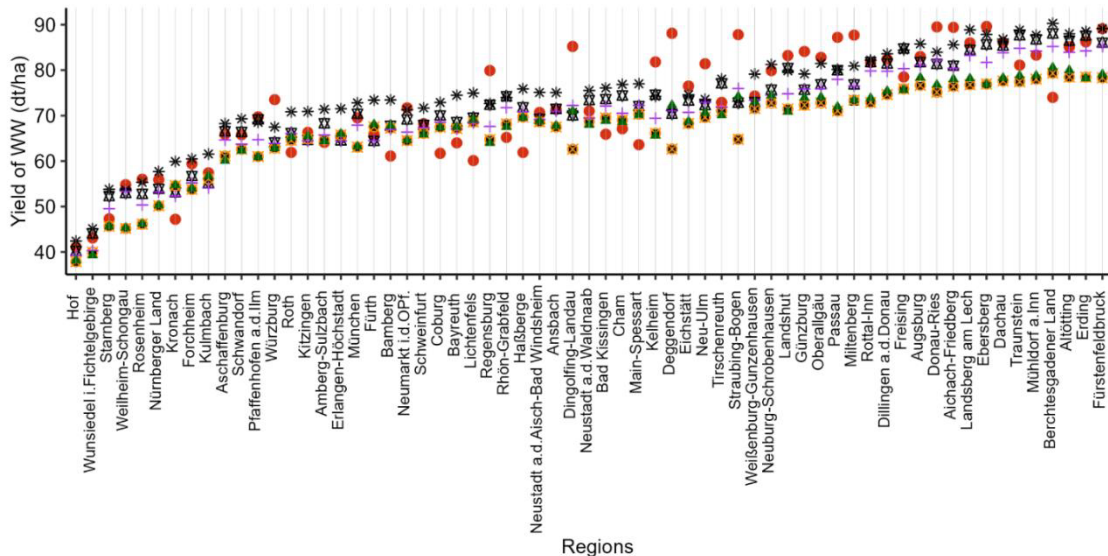


Figure 3.10. Spatial distribution of referenced yields and the predicted yields for WW using MOD13Q1 (8- and 16-days), L-MOD13Q1 (8- and 16-days), and S-MOD13Q1 (8- and 16-days) with LUE and WOFOST models for the state of Bavaria. The white color represents no data available. Detailed map of the administrative regions of Bavaria is shown in Figure A1.



(a)



(b)

Figure 3.11. The dot plots show the region-wise distribution of referenced yields and modelled yields obtained from multi-source data (MOD13Q1 (8- and 16-days), L-MOD13Q1 (8- and 16-days), and S-MOD13Q1 (8- and 16-days)) for WW using (a) LUE, (b) WOFOST, in 2019. The regional referenced yields are displayed in red dots.

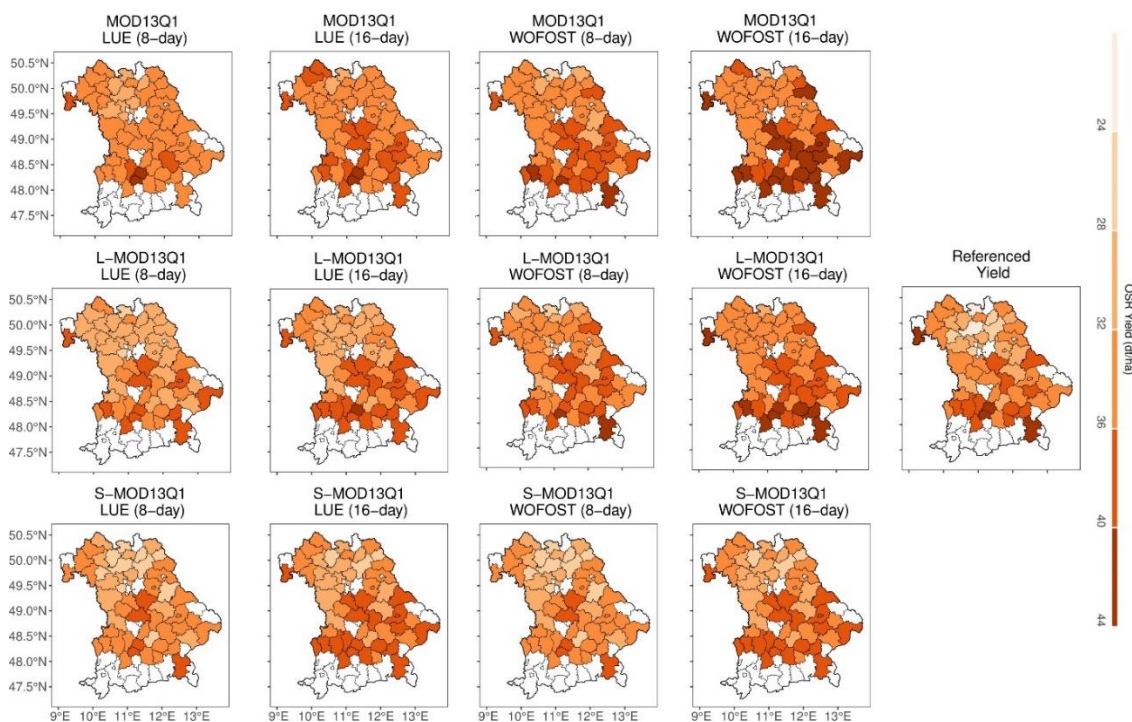


Figure 3.12. Spatial distribution of referenced yields and the predicted yield for OSR using MOD13Q1 (8- and 16-days), L-MOD13Q1 (8- and 16-days), and S-MOD13Q1 (8- and 16-days) with LUE and WOFOST models for the state of Bavaria. The white color represents no data available. Detailed map of the administrative regions of Bavaria is shown in Figure A1.

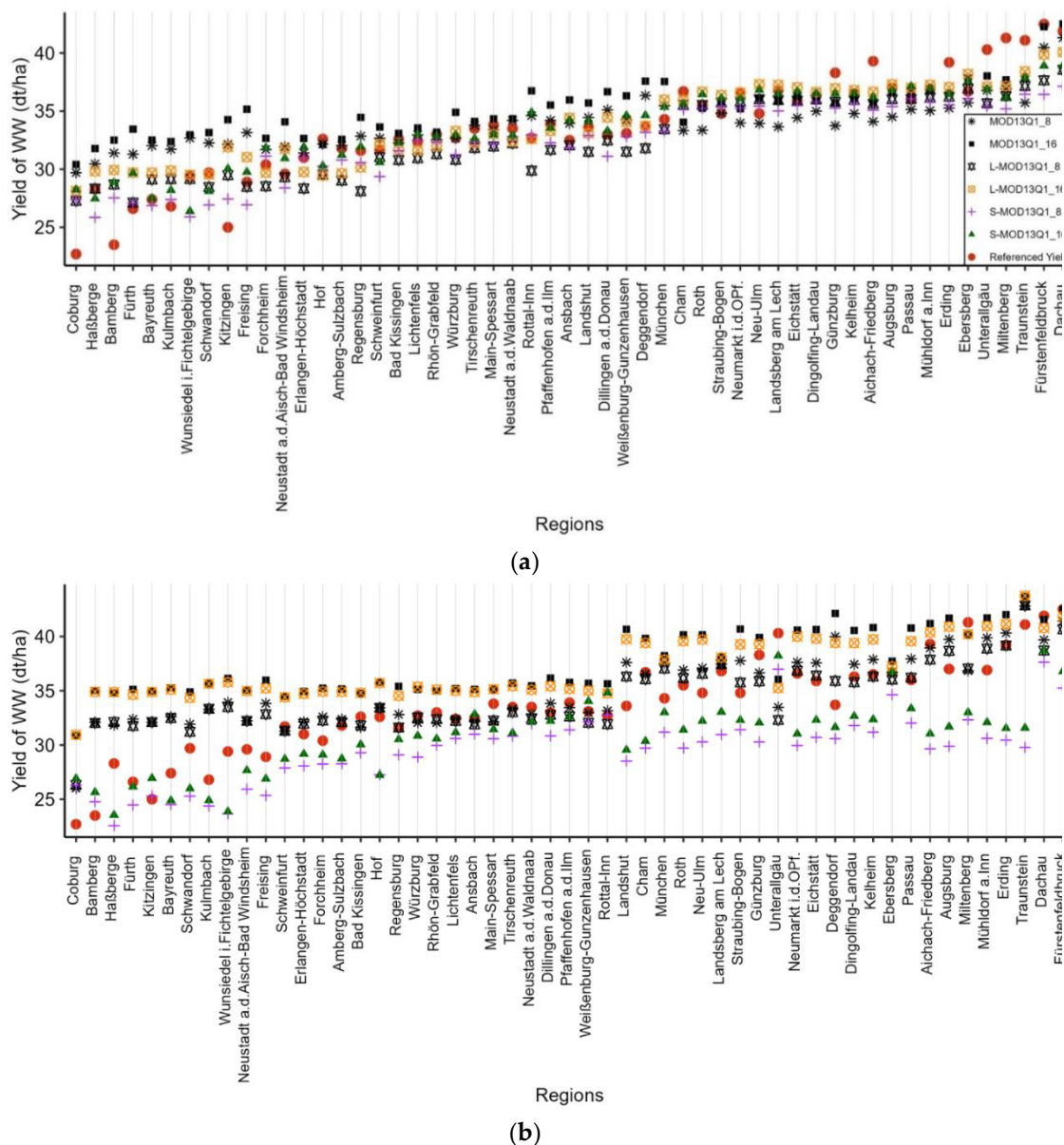


Figure 3.13. The dot plots show the region-wise distribution of referenced yields and modelled yields obtained from multi-source data (MOD13Q1 (8- and 16-days), L-MOD13Q1 (8- and 16-days), and S-MOD13Q1 (8- and 16-days)) for OSR using (a) LUE, (b) WOFOST, in 2019. The regional referenced yields are displayed in red dots.

3.3.4. Sensitivity Analysis

The sensitivity analysis compared the models’ (LUE and WOFOST) performance by excluding the effect of climate stress factors for both WW and OSR in Bavaria in 2019. The LUE and WOFOST modelled yields showed a higher correlation with the referenced yield when the climate stress factors were included and vice versa. Both models showed higher R^2 and lower RMSE values compared with the yield values obtained during the sensitivity analysis (Figure 3.14). The overall accuracies obtained during the sensitivity analysis of both LUE and WOFOST were recorded as R^2 of 0.61

and 0.58 and RMSE of 6.13 dt/ha and 6.32 dt/ha, respectively (Figure 3.14). Including climate parameters improved both models' performance, reducing the RMSE by -38% (LUE) and -11% (WOFOST) and increasing the R^2 from 19% to 12%, respectively.

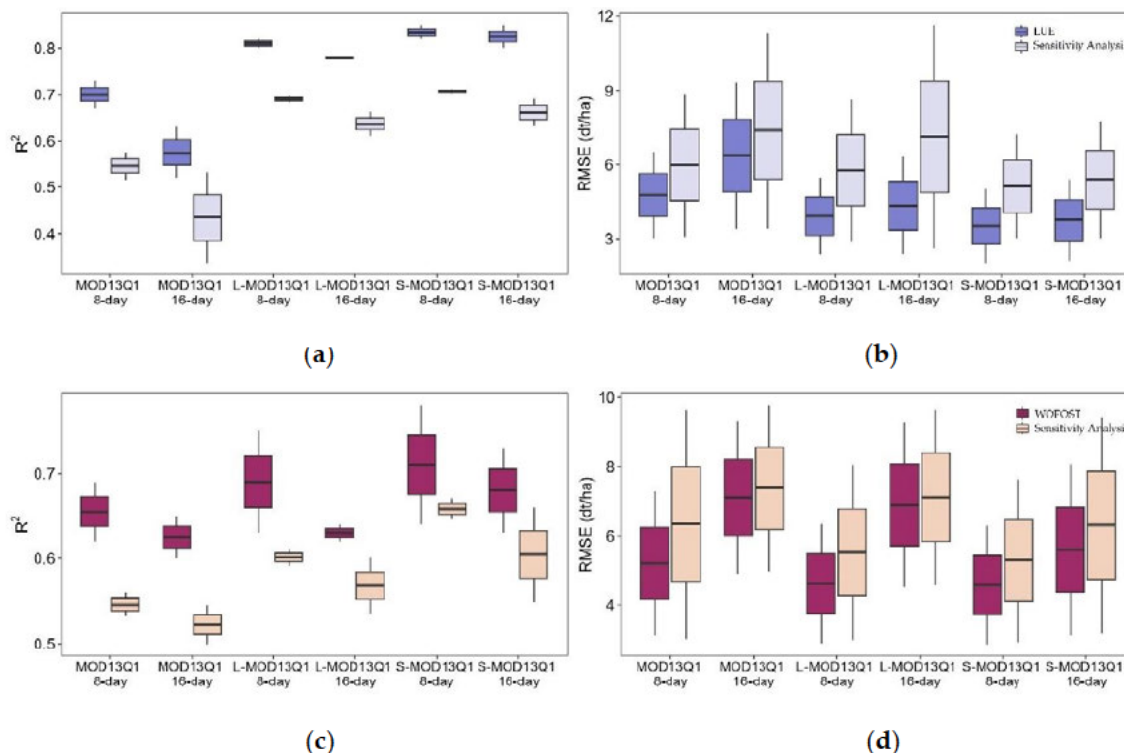


Figure 3.14. The box plots show the comparison of accuracies (a,c) R^2 values and (b,d) RMSE values, obtained from the referenced yields (at 95% confidence interval), with LUE (a,b) and WOFOST (c,d) modelled yields including climate stress factors (dark blue and pink) and the modelled yields excluding the climate stress factors (sensitivity analysis) (light blue and pink).

3.3.5. Best Crop Growth Model

The statistical analysis showed the R^2 , RMSE, RRMSE and ME values of the model's (LUE and WOFOST) performance, including climate stress factors' effect on both WW and OSR in Bavaria in 2019 (Figure 3.15). The LUE model resulted in a higher R^2 (>0.78) for the 8- and 16-day products of L-MOD13Q1 and S-MOD13Q1, than the WOFOST model (R^2 <0.71). Similarly, the RMSE and ME of these products show more accurate results with the LUE model (RMSE <4.5 dt/ha, ME <3.3 dt/ha) than the WOFOST model (RMSE <7.0 dt/ha, ME <6.0 dt/ha). MOD13Q1 8-day (R^2 <0.66, RMSE <5.19 dt/ha, ME <4.03 dt/ha) achieved higher accuracy than MOD13Q1 16-day (R^2 <0.62, RMSE <7.10 dt/ha, ME <5.86 dt/ha) with both LUE and WOFOST. The RRMSE for both models showed better agreement (<15%) between the observed and modelled yields for all satellite products. However, the LUE model (<11.50%) showed an overall lower RRMSE

than the WOFOST model (<13.67%) at different spatial and temporal scales. Irrespective of the crop type and satellite spatial scale, the LUE model obtained higher R^2 and lower RRMSE (average $R^2 = 0.77$, RRMSE = 8.17 %) than the WOFOST model (average $R^2 = 0.66$, RRMSE = 11.35%) (Figure 3.16).

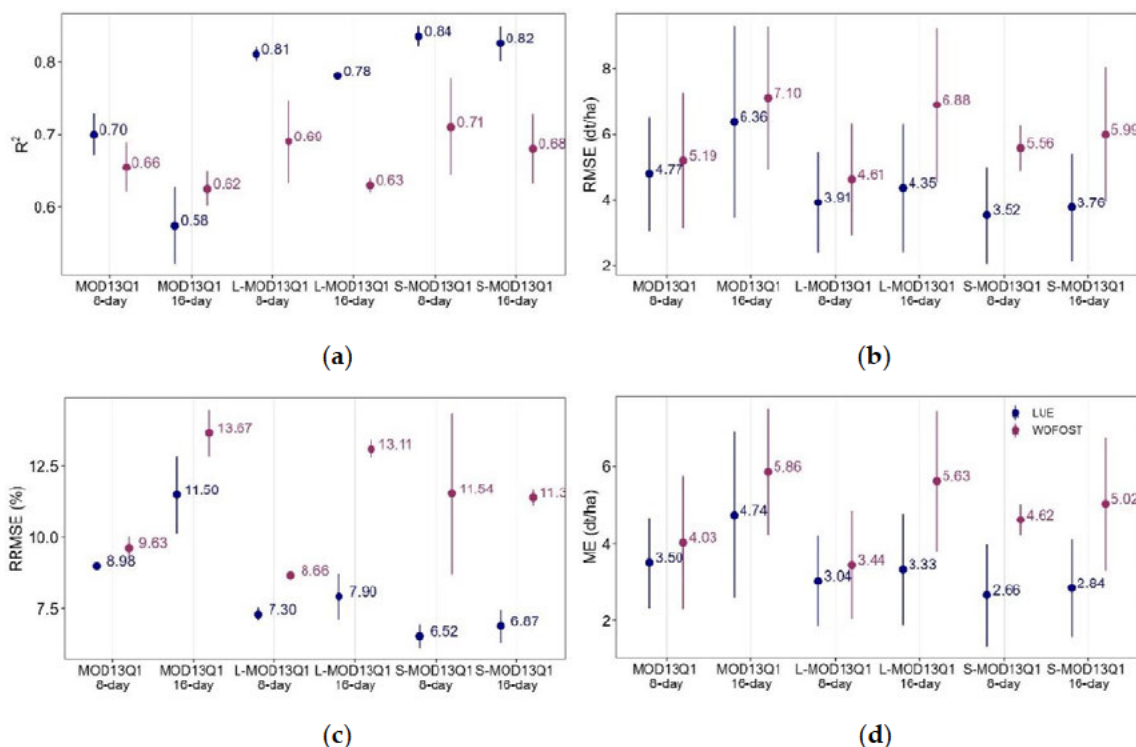


Figure 3.15. The dot plots show the comparison of accuracies (a) R^2 values, (b) RMSE, (c) RRMSE and (d) ME values obtained from the referenced yields (at 95% confidence interval) for LUE (dark blue) and WOFOST (dark pink) models.

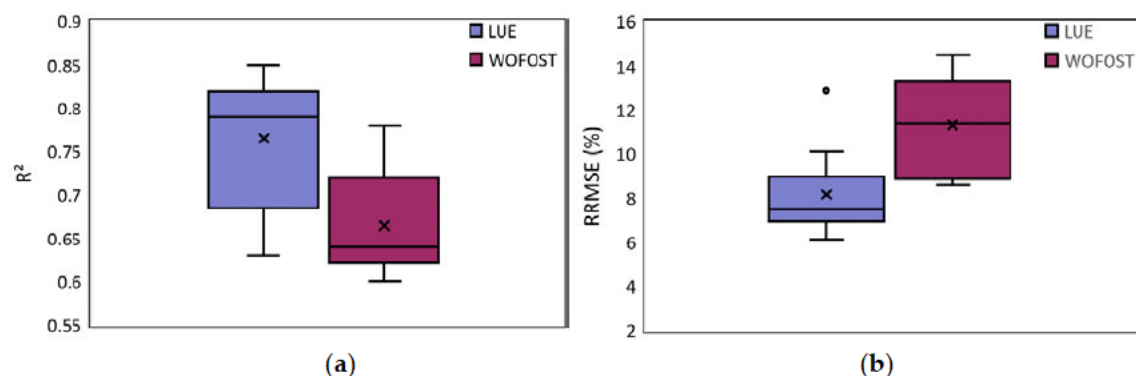


Figure 3.16. The box plots compare the accuracies for (a) R^2 and (b) RRMSE of referenced (at 95% confidence interval) and modelled yields obtained from multi-source data using LUE and WOFOST models in 2019.

3.3.6. Visualization of the Modelled Crop Biomass by the Best Fit Model in 2019

Figure 3.17 shows the spatial distribution of simulated crop biomass for WW and OSR by the LUE model at 10 and 30 m spatial resolutions with 8- and 16-day temporal

resolution for Sentinel-2 (S-MOD13Q1) and Landsat (L-MOD13Q1), respectively. The field-based biomass OSR and WW biomass values vary between 771.36 and 1112.58 g/m², respectively. These values were obtained considering the climate stress factors, such as temperature, VPD, and soil moisture stress. Every figure shows the difference between the 8-day and 16-day biomass products. The difference in 8- and 16-day WW products varies between -72.57 g/m² and 80.50 g/m², respectively. Results indicated that for WW, S-MOD13Q1 had almost similar results at both temporal resolutions; however, a slight variation in L-MOD13Q1 was seen. For OSR, a slight difference in the field-based biomass was observed in both 8- and 16-day products of Sentinel-2 and Landsat. The 8-day products in WW and OSR for L-MOD13Q1 and S-MOD13Q1 showed an overestimation in crop biomass compared to the 16-day products.

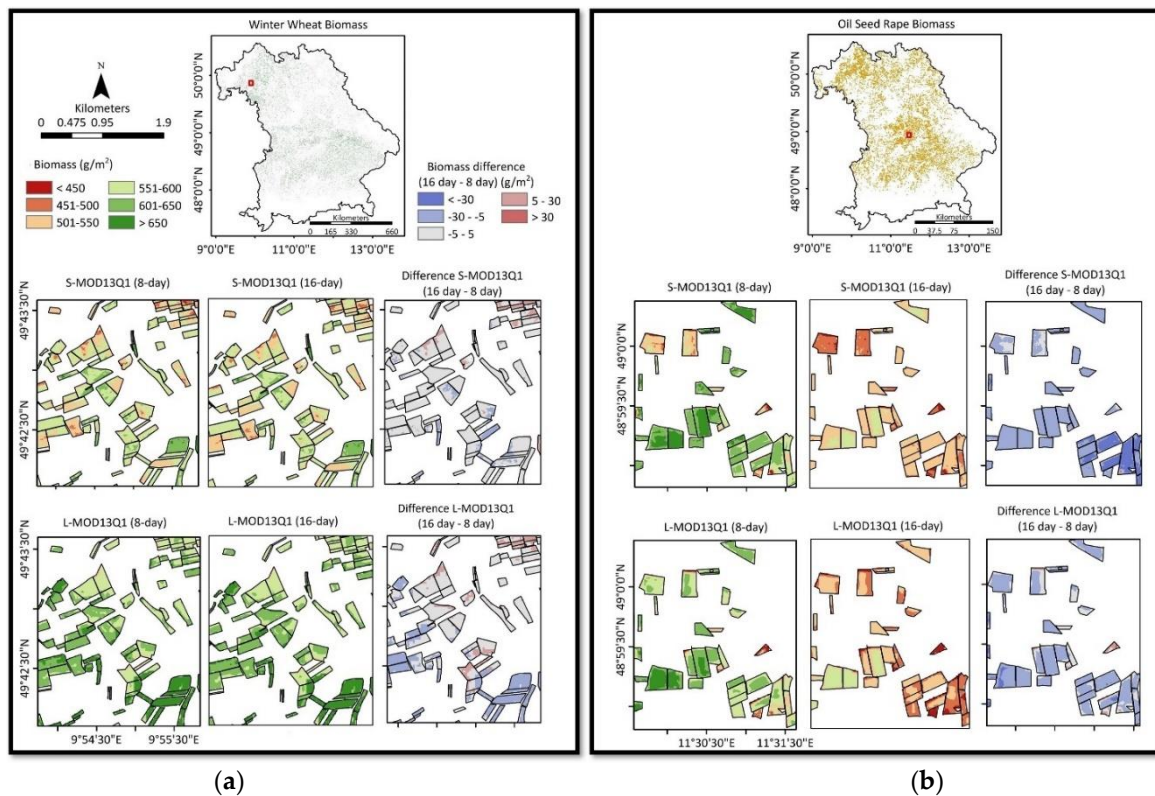


Figure 3.17. Visualization of field level biomass of L-MOD13Q1 and S-MOD13Q1 with 8-days, 16-days, and the difference (16-days – 8-days) obtained using the LUE model for (a) WW and (b) OSR.

3.4. Discussion

This study finds the RS data's optimal spatial and temporal resolutions combined with CGMs for accurate crop yield predictions for Bavaria in 2019. The results are obtained using WOFOST (complex model) and LUE (simple model) CGMs by

individually inputting them with climate variables plus six different remote sensing products (Real: MOD13Q1 (250 m), and Synthetic: L-MOD13Q1 (30 m) and S-MOD13Q1 (10 m)) at 8 or 16-days of temporal resolution. This study investigates the significance of the more straightforward, more accurate and faster LUE model with less input requirement than the complex WOFOST model with a high demand of climatic input variables. The sensitivity analysis is performed to obtain the influence of climate stress factors on crop yield predictions with different satellite inputs. The following sections provide a brief discussion of the points mentioned above.

3.4.1. Importance of the Synthetic Data in Crop Yield Modelling

Many studies employing satellite images aimed to compensate for the gaps in the primary data by fusing data with another source for various remote sensing applications (Barbedo, 2022; Dhillon, Dahms, Kübert-Flock, et al., 2023; Dhillon et al., 2022; Dhillon et al., 2020). The data fusion is to increase the spatial resolution of the relatively coarse images collected by satellites with high revisit frequencies. The fused results usually inherit the details of the high spatial resolution images and the temporal revisit of the frequencies of their counterparts (Barbedo, 2022). In the past two decades, data fusion techniques, such as the STARFM and its variants, have been applied to satellite images for different applications such as phenology analysis (Bhandari et al., 2012; Hwang, Song, Bolstad, & Band, 2011; J. Walker, K. De Beurs, R. Wynne, & F. Gao, 2012), yield and drought monitoring (Benabdelouahab et al., 2019; Htitiou et al., 2019; Lebrini et al., 2020), forest mapping (Hilker et al., 2009; Xin et al., 2013), and biophysical parameter estimation (Anderson et al., 2011; F. Gao et al., 2012; Lebrini et al., 2020; Singh, 2011). Landsat and MODIS images dominate data fusion; however, other satellite combinations, such as Sentinel-2, Sentinel-1, or Worldview, are being increasingly adopted. However, despite its advantages, the data fusion technique could have challenges. For example, combining different sensors could result in misalignment and inaccuracy. In addition, lower sensor quality in data fusion can affect the results' accuracy (M. Liu, Ke, Yin, Chen, & Im, 2019). Therefore, to analyse the quality of data fusion products, this study evaluated the significance of real and synthetic NDVI products by considering the mean NDVI of 10,000 randomly selected points and comparing their mean values at different DOYs. For both L-MOD13Q1 and S-

MOD13Q1, the mean values obtained lie close to their respective high-resolution product. Therefore, the accuracy of these products is higher. It leads this study to investigate the potential of synthetic products in crop yield modelling.

Moreover, to further improve the data quality and reduce the computation cost of data fusion, this research employs the "index-then-blend" (IB) technique, which creates the NDVI from both the high pair and low pair images before blending them for data fusion (X. Chen et al., 2018). The results of a preliminary study (Hansen & Jones, 2000) also indicate that the STARFM could successfully fuse MODIS (MOD13Q1, 250 m, 16-days) with Landsat (output: L-MOD13Q1, 30 m, 16-days) and Sentinel-2 (output: S-MOD13Q1, 10 m, 5-6-days) imagery using the above approach (Dhillon et al., 2022; Dhillon et al., 2020; Gevaert & García-Haro, 2015; Thorsten et al.). The low RMSE and high R^2 obtained for the agricultural class with both L-MOD13Q1 ($R^2 = 0.60$, RMSE = 0.11) and S-MOD13Q1 ($R^2 = 0.68$, RMSE = 0.13) through the STARFM are comparable to those obtained by other studies (Anderson et al., 2016; Dubovik et al., 2021b; J. L. Monteith, 1972; Zhao et al., 2013). One of our previous studies stated the high potential of data fusion between Landsat and MCD43A4 MODIS products on achieving an R^2 of 0.61 and RMSE of 0.10 for WW biomass monitoring at Mecklenburg-West Pomerania in Germany. (Dhillon et al., 2020). The higher correlations between the observed and predicted NDVI values indicate the suitability of the algorithm for vegetation monitoring. Other studies with spatiotemporal data fusion have used NDVI as their primary input for applications such as crop biomass and yield monitoring (Anderson et al., 2011; Benabdelouahab et al., 2019; Bhandari et al., 2012; F. Gao et al., 2012; Htitiou et al., 2019; Hwang et al., 2011; Lebrini et al., 2020; Singh, 2011; J. Walker et al., 2012). The present study highlights the importance of the synthetic NDVI time series in crop yield modelling by analysing the accuracy assessment between the real satellite imagery MOD13Q1 (without fusion) and L- and S-MOD13Q1 (with fusion). The crop yield prediction results conclude the need for data fusion (obtaining high-resolution satellite data) for accurate crop yield prediction. Many studies demonstrated the potential of high spatial and temporal remote sensing data to describe the spatiotemporal variability of crop biophysical parameters (Battude et al., 2016), where the availability of Landsat and Sentinel-2 images offer new perspectives for crop monitoring and modelling.

This study obtains higher crop yield accuracy with the fused products (L- and S-MOD13Q1: $R^2 = 0.72$ and 0.76 and $RMSE = 4.91$ and 4.49 dt/ha) than the non-fused product (MOD13Q1: $R^2 = 0.63$ and $RMSE = 5.85$ dt/ha) for both WW and OSR irrespective of the crop model (LUE or WOFOST) (Figure 3.9a,b). While comparing the yield prediction accuracies of both fused products, S-MOD13Q1 results are more accurate than the L-MOD13Q1. Due to its higher temporal frequency, Sentinel-2 (5-6 days) had six cloud-free scenes (DOYs: 49, 81, 97, 113, 145, and 177) than the Landsat (16-days), with only four cloud-free scenes (DOYs: 49, 81, 145, and 177) available for the analysis (Figure 3.3). Due to this lower gap in Sentinel-2 DOYs, the NDVI-fused product (S-MOD13Q1) results in higher accuracy than the Landsat-based product (L-MOD13Q1) (Dhillon et al., 2022), which further improves the crop yield prediction accuracy of the former more than the latter. However, the L-MOD13Q1 product is still advantageous for generating and exploring the long-term yield time series due to the availability of Landsat data since 1982 with a maximum resolution of 30 m (Dhillon, Dahms, Kübert-Flock, et al., 2023).

Results from previous studies have also shown that the assimilation of RS with high spatial-temporal resolution can significantly improve the accuracy of the output, e.g. with an R^2 of 0.86 for the LAI measurements using Sentinel-2 as shown by (Z.-c. LIU et al., 2021). Dhillon et al. (Dhillon et al., 2020) measured the accuracy of LUE with MODIS and the STARFM; both proved to be more reliable and significant with high R^2 (> 0.64 , > 0.82), and low $RMSE$ (< 650 g/m², < 600 g/m²), where MODIS resulted in lower accuracy due its coarser resolution. Further, Huang et al. (J. Huang et al., 2016) found that the low spatial resolution of MODIS degrades the output accuracy in crop modelling up to 60%.

The high temporal resolution data help to improve a crop's accuracy by covering the complete crop stages and measuring climate variables' impact. The lower the temporal gaps, the higher the attainable accuracies by the crop models (Waldner, Horan, Chen, & Hochman, 2019). The present study shows that the 8-day products are more accurate for yield prediction than the 16-day products. The 8-day products are more likely to cover fine details of the crop physiology, resulting in higher accuracy. Analysing the different temporal resolutions of 8- and 16-day products with LUE and

WOFOST models, the 8-day products (median $R^2 = 0.77$, RMSE= 6.14 dt/ha) show a better relationship between the referenced and modelled yields than the 16-day products (median $R^2 = 0.69$, RMSE= 8.0 dt/ha) (Figure 3.9c,d). Therefore, this study concludes that high spatial and temporal remote sensing products are essential for crop growth monitoring influenced by climatic factors (Dhillon et al., 2020; Dhillon, Dahms, Kuebert-Flock, et al., 2023).

Even though the data fusion products obtained in this study resulted in higher accuracy than the non-fused products, many studies have suggested more improvements in the STARFM algorithm (Dubovik et al., 2021b; C. Liu et al., 2014; Whitcraft et al., 2015). For example, (Tao et al., 2021) discussed the inevitable role of different sensors and image-processing algorithms causing inconsistency in the data.

3.4.2. Importance of Linking Crop Growth Models with RS in Crop Yield Modelling

Crop yield prediction has been considered significant to food security and sustainable agricultural development (J. Huang, Tian, et al., 2015). The study merged remotely sensed data with process-oriented crop models, which can yield more accurate estimates of model outputs. It gives our approach an advantage over conventional studies that use CGMs (J. Huang et al., 2020; Ines, Hansen, & Robertson, 2011; L. Wang et al., 2020). The current study used the traditional technique of CGMs to monitor WW and OSR yields of Bavaria by integrating STARFM-generated S-MOD13Q1 (10 m, 8- and 16-days) and L-MOD13Q1 (30 m, 8- and 16-days) and real MOD13Q1 (250 m, 8- and 16-days) products in the two CGMs: WOFOST and LUE.

The performance of both models is compared based on their complexity in design, processing speed, accuracy, and precision. This study found that the WOFOST model, which requires more input parameters, is complex in its design and needs more computing time to generate the output than the LUE model. Compared to the other CGMs, the LUE model is based on the fundamental principles of photosynthesis, considers each crop's unique properties, and can be calibrated and validated using RS technology (Lobell, Asner, Ortiz-Monasterio, & Benning, 2003; J. L. Monteith, 1972; John Lennox Monteith, 1977). The model accounts for the crop's ability to use solar radiation

for photosynthesis by correlating its biomass with the amount of solar radiation it receives (J. Liu et al., 2010; Yuan et al., 2016). By using RS-derived NDVI with the amount of solar radiation the crop is absorbing (i.e. APAR), the LUE model can use these variables for its calibration and validation, which makes it more accurate in predicting crop yields (Groten, 1993; Yuan et al., 2007). The performance of the LUE model in forecasting crop yields also shows consistency with other studies (Dhillon et al., 2020; Dhillon, Dahms, Kuebert-Flock, et al., 2023; W. Zhou et al., 2022). Yuan et al. (Yuan et al., 2016) successfully validated the crop yields using the satellite-based LUE model at 36 crop sites. Similar research effectively used the Light Use Efficiency variable for biomass estimation of WW and maize using the Production Efficiency Model (T. Dong, Liu, Qian, Jing, et al., 2016). Comparing the results of LUE obtained by (Dhillon et al., 2020), the model resulted in an R^2 of 0.83 and RMSE of 581.82 g/m², which is very close to the results obtained in the present study ($R^2 = 0.81$, RMSE = 5.17 dt/ha). Irrespective of the crop type and satellite spatial scale, the results of this study show that the LUE model (average $R^2 = 0.77$, RMSE = 4.45 dt/ha) performed more accurately than the WOFOST model (average $R^2 = 0.66$, RMSE = 7.75 dt/ha) (Figure 3.16).

The WOFOST model differs from the LUE model by making the potentially unrealistic assumption that crop growth rates are constant throughout the growing season (Confalonieri et al., 2016). For instance, crops may experience periods of stress or damage from pests or diseases, which can affect their growth rate and, ultimately, their yield. It makes the model rely heavily on input data, such as LAI, soil, weather and management parameters, which may only sometimes be available, and could be the reason for inaccuracies in yield predictions (Zhuo et al., 2020). However, many studies have successfully used the WOFOST model combined with RS-based LAI to predict crop yields accurately and have discussed its potential limitations (G. Ma et al., 2013; Tang, Tang, Guo, & Wei, 2022). Similar to this study, a comparison of five different crop growth models was made, where the WOFOST model resulted in an average R^2 of 0.77 and RMSE of 651 g/m², which matches the results of the present study, where the model for WW resulted in an R^2 of 0.71 and RMSE of 7.75 dt/ha (Dhillon et al., 2020).

Comparing the crop yield at a regional level, the LUE model showed consistency in yield prediction in districts such as Straubing Bogen, Bad Kissingen, Landsberg am Lech, Dillingen a.d. Donau, Fresing, Würzburg, Neuburg-Schrobenhausen, Fürth, Neustadt a.d.Aisch, Bad Windsheim, Rhön-Grabfeld, Oberallgäu, Regensburg, Aschaffenburg, and Ansbach, for all satellite inputs. However, the WOFOST model showed stability for regions such as Freising, Tirschenreuth, Neustadt a.d.Waldnaab, Kitzingen, Fürth, Schweinfurt, Weißenburg-Gunzenhausen, Neustadt a.d.Aisch-Bad Windsheim, and Kulmbach. Both models are uncertain in districts at higher elevations in the south (Bavarian Alps) and east (Bavarian Forest and Fichtel Mountains) of Bavaria for both WW and OSR. The models overestimated the crop yield in regions such as Regen, Freyung-Grafenau, Bad Tölz-Wolfratshausen, and Garmisch-Partenkirchen. The reason could be the complex topography and different climate and management practices of these regions, which have impacted the performance of both models (Anderson et al., 2016; Semwal & Maikhuri, 1996). Comparing the two models, the LUE model with S-MOD13Q1 8-day showed higher spatial accuracy than the WOFOST model. Like the referenced yield, the S-MOD13Q1 8-day product with LUE predicted a higher yield of more than 85 dt/ha for regions such as Altötting, Passau, Straubing-Bogen, Deggendorf, Fürstenfeldbruck, Donau-Ries, Ebersberg, and Unterallgäu. However, when inputted into the WOFOST model, the exact product underestimated the yield for all regions (except Fürstenfeldbruck and Unterallgäu). The instability of models at higher elevations could be due to the bad quality of the synthetic NDVI products for specific districts. Like OSR, the WOFOST model overestimated the crop yields with MOD13Q1 (8-and 16-days) for nearly 18 regions by predicting a yield of more than 40 dt/ha compared to the referenced yield. S-MOD13Q1 and L-MOD13Q1 8-day performed better when inputted to the LUE model than the WOFOST.

The quality of the synthetic NDVI product might vary for these regions as the districts have no horizontal or vertical overlay of Landsat scenes within the path row, limiting their coverage frequency. Moreover, the continuous cloud cover in some regions of Bavaria could have negatively impacted the yield prediction accuracy of models (Figure 3.3).

3.4.3. Sensitivity Analysis

The climate variables invest essential contribution impacting the accuracy of crop yield predictions (Cabas, Weersink, & Olale, 2010; Dhillon, Dahms, Kuebert-Flock, et al., 2023; Sidhu, Mehrabi, Ramankutty, & Kandlikar, 2023). This study analyses the impact of climate elements by performing a sensitivity analysis where the LUE and WOFOST models calculate crop yields of WW and OSR without including the climate stress factors in 2019. Having already been influenced by the effect of climate elements, the obtained referenced yield shows poor accuracy with crop model yield results after excluding climate stress factors from both models. This study shows that including climate stress indices improves the performance of both models reducing the RMSE by -38% (LUE) and -11% (WOFOST) and increasing the R^2 from 19% to 12%, respectively. In our previous study, we combined the machine learning approach with crop modelling to identify the impact of every climate element used in crop yield predictions (Dhillon, Dahms, Kuebert-Flock, et al., 2023). This study found that solar radiation, soil moisture and temperature are the most influential variables in increasing the yield accuracy for WW and OSR.

3.4.4. Outlook

The major outlook is to enhance synthetic NDVI for accurate crop yield predictions of different crop types. Both S-MOD13Q1 and L-MOD13Q1 resulted as reliable input products for the application of crop yield forecasting; therefore, their potential needs to be investigated in different parts of the world. This study validates the crop yield data at a regional level; however, for future studies, validating the CGMs at field level yield data could improve models' performance and promote sustainable and precision farming. The accurate yield results predicted by this study could be used to investigate the impact of biodiversity or further land use diversity on crop yields at a large scale. As CGMs can only input limited input variables, this study recommends coupling the same methodology with machine or deep learning algorithms to include more climate factors into the analysis for precise results.

3.5. Conclusions

The present study compares the performance of six different remote sensing products (synthetic: Landsat (L)-MOD13Q1 (30 m, 8- and 16-days) and Sentinel-2 (S)-MOD13Q1 (10 m, 8- and 16-days); real: MOD13Q1 (250 m, 8- and 16-days)) when inputted to crop growth models (CGMs) (WOFOST and LUE) to estimate crop yields of winter wheat (WW) and oil seed rape (OSR) for the entire state of Bavaria in 2019. This study aims to minimise future research efforts by identifying and recommending the most suited synthetic satellite inputs for estimating crop yields by discovering the optimal spatial (10 m, 30 m, or 250 m) and temporal (8- or 16-day) resolutions on a regional scale. Lastly, this study finds the potential of LUE and WOFOST models in generating accurate crop yield results. This research paper concludes the findings as follows:

- (i) To discover the optimal spatial resolution for accurate crop yield predictions, this paper recommends S-MOD13Q1 (10 m) due to its lower uncertainty of mixed pixels information resulting in an increase in the accuracy and precision of the modelled yield. This study obtains higher crop yield accuracy with S-MOD13Q1 ($R^2 = 0.76$ and $RMSE = 4.49$ dt/ha) than L-MOD13Q1 and MOD13Q1 ($R^2 = 0.72$ and 0.63 and $RMSE = 4.91$ and 5.85 dt/ha) for both WW and OSR, respectively. However, the L-MOD13Q1 product is more advantageous for generating and exploring the long-term yield time series due to the availability of Landsat data since 1982, with a maximum resolution of 30 m.
- (ii) To investigate the optimal temporal resolution in yield forecasting, this paper recommends S-MOD13Q1 and L-MOD13Q1 (8-day) as they could improve the accuracy of yield prediction with detailed coverage of crop growth stages and briefly analyse the impact of climate variables simultaneously. The 8-day products (median $R^2 = 0.77$, $RMSE = 6.14$ dt/ha) show a better relationship of referenced yield with the modelled yield than the 16-day products (median $R^2 = 0.69$, $RMSE = 8.0$ dt/ha).
- (iii) To find the suitable crop model with the available input variables, this study finds the LUE model simpler, more reliable, and more accurate than the

WOFOST model. Moreover, the LUE model inputs fewer variables, which makes the processing faster than the WOFOST model. Comparably, the LUE model results in a higher mean $R^2 = 0.77$ and $RMSE = 4.45$ dt/ha, while the WOFOST model results in a lower $R^2 = 0.66$ and $RMSE = 7.75$ dt/ha for both WW and OSR yield validations in Bavaria in 2019.

The accurate crop yield measures obtained at the field scale before harvest can contribute to crop yield management decision-making, which could play a crucial role in achieving sustainability in agriculture. However, the availability of field-based yield information in future could be more helpful in testing the potential of high spatial resolution RS products at local scales. The ease of using spatiotemporal modelling with crop growth models would be more comprehensive than one geographical region; therefore, the methodology should be applied globally to obtain food security and maintain biodiversity. For even better accuracy, the synergistic approach of linking RS and CGMs could be linked and tested with machine learning algorithms for various crop fields.

Chapter 4

This chapter is a verbatim reproduction (except the figure and table numbers) of the paper:

Impact of STARFM on Crop Yield Predictions: Fusing MODIS with Landsat 5, 7, and 8 NDVIs in Bavaria, Germany

Dhillon, M. S., Dahms, T., Kübert-Flock, C., Liepa, A., Rummler, T., Arnault, J., . . . Ullmann, T. (2023). Impact of STARFM on Crop Yield Predictions: Fusing MODIS with Landsat 5, 7, and 8 NDVIs in Bavaria Germany. *Remote Sensing*, 15(6), 1651.

Published in MDPI Remote Sensing

Abstract

Rapid and accurate yield estimates at both field and regional levels remain the goal of sustainable agriculture and food security. Hereby, the identification of consistent and reliable methodologies providing accurate yield predictions is one of the hot topics in agricultural research. This study investigated the relationship of spatiotemporal fusion modelling using STRAFM on crop yield prediction for winter wheat (WW) and oil-seed rape (OSR) using a semi-empirical light use efficiency (LUE) model for the Free State of Bavaria (70,550 km²), Germany, from 2001 to 2019. A synthetic normalised difference vegetation index (NDVI) time series was generated and validated by fusing the high spatial resolution (30 m, 16 days) Landsat 5 Thematic Mapper (TM) (2001 to 2012), Landsat 7 Enhanced Thematic Mapper Plus (ETM+) (2012), and Landsat 8 Operational Land Imager (OLI) (2013 to 2019) with the coarse resolution of MOD13Q1 (250 m, 16 days) from 2001 to 2019. Except for some temporal periods (i.e., 2001, 2002, and 2012), the study obtained an R² of more than 0.65 and a RMSE of less than 0.11, which proves that the Landsat 8 OLI fused products are of higher accuracy than the Landsat 5 TM products. Moreover, the accuracies of the NDVI fusion data have been found to correlate with the total number of available Landsat scenes every year (N), with a correlation coefficient (R) of +0.83 (between R² of yearly synthetic NDVIs and N) and -0.84 (between RMSEs and N). For crop yield prediction, the synthetic NDVI time series and climate elements (such as minimum temperature, maximum temperature, relative humidity, evaporation, transpiration, and solar radiation) are inputted to the LUE model, resulting in an average R² of 0.75 (WW) and 0.73 (OSR), and RMSEs of 4.33 dt/ha and 2.19 dt/ha. The yield prediction results prove the consistency and stability of the LUE model for yield estimation. Using the LUE model, accurate crop yield predictions were obtained for WW (R² = 0.88) and OSR (R² = 0.74). Lastly, the study observed a high positive correlation of R = 0.81 and R = 0.77 between the yearly R² of synthetic accuracy and modelled yield accuracy for WW and OSR, respectively.

4.1. Introduction

Accurate predictions of grain yield at both field and regional scales remain a goal for sustainable agriculture and food security (Bian et al., 2022; Mueller et al., 2012). The delivery of timely crop monitoring and accurate crop yield estimates is of great value for the formulation of food policies, the regulation of food prices, and agricultural management and is urgently needed for the development of sustainable agriculture (Fritz et al., 2019; Ziliani et al., 2022). Among different crop types, oil-seed rape (OSR) (*Brassica napus*) and winter wheat (WW) (*Triticum aestivum*) are major crops with high economic value for animal feed, biodiesel production, pollination, biodiversity, and human consumption in the European Union (Alarcón-Segura et al., 2022; Eurostat, 2019). In Germany, WW (total production in 2016 was 24.6 million tons) and OSR (4.9 million tons) are crops of significant importance, generally cultivated as high input and conventionally managed monocultures (Alarcón-Segura et al., 2022; Economics; Stephan Lutter, (UBA); & Manstein, 2018; Macholdt & Honermeier, 2017; UFOP., 2019). The future climatic changes and increasing climatic variability have diverted the increasing grain yield trend of these crops towards maintaining yield stability (Macholdt & Honermeier, 2017). Therefore, the accurate yield estimates of WW and OSR could contribute positively to agricultural management practises and optimise resource use to stabilise yields in the future.

Remote sensing (RS) technology can be used to determine and monitor the features of the earth's surface by providing synoptic, timely, and cost-effective information about the earth's surface (Ali et al., 2022; Justice et al., 2002). Many studies have implemented RS-based methodologies to estimate the crop production of different crop types at different geographical locations (Ahmad, Ghafoor, Bhatti, Akhtar, & Ibrahim, 2014; Dhillon et al., 2020; Friedl et al., 2010; Karila, Nevalainen, Krooks, Karjalainen, & Kaasalainen, 2014; Lobell, 2013; Ogotu & Dash, 2013). Landsat (L), Satellite Pour l'Observation de la Terre (SPOT), World View, and Sentinel-2 (S) satellite data with a medium spatial resolution of 10–100 m were utilised to assess and estimate agricultural production at regional and local scales (Ali et al., 2022; Mueller et al., 2012). The availability of historical RS data since 1972 has also increased the potential of science to

invest, design, and implement accurate and reliable methodologies by validating the methods with old yield data sets (Wulder et al., 2019; Wulder, Masek, Cohen, Loveland, & Woodcock, 2012; Wulder et al., 2016). Until now, various studies have implemented different methodologies (such as interpolation (Mariano & Monica, 2021; Souza, Bazzi, Khosla, Uribe-Opazo, & Reich, 2016), extrapolation (Atamanyuk et al., 2019; Nemecek et al., 2012), vegetation indices (Bolton & Friedl, 2013; Johnson, Hsieh, Cannon, Davidson, & Bédard, 2016), linear regression models (Ramesh & Vardhan, 2015), crop growth models (CGMs) (Dhillon et al., 2020; Mo et al., 2005), machine learning (ML) (Dhillon, Dahms, Kuebert-Flock, et al., 2023; Ghadge, Kulkarni, More, Nene, & Priya, 2018; Van Klompenburg, Kassahun, & Catal, 2020), and deep learning (DL) (Elavarasan & Vincent, 2020; Kuwata & Shibasaki, 2015) using the RS data and accurately predicted crop yields in almost every corner of the world. However, to adequately justify their methods' reliability, stability, and preciseness, very few studies have consistently tested their methodologies for yield prediction for more than five years.

CGMs using the RS data as input parameters successfully attempted to estimate crop yields by covering vast spatial scales and updating the information temporally (Dhillon et al., 2020; Kasampalis et al., 2018; Mirschel et al., 2004; Murthy, 2004; Zhuo et al., 2022). Many CGMs have been used in crop monitoring for different design purposes, regional environments, and crop types (Kasampalis et al., 2018). Some very famous models driven by various factors such as radiation, water, or soil are named as AquaCrop (Iqbal et al., 2014), soil–water–atmosphere–plant (SWAP) (Van Dam et al., 1997), agricultural production systems simulator (APSIM) (E. Wang et al., 2002), simple and universal crop growth simulator (SUROS) (C. Spitters, Van Keulen, & Van Kraalingen, 1989), semi-empiric light use efficiency (LUE) model (Shi et al., 2007), world food study model (WOFOST) (Van Diepen et al., 1989), Carnegie–Ames–Stanford Approach (CASA) (Potter et al., 1993), and the simple algorithm for yield estimate (SAFY) model (Duchemin, Maisongrande, Boulet, & Benhadj, 2008). However, most CGMs are complicated and time-consuming and require many input parameters that could be difficult to obtain or substitute through RS data. LUE and AquaCrop are proven to be more precise, accurate, and reliable by the previous literature (Dhillon et

al., 2020). However, their performance stability is not determined, as no study has analysed their performance for more than two years at the same study site.

Crop yield prediction at regional, national, and global scales has been conducted based on both climate data and RS data (Schwalbert et al., 2020). Temperature, solar radiation, and precipitation, as well as the normalised difference vegetation index (NDVI) and leaf area index (LAI), are generally considered the primary climatic and satellite-based input variables used in CGMs (Kern et al., 2018; Shammi & Meng, 2021). Therefore, the quality of RS input to CGMs might impact the accuracy of the predicted yield. Even though the RS has broadened the spatial and temporal range of CGMs, the cloud and shadow gaps in the optical satellite data can hinder or limit CGMs from producing accurate yield results (Gevaert & García-Haro, 2015; David P. Roy et al., 2008). Many studies have successfully used multitemporal data fusion, combining the data obtained from two different sensors with different spatial and temporal scales, to fill the data gaps (Benabdelouahab et al., 2019; Dhillon et al., 2020; Htitiou et al., 2019; Lebrini et al., 2020). Due to its public availability of code and simplicity of usage, the spatial and temporal adaptive reflectance fusion model (STARFM) (F. Gao et al., 2006) is widely used to combine L/S with the moderate resolution imaging spectroradiometer (MODIS) for the application of crop monitoring (Cui et al., 2018; Lee et al., 2019; Xie et al., 2016; L. Zhu et al., 2017). In a previous study, we tested blending different high (L (30 m, 16 days) and S (10 m, 5–6 days)) and coarse (MODIS: MCD43A4, MOD13Q1, MOD09GQ, and MOD09Q1) spatial resolution products for different land use classes using the STARFM. The study found that both L-MOD13Q1 (30 m, 16 days) ($R^2 = 0.62$ and $RMSE = 0.11$) and S-MOD13Q1 (10 m, 16 days) ($R^2 = 0.68$ and $RMSE = 0.13$) are suitable for the application of agricultural monitoring, with the former having the upper hand due to its fast and easy processing with lesser storage requirements (Dhillon et al., 2022).

Thus, the present study uses the L-MOD13Q1 NDVI product and high-resolution climate parameters (2 km, eight days) as inputs to the LUE model (considered the most accurate, precise, and reliable (Dhillon et al., 2020)) for predicting crop yields of WW and OSR at a regional scale for Bavaria from 2001 to 2019. This long-term yield prediction of both crop types would investigate the stability and preciseness of the LUE

model by validating the modelled yield with district level Bayerisches Landesamt für Statistik (LfStat) data of Bavaria with a 95% confidence interval. The specific research objectives include: (i) finding the potential of STARFM for blending the long-term NDVI time series; (ii) investigating the preciseness and stability of the LUE model by validating the modelled yield at district level in Bavaria from 2001 to 2019; and (iii) exploring the impact of the fused NDVI input time series on the accuracy of the modelled yields.

4.2. Materials and Methods

The general workflow of the study is shown in Figure 4.1. The flow diagram is divided into three parts: (1) data fusion; (2) generation and validation of L-MOD13Q1 NDVI time series from 2001 to 2019; and (3) comparative analysis between fused (L-MOD13Q1) and non-fused (L-MOD13Q1) products in crop yield modelling 2019; and then, modelling crop yields using L-MOD13Q1 NDVI for WW and OSR from 2001 to 2019. The first part was a testing phase that investigated the suitable synthetic NDVI product (which is L-MOD13Q1) for the agricultural class of Bavaria for the year 2019 (completed in the preceding work (Dhillon et al., 2022)). The second section is an extension of the first section, and it generates and validates the NDVI time series of L-MOD13Q1 for eighteen more years (i.e., from 2001 to 2018) using the same methodology as the previous section (as used for 2019). In the third section, the output NDVI time series of part 2 and the climate elements are used as inputs to the LUE model, which estimates the crop yields of WW and OSR from 2001 to 2019 in Bavaria. The satellite NDVI and the climate data are selected for the respective starts and ends of the seasons for WW and OSR from 2001 to 2019. Both inputs are masked for WW and OSR using the InVeKos data that was available from 2005 to 2019 (source: www.ec.europa.eu/info/index_en, accessed on 21 June 2021).

As crop field information was unavailable from 2001 to 2004, InVeKos field data from 2005 to 2009 was used to classify the WW and OSR fields in their respective years. Finally, the obtained crop yield is validated using the LfStat data at the regional level in Bavaria (the regional map is shown in Figure 2). Because the validation data is available at a regional scale, the field outputs of every region were converted to a single regional

value by totalling the pixel values of every field. The satellite data sets were downloaded and preprocessed in Google Earth Engine (GEE), and the fusion analysis is performed in R (version 4.0.3) using R-Studio.

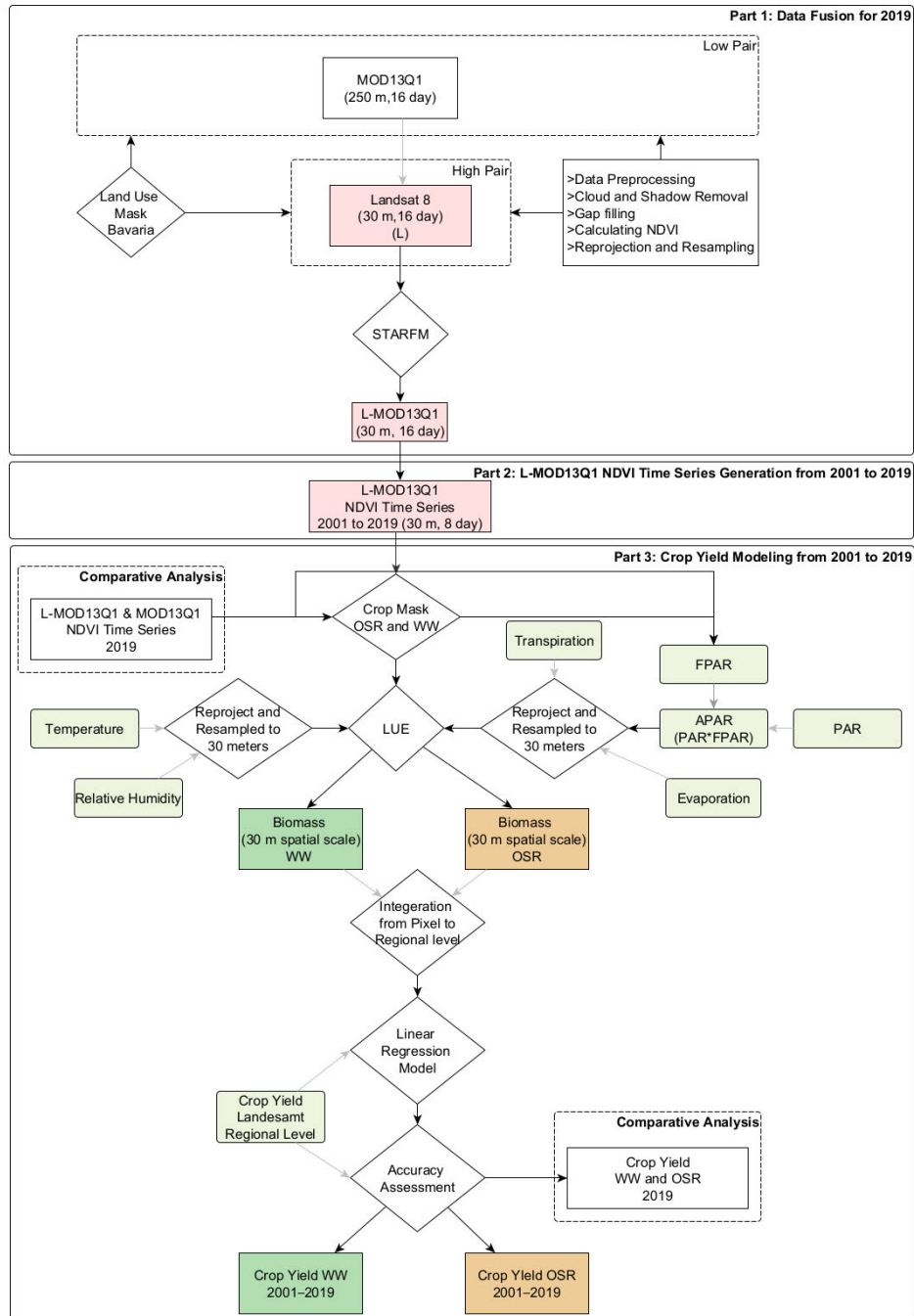


Figure 4.1. The conceptual framework of the study is divided into three parts: Part 1 states the data fusion for 2019 to investigate the best synthetic NDVI time series product (this section was already completed in our previous study (Dhillon et al., 2022)); Part 2 generates and validates the synthetic NDVI time series from 2001 to 2019 for the product L-MOD13Q1; and Part 3 performs the comparative analysis to compare the performance of fused (L-MOD13Q1) and non-fused (MOD13Q1) NDVI time series in crop yield prediction for 2019 and then estimates and validates the crop yield for Bavaria by inputting the L-MOD13Q1 time

series and climate elements to a semi-empiric Light Use Efficiency (LUE) model; STARFM = Spatial and Temporal Adaptive Reflectance Fusion Model; NDVI = Normalised Difference Vegetation Index; L-MOD09GQ = Landsat-MOD09GQ; L-MOD09Q1 = Landsat-MOD09Q1; L-MCD43A4 = Landsat-MCD43A4; L-MOD13Q1 = Landsat-MOD13Q1; S-MOD09GQ = Sentinel-2-MOD09GQ; S-MOD09Q1 = Sentinel-2-MOD09Q1; S-MCD43A4 = Sentinel-2-MCD43A4; S-MOD13Q1 = Sentinel-2-MOD13Q1; PAR is photosynthetically active radiation, and FPAR is the fraction of PAR absorbed by the canopy. APAR = Absorbed Photosynthetically Active Radiation.

4.2.1. Study Area

The study area is Bavaria which is one of the federal states of Germany located between 47°N and 50.5°N, and between 9°E and 14° E (Figure 4.2). As the largest state of Germany, Bavaria covers an area of approx. 70,550 km², covering almost one-fifth of Germany. The diverse topography of the region with higher elevations in the south (Bavarian Alps) and east (Bavarian Forest and Fichtel Mountains) impacts the climate of the state. The mean annual temperature ranges from -3.3 °C to 11 °C and the mean annual precipitation sums range from approx. 500 to above 3100 mm. In 2019 about 36.91% of the area of the State is covered by forest, and 31.67% by agriculture (Dhillon et al., 2022). More than half of the arable land is used to grow cereals where WW predominates with 37% followed by winter barley (25%), summer barley (12%), and grain maize (8%) (Miller, 2002). Whereas OSR predominates in the oil-producing crops in the state. The federal state is divided into 71 Landkreise (rural districts) and 26 Kreisfreie Städte (city districts). Brief description of the regions of Bavaria is shown in Figure A1.

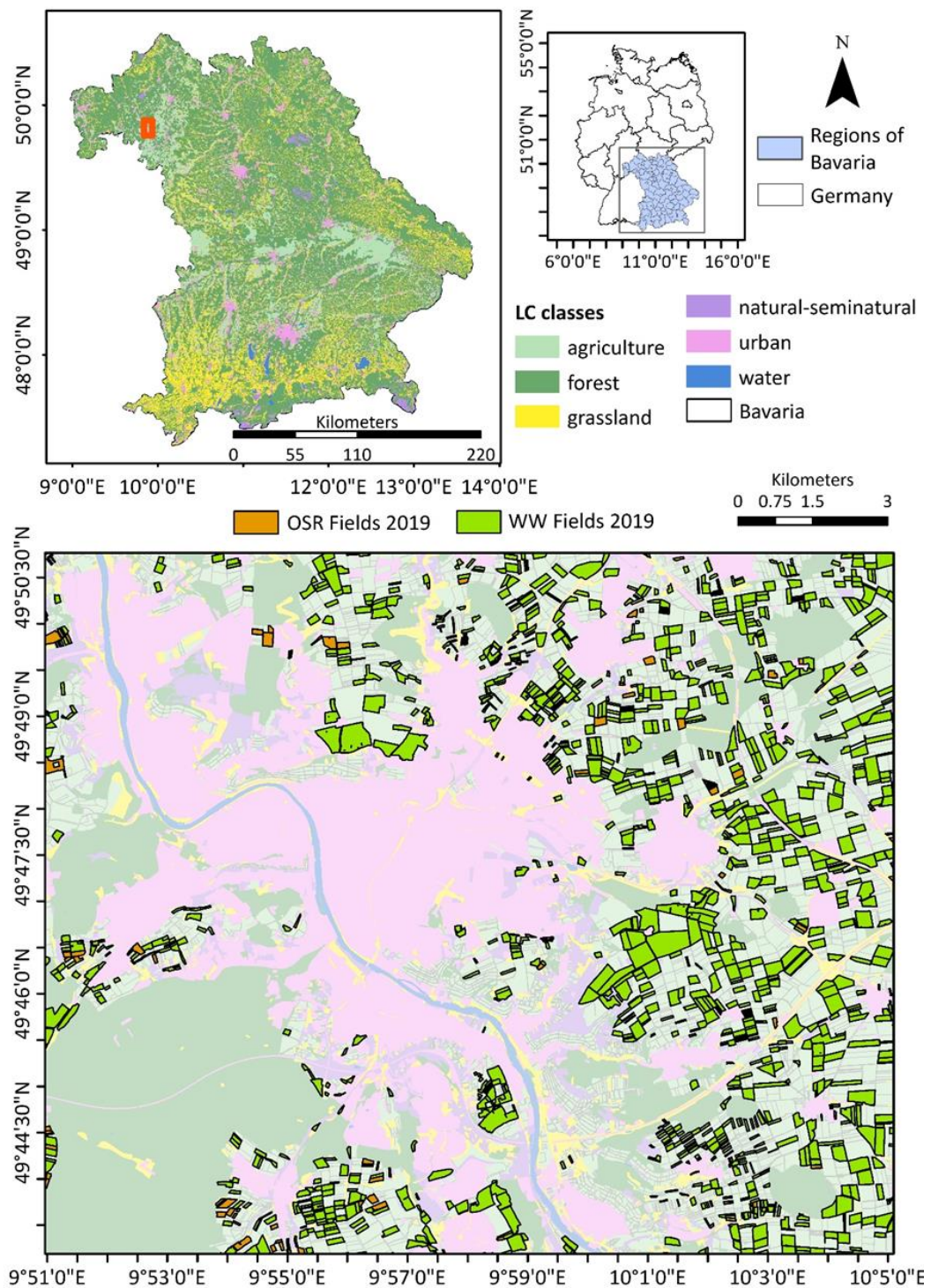


Figure 4.2. Overview of the study region. The LC map of Bavaria is obtained by combining multiple inputs of landcover maps, such as the Amtliche Topographisch-Kartographische Informations System, Integrated Administration Control System (which provides the crop field information), and the Corine LC, into one map. Agriculture (peach green) dominates mainly in the northwest and southeast of Bavaria, while forest and grassland classes (dark green and yellow, respectively) dominate in the northeast and south. The LC map is overlaid by the district map of Bavaria. The enlargement (displayed with a dark red box on the top right map) shows the urban area of the city of Würzburg, with the oil-seed rape (OSR) fields (dark orange) and the winter wheat (WW) fields (dark green) in 2019. A brief description of the regions of Bavaria is shown in Figure A1

4.2.2. Data

The study collected satellite data (with different spatial and temporal resolutions), climate data and vector data for the period of 2001 to 2019. A brief description of the data used in the present study with their spatial and temporal resolutions, and references are shown in Table 4.1.

Table 4.1. A summary of the collected datasets for fusion modelling and winter wheat's (WW) and oil seed rape's (OSR) crop modelling. The satellite data used for fusion and crop modelling are Landsat 5, 7 and 8 and Moderate Resolution Imaging Spectroradiometer (MODIS) MOD13Q1; the climate parameters are minimum temperature (°C) (Tmin), maximum temperature (°C) (Tmax), dewpoint temperature (°C) (Tdew), relative humidity (%) (RH), evaporation (mm) (Ep), Transpiration (mm) (Tp), and solar radiation ($\text{MJm}^{-2}\text{day}^{-1}$) (Rs); Shuttle Radar Topography Mission (SRTM) elevation data of Bavaria; InVeKos data provides the fields of WW and OSR for Bavaria from 2005 to 2019; the Bayerisches Landesamt für Statistik (LfStat) data provides the crop yield information (dt/ha) of WW and OSR at district level of Bavaria from 2001 to 2019.

| Data | Product Name | Resolution Spatial-Temporal | References |
|----------------|----------------------------------|-----------------------------|--|
| Climate data | Tmin, Tmax, Tdew, RH, Ep, Tp, Rs | 2000 m, 1-day
2001-2019 | https://www.uni-augsburg.de/de/fakultaet/fai/geo/ (assessed on 21 June 2021) |
| Satellite data | Landsat | 30 m, 16-days
2001-2019 | www.usgs.gov (assessed on 21 June 2021) |
| | MODIS (MOD13Q1) | 250 m, 16-days
2001-2019 | www.lpdaac.usgs.gov (assessed on 21 June 2021) |
| Elevation data | SRTM | 30 m | https://www.usgs.gov/centers/eros (assessed on 15 December 2022) |
| Vector data | InVeKos | 2005-2019 | www.ec.europa.eu/info/index_en (assessed on 21 June 2021) |
| | LfStat | 2001-2019 | https://www.statistikdaten.bayern.de/gensis/online/ (assessed on 21 June 2021) |

4.2.2.1. Satellite Data

The present study used L-MOD13Q1 (30 m, 16 days) NDVI time series generated by (Dhillon et al., 2022) as an input to the LUE model for nearly two decades (2001 to 2019). The L-MOD13Q1 time series needed a pair of high (Landsat: high pair) and coarse (MODIS: low pair) spatial resolution data for fusing together to generate a cloud and shadow-free synthetic time series using the STARFM algorithm. With the aim of generating a continuous cloud-free and shadow-free time series (that covers the time frame of 2001 to 2019), high-pair data sets such as Landsat 5 Thematic Mapper (TM) (1984 (launched)-2013 (ended)), Landsat 7 Enhanced Thematic Mapper Plus (ETM+) (1999–2003 (stripes in the data after this date due to scan line corrector failure)), and Landsat 8 Operational Land Imager (OLI) (2013-present) were used. The Landsat data

arrived with different spectral bands, i.e., coastal/aerosol, blue, green, red, near-infrared (NIR), shortwave infrared (SWIR) 1, and SWIR 2. The snow, shadow, and cloud cover were removed from the Landsat data using the “pixel_qa” quality assessment band generated using the C function of the mask (CFMask) algorithm. The number of cloud-free scenes (0% cloud cover based on CFMask) available every year (N) is shown in Table 2. Due to the difference in surface reflectance and atmospheric conditions, there is a considerable variation between the spectral values of Landsat sensors, which may have significant influences depending on the Landsat data application (David P Roy et al., 2016). Therefore, the study performed the inter-sensing harmonisation of the NDVI bands (calculated using NIR and red bands) of Landsat sensors, applying the coefficients proposed by (David P Roy et al., 2016) and derived using ordinary least squares (OLS) regression. The pre-processing steps were performed using the platform Google Earth Engine.

The Landsat products were generated using the Landsat Ecosystem Disturbance Adaptive Processing System (LEDAPS), which applies atmospheric correction, geometric correction, and calibration procedures to the raw data. During the atmospheric correction step, the impact of atmospheric scattering and absorption is removed from the raw data, and a surface reflectance product is generated independent of atmospheric effects. The geometric correction corrected the viewing angles to remove the effects of the satellite’s position and attitude at the time of image acquisition. This correction ensures that the pixels are accurately georeferenced and aligned with each other. Lastly, the calibration procedures applied during the LEDAPS processing correct for spectral band configuration, ensuring that the reflectance values across different spectral bands are consistent and accurate.

In addition, for the low pair, the study selected the MOD13Q1 V6 product, which provides an NDVI value per pixel with 250 m spatial and 16-day temporal resolution. Based on the quality information, pixels with noise (NDVI values < -1 and $> +1$) were masked out. Both the day of acquisition and quality information were considered while generating the NDVI values from the product. For crop modelling, this study input the

Chapter 4

eight-day satellite datasets from the stem elongation phases till the flowering stages of both WW and OSR. The parameters for the growth season of OSR were taken from a literature review that accurately monitored the growth timing and condition of the crop based on NDVI and the normalised difference yellowness index (NDYI) (calculated using the green and blue bands (Sulik & Long, 2015)) using the unmanned aerial vehicles (UAVs) in Germany (Zamani-Noor & Feistkorn, 2022). The phenological stages for WW were referenced from the literature that detected the phenological development of the crop using the time series of Sentinel-1 and Sentinel-2 in Germany (Harfenmeister et al., 2021). The study compared the phenology results with the BBCH scale (Biologische Bundesanstalt, Bundessortenamt, and Chemische Industrie), which is a system used worldwide by research and administration to standardise phenologically similar growth stages of multiple plant species (Harfenmeister et al., 2021; Meier et al., 2009). Therefore, the start (the stem elongation phase) and end (the flowering stage) of the seasons of OSR and WW were taken as 15 February to 20 April (Zamani-Noor & Feistkorn, 2022) and 15 April to 30 June from 2001 to 2019 (Harfenmeister et al., 2021), respectively.

Table 4.2. A summary of the collected cloud and shadow free Landsat 5, Landsat 7 and Landsat 8 datasets available every year with their day of the years (DOYs) between start-and end of the seasons of WW and OSR from 2001 to 2019. N is the total number of Landsat scenes available per year for WW and OSR.

| Year | N | DOYs | Year | N | DOYs |
|------|---|------------------------|------|---|-------------------------------|
| 2001 | 2 | 81,161 | 2011 | 7 | 65,81,113,129,145,177,
225 |
| 2002 | 3 | 33,145,161 | 2012 | 5 | 49,65,81,129,145 |
| 2003 | 4 | 65,129,177,193 | 2013 | 5 | 65,129,161,193,209 |
| 2004 | 4 | 33,65,97,161 | 2014 | 6 | 65,81,113,161,177,
209 |
| 2005 | 6 | 17,65,81,97,177,241 | 2015 | 4 | 65,97,145,209 |
| 2006 | 6 | 33,129,145,161,177,193 | 2016 | 8 | 17,65,81,113,129,161,177,193 |
| 2007 | 6 | 49,81,113,145,161,193 | 2017 | 4 | 97,129,145,225 |
| 2008 | 6 | 65,81,129,145,177,193 | 2018 | 7 | 49,81,113,129,145,177,193 |
| 2009 | 6 | 33,97,113,145,161,209 | 2019 | 5 | 49,81,145,177,193 |
| 2010 | 5 | 33,113,129,145,193 | | | |

4.2.2.2. Climate Data

For this study, the climate data from 2001 to 2019 with one-day temporal resolution were obtained by dynamically downscaling the ECMWF reanalysis 5th generation (ERA5) dataset to a horizontal grid resolution of 2000 m using the hydrologically enhanced weather research and forecasting model (Gochis et al., 2018; Hersbach et al., 2020; Skamarock et al., 2019). The ERA5 data were provided by the European Centre for medium-range weather forecasts. A detailed analysis of the downscaling approach is provided by (Arnault et al., 2018). The climate data were used as one of the inputs to the LUE model, which requires temperature, solar radiation, evapotranspiration, and relative humidity (Figure 4.1). Prior to input to the model, all climate elements were synchronised with the LUE model by aggregating them into eight days of temporal periods. Similar to the satellite data, the present study considered the eight-day climate data for the same start and end of the seasons for WW and OSR as described in the section 4.2.1.1.

4.2.2.3. Elevation Data

The study made use of the shuttle radar topography mission (SRTM) digital elevation data for Bavaria (Farr et al., 2007). The data had a spatial resolution of 30 m. For this study, the SRTM was used to correlate modelled crop yields with the elevation above sea level. The visualisation of the data is shown in Figure A3.

4.2.2.3. InVeKos Data

The present study made use of the InVeKos data to obtain the field base information of WW and OSR from 2005 to 2019 for Bavaria. The InVeKos data were collected through the integrated administration control system (www.ec.europa.eu/info/index, accessed on 21 June 2021), which was available for all agricultural plots in European Union (EU) countries by allowing farmers to graphically indicate their agricultural area.

4.2.2.4. LfStat Data

The Bayerisches Landesamt für Statistik (LfStat) provided the crop yield information for 29 crop categories, including WW and OSR, in Bavaria on a district level from 2001 to 2019 (source: www.statistikdaten.bayern.de/genesis/online/, accessed on 21 June 2021, Statistics Code: 41241). The LfStat data were used to validate the modelled yield information of the LUE model. The validation results were used to check the model's accuracy, consistency, and stability in generating the yield results in the region. The validation was limited to the rural regions, and the city districts were excluded (Figure A1).

4.2.3. Method

4.2.3.1. STARFM

The STARFM method (F. Gao et al., 2006) was used to fuse Landsat and MOD13Q1 to generate the synthetic NDVI time series with high spatial and temporal resolution from 2001 to 2019. As this paper is an extension of our previous paper, the detailed methodology of STARFM's generation of L-MOD13Q1 time series was explained in (Dhillon et al., 2022; Dhillon et al., 2020)

4.2.3.2. LUE Model

The LUE model was based on a light use efficiency principle (J. L. Monteith, 1972; John Lennox Monteith, 1977) and it was coupled with the RS data by using a similar methodology as (Dhillon et al., 2020; Shi et al., 2007). The model was based on a semi-empirical approach and calculated the FPAR (Asrar et al., 1992) and daily aboveground biomass as:

$$\text{Biomass} = \sum (\text{PAR} * \text{FPAR}) * \epsilon \quad (4.1)$$

$$\text{FPAR} = 1.222 * \text{NDVI} + 0.1914 \quad (4.2)$$

$$\epsilon = \sum (\text{Tmin}_{\min}' * \text{VPD}' * \text{Ks}) * \epsilon_0 \quad (4.3)$$

where PAR is photosynthetically active radiation ($\text{MJ m}^{-2} \text{d}^{-1}$), FPAR is the fraction of PAR absorbed by the canopy, SOS and EOS are the start and end of seasons of WW and OSR, and ϵ is the actual light-use efficiency (g C M J^{-1}). The total aboveground biomass calculated by the LUE model is equivalent to the net primary productivity (NPP) ($\text{kg ha}^{-1} \text{yr}^{-1}$). A brief explanation of the model with a flow diagram was described in our previous study (Dhillon et al., 2020). The specific model was not only selected for its performance but also for its high processing speed and low requirement of input parameters as compared to the other CGMs. The model was calibrated by using values from the previous literature, as follows: The study used a minimum lethal temperature value of $-2 \text{ }^\circ\text{C}$ for both WW and OSR (Habekotté, 1997; Hodgson, 1978; Single, 1985). In the other studies, the optimal minimum values of temperature for WW and OSR at growth stages were $10 \text{ }^\circ\text{C}$ and $12 \text{ }^\circ\text{C}$, respectively (Habekotté, 1997; Hodgson, 1978; Single, 1985). For the vapour pressure deficit (VPD), the present study followed (Russell & Wilson, 1994), which had analysed the environmental impact on leaf gas exchange in WW with minimum and maximum values of 1.5 and 4.0 kPa, respectively. The value for optimal light use efficiency was used as 3 gC/MJ (Djumaniyazova et al., 2010).

4.2.3.3. Sensitivity Analysis

The study performed the sensitivity analysis of the LUE model for both WW and OSR in Bavaria from 2001 to 2019. During the analysis, the impact of climate stress factors was nullified, and the biomass is calculation replaced the actual light use efficiency (ϵ) values with the optimal (ϵ_0) values (Equation 4.4).

$$\text{Biomass} = \sum_{\text{SOS}}^{\text{EOS}} (\text{PAR} * \text{FPAR}) * \epsilon_0 \quad (4.4)$$

4.2.3.4. Statistical Analysis

Both the STARFM NDVI and the LUE modelled crop yield of WW and OSR were validated using the observed NDVI and LfStat crop yield (with 95% confidence interval) from 2001 to 2019, respectively. The quality (R^2) and the precision (root mean square error (RMSE)) of the obtained results were calculated using the linear regression model (LRM) which aimed to establish a linear relationship between the referenced NDVI/or measured yield (independent variable) and synthetic NDVI/or modelled yield (dependent variable). The correlation plots between the number of Landsat scenes and the synthetic NDVI accuracy from 2001 to 2019 were generated by calculating the correlation coefficient (R) (Equation (4.5)). R values lie between -1 (strong negative correlation between two variables) to 1 (strong positive correlation between two variables). The statistical parameters used to validate the accuracy of modelled yield and synthetic NDVI are R^2 (Equation (4.6)), Mean Error (ME) (Equation (4.7)) and RMSE (Equation (4.8)). The Equation (4.9) calculates the yield percent difference (%) which were calculated for every region of Bavaria. The yield percent difference was analysed on six categories, less than -4, -4 to -2, -2 to 0, 0 to 2, 2 to 4, and more than 4.

$$R = \frac{n(\sum O_i * P_i) - (\sum O_i)(\sum P_i)}{\sqrt{((n \sum O_i^2) - (\sum O_i)^2)((n \sum P_i^2) - (\sum P_i)^2)}}, \quad (4.5)$$

$$R^2 = \frac{((\sum P_i - P') (O_i - O'))^2}{(\sum P_i - P')^2 (\sum O_i - O')^2}, \quad (4.6)$$

$$ME = \frac{1}{n} \sum_{i=1}^n (O_i - P_i)^2 \quad (4.7)$$

$$RMSE = \sqrt{ME}, \quad (4.8)$$

$$\text{Yield Percent Difference} = \text{Mean} \left(\left(\frac{\text{referenced yield}_y - \text{modelled yield}_y}{\text{referenced yield}_y} \right) * 100 \right) \quad (4.9)$$

where P_i is the predicted value, O_i is the observed value, P' is the predicted mean, O' is the observed mean value, n is the total number of observations, referenced yield_y is the LfStat yield of every district from 2001 to 2019, and modelled yield_y is the LUE generated yield of every district from 2001 to 2019. The significance of the obtained

results was obtained by observing the probability value (*p-value*) which was calculated using the LRM with a H_0 that there is no correlation between the referenced and the modelled or synthetic values, and an H_1 that the correlation exists. The test was performed with at a significance level (or alpha (α)) of 0.05. A *p-value* lower than 0.05 indicated that the model is significant, and it rejected the H_0 that there was no correlation. The correlation was calculated between the accuracies of synthetic NDVI and crop yield on yearly basis using the Equation (4.5). This calculated the relationship of data fusion with crop yield prediction results by the LUE model.

4.3. Results

4.3.1. Validation of Synthetic Remote Sensing Time Series from 2001 to 2019

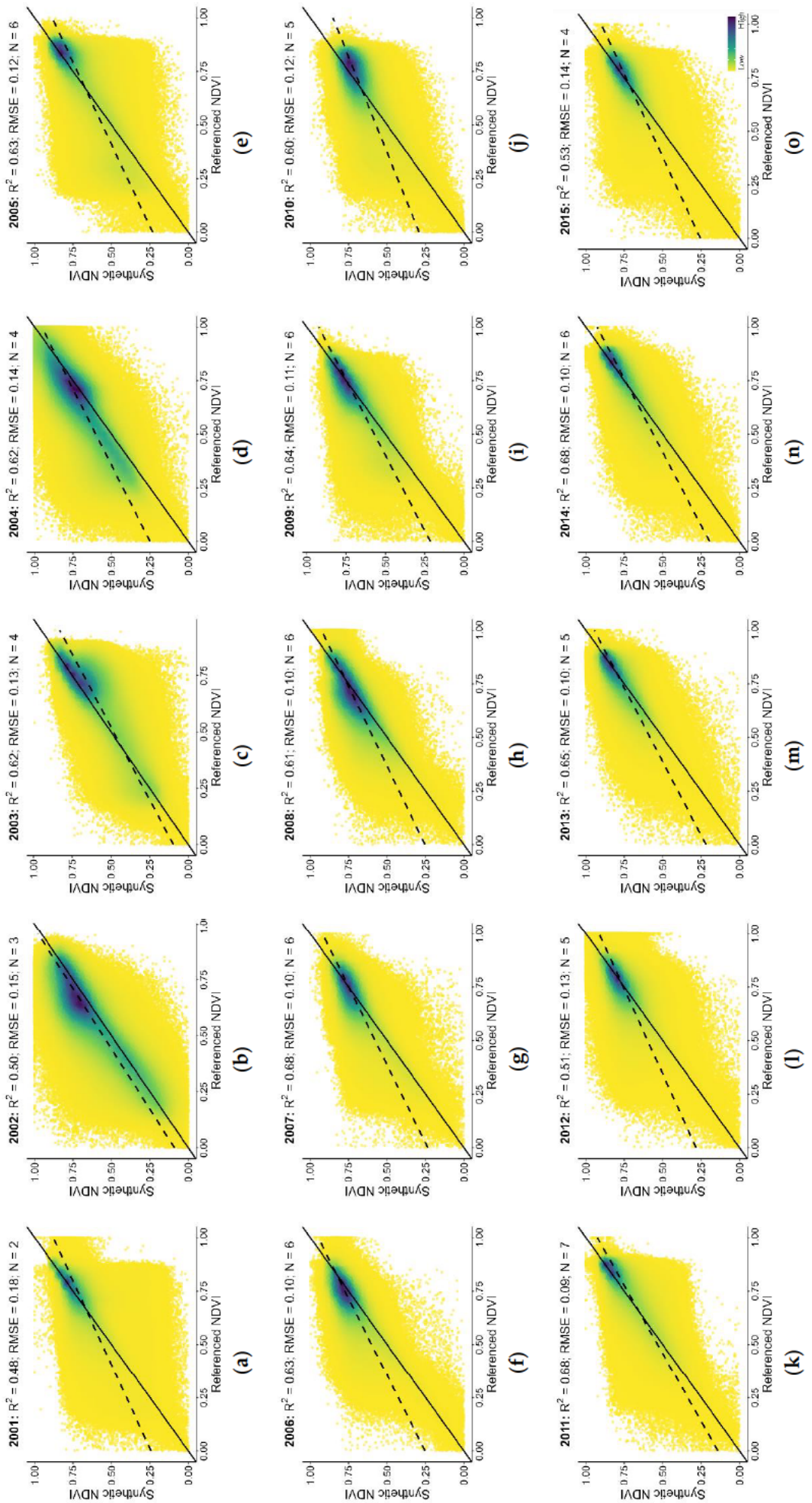
For nineteen years (i.e., from 2001 to 2019), the STARFM performed significantly for yearly synthetic output (having a *p-value* < 0.05); this rejected the H_0 of the linear regression model that there was no correlation between the synthetic and referenced NDVI (Figure 4.3a–s). After generating the yearly scatter plots, the synthetic products' R^2 and RMSE values were analysed. Among all years, the highest accuracy and precision were obtained for 2016 and 2018, with an average R^2 of 0.75 and RMSE of 0.09. For 2005, 2006, 2007, 2009, 2011, 2013, 2014, 2017, and 2019, the R^2 values were higher than 0.60 and the RMSE values were lower than 0.12. In other years, such as 2003, 2004, 2008, and 2010, the R^2 and RMSE values lied within 0.60 to 0.62 and 0.10 to 0.14, respectively. However, the rest of the temporal period (i.e., 2001, 2002, 2012, and 2015) resulted in lower R^2 (<0.60) and RMSE (>0.13) values.

The results proved that the yearly accuracy assessment of the synthetic products is impacted by the total number of Landsat scenes (N) available every year (Figure 4.4a,b). A high positive ($R = +0.83$) and negative ($R = -0.84$) correlation was seen between the yearly quality (R^2) and preciseness (RMSE) of the synthetic NDVI products with N , respectively. For example, 2011, 2016, and 2018 were the most accurate years ($R^2 > 0.68$ and RMSE = 0.09) with a total N of more than 7. Similarly, 2001 and 2002 had the least R^2 (< 0.50) and highest RMSE (> 0.15) with the fewest available Landsat scenes ($N = 2/3$)

Chapter 4

in both years. The overall accuracy of L-MOD13Q1 for nineteen years was R^2 of 0.62 and RMSE of 0.12, with an average of 5 N every year.

On comparing the yearly fusion results on a DOY basis, the DOYs 113, 129, and 193 had the highest average accuracy with an R^2 of more than 0.65 and a RMSE lesser than 0.10 (Figure 4.5a,b). The DOYs of 33 to 97 and 145 to 177, with low R^2 (<0.60) and high RMSE (>0.11), were obtained.



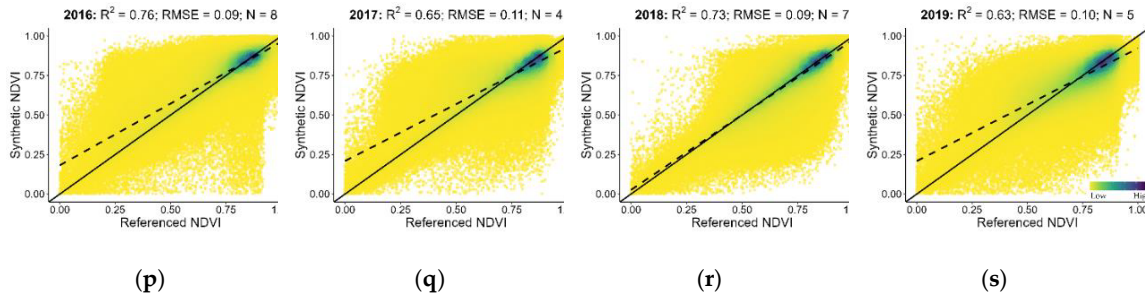


Figure 4.3. The scatter plots (a–s) compare the accuracies of Landsat (referenced NDVI) with L-MOD13Q1 (synthetic NDVI) for 2001 to 2019. The values of the statistical parameters such as R^2 and RMSE and the total number of Landsat scenes available every year (N) are displayed at the top of each plot. Every plot contains a solid line (1:1 line) that is used to visualise the correlation of pixels between the referenced and synthetic NDVI values. The dashed line represents the regression line. The colour of scatter plots depicts the density of points (yellow: low, blue: high).

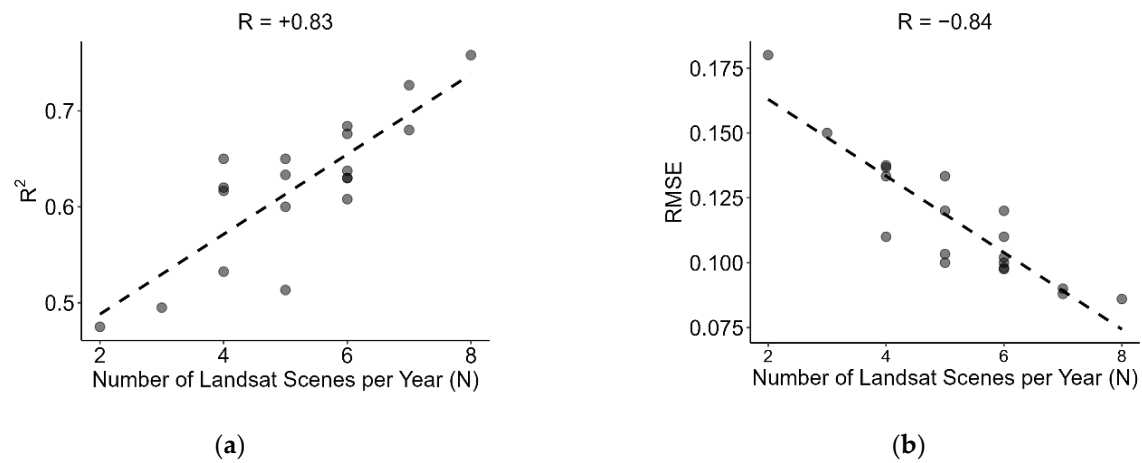


Figure 4.4. The correlation plots between the total number of Landsat scenes per year (N) and (a) R^2 values and (b) RMSE values obtained during the accuracy assessment of referenced and synthetic NDVI products from 2001 to 2019. The correlation coefficient refers to R (see Equation (4.5)).

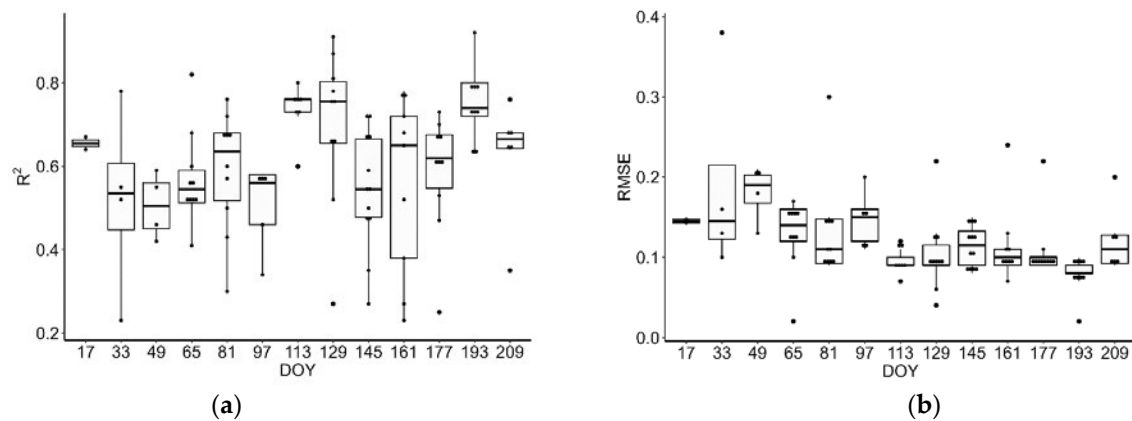


Figure 4.5. The day of the year (DOY)-based comparison of correlation coefficients between (a) R^2 values and (b) RMSE values obtained during the accuracy assessment of referenced and synthetic NDVI products from 2001 to 2019. The correlation coefficient refers to R (see Equation (4.5)).

4.3.2. Comparative Analysis between Crop Yield Accuracy of MOD13Q1 and L-MOD13Q1 Using the Light Use Efficiency Model in 2019

Figure 4.6a–c displayed the crop yield accuracies between the modelled and referenced crop yields of WW and OSR obtained with different satellite products using the LUE model in 2019. The figures show that the fused product (L-MOD13Q1) obtained a higher R^2 (0.81) and a lower RMSE (3.91 dt/ha) than the non-fused product (MOD13Q1: $R^2 = 0.70$ and RMSE = 4.77 dt/ha) for both WW and OSR. Analysing the ME of both products with LUE, the L-MOD13Q1 resulted in a lower ME (3.04 dt/ha) than the MOD13Q1 (3.50 dt/ha) (Figure 4.6c).

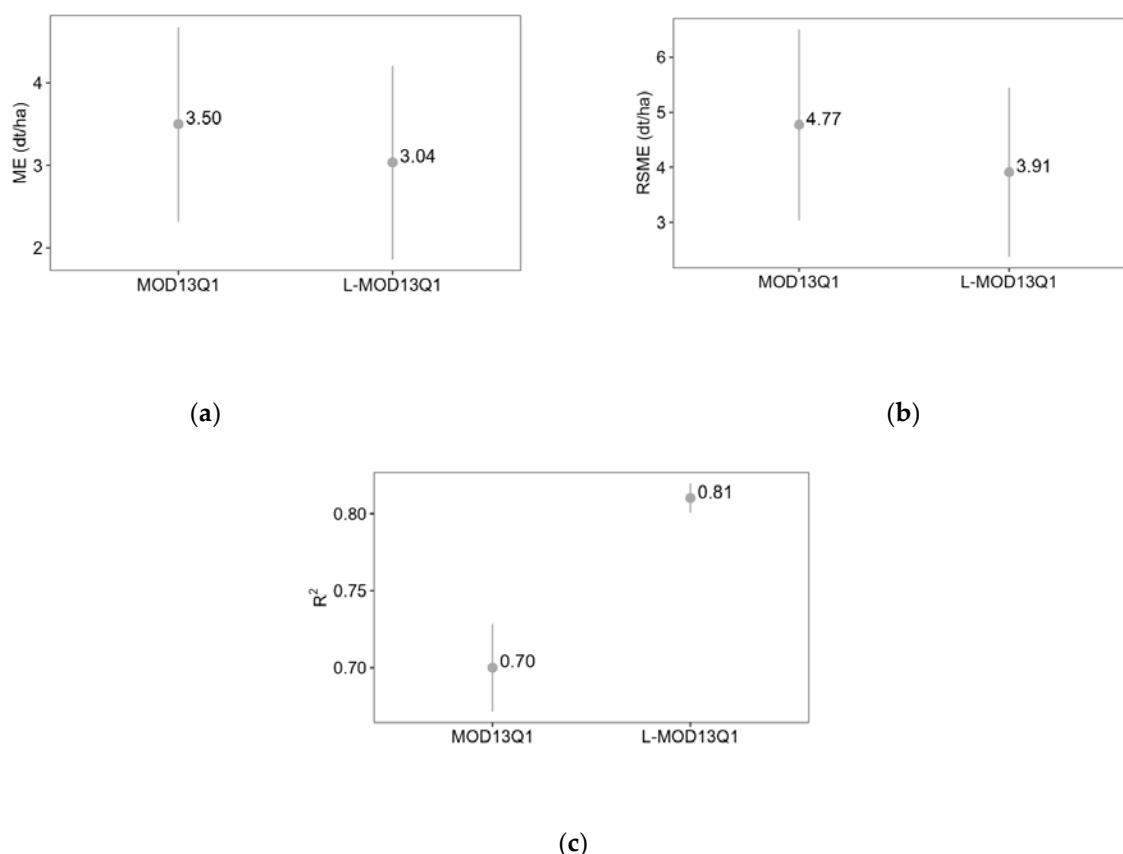


Figure 4.6. The dot plots compare the accuracies (a) R^2 , (b) RMSE, and (c) ME of referenced data (at 95% confidence intervals) and modelled yields obtained from multi-source data: MOD13Q1 and L-MOD13Q1 in 2019.

4.3.3. Statistical Analysis between Reference and Modelled Crop Yields of WW and OSR from 2001 to 2019 using the Light Use Efficiency Model

For both WW and OSR, the LUE model performed significantly for every year (having a p -value < 0.05); this rejected the H_0 of the linear regression model that there was no correlation between the referenced and modelled crop yield from 2001 to 2019

(Figure A4a-s and Figure A5a-s). After generating the scatter plots, all crop yield products' R^2 , RMSE, and ME values were analysed. For both WW and OSR, the years 2007 through 2018 and 2019 were the most accurate years where the estimated crop yield resulted in high R^2 values (>0.79). However, both 2018 and 2019 for WW resulted in higher RMSE (4.74 and 4.98 dt/ha) and ME (3.46 and 3.71 dt/ha) values, respectively (Figure A4). The remaining years for WW showed a similar trend in R^2 (>0.65), RMSE (<4.50 dt/ha), and ME (<3.60 dt/ha) values, with the exceptions of 2001 and 2013, which had RMSE values more than 5.40 dt/ha and ME values more than 4.30 dt/ha. Similarly, for OSR, the RMSE values for 2001, 2005, and 2012 resulted in higher RMSE (>3.22 dt/ha) and ME (>2.47 dt/ha) (Figure A5). A mostly, similar trend in R^2 values was observed in the OSR, with values ranging from 0.63 to 0.80. The overall accuracies of both WW and OSR for 19 years were recorded as R^2 of 0.79 and 0.86 and RMSE of 4.51 dt/ha and 2.47 dt/ha, respectively (Figure 4.7a,b). Negative correlations were seen between the regional mean elevations and the modelled yields of WW (-0.30) and OSR (-0.38), respectively (Figure 4.8a,b).

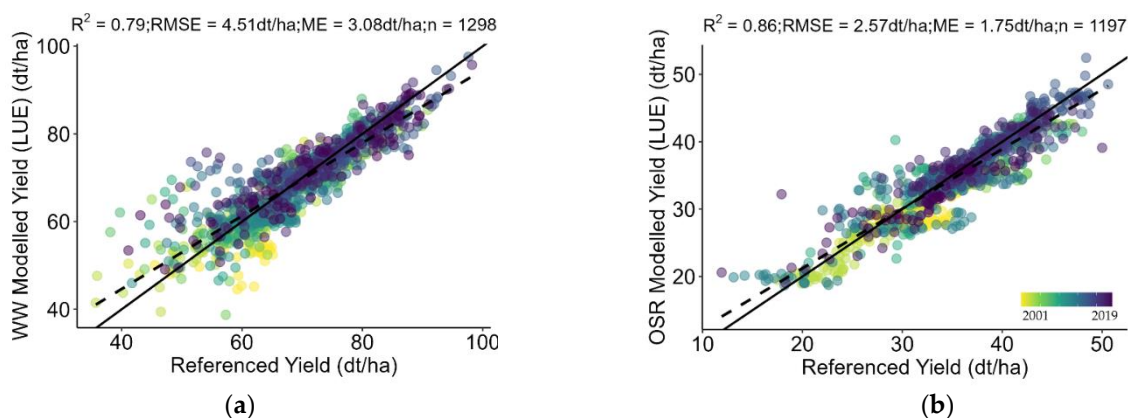


Figure 4.7. The scatter plots compare the accuracies of modelled and referenced yields (at 95% confidence interval) of (a) WW and (b) OSR for 19 years together (i.e., from 2001 to 2019). The values of the statistical parameters such as R^2 , RMSE (dt/ha), ME (dt/ha) and total number of points (n) are displayed at the top of each plot. Every plot contains a solid line (1:1 line) that is used to visualise the correlation of pixels between the modelled and referenced yield values. The dashed line represents the regression line. Different colors to the points display different years.

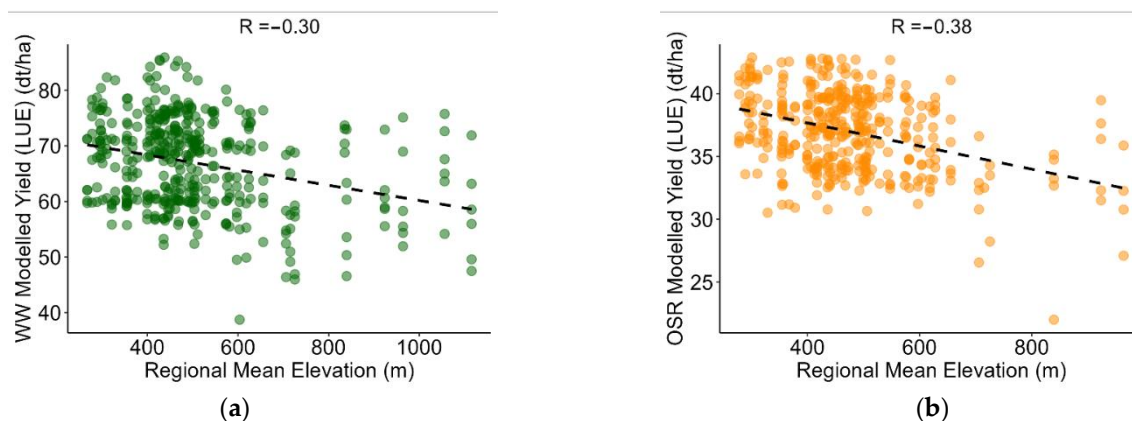
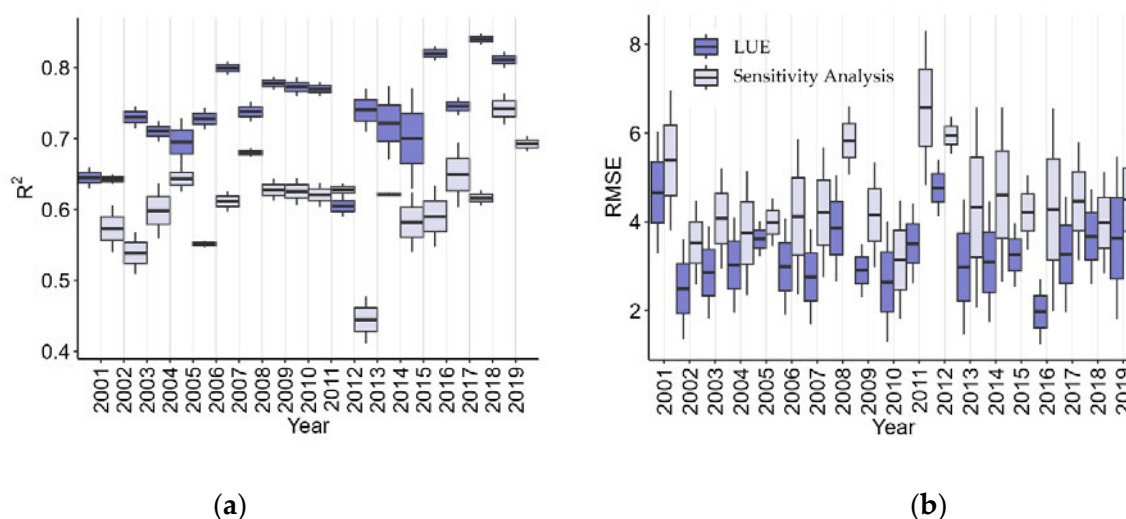


Figure 4.8. The scatter plots correlating the modelled yield and regional mean elevation for (a) WW and (b) OSR. The dashed line represents the regression line. Different colors to the points display different crop types (Green: WW and Orange: OSR). The correlation coefficient refers to R (see Equation (4.5)).

4.3.4. Sensitivity Analysis

The sensitivity analysis compared the model's performance by excluding the effect of climate stress factors from 2001 to 2019 for both WW and OSR in Bavaria. The LUE-modelled yield showed a higher correlation with the referenced yield when the climate stress factors were included, and vice versa. The model showed higher R^2 and lower RMSE values when compared with the yield values obtained during the sensitivity analysis (Figure 4.9a,b). The overall accuracies obtained during the sensitivity analysis of both WW and OSR for 19 years were recorded as R^2 of 0.68 and 0.78 and RMSE of 5.88 dt/ha and 3.41 dt/ha, respectively (Figure 4.9c,d).



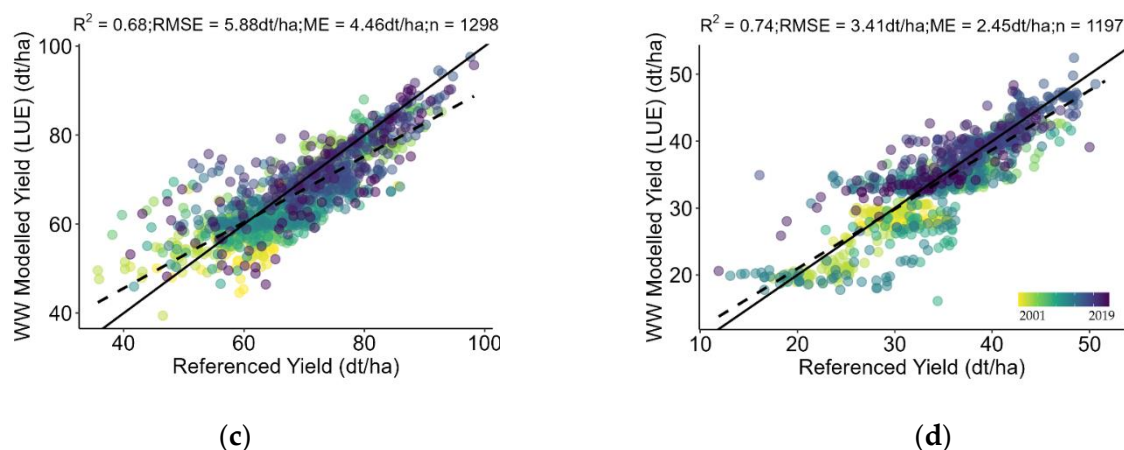


Figure 4.9. The bar plots show the yearly comparison of accuracies (a) R^2 values and (b) RMSE values obtained from the referenced yields (at a 95% confidence interval), with LUE-modelled yields including climate stress factors (dark blue) and LUE-modelled yields excluding the climate stress factors (sensitivity analysis) (light blue). The scatter plots compare the accuracies of the modelled and referenced yields (at a 95% confidence interval) of (c) WW and (d) OSR for 19 years together (i.e., from 2001 to 2019). The values of the statistical parameters such as R^2 , RMSE (dt/ha), ME (dt/ha), and total number of points (n) are displayed at the top of each plot. Every plot contains a solid line (1:1 line) that is used to visualise the correlation of pixels between the modelled and referenced yield values. The dashed line represents the regression line. Different colours of the points display different years.

4.3.5. Statistical Analysis between Reference and Modelled Crop Yields of WW and OSR from 2001 to 2019 using the Light Use Efficiency Model at Regional Level

On comparing the long-term crop yield at the regional level, the yearly spatial change from the mean referenced and modelled yield was displayed for both WW and OSR (Figures 4.10 and 4.11). For WW, most of the regional yield lied between 65 and 80 dt/ha (Figure 4.10). Districts such as, Regen, Freyung-Grafenau, Bad Tölz-Wolfratshausen, and Garmisch-Partenkirchen, the average percent difference was calculated as -25.10% (LUE: ~75 dt/ha), -18.68% (~60 dt/ha), -8.08% (~62 dt/ha), and -5.58% (~65 dt/ha), which showed that the model highly overestimated the crop yield values as compared to the referenced yield (Figures 4.12a and A6a). The positive yield percent difference (where the model underestimated the crop yield) between 0 and 4% had an accuracy greater than 0.80 as compared to the negative yield percent difference between -4 and 0% with an accuracy less than 0.70 (Figure 4.13). Similarly, the model underestimated the crop yield of Oberallgäu, Miltenberg, Deggendorf, and Dachau with 4.65% (~78 dt/ha), 3.91% (~68 dt/ha), 3.30% (~75 dt/ha) and 3.15% (~78 dt/ha), respectively. For OSR, the model overestimated the yield for Aichach-Friedberg,

Deggendorf, Dingolfing-Lindau, Traunstein, Unterallgäu, Dachau, Rottal-Inn, Miltenberg and Günzburg with 7.13% (LUE: ~38 dt/ha), 5.12% (~39 dt/ha), 4.91% (~37 dt/ha), 4.80% (~35 dt/ha), 4.53% (~36 dt/ha), 4.36% (~38 dt/ha), 4.25% (~35 dt/ha), 4.24% (~37 dt/ha) and 4.06% (~34 dt/ha), respectively (Figures 4.12b, and A6b). However, unlike WW, both the over- and underestimation of OSR yield values resulted in a similar increase and decrease in accuracy (Figure 4.13).

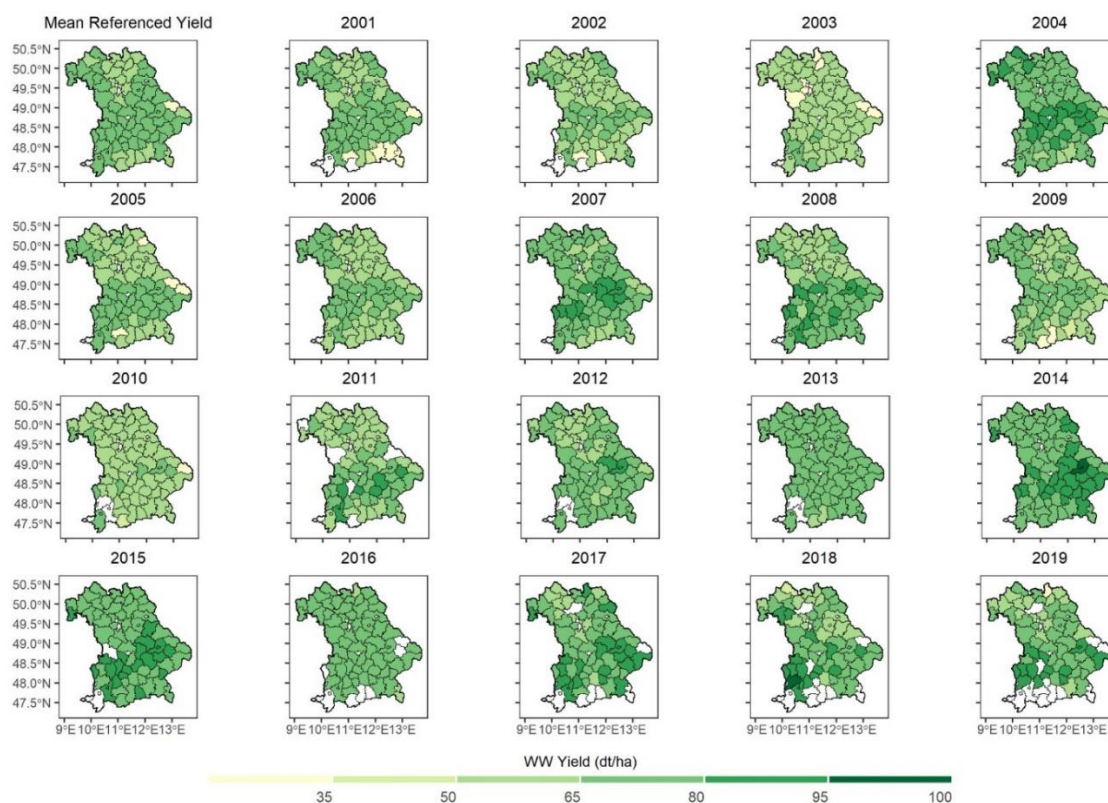


Figure 4.10. Spatial distribution of mean referenced yield (2001-2019) and the year-wise predicted yield for WW from 2001 to 2019 using the LUE model for the state of Bavaria. The white color represents no data available. Detailed map of the administrative regions of Bavaria is shown in Figure A1.

Chapter 4

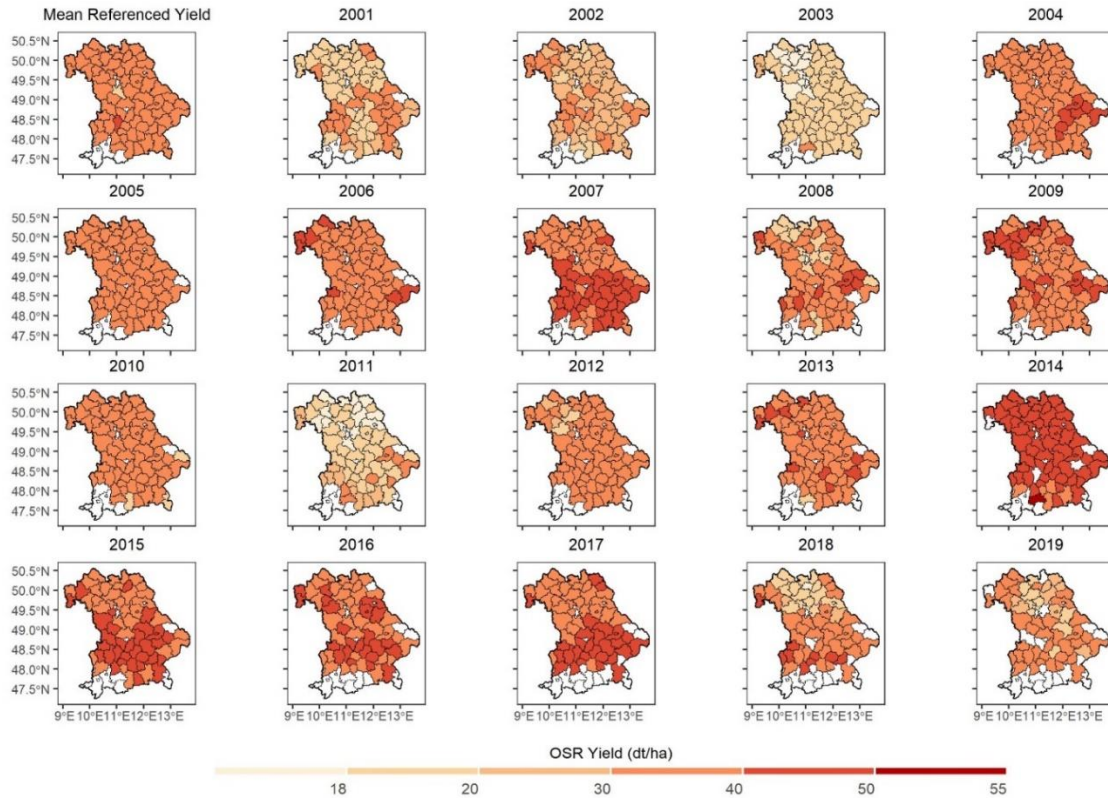
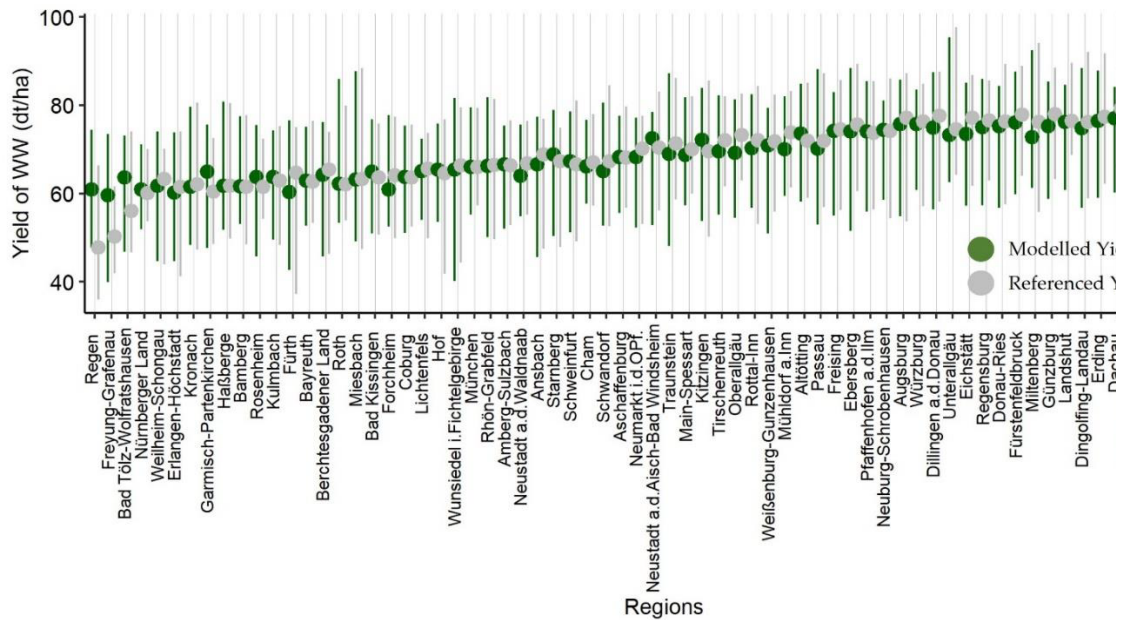
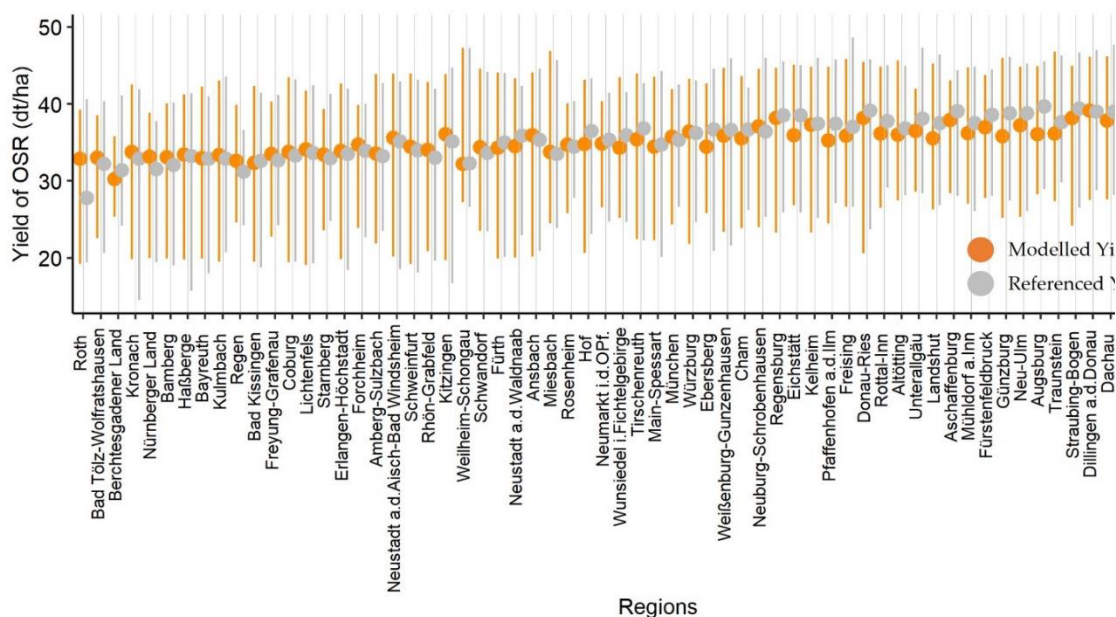


Figure 4.11. Spatial distribution of mean referenced yield (2001-2019) and the year-wise predicted yield for OSR from 2001 to 2019 using the LUE model for the state of Bavaria. The white color represents no data available. Detailed map of the administrative regions of Bavaria is shown in Figure A1.



(a)



(b)

Figure 4.12. The dot plots show the district-wise distribution of modelled yield for (a) WW, (b) OSR, from 2001 to 2019. The green color depicts the modelled yield of WW, the orange color depicts modelled yield of OSR, and the gray color depicts both referenced yields of WW and OSR.

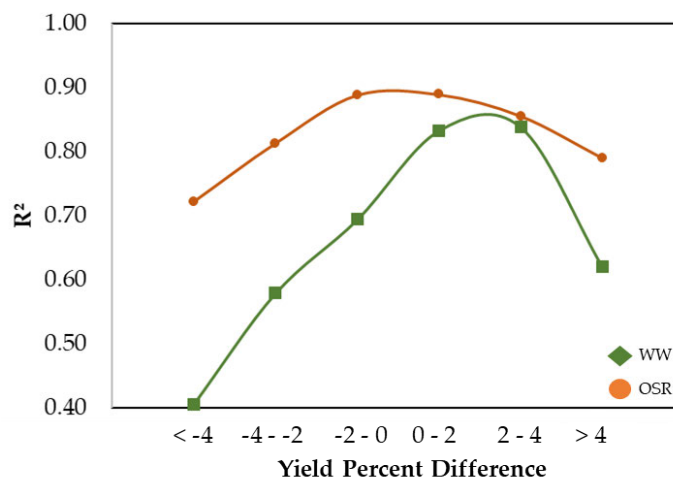


Figure 4.13. The line plots compare the accuracies with the mean yield percent difference (as calculated in Equation (4.9)) for WW and OSR for 19 years (i.e., from 2001 to 2019). The accuracies of WW and OSR are analysed with six categories (less than -4, -4 to -2, -2 to 0, 0 to 2, 2 to 4, and more than 4 %) of yield percent difference. The negative range shows the overestimation and positive range shows the underestimation of modelled yield values by the LUE than the referenced yield values. The green color depicts WW, and the orange color depicts OSR.

4.3.6. Correlation Analysis between the Accuracy Assessments of the Input Synthetic Products and the Crop Yield Modelling

The bar and scatter plots compared and linked the yearly accuracies of the input synthetic time series with the crop yield modelling for WW and OSR from 2001 to 2019, respectively (Figures 4.14 and 4.15). For WW, the correlation coefficient showed a higher positive correlation of 0.81 between the R^2 of synthetic accuracy and the modelled yield accuracy (Figure 4.15a). Except 2015 (yield R^2 : 0.77, synthetic R^2 : 0.53) and 2013 (yield R^2 : 0.71, synthetic R^2 : 0.65), where the fusion accuracies were negatively correlated with crop yield accuracy (Figure 4.14a). Similarly, for OSR, the correlation coefficient was found to be 0.77 (Figure 4.15b). For 2001 and 2002, the fusion accuracy was lower ($R^2 < 0.50$); however, the crop yield accuracy for the same years resulted in an R^2 of more than 0.65 (Figure 4.14b).

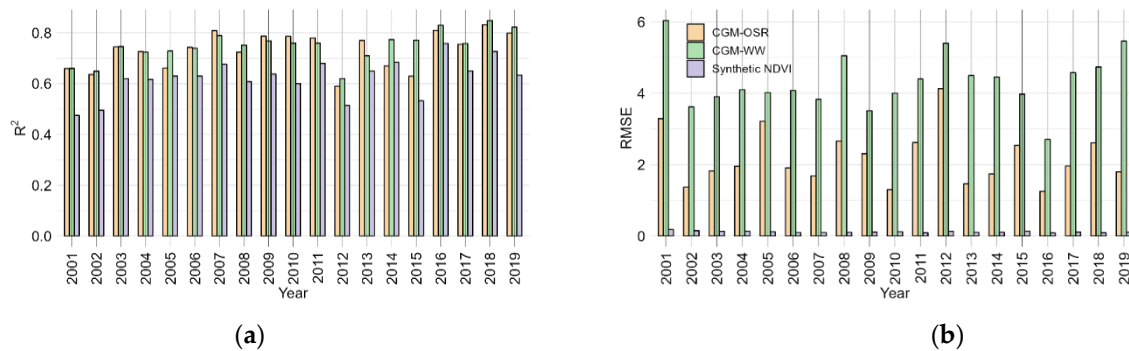


Figure 4.14. The bar plots compare the yearly (a) R^2 and (b) RMSE values, of estimated OSR yield (orange), WW yield (green) and synthetic NDVI (purple) from 2001 to 2019. The units of RMSE values of both WW and OSR yields are dt/ha.

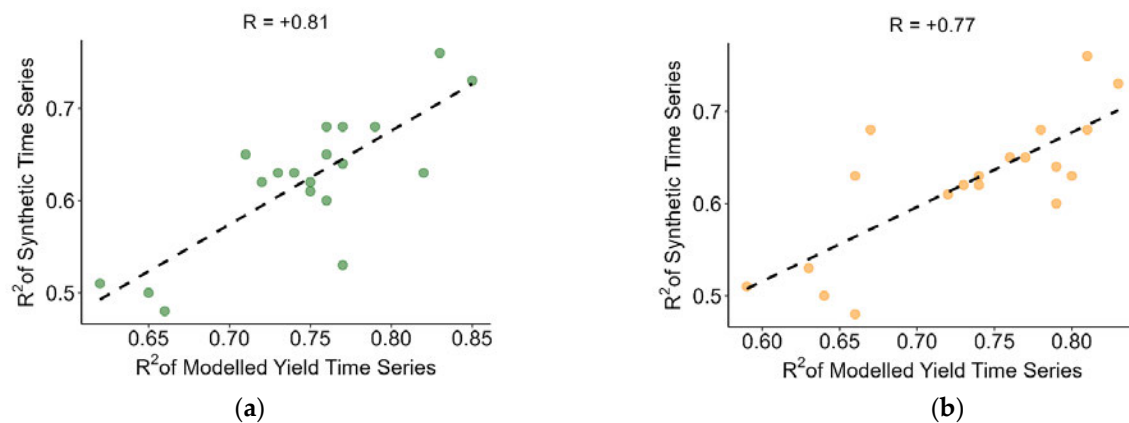


Figure 4.15. The correlation plots between R^2 of Synthetic NDVI time series and R^2 of modelled yield time series for (a) WW (green), and (b) OSR (orange), from 2001 to 2019. The correlation coefficient refers to R (see Equation (4.5)).

4.3.7. Visualization of the Modelled Crop Biomass and the NDVI of different Years at a Field Level

The side-by-side spatial visualisation of the input synthetic NDVI product (DOY 169: 18 June) and the WW-modelled biomass for selected years (2005, 2013, and 2019) is shown in Figure 4.16, respectively. For every year, the spatial trend of crop biomass and NDVI in every field was seen differently. Likewise, NDVI values were rising from 2005 to 2019 from 0.4 to 0.8, and crop biomass had been observed rising from less than 550 g/m² in 2005 to more than 850 g/m² in 2019. In most of the fields, the crop biomass was dependent on the higher NDVI values. The NDVI values higher than 0.8 impacted higher crop biomass of more than 850 g/m² in almost every year. In 2005, the average field crop biomass resulted in less than 650 g/m²; however, in 2019, the crop biomass resulted in more than 650 g/m².

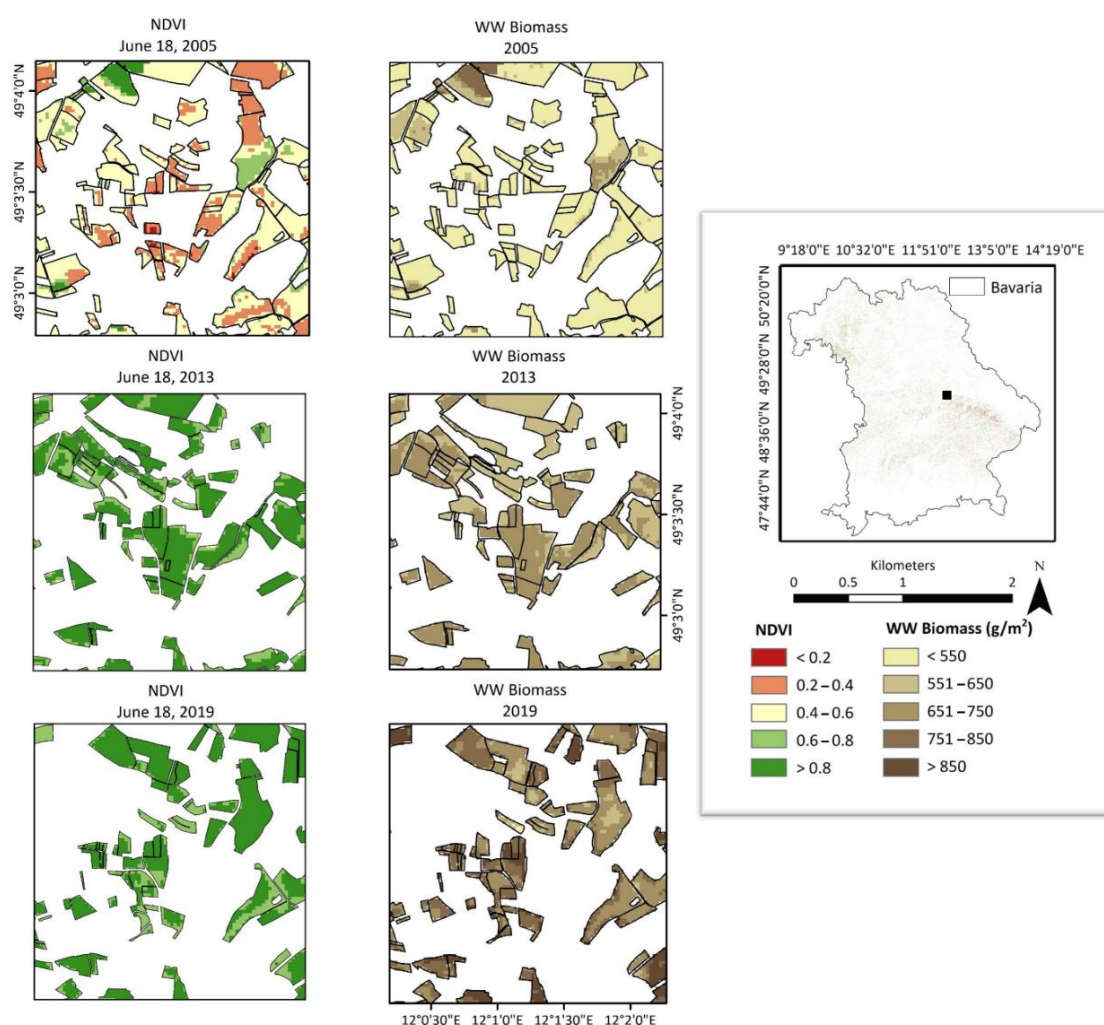


Figure 4.16. The side-by-side visualisation of synthetic NDVI products obtained on June 18th of 2005, 2013 and 2019 (left) with the WW biomass obtained from the LUE modelled for the years of 2005, 2013 and 2019 (right).

4.4. Discussion

4.4.1. Quality Assessment of Synthetic Remote Sensing Time Series from 2001 to 2019

The present study investigates the potential of the STARFM over the Bavarian state of Germany to generate the synthetic NDVI time series from 2001 to 2019 by selecting the best-performing high (Landsat) and low (MODIS) pair obtained for the agricultural class from the previous literature. Many studies prefer using ESTARFM (Enhanced STARFM) for better fusion accuracy (Tewes et al., 2015; X. Zhu et al., 2010); however, some studies found STARFM performing significantly better than ESTARFM (Ghosh, Gupta, Tolpekin, & Srivastav, 2020; J. Xue, Leung, & Fung, 2017). Simple in its design, faster to implement, and capable of fusing the entire state of Bavaria (which covers almost one-fifth of the area of Germany) for two decades, the study finds STARFM to be more advantageous over ESTARFM. ESTARFM was complex, time-consuming, and computationally expensive for covering extensive data for extended periods (B. Chen, Huang, & Xu, 2015; Guo, Wang, Lei, Yang, & Zhao, 2020). One of the strengths of ESTARFM is that it incorporates additional information, such as a land-cover map, to improve the accuracy of the fusion (X. Zhu et al., 2010). The study incorporates Bavaria's accurate and updated land cover map into the STARFM to balance its input requirements with the ESTARFM. It provided homogeneity to the STARFM and increased its fusion accuracy (as discussed briefly in our previous study (Dhillon et al., 2022)).

In our previous study, we found that L-MOD13Q1 (30 m, 16 days) ($R^2 = 0.62$ and $RMSE = 0.11$) was suitable for the application of agricultural monitoring due to its fast and easy processing with lesser storage requirements (Dhillon et al., 2022). Moreover, the present study focuses on two decades (2001 to 2019); therefore, the paper generates and validates a Landsat-based synthetic NDVI time series (L-MOD13Q1) due to its continuous availability since 1982 with a maximum resolution of 30 m. As NDVI is among the most effective and widely used vegetation indices and many spatiotemporal fusion-based studies have used it as their primary input (Mirschel et al., 2004; Murthy, 2004; Van Klompenburg et al., 2020). However, many spatiotemporal fusion algorithms

are based on reflectance fusion, which requires more processing time and storage than NDVI (or one-band blending) fusion (T. Dong, Liu, Qian, Zhao, et al., 2016; J. J. Walker et al., 2012). Having high computation power with fewer storage problems for the long-term time series of 2001 to 2019 for complete Bavaria (70,550 km²), the research uses the strategy “index-then-blend” (IB), which generates the NDVI from Landsat and MOD13Q1 before they are blended for fusion (X. Chen et al., 2018). The IB strategy is used in multiple works of the literature with highly accurate and precise fusion outputs (X. Chen et al., 2018; Dhillon et al., 2022; Dhillon et al., 2020).

The analysis found that the accuracies of the fusion products are dependent on the available number of Landsat scenes per year (N) (Dhillon et al., 2022), such that the higher N, the higher the fusion accuracy of the synthetic NDVI product in a respective year. For instance, the positive R (+0.75) shows the positive correlation between R² of yearly synthetic NDVIs and N (representing the higher quality of the fused product), and the negative R (-0.73) shows the negative correlation between RMSEs and N (representing the higher precision). However, as the research made use of Landsat 8 Operational Land Imager (OLI) (from 2013 to 2019) and Landsat 5 Thematic Mapper (TM) (from 2001 to 2013), it was found that Landsat OLI-based fusion with MOD13Q1 resulted in higher accuracy as compared to Landsat TM (Poursanidis, Chrysoulakis, & Mitraka, 2015). For example, the years 2001, 2002, 2004, 2005, and 2012 (using Landsat 5 and 7) have a lower R² (<0.60) and a higher RMSE (>0.12) than the remaining years (using Landsat 8). The reason could be that Landsat 8 has improved upon the quality of Landsat 5 and 7, offering improved data accuracy. Moreover, the accuracy of the year 2012 is affected due to the gaps generated by the scan line corrector (SLC) failure in Landsat 7.

On comparing the fusing results on a DOY basis, the study finds that the few cloud-free DOYs could create large gaps between the available Landsat scenes that might affect the accuracy of the fusion product (Dhillon et al., 2022; Dhillon et al., 2020). For example, the DOYs 33 to 97 (N = ~6) result in a low R² (0.54) and a high RMSE (0.16) as compared to the DOYs 113 to 193 (N = ~8), which have a high R² (0.64) and a low RMSE (0.10).

4.4.2. Impact of Synthetic Time Series on Crop Yield Modelling

The objective of the present study is to generate and validate the long-term crop yield time series using the semi-empiric LUE model, which has proven to be more reliable, precise, and simple in the previous literature (Dhillon et al., 2020; Shi et al., 2007). The present study validates the crop yield results of WW and OSR obtained by inputting the synthetic NDVI and climate elements to the LUE model at a regional scale in Bavaria from 2001 to 2019. However, before generating the long-term time series using the synthetic NDVI product, the study finds the potential of fused (L-MOD13Q1) in crop yield prediction by comparing its accuracies with the non-fused (MOD13Q1) product in 2019. The study obtains higher crop yield accuracy with the L-MOD13Q1 ($R^2 = 0.81$ and $RMSE = 3.91$ dt/ha) than the MOD13Q1 ($R^2 = 0.70$ and $RMSE = 4.77$ dt/ha) irrespective of the crop type (Figure 4.6a,b). It proves the importance of high-resolution synthetic data for accurate modelling of crop yields.

After generating the long-term crop yield time series, the research finds the significant yearly performance of the model for both WW and OSR; however, some years obtained higher accuracy than the others. For example, 2007, 2018, and 2019 are the most accurate years, with R^2 values of more than 0.79 for both crop types. However, the RMSEs of both 2018 and 2019 are relatively higher (>4.74 dt/ha) than in the other years. Similarly, 2011 and 2016, with a higher number of N (~6), result in lower crop yield accuracy than 2007, 2008, and 2011 ($N = \sim 8$). This might be due to the impact of climate variables inputted into the LUE model (discussed briefly in Section 4.4.3).

The study discusses briefly how the quality of the input data fusion product impacts the accuracy of the CGM. For example, due to the low quality of synthetic NDVI products in 2001, 2002, and 2012, which might impact the accuracy of the input FPAR products generated, the yield prediction accuracy of both WW and OSR is low. The analysis tries to prove that even though synthetic time series would be the preferable solution to input a CGM for yield prediction when the quality of the combined fusion product is low, it could negatively affect the crop yield estimation. In relevance to the above point, high positive correlations have been seen when the accuracies of the synthetic NDVI time series are plotted with the accuracies of modelled crop yield from

2001 to 2019 for WW ($R = 0.81$) and OSR (0.77). For example, the quality of the NDVI time series for the years 2016 and 2018 is higher with $R^2 (>0.73)$, and the crop yield accuracies are also higher with R^2 of 0.83 (WW)/0.81 (OSR), 0.85/0.83, respectively (Figure 4.3p,r). Similarly, the striped data collected from Landsat 7 in 2012 has deteriorated the quality of the synthetic NDVI product ($R^2 = 0.51$; RMSE = 0.13), which further negatively affected the crop yield estimations for WW ($R^2 = 0.62$; RMSE = 5.40 dt/ha) and OSR ($R^2 = 0.49$; RMSE = 4.13 dt/ha) (Figure 4.3l). Moreover, the Landsat images were available at different times of the year. This has an impact on the prediction accuracy of both crops. For example, the WW yield results are more accurate than the OSR because the synthetic data in late spring and early summer (DOYs 113 to 193) is usually more precise.

The study compares the long-term crop yield time series by calculating the average percent change from the referenced and modelled yields for both crop types. Previous studies found that the elevation plays a significant role in impacting the regional crop yield (Bhatt, Maskey, Babel, Uhlenbrook, & Prasad, 2014; Thomson et al., 2002). Most of the studies found lower crop productivity at higher elevations due to complex topography, different climates, and management practices (Anderson et al., 2016; Semwal & Maikhuri, 1996). Moreover, the cropping intensity at lower elevations is higher as compared to the higher elevations. The survey finds negative correlations between the mean regional elevations and the crop yields of WW (-0.30) and OSR (-0.38). The model is precarious in specific regions, especially the districts at higher elevations in the south (Bavarian Alps) and east (Bavarian Forest and Fichtel Mountains) of Bavaria for both WW and OSR. In regions such as Regen, Freyung-Grafenau, Bad Tölz-Wolfratshausen, and Garmisch-Partenkirchen, the model highly overestimates the crop yield, and for regions such as Oberallgäu, Miltenberg, Deggendorf, and Dachau, it underestimates the yield as compared to the referenced yield for WW. This overestimation of WW yield values has resulted in a decrease in accuracy. The model shows yearly stability in predicting crop yields of WW between 65 and 80 dt/ha for most of the regions. The positive yield percent change (where the model underestimated the

crop yield) between 0 and 4% had higher accuracy ($R^2 > 0.80$) as compared to the percent change between -4 and 0% ($R^2 < 0.70$). For 48 of the 71 total districts, the model performs relatively well, with a percent change between -2% and +2%. However, unlike WW, both the over- and underestimation-yield values have resulted in a similar increase and decrease in the accuracy of OSR. The positive and negative yield percent change (where the model under- and over-estimates the crop yield, respectively) between 0 and +/-4% had an accuracy of more than 0.80. For OSR, the model overestimates the yield for Aichach-Friedberg, Deggendorf, Dingolfing-Lindau, Traunstein, Unterallgäu, Dachau, Rottal-Inn, Miltenberg, and Günzberg and underestimates the yield for Roth, Regen, Kronach, Kitzingen, and Bad Tölz-Wolfratshausen. However, for the 27 districts with OSR, the model performs steadily. Interestingly, the regions where the model's performance went unstable were primarily located in the southern alps, except for Regen, Freyung-Grafenau, Kitzingen, Roth, and Miltenberg. The reason could be the instability of the model at higher elevations or the bad quality of the synthetic NDVI products in specific districts. The quality of the synthetic NDVI product might vary for these regions as the districts have no horizontal or vertical overlay of Landsat scenes within the path row, limiting their coverage frequency.

4.4.3. Sensitivity Analysis

Besides the impact of data fusion, climate variables play an essential role in affecting the accuracy of crop yield predictions (Cabas et al., 2010; Dhillon, Dahms, Kuebert-Flock, et al., 2023; Sidhu et al., 2023). To analyse the impact of climate elements, the study performs sensitivity analysis, where the LUE model calculates the crop yields of WW and OSR without including the climate stress factors from 2001 to 2019. As the referenced yield is already influenced by the climate, the results of the study show that the accuracy of crop yield predictions worsens with the exclusion of climate variables, with a lower R^2 (0.68 (WW)/0.74 (OSR)) and a higher RMSE (5.88/3.41 dt/ha). However, an increase in R^2 (0.79/0.86) and decrease in RMSE (4.51/2.57 dt/ha) have been seen when the climate effect is included in the model. As the relationship between climate and crop yield undergoes significant shifts, it might be the reason that some years (2011 and 2016) with higher N (8) obtained lower crop yield accuracy than years (2007, 2018 and 2019) with comparably lower N (6). Moreover, our previous study, which made use of the

machine learning approach with the LUE model, identified the impact of every individual climate element used in crop yield predictions (Dhillon, Dahms, Kuebert-Flock, et al., 2023).

Furthermore, many studies stated that the availability of coarse climate data negatively affected yield prediction accuracy. In a previous study, the coarse spatial resolution of climate data (ECMWF: ~80 km) used to estimate the biomass resulted in low R^2 and high RMSE using CGMs by inputting coarse synthetic NDVI products (Dhillon et al., 2020; Shi et al., 2007). However, while inputting high spatial resolution NDVI products, the low impact of the high spatial resolution of climate elements is observed. The present study inputs high spatial resolution climate data time series (2 km, daily) to the LUE model, resulting in stable yearly accuracies from 2001 to 2019. Notably, selecting climate thresholds according to the geographical location and crop types is essential in achieving high crop yield accuracy (Grace; John R. Porter & Gawith, 1999; J. R. Porter & Moot). Different climate thresholds are used for WW and OSR, resulting in accurate and stable yield predictions in Bavaria during the study period.

4.4.4. Validation at the District Level

The crop yield validation for the more extended time series of 2001 to 2019 is performed using the LfStat crop yield data (used for validation at a 95% confidence interval) for WW and OSR provided by the Bavarian State Office of Statistics. As the validation data set is provided at a regional scale, pixel-based yield information is converted for both crop types to the regional level. However, transferring the field-based information to the district level could result in some uncertainties in the validation process. For example, in some regions of southern Bavaria (Bad Tölz-Wolfratshausen, Garmisch-Partenkirchen, Traunstein, Unterallgäu, and Oberallgäu), where the model's performance is volatile, this might be due to the uncertainty occurring while transferring the pixel-level information to the district level. The availability of fewer fields of WW and OSR in those regions might be the reason for the model's instability, as the validation data recorded high yield values for the same districts. Therefore, future work should aim to validate crop yield results at the field level, which could help achieve

more precise results. Additionally, the availability of field data for FPAR, an important input to the LUE model, would help to validate the FPAR product generated using the NDVI time series.

4.5. Conclusions

The present study investigates the relationship of spatiotemporal fusion modelling using STRAFM on crop yield prediction for winter wheat (WW) and oil-seed rape (OSR) using a semi-empirical light use efficiency (LUE) model for Bavaria, Germany, from 2001 to 2019. The research paper concludes the findings as follows:

- (i) To find the potential of STARFM for long-term time series, the paper generates and validates a synthetic normalised difference vegetation index (NDVI) time series blending the high spatial resolution (30 m, 16 days) of Landsat 5 Thematic Mapper (TM) (2001 to 2012), Landsat 7 Enhanced Thematic Mapper Plus (ETM+) (2002), and Landsat 8 Operational Land Imager (OLI) (2013 to 2019) with the coarse resolution of MOD13Q1 (250 m, 16 days) from 2001 to 2019. Overall, the average accuracy of data fusion for nineteen years has an R^2 of 0.66 and an RMSE of 0.11. The accuracy of data fusion is found to be dependent on the number of Landsat scenes available per year (N). The higher the N , the more accurate is the synthetic NDVI time series per year.
- (ii) To investigate the stability and precision of the LUE model in crop yield prediction, the paper inputs the synthetic NDVI time series and climate elements to the crop model to estimate and validate yearly crop yields for WW and OSR from 2001 to 2019. The validation of crop yield at regional scale results in an average R^2 of 0.79 (WW)/0.86 (OSR) and an RMSE of 4.51 dt/ha/2.46 dt/ha, respectively.
- (iii) Identifying the impact of the input data fusion product on the accuracy assessment of the LUE model, high positive correlations are seen when the accuracies of the synthetic NDVI time series are plotted with the accuracies of modelled crop yield from 2001 to 2019 for WW ($R = 0.81$) and OSR (0.77).

The present study recommends validating crop yields at the field scale, as transferring the pixel-based information to the district level could cause uncertainties in the validation process. The accurate crop yield predictions from the analysis for WW and OSR could be further used for the application of biodiversity, where the impact of land use diversity on crop yields could be estimated. The ease of using spatiotemporal modelling with crop growth models would not be limited to Bavaria. The study's methodology could also be tested by coupling machine/deep learning (ML/DL) approaches with CGMs, which might help to include more climate elements to achieve more precise results. Lastly, the study's two decades of accurate yield estimations could strengthen trust in the decision(/policy) making to achieve sustainability in agriculture.

Chapter 5

This chapter is a verbatim reproduction (except the figure and table numbers) of the paper:

Integrating Random Forest and Crop Modelling Improves the Crop Yield Prediction of Winter Wheat and Oil Seed Rape

Dhillon, M. S., Dahms, T., Kuebert-Flock, C., Rummler, T., Arnault, J., Stefan-Dewenter, I., & Ullmann, T. (2023). Integrating random forest and crop modelling improves the crop yield prediction of winter wheat and oil seed rape. *Frontiers in Remote Sensing*, 3, 109.

Published in *Frontiers in Remote Sensing*

Abstract

The fast and accurate yield estimates with the increasing availability and variety of global satellite products and the rapid development of new algorithms remain a goal for precision agriculture and food security. However, the consistency and reliability of suitable methodologies that provide accurate crop yield outcomes still need to be explored. The study investigates the coupling of crop modelling and machine learning (ML) to improve the yield prediction of winter wheat (WW) and oil seed rape (OSR) and provides examples for the Free State of Bavaria (70,550 km²), Germany, in 2019. The main objectives are to find whether a coupling approach (Light Use Efficiency (LUE) + Random Forest (RF)) would result in better and more accurate yield predictions compared to results provided with other models not using the LUE. Four different RF models (RF1 (input: NDVI), RF2 (input: climate variables), RF3 (input: Normalized Difference Vegetation Index (NDVI) + climate variables), RF4 (input: LUE generated biomass + climate variables), and one semi-empiric LUE model were designed with different input requirements to find the best predictors of crop monitoring. The results indicate that the individual use of the NDVI (in RF1) and the climate variables (in RF2) could not be the most accurate, reliable, and precise solution for crop monitoring; however, their combined use (in RF3) resulted in higher accuracies. Notably, the study suggested the coupling of the LUE model variables to the RF4 model can reduce the relative root mean square error (RRMSE) from -8% (WW) and -1.6% (OSR) and increase the R² by 14.3% (for both WW and OSR), compared to results just relying on LUE. Moreover, the research compares models yield outputs by inputting three different spatial inputs: Sentinel-2(S)-MOD13Q1 (10 m), Landsat (L)-MOD13Q1 (30 m), and MOD13Q1 (MODIS) (250 m). The S-MOD13Q1 data has relatively improved the performance of models with higher mean R² (0.80 (WW)/0.69 (OSR)), and lower RRMSE (%) (9.18, 10.21) compared to L-MOD13Q1 (30 m) and MOD13Q1 (250 m). Satellite-based crop biomass, solar radiation, and temperature are found to be the most influential variables in the yield prediction of both crops.

5.1. Introduction

Accurate crop monitoring in response to climate change at a regional scale plays a significant role in developing agricultural policies, improving food security, forecasting, and analysing global trade trends (Jeong et al., 2016). The emergence of new technologies, such as simulation crop growth models (CGMs) and machine learning (ML), to synthesize and analyse large-scale data with high computing performance has increased the ability to accurately predict crop yields (Archontoulis et al., 2020; Bogard et al., 2020; Ersoz, Martin, & Stapleton, 2020; Shahhosseini, Hu, & Archontoulis, 2020; Washburn, Burch, & Franco, 2020). These technologies have each provided unique capabilities and significant advancements in prediction performance; however, they have been mainly assessed separately, and there may be benefits in integrating them to increase further prediction accuracy (Daw, Karpatne, Watkins, Read, & Kumar, 2017; Shahhosseini, Hu, Huber, & Archontoulis, 2021).

Since the 1960s, CGMs have reached a high degree of success in simulating the behavior of real crops (i.e., by predicting their final state of total biomass or harvestable yield) (Dhillon et al., 2020). CGMs are a set of mathematical equations pre-trained using a diverse set of experimental data from various environments and are further refined (or calibrated) for more accurate predictions in each study (Kasampalis et al., 2018). They are increasingly applied as tools for decision-making and research, providing quantitative and temporal information on plant growth and development by including the effect of various climate variables (Mirschel et al., 2004; Murthy, 2004). Because CGMs lack spatial information, many studies have used them for forecasting applications by integrating them with remote sensing (RS) data (Clevers et al., 2002). The RS technology provides synoptic, timely, repetitive, and cost-effective information about the surface of the earth (Ali et al., 2022; Justice et al., 2002); however, the cloud and shadow gaps in the optical satellite data can hinder or limit CGMs from producing accurate yield results (Gevaert & García-Haro, 2015; David P. Roy et al., 2008). To fill the data gaps, many studies have successfully used multitemporal data fusion, combining the data obtained from two different sensors of different spatial and temporal scales

(Benabdelouahab et al., 2019; Dhillon et al., 2020; Htitiou et al., 2019; Lebrini et al., 2020). Due to its public availability of code and simplicity of usage, the spatial and temporal adaptive reflectance fusion model (STARFM) (F. Gao et al., 2006) is widely used in the literature to combine Landsat or Sentinel-2 with the Moderate Resolution Imaging Spectroradiometer (MODIS) (Cui et al., 2018; Lee et al., 2019; Xie et al., 2016; L. Zhu et al., 2017). Numerous studies successfully utilized the multi-temporal data fusion for deriving the leaf area index (LAI), or fraction of absorbed photosynthetic active radiation (FPAR) obtained from vegetation indices, e.g., the normalized difference vegetation index (NDVI), in combination with CGMs to estimate crop biomass or yield in different study regions around the world (Bhandari et al., 2012; Hwang et al., 2011). Similarly, many studies have compared the performance of different CGMs by implementing them on the same crop and in the same study region (Dhillon et al., 2020; Eitzinger, Trnka, Hösche, Žalud, & Dubrovský, 2004). For example, in the preceding work, we compared five CGMs for simulating the biomass of selected winter wheat (WW) fields in the federal state of Mecklenburg-West Pomerania in northeast Germany. We found that the AquaCrop and semi-empiric Light Use Efficiency (LUE) are highly applicable and precise than the WOFOST, CERES-Wheat, and CropSyst (Dhillon et al., 2020).

Even though CGMs have a reasonable prediction accuracy, they are not readily applicable due to the data calibration requirements, long runtimes, and data storage constraints (Drummond et al., 2003; Puntel et al., 2016; Shahhosseini et al., 2019). Moreover, their specified designs restrict them to considering only limited climate parameters, whereas the other essential climate elements were neglected, which might benefit from further increasing the prediction accuracy. On the other hand, ML models can deal with linear and nonlinear relationships by obtaining quality results with lower runtimes – plus, they can input a vast range of climate elements, likely positively affecting the accuracy of crop yields (De'ath & Fabricius, 2000). Moreover, they are easy to implement as they usually provide a less complex calibration and have fewer data storage constraints (Shahhosseini et al., 2019). Numerous ML algorithms (such as linear regression, decision tree, relevance vector machines (RVM), and random forest (RF)) were applied to the RS data for various applications like flood mapping or detection and

prediction of agronomic variables (Basso & Liu, 2019; Haque et al., 2020; Khaki & Wang, 2019; Khaki et al., 2020; Sharifi, 2020, 2021). Exemplary, the RF is a non-parametric advanced classification and regression tree (CART) analysis method that has been researched widely in many scientific fields. Most applications of RF have been focused on its utility as a classification tool with only limited studies exploring its regression capabilities for predicting crop yields (Fukuda et al., 2013; Mutanga et al., 2012; Vincenzi et al., 2011). However, some studies found that the RF could overfit data, making it unstable for crop yield estimation (Breiman, 2001; Segal, 2004). Moreover, RF could partially depend on variables of less importance that might affect the prediction accuracy negatively (Jeong et al., 2016). Therefore, coupling ML models with CGMs could be tested by training an RF model with the output of a crop model so that the RF can have the potential of overfitting issues within the range of training data.

Many studies have combined CGMs with simple regression models; however, to our knowledge, there are rare studies systematically investigating the effect of coupling ML and CGMs (Shahhosseini et al., 2021). The present study hypothesized that merging CGMs with ML models will improve yield prediction accuracy by combining the spatial crop biomass output of the LUE model (considered the most accurate, precise, and reliable by literature (Dhillon et al., 2020)) with the RF model for WW and oil seed rape (OSR) in Bavaria. For this study, different RF models (RF1 (input: NDVI), RF2 (input: climate variables), RF3 (input: Normalized Difference Vegetation Index (NDVI) + climate variables), RF4 (input: LUE generated biomass + climate variables), and one semi-empiric LUE model were designed with different input requirements to find the best predictors of crop monitoring. In addition, the study investigates the accuracy of model outputs based on the spatial resolution of the RS products (without cloud and shadow gaps) inputting two STARFM-derived synthetic NDVI products (Landsat (L)-MOD13Q1 (30 m, 8-days) and Sentinel-2 (S)-MOD13Q1 (10 m, 8-days) and one real NDVI product (MOD13Q1 (250 m, 8-days)) (Dhillon et al., 2022). The specific research objectives include:

- (i) Explore whether only NDVI (RF1) or climate elements (RF2) or both NDVI and climate elements (RF3) are the best predictors of crop monitoring using RF models;
- (ii) Investigate the performance of LUE alone and its coupling with RF (RF4) for crop yield prediction of WW and OSR;
- (iii) Highlight the effect of different spatial scales (10 or 30 or 250 m) for crop yield estimation.

5.2. Materials and Methods

The study's general workflow shows the input criteria for four different RF models (RF1, RF2, RF3, and RF4) and one LUE model designed to calculate the crop yield for Bavaria in 2019 (Figure 5.1). All RF models are trained with 70% and tested with 30 % of the crop yield data available at the regional level for both WW and OSR from the legal authorities ((i.e. Bayerisches Landesamt für Statistik (LfStat)). Two synthetic (L-MOD13Q1: 30 m and 8-day; S-MOD13Q1: 10 m and 8-day) and one real-time (MOD13Q1: 250 m and 8-day) satellite NDVI time series (completed in preceding work (Dhillon et al., 2022)) is used as an input criterion for the RF and LUE models. The input NDVI and the climate data are selected for the respective start of the season (SOS) and end of the season (EOS) for WW and OSR in 2019.

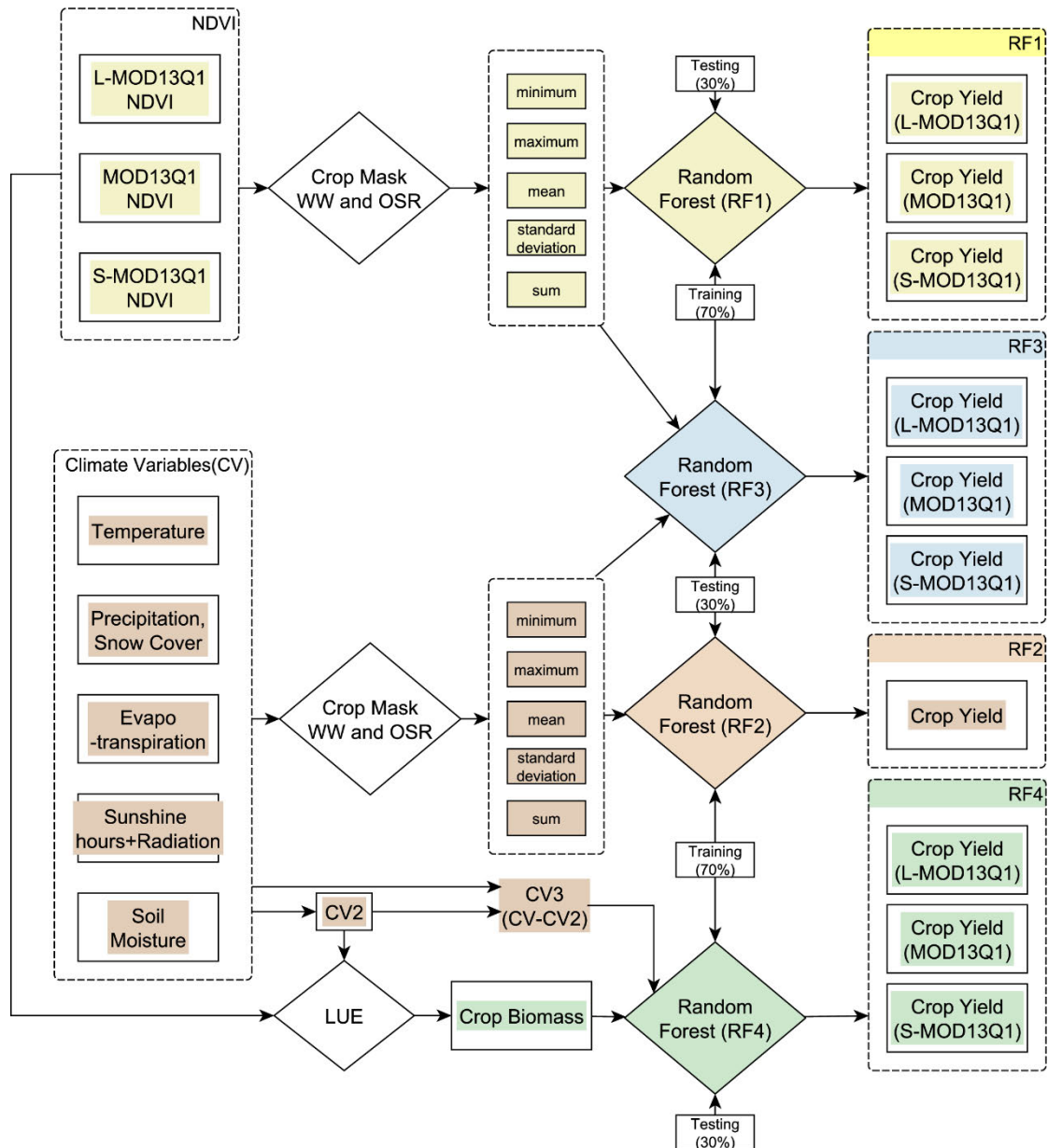


Figure 5.1. Conceptual framework of the study that explains the methodology of four random forest (RF1, RF2, RF3 and RF4) models with different input requirements to predict crop yield for winter wheat (WW) and oil seed rape (OSR). The semi-empiric light use efficiency (LUE) model is coupled with the RF4 model. CV belongs to climate variables and CV2 are the set of CV required by the LUE model. CV3 (CV minus CV2) are the set of CV required by the RF4 model. Landsat(L)-MOD13Q1, Sentinel-2(S)-MOD13Q1, and MOD13Q1 are the satellite inputs (generated by (Dhillon et al., 2022)).

Firstly, the pixel level satellite and climate inputs are masked out for every field of every region of Bavaria using the InVeKos data (source: www.ec.europa.eu/info/index_en, accessed on 21 June 2021) for WW and OSR. Secondly, the spatiotemporal-metrics (STMs) (such as minimum, maximum, mean, standard deviation (sd) and sum) for pixel-based time series (between the SOS and the

EOS of WW and OSR) are calculated for every field. Then the field values are integrated at a regional level.

The STMs of NDVI data and climate elements are inputted into respective RF models in the following steps. The NDVI is the only spatial input for the RF1, whereas the yield output of the model is tested at different spatial resolutions of 10, 30 and 250 m. Similarly, the climate variables (CV) are used as input for the RF2 model. The RF3 model combines satellite NDVI and CV and tests the yield prediction at different spatial scales. Prior to that, LUE model results of crop yield are generated by inputting NDVI data and climate elements (CV2) required by the model. In the last steps, the LUE model (crop biomass as an input) is linked with the RF4 model. As CV2 is already inputted in the LUE model, for RF4, CV3 (CV2 are subtracted from the CV) is used as an input. The study's main objective is to test the performance by coupling the crop simulation model and machine learning; therefore, the LUE model is coupled with the RF4 model, and the crop yield performance is tested for different satellite products.

All RF models are trained with 70% and tested with 30 % of the crop yield data available at the regional level for both WW and OSR from the legal authorities (i.e. Bayerisches Landesamt für Statistik (LfStat)). Two synthetic (L-MOD13Q1: 30 m and 8-day; S-MOD13Q1: 10 m and 8-day) and one real-time (MOD13Q1: 250 m and 8-day) satellite NDVI time series (completed in preceding work (Dhillon et al., 2022)) is used as an input criterion for the RF and LUE models. The input NDVI and the climate data are selected for the respective start of the season (SOS) and end of the season (EOS) for WW and OSR in 2019.

5.2.1. Study Area

The study region is the federal state of Bavaria located between 47°N and 50.5°N, and between 9°E and 14°E, in the southeastern part of Germany (Figure 5.2). The climate of the region is influenced by the region's topography, with higher elevations in the south (northern edge of the Alps) and east (Bavarian Forest and Fichtel Mountains). The mean annual precipitation sums range from approx. 500 to above 3100 mm, with wetter conditions in the southern parts of Bavaria. The mean annual temperature ranges from -3.3 to 11°C, but in most the regions, the temperature ranges between 8 and 10°C (Dhillon

et al., 2022). As the largest state in Germany, Bavaria covers an area of approx. 70,500 km², covering almost one-fifth of Germany. The federal state is divided into 96 counties with 71 rural districts (so-called “Landkreise”) and 25 city districts (so-called “Kreisfreie Städte”). For the year 2019, the landcover of Bavaria covers 31.56% of the area under agriculture Data (Dhillon et al., 2022).

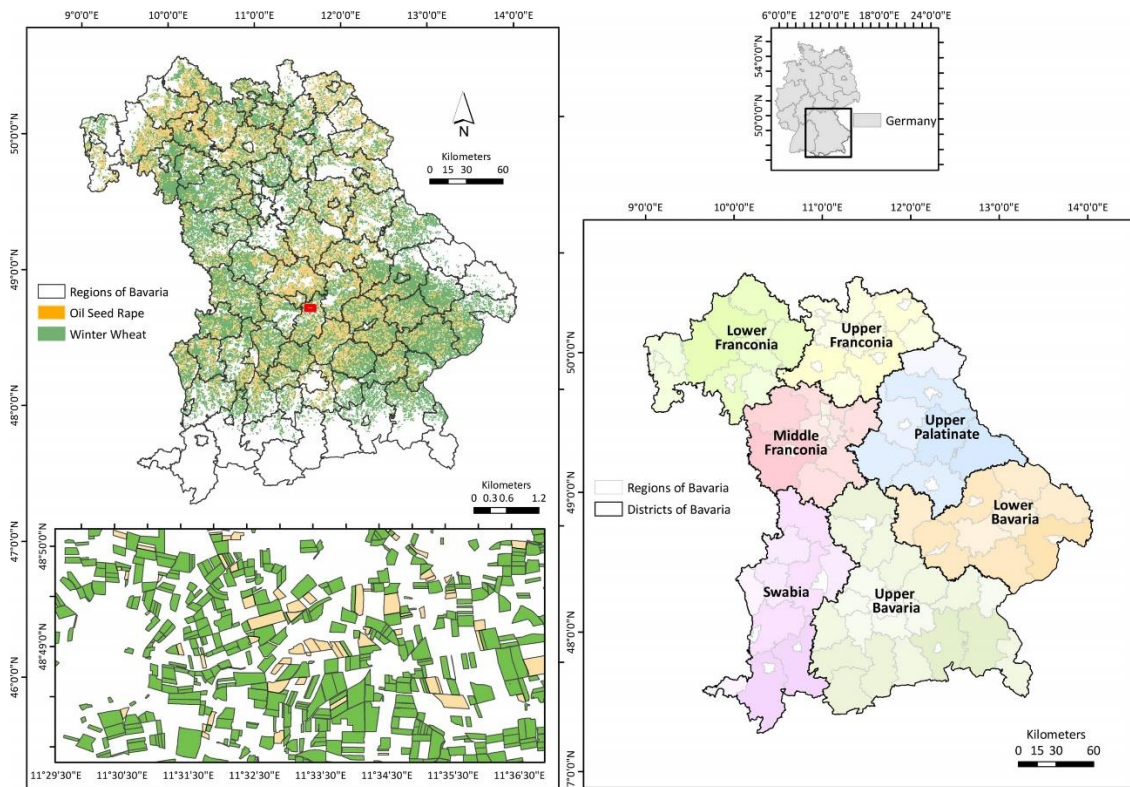


Figure 5.2. Overview of the study region with spatial information of Winter Wheat (WW) and Oil Seed Rape (OSR) fields (left). The dark green color shows the fields of WW and dark orange shows the fields of OSR in 2019. The enlargement (displayed with a dark red box on the top left map) shows the detailed version of WW and OSR fields. The bottom right map shows the different districts with their administrative zones in Bavaria.

The study investigates the importance of 8-day temporal satellite data with different spatial resolutions and climate data of several meteorological parameters in crop yield prediction. The updated InVeKos data (of 2019) is used to obtain the reference field information of WW and OSR for every district of Bavaria. Table 5.1 briefly describes the user data and indicates the spatial and temporal resolutions.

Table 5.1. Summary of collected datasets for Winter Wheat (WW) and Oil Seed Rape (OSR) crop modelling.

| Data | Product Name | Resolution
Spatial, Temporal | References |
|----------------|---|---------------------------------|---|
| Climate data | Tmax, Tmin, Tdew, Rs, Ra,
N, Sm, E, RO, P, RH,n,
WS,DP,Snow | 2000 m, 8-days | https://www.uni-augsburg.de/de/fakultaet/fai/geo/
(accessed on 21 June 2021) |
| | L-MOD13Q1 | 30 m, 8-days | (Dhillon et al., 2022) |
| Satellite data | S-MOD13Q1 | 10 m, 8-days | (Dhillon et al., 2022) |
| | MOD13Q1 | 250 m, 8-days | www.lpdaac.usgs.gov
(accessed on 21 June 2021) |
| Vector data | InVeKos | 2019 | www.ec.europa.eu/info/index_en
(accessed on 21 June 2021) |
| | Landesamt crop yield | 2019 | https://www.statistikdaten.bayern.de/geoneis/online/
(accessed on 21 June 2021) |

5.2.2. Satellite Data

The present study used two synthetic (L-MOD13Q1 (30 m, 8-days) and S-MOD13Q1 (10 m, 8-days)) and one real-time (MOD13Q1 (250 m, 8-days)) NDVI time series, which were generated in preceding work by (Dhillon et al., 2022)) as an input to the RF and LUE models. In the synthetic NDVI products, the cloud and shadow gaps in the real-time Sentinel-2 and Landsat data for 2019 were filled using the spatial and temporal adaptive reflectance fusion model (STARFM), which blends the coarse spatial resolution of MODIS and high spatial resolution of Landsat/Sentinel-2 data. In addition, the MOD13Q1 V6 product (just the MODIS NDVI time series without image fusion) is also selected as an input to the RF and LUE models to allow the comparison of crop yield outputs at high (10 m), medium (30 m) and coarse (250 m) spatial scales. The 8-day time series for the RS products are considered starting at the day of the year (DOY) 1 (1 January) till 353 (19 December) for 2019. For crop modelling and machine learning algorithms, this study inputs the 8-day satellite datasets from the stem elongation phases till the flowering stages of both WW and OSR. For OSR, the SOS is 15th February, and the EOS is 20th April 2019 (Zamani-Noor & Feistkorn, 2022). And for WW, the SOS and EOS period lies between 15th of April to 31st of June 2019 (Harfenmeister et al., 2021).

5.2.3. Climate Data

For input to the RF and LUE models, the climate data for 2019 with daily temporal resolution includes 80 variables considering the sum, mean, maximum, minimum, and standard deviation (sd) for each variable during the time frame. The climate variables

included are maximum (T_{\max} , °C), minimum (T_{\min} , °C) and dew point (T_{dew} , °C) temperature, solar radiation (R_s , $\text{MJm}^{-2}\text{day}^{-1}$), sunshine hours (N , hours), relative sunshine duration (n , hours), precipitation (P , mm), soil moisture (S_m , mm), relative humidity (RH , %), wind speed at 2 m height (WS , ms^{-1}), runoff (RO , mm), deep percolation (DP , mm), snow cover (S_{snow} , mm), extra-terrestrial radiation (R_a , $\text{MJm}^{-2}\text{day}^{-1}$), Sublimation (S_{sublim} , mm) and evapotranspiration (E , mm). The CV were obtained by dynamical downscaling the ERA5 reanalysis dataset (Hersbach et al., 2020), provided by the European Centre for Medium-Range Weather Forecasts, to a horizontal grid resolution of 2000 m using the hydrologically enhanced Weather Research and Forecasting model (Gochis et al., 2018; Skamarock et al., 2019). A detailed description of the selected downscaling approach is provided by (Arnault et al., 2018) and (Rummler et al., 2019). For this research, the daily climate data is aggregated into 8-days' temporal products and adapted to the RF and LUE models. Like the satellite data, the present study considers the 8-day climate data for the same SOS and EOS for WW and OSR as described in the section 2.1.1.

5.2.4. InVeKos Data

The InVeKos data is field-based data used to identify the fields of WW and OSR in 2019. The data is collected through the Integrated Administration Control Systems (IACS) that is available for all agricultural plots in the European Union (EU) countries by allowing farmers to graphically indicate their agricultural areas. In the IACS, EU countries are responsible for administering and controlling payments to farmers through a principle called shared management.

5.2.5. Bayerisches Landesamt für Statistik (LfStat) Crop Yield Data

The LfStat crop yield is a database that provides crop yield of 29 crop categories including WW and OSR in Bavaria at a regional level (Statistics Code: 41241). In this study, LfStat crop yield data of WW (total number of observations (n)=65 and OSR (n =50)) is used for training (70%) and testing (30%) the RF models and for validating the LUE model (100%), respectively (see Figure 5.1).

5.2.3. Method

5.2.3.1. LUE Model

The study used the semi-empiric LUE model based on the principle of light use efficiency theory (J. L. Monteith, 1972; John Lennox Monteith, 1977). As it is proven to be reliable, precise, and accurate, this study used the same approach to calculate crop yield and biomass as adopted by (Dhillon et al., 2020). The model monitors the growth of WW and OSR by assessing the impact of climate variables over a period of 8-days between their respective SOS and EOS and calculates the crop biomass as a cumulative sum. The climate variables used by the LUE model are (CV2) T_mean, T_max, T_dew, Rs, and RH. The model is based on a semi-empirical approach and calculates the aboveground biomass as a cumulative sum between the stem elongation phase till the flowering stage of both WW and OSR (Equation 1),

$$\text{Biomass} = \sum_{\text{SOS}}^{\text{EOS}} (\text{PAR} * \text{FPAR}) * \epsilon \quad (5.1)$$

where PAR is photosynthetically active radiation ($\text{MJ m}^{-2} \text{d}^{-1}$), FPAR is the fraction of PAR absorbed by the canopy, and ϵ is the actual light-use efficiency (g C M J^{-1}). The total aboveground biomass calculated by the LUE model is equivalent to the net primary productivity (NPP) ($\text{kg ha}^{-1} \text{yr}^{-1}$) (Gitelson et al., 2012; J. L. Monteith, 1972). The detailed stepwise procedure of the LUE model is explained in (Dhillon et al., 2020).

5.2.3.2. Random Forest (RF) Model

The study trained and used four RF models (RF1, RF2, RF3, and RF4) (see Figure 5.1), binary-bias machine-learning methods, to predict crop yields for WW and OSR. RF can be used for classification and regression purposes and this study used it as a regression tool. The RF model is trained by many classification and regression trees (CARTs) that are grown with a random subset of predictors. Many random trees are generated when the source data for the model is bootstrapped and, finally, the forest (group of random trees) of the CART is averaged. A more detailed explanation of the model is provided by (Breiman, 2001). The study used the 'randomForest' package in the software R for each RF model (Liaw & Wiener, 2002; Team, 2013) (Table 4.2). The value of mtry has been approximately considered by dividing the total number of

predictors by 3. A variable analysis tool from the randomForest package analyses the variable importance. The mean decrease accuracy is used as a measure of variable importance. The out-of-bag (OOB) performance estimation is analysed for assessing the performance by averaging the node's mean decrease accuracy before and after permuted.

Table 5.2. Input requirements of different Random Forest (RF) models (RF1, RF2, RF3 and RF4) implemented using the package 'randomForest' in the software R. CV represents to climate variables.

| Model | mtry | ntree | nodesize | Number of samples (n) | Training and Testing | Input |
|-------|------|-------|----------|-----------------------|----------------------|--|
| RF1 | 1 | 500 | 5 | WW: 65, OSR: 50 | 70% and 30% | NDVI (mean, max, min, sd and sum) |
| RF2 | 27 | 500 | 5 | WW: 65, OSR: 50 | 70% and 30% | CV (mean, max, min, sd and sum) |
| RF3 | 29 | 500 | 5 | WW: 65, OSR: 50 | 70% and 30% | NDVI (mean, max, min, sd and sum) + CV (mean, max, min, sd and sum) |
| LUE | - | - | - | WW: 65, OSR: 50 | Only Testing (100%) | NDVI (mean, max, min, sd and sum) + CV2 (mean, max, min, sd and sum) |
| RF4 | 17 | 500 | 5 | WW: 65, OSR: 50 | 70% and 30% | LUE Biomass + CV3 (mean, max, min, sd and sum) |

5.2.3.3. Statistical Analysis

The modelled crop yield data from four RF and LUE models are validated with the Landesamt district-wise yield data collected from the statistics department of Bavaria for the year 2019. From the modelled and referenced yield, the determination coefficient (R^2) (Equation (5.2)), mean error (ME), root mean square error (RMSE), and relative RMSE (RRMSE) (Equation (5.3), Equation (5.4) and Equation (5.5)) are calculated. The lower the value of ME, RMSE and RRMSE the better the model performed. This study considers RRMSE < 15% as good agreement; 15-30% as moderate agreement; and > 30% as poor agreement (Yang et al., 2014). A linear regression model (LRM) is performed to establish a linear relationship between the referenced and modelled yield of WW and OSR at different spatial scales (10, 30, and 250 m).

$$R^2 = \frac{(\sum(P_i - \bar{P})(O_i - \bar{O}))^2}{(\sum(P_i - \bar{P}))^2 (\sum(O_i - \bar{O}))^2} \quad (5.2)$$

$$ME = \frac{1}{n} \sum_{i=1}^n (O_i - P_i)^2 \quad (5.3)$$

$$RMSE = \sqrt{ME}, \quad (5.4)$$

$$RRMSE (\%) = \frac{RMSE}{\frac{1}{n} \sum_{i=1}^n O_i} * 100, \quad (5.5)$$

where P_i is the predicted value, O_i is the observed value, \bar{O} is the observed mean value, and n is the total number of observations. The significance of the used models is checked by analysing the probability value (p-value), which is calculated using the LRM with a H_0 that there is no correlation between the referenced and modelled yield, and an H_1 that the relationship exists. To perform this test, a significance level (called alpha (α)) is set to 0.05. A p-value of less than 0.05 shows that a model is significant, and it rejects the H_0 that there is no relationship.

5.3. Results

5.3.1. RF1: NDVI as the Only Predictor of Crop Yield Monitoring

With L-MOD13Q1, S-MOD13Q1, and MOD13Q1 NDVI inputs, the RF1 model performed significantly for WW and OSR (p-value < 0.05). The R^2 obtained from the S-MOD13Q1 NDVI product has a higher accuracy than the L-MOD13Q1 and MOD13Q1 (Figure 5.3). Based on the R^2 of different spatial resolutions of the NDVI products for WW and OSR, the RF models resulted in descending order as S-MOD13Q1 (10 m), L-MOD13Q1 (30 m), and MOD13Q1 (250 m), with R^2 values as 0.66/0.61, 0.66/0.50, and 0.60/0.26, respectively. For quality and precision, the ME and RMSE values give a more complete picture of the performance of RF with NDVI as the only predictor. The ME and RMSE of WW from MOD13Q1 (8.21 dt/ha and 10.30 dt/ha) are higher than that of L-MOD13Q1 (8.18 dt/ha and 10.20 dt/ha) and S-MOD13Q1 (5.65 dt/ha and 7.96 dt/ha), respectively (Figure 5.3a,c,e). Similarly, for OSR, S-MOD13Q1 has the lowest ME and RMSE of 2.76 dt/ha and 3.76 dt/ha, as compared to L-MOD13Q1 and MOD13Q1 (Figure 5.3b,d,f). Overall, the S-MOD13Q1 (RRMSE = 11.40 % (WW)/11.23% (OSR)) results are more accurate than L-MOD13Q1 (14.33%/12.28%) and MOD13Q1 (14.83%/14.32%) for both WW and OSR.

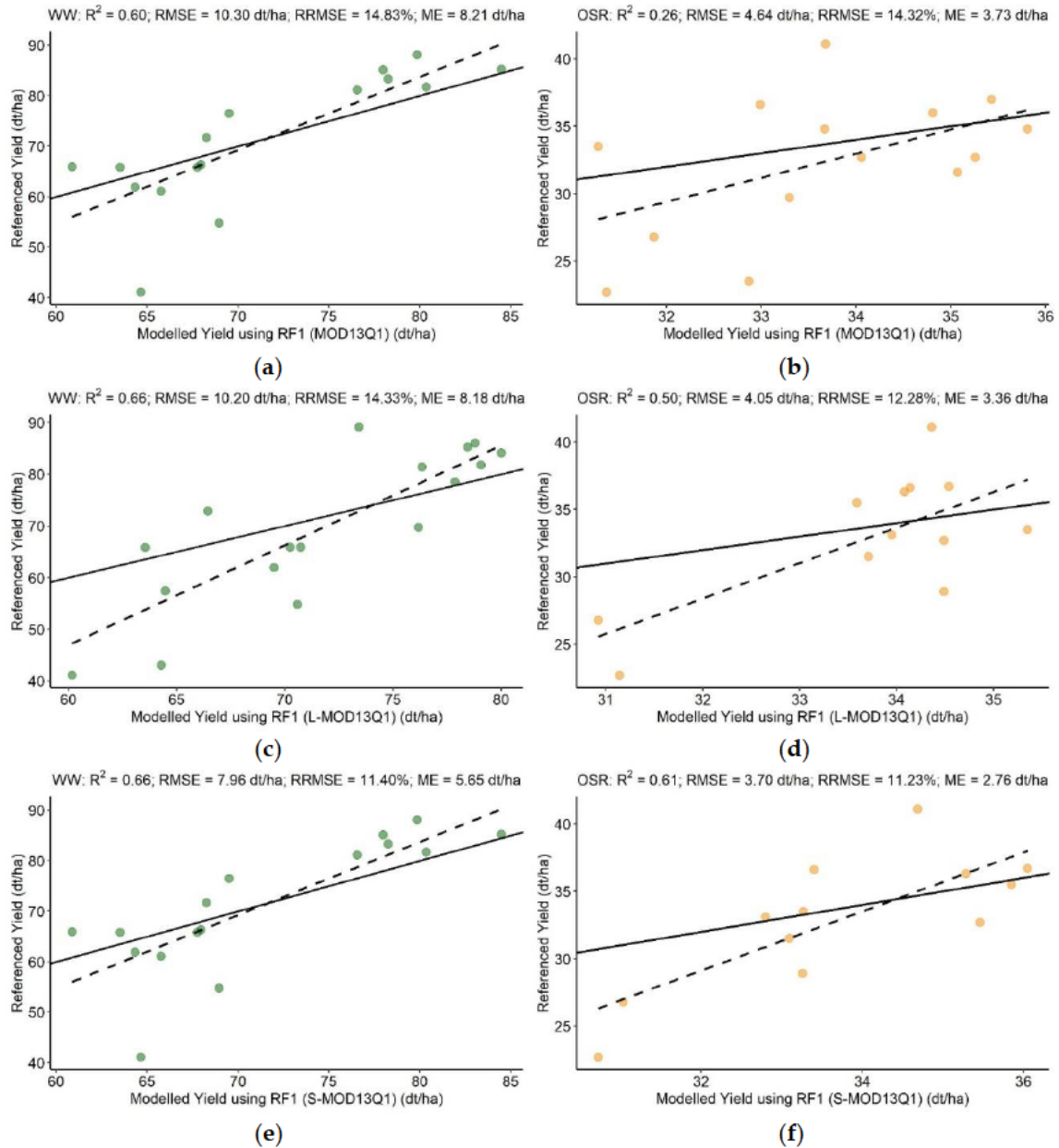


Figure 5.3. Scatter plots of the validation of WW and OSR modeled yield using RF1 model with referenced yield. The green dots represent WW, and the orange dots represent OSR. (a) MOD13Q1 (RF1(WW); just MODIS) versus referenced yield. (b) MOD13Q1 (RF1(OSR); just MODIS) versus referenced yield. (c) L-MOD13Q1 (RF1(WW); Landsat and MODIS) versus referenced yield. (d) L-MOD13Q1 (RF1(OSR); Landsat and MODIS) versus referenced yield. (e) S-MOD13Q1 (RF1(WW); Sentinel-2 and MODIS) versus referenced yield. (f) S-MOD13Q1 (RF1(OSR); Sentinel-2 and MODIS) versus referenced yield. Every plot contains a solid 1:1 line that is used to visualise the correlation between referenced and synthetic yield.

5.3.2. RF2: Climate Variables (CV) as the Only Predictors of Crop Yield Monitoring

With climate elements as input parameters, the RF2 model performed significantly for both WW and OSR (p -value < 0.05) (Figure 5.4a,b). The R^2 obtained for WW has shown a higher accuracy ($R^2 = 0.57$) than the OSR ($R^2 = 0.50$). However, the OSR (RMSE = 4.23 dt/ha) resulted in higher preciseness than the WW (RMSE = 10.60 dt/ha). Moreover, the RRMSE for WW shows moderate agreement (15.28%) between the observed and predicted yield. The CV importance for WW are mainly N, E, Ra, Tdew, Sm, and Rs; however, for OSR, Tmin, WS, Ra, Rs, and Snow are of high importance (Figure 5.4c,d).

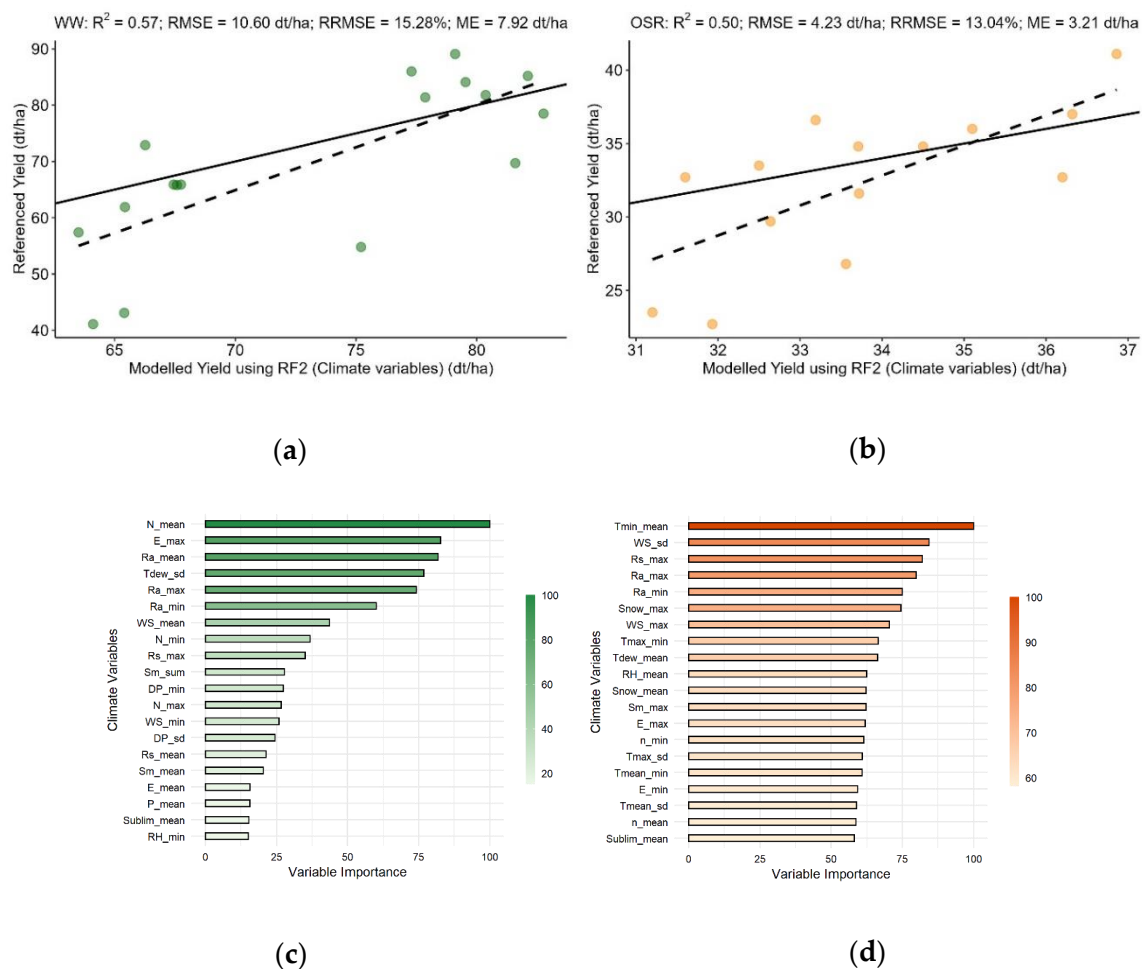


Figure 5.4. Scatter and bar plots of the validation of WW and OSR modeled yield with referenced yield and the variable importance using the RF2 model, respectively. The green color represents WW, and the orange color represents OSR. (a) RF2 (WW using climate variables (CV)) versus referenced yield. (b) RF2 (OSR using climate variables (CV)) versus referenced yield. (c) Variable importance for WW (d) Variable importance for OSR.

5.3.3. RF3: NDVI and CV Predictors for Crop Monitoring

With climate parameters and L-MOD13Q1, S-MOD13Q1, and MOD13Q1 NDVI inputs, the RF3 model performed significantly for WW and OSR (p -value < 0.05). The R^2 obtained from the S-MOD13Q1 NDVI product has a higher accuracy than the L-MOD13Q1 and MOD13Q1 (Figure 5.5). Based on the R^2 of different spatial resolutions of the NDVI products for WW and OSR, the RF models resulted in descending order as S-MOD13Q1 (10 m), L-MOD13Q1 (30 m), and MOD13Q1 (250 m), with R^2 values of 0.75 (WW)/0.66(OSR), 0.72/0.61, and 0.67/0.53, respectively. For quality and precision, the ME and RMSE values give a more complete picture of the performance of RF with NDVI as the only predictor. The ME and RMSE of WW from MOD13Q1 (5.56 dt/ha and 8.10 dt/ha) are higher than that of L-MOD13Q1 (5.45 dt/ha and 7.98 dt/ha) and S-MOD13Q1 (4.94 dt/ha and 7.56 dt/ha), respectively (Figure 5.5a,c,e). Similarly, for OSR, S-MOD13Q1 has the lowest ME and RMSE of 2.70 dt/ha and 3.78 dt/ha, as compared to L-MOD13Q1 (2.77 dt/ha and 3.85 dt/ha) and MOD13Q1 (3.11 dt/ha and 4.08 dt/ha) (Figure 5.5b,d,f). The RRMSE is decreased by -6.57% and -7.23% between S-MOD13Q1 (10.66% (WW) and 11.67% (OSR)) and MOD13Q1 (11.41% and 12.58%) for WW and OSR, respectively. The mean and sum of NDVI have a higher impact on the accuracy assessment of WW yield; however, NDVI has less impact on the crop yield prediction of OSR (Figure 6). Other than that, E, Ra, Sm, and N have a higher influence on WW's yield prediction (Figure 5.6a). For OSR, Snow, Temperature, and Sm have shown a higher influence (Figure 5.6b).

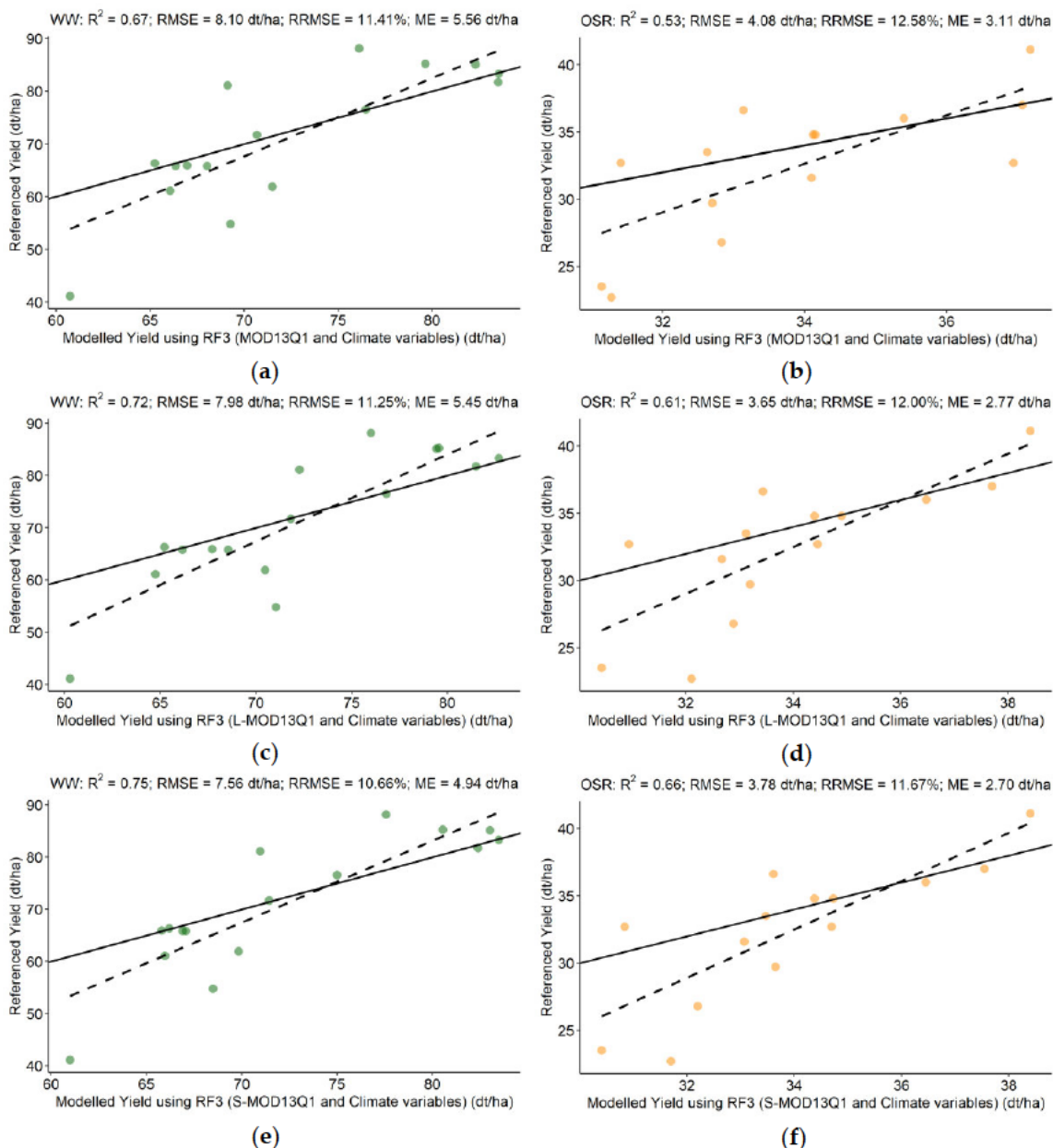


Figure 5.5. Scatter plots of the validation of WW and OSR modeled yield using RF3 model with referenced yield. The green dots represent WW, and the orange dots represent OSR. (a) MOD13Q1 (RF3(WW); just MODIS) versus referenced yield. (b) MOD13Q1 (RF3(OSR); just MODIS) versus referenced yield. (c) L-MOD13Q1 (RF3(WW); Landsat and MODIS) versus referenced yield. (d) L-MOD13Q1 (RF3(OSR); Landsat and MODIS) versus referenced yield. (e) S-MOD13Q1 (RF3(WW); Sentinel-2 and MODIS) versus referenced yield. (f) S-MOD13Q1 (RF3(OSR); Sentinel-2 and MODIS) versus referenced yield. Every plot contains a solid 1:1 line that is used to visualise the correlation between referenced and synthetic yield.

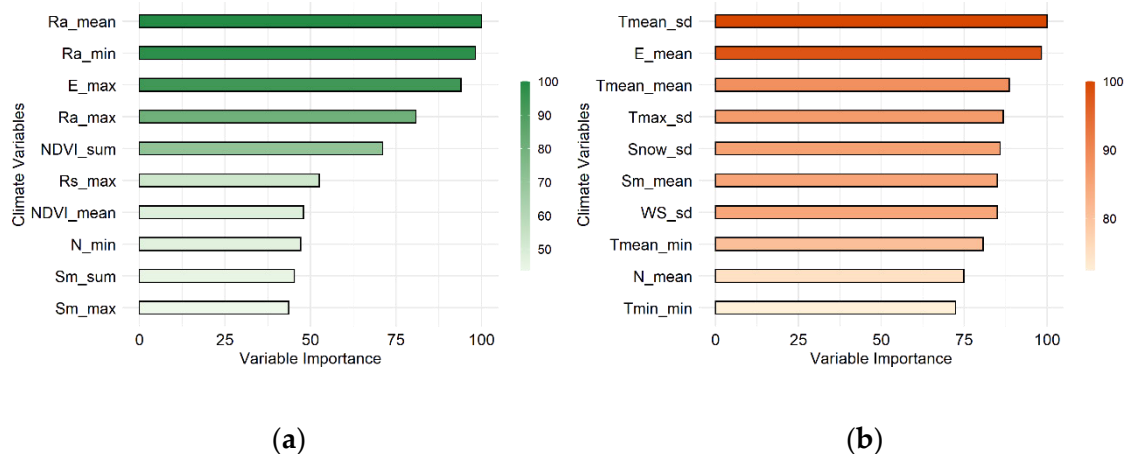


Figure 5.6. Bar plots of the variable importance of WW and OSR after validation of the modeled yield with referenced yield using the RF3 model. The green color represents WW, and the orange color represents OSR. (a) Variable importance for WW (b) Variable importance for OSR.

5.3.4. Light Use Efficiency (LUE) Model

With the different spatial outputs, the LUE model performed significantly for WW and OSR (p -value < 0.05) (Figure 5.7). For WW, the S-MOD13Q1 ($R^2 = 0.86$, RMSE = 5.03 dt/ha, RRMSE = 7.36%) has higher accuracy and preciseness than the L-MOD13Q1 ($R^2 = 0.83$, RMSE = 5.64 dt/ha, RRMSE = 9.76%) and MOD13Q1 ($R^2 = 0.65$, RMSE = 7.63 dt/ha, RRMSE = 9.84%) (Figure 5.7a,c,e). Similarly, for OSR, the LUE model ordered as S-MOD13Q1, L-MOD13Q1, and MOD13Q1, with high R^2 and low RMSE and RRMSE values as 0.82/ 2.14 dt/ha/ 9.12%, 0.80/ 2.17 dt/ha/ 9.46%, and 0.66/ 3.12 dt/ha/ 10.51%, respectively (Figure 5.7b,d,f).

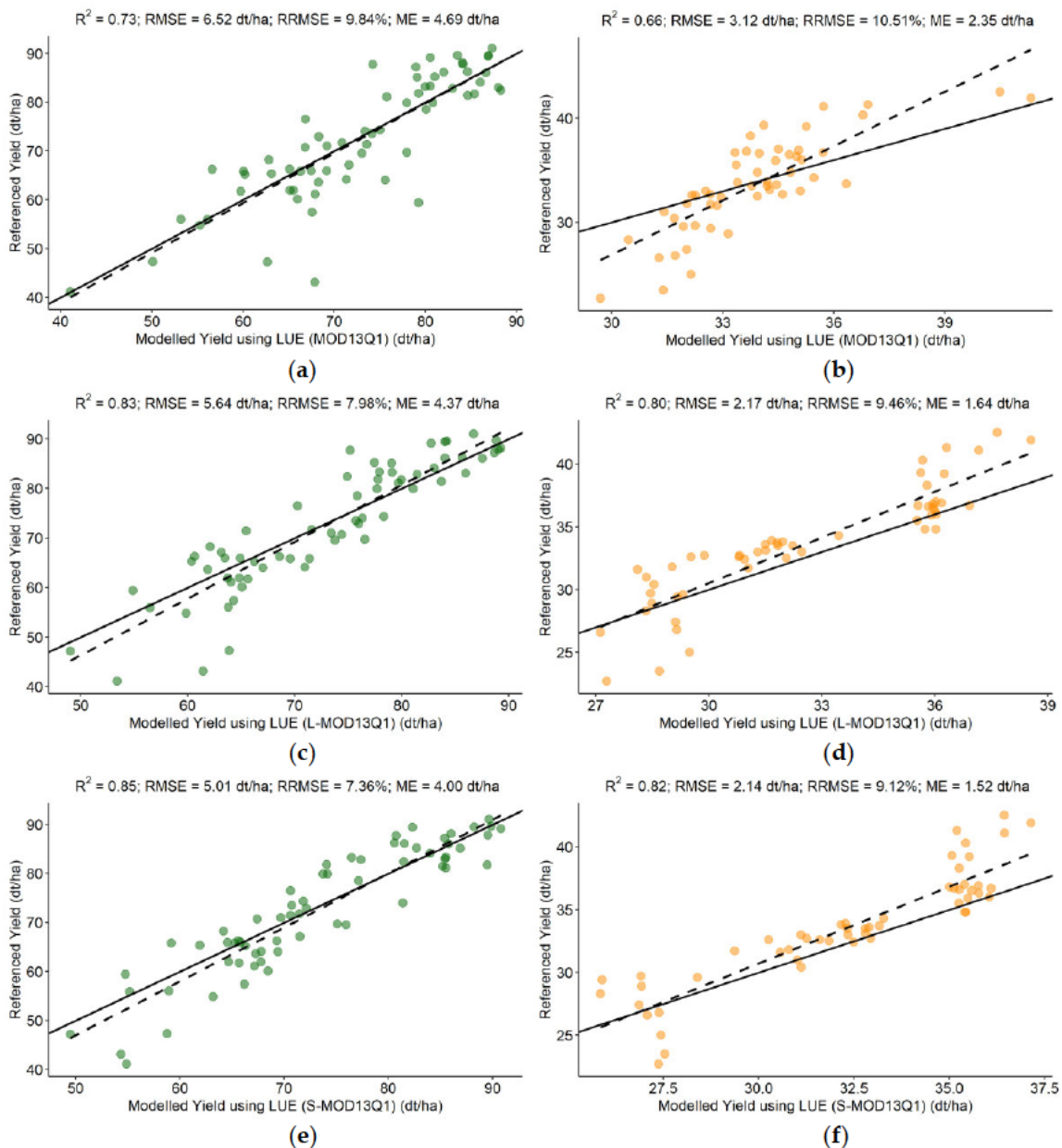


Figure 5.7. Scatter plots of the validation of WW and OSR modeled yield using LUE model with referenced yield. The green dots represent WW, and the orange dots represent OSR. (a) MOD13Q1 (LUE(WW); just MODIS) versus referenced yield. (b) MOD13Q1 (LUE(OSR); just MODIS) versus referenced yield. (c) L-MOD13Q1 (LUE(WW); Landsat and MODIS) versus referenced yield. (d) L-MOD13Q1 (LUE(OSR); Landsat and MODIS) versus referenced yield. (e) S-MOD13Q1 (LUE(WW); Sentinel-2 and MODIS) versus referenced yield. (f) S-MOD13Q1 (LUE(OSR); Sentinel-2 and MODIS) versus referenced yield. Every plot contains a solid 1:1 line that is used to visualise the correlation between referenced and synthetic yield. The validation of LUE model is performed for a total number of samples for both WW and OSR which increases the number of points in the scatter plot.

5.3.5. RF4: Coupling LUE and RF for Crop Yield Prediction

On linking the LUE model outputs with climate parameters (CV3), the S-MOD13Q1 ($R^2 = 0.91$, RMSE = 4.98 dt/ha, RRMSE = 7.29%) has higher accuracy and preciseness than the L-MOD13Q1 ($R^2 = 0.88$, RMSE = 5.63 dt/ha, RRMSE = 7.93%) and MOD13Q1 ($R^2 = 0.77$, RMSE = 6.80 dt/ha, RRMSE = 9.58%) for WW (Figure 5.7a,ce). Similarly, for OSR, the RF4 model ordered as S-MOD13Q1, L-MOD13Q1, and MOD13Q1, with high R^2 and low RMSE and RRMSE values as 0.84/ 2.11 dt/ha/ 8.83%, 0.84/ 2.16 dt/ha/ 9.42%, and 0.74/ 3.11 dt/ha/10.37%, respectively (Figure 5.8b,d,f). For both WW and OSR, the biomass output of the LUE model has shown the highest impact in improving the accuracy of the respective crop yields (Figure 5.9).

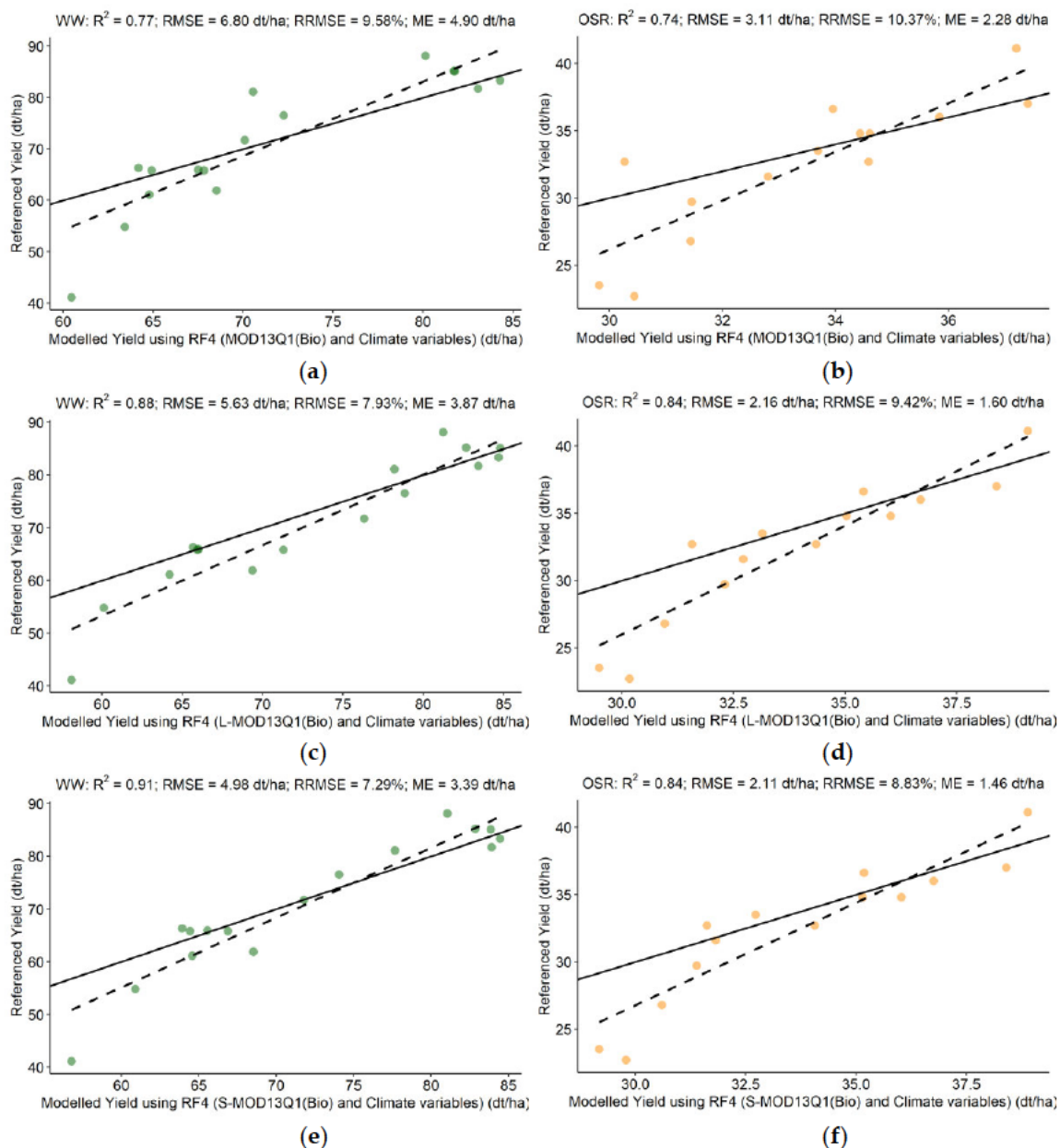


Figure 5.8. Scatter plots of the validation of WW and OSR modeled yield using RF4 model with referenced yield. The green dots represent WW, and the orange dots represent OSR. (a) MOD13Q1 (RF4(WW)); just MODIS versus referenced yield. (b) MOD13Q1 (RF4(OSR)); just MODIS versus referenced yield. (c) L-MOD13Q1 (RF4(WW)); Landsat and MODIS versus referenced yield. (d) L-MOD13Q1 (RF4(OSR)); Landsat and MODIS versus referenced yield. (e) S-MOD13Q1 (RF4(WW)); Sentinel-2 and MODIS versus referenced yield. (f) S-MOD13Q1 (RF4(OSR)); Sentinel-2 and MODIS versus referenced yield. Every plot contains a solid 1:1 line that is used to visualise the correlation between referenced and synthetic yield.

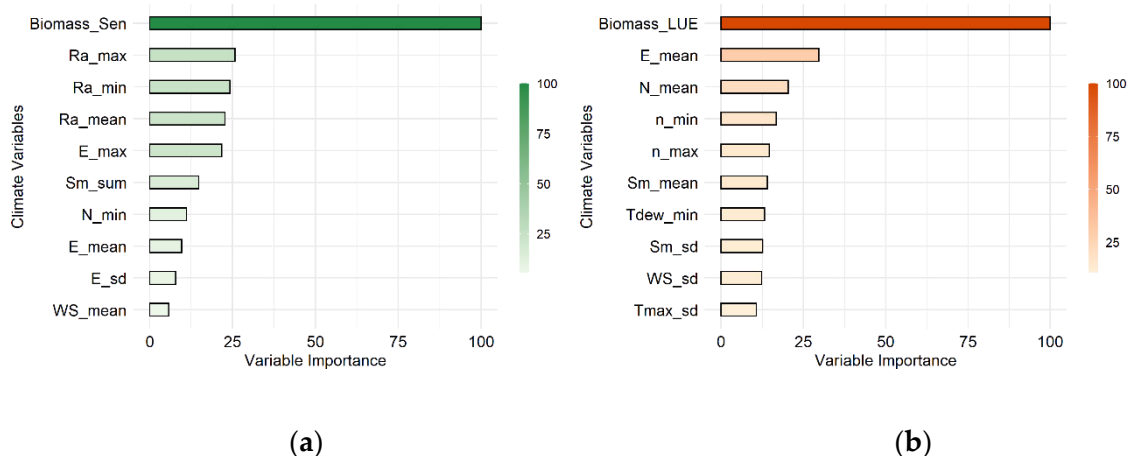


Figure 5.9. Bar plots of the variable importance of WW and OSR after validation of the modeled yield with referenced yield using the RF4 model. The green color represents WW, and the orange color represents OSR. (a) Variable importance for WW (b) Variable importance for OSR.

5.3.6 Overall Comparison of Models

The bar plots in Figure 5.10 show the accuracy assessment of estimating crop yields of WW and OSR using different models with different inputs. For the model RF1 (where NDVI is the only predictor), the MOD13Q1 has the lowest R^2 (0.60 (WW) / 0.26 (OSR)) while both L-MOD13Q1 and S-MOD13Q1 have almost the same R^2 values (0.66 / 0.50) for both WW and OSR. However, for WW, the RMSE and RRMSE has shown a different trend with lower values (7.96 dt/ha, 11.40%) for S-MOD13Q1, and higher (10.22 dt/ha, >14.00%) for both MOD13Q1 and L-MOD13Q1. The RF2 model (where climate variables are predictors), has shown the lowest accuracy (R^2 : 0.57 (WW), 0.50 (OSR)) and preciseness (RMSE: 10.6 dt/ha, 4.23 dt/ha) as compared to the RF1 model. The RF3 model (where CV and NDVI are the predictors), has improved the accuracy estimation of RF1 with higher R^2 (CV+S-MOD13Q1 > CV+L-MOD13Q1 > CV+MOD13Q1) and lower RMSE and RRMSE (CV+S-MOD13Q1 < CV+L-MOD13Q1 < CV+MOD13Q1) for both WW and OSR. On the other hand, the LUE model has further improved the R^2 and RMSE values for both crops than the RF3 model. The accuracy of the LUE model is in descending order from CV2+S-MOD13Q1, CV2+L-MOD13Q1, and CV2+MOD13Q1. The CV2 are the climate variables inputted by the LUE model. Lastly the RF4 model (which combines the biomass output of LUE with additional CV3(CV minus CV2)), S-MOD13Q1 provided the highest accuracy (0.91 (WW) / 0.84 (OSR)) and lower RRMSE

(7.29%/8.83%) for both WW and OSR among the investigated models. The coupling of the LUE model variables to the RF4 model can decrease the RMSE by -1.00% (for WW) and -8.4% (for OSR), decrease the RRMSE from -8% (WW) and -1.6% (OSR), and increase the R^2 by 14.3% (for both WW and OSR), compared to results just relying on LUE. Similarly, between RF1 and RF4, the RRMSE has been decreased by -36.05% (WW) and -21.37% (OSR).

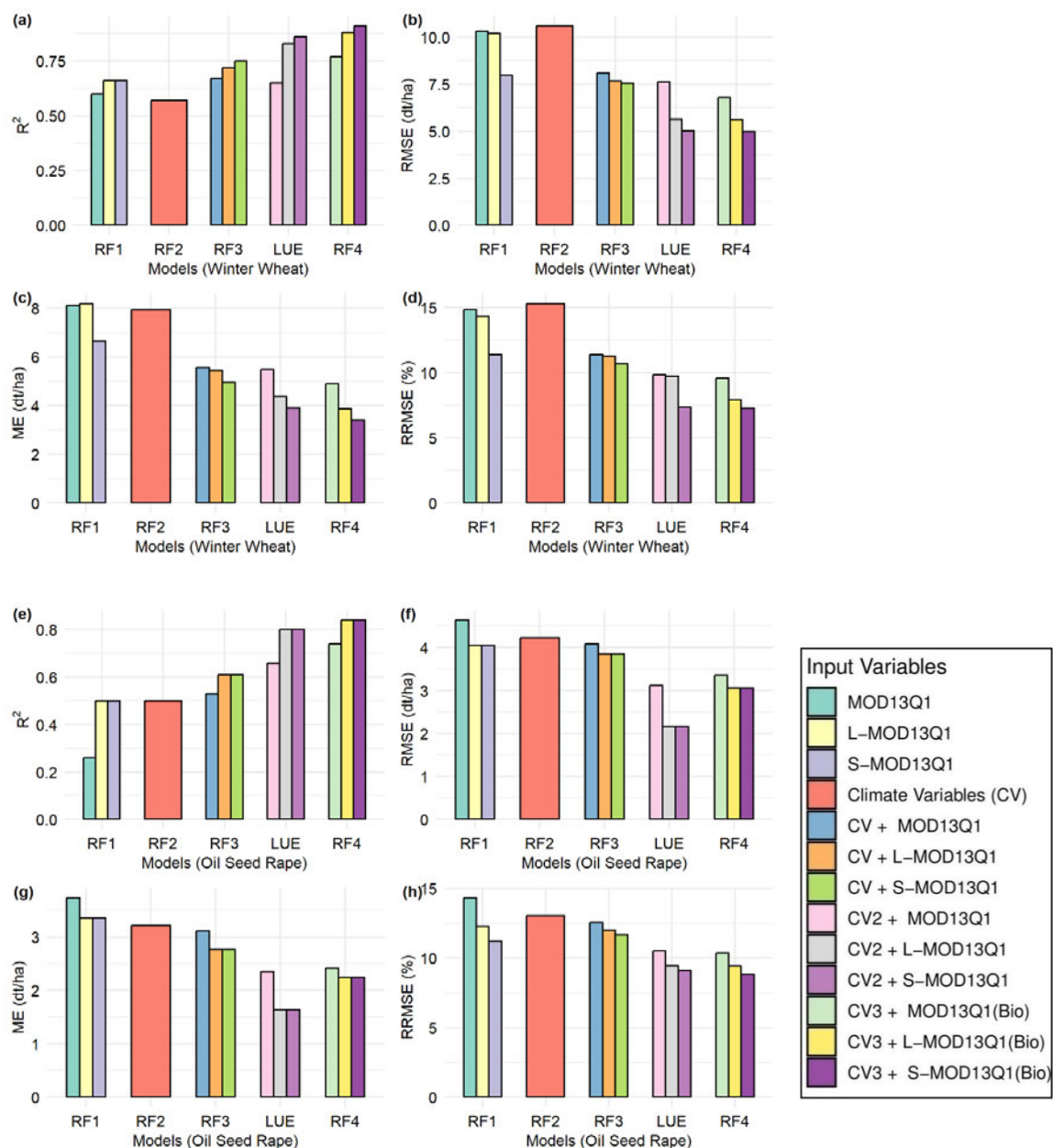


Figure 5.10. Bar plots for the overall accuracy assessment of WW and OSR with four RF (RF1, RF2, RF3, RF4) and one LUE model with different input variables (shown in the legend at right). (a) R^2 , (b) RMSE, (c) ME, and (d) RRMSE for WW and (e) R^2 , (f) RMSE, (g) ME, and (h) RRMSE for OSR using different models with various inputs, respectively.

5.3.7. Accuracy Assessment Based on Different Spatial Inputs

The box plots in Figure 5.11 show the contribution of different spatial inputs to LUE and RF models crop yield estimations of Bavaria for WW and OSR. Among all models, the S-MOD13Q1(10 m) result in higher mean R^2 (0.80 (WW)/0.69 (OSR)), lower RMSE (dt/ha) (6.38/ 3.05), lower RRMSE (%) (9.18, 10.21) compared to L-MOD13Q1 (30 m) and MOD13Q1 (250 m). For WW, both S-MOD13Q1 and L-MOD13Q1 resulted in similar accuracy; however, for OSR, S-MOD13Q1 performed better than L-MOD13Q1. Moreover, the MOD13Q1 resulted in better performance for OSR than WW. For L-MOD13Q1 and MOD13Q1, the mean R^2 (0.77 (WW)/0.69 (OSR), 0.67/0.55), RMSE (dt/ha) (7.29/3.06, 8.21/3.74) and RRMSE (%) (10.82/10.79, 11.42/11.95) values vary in an order of higher accuracy.

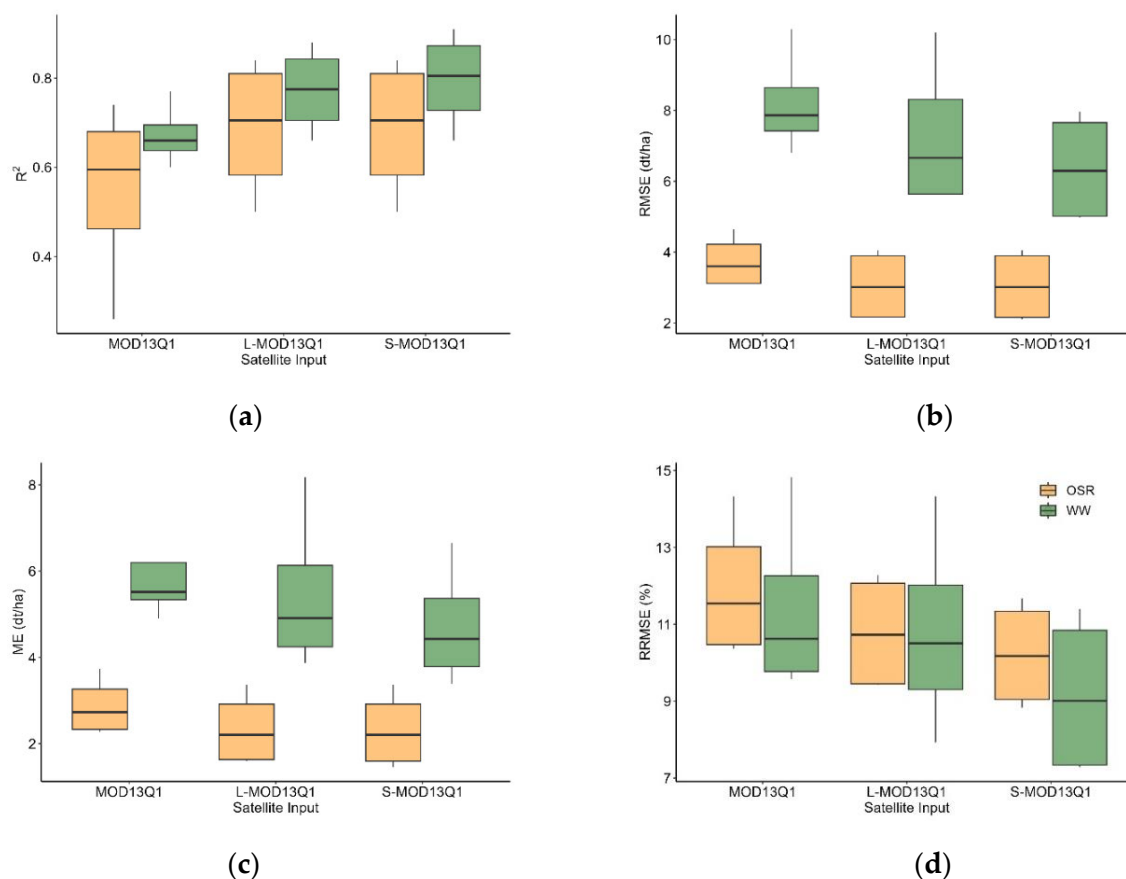


Figure 5.11. Box plots show the comparison of the accuracy assessment of three satellite inputs (S-MOD13Q1 (10 m), L-MOD13Q1 (30 m) and MOD13Q1 (250 m)) used in four models (RF1, RF3, LUE and RF4) for yield prediction of WW (green) and OSR (orange). (a) R^2 (b) RMSE (c) ME and (d) RRMSE.

5.3.8. Spatial Distribution of Crop Yields for WW and OSR on Regional Scale

The maps in Figure 5.12 and Figure 5.13 describe the region-wise spatial distribution of referenced and predicted (obtained from RF1, RF2, RF3, LUE and RF4) yield for WW and OSR by inputting S-MOD13Q1 (10 m) in Bavaria for the year of 2019, respectively. For both crops, the yield prediction by the RF4 (coupling of LUE and RF) has better synchronization with the observed yield results compared to the other four models. The referenced OSR and WW yields have higher values in the southern regions of Bavaria. Almost all models for OSR have shown higher values in respective regions; however, for WW, only RF4 and LUE modelled yields obtained higher values (> 85 dt/ha) and other models have estimated between 55 to 85 dt/ha. The referenced OSR yield values for the central part of Bavaria observed higher yield between 32 to 44 dt/ha; however only RF4 and RF3 models had predicted the accurate amount.

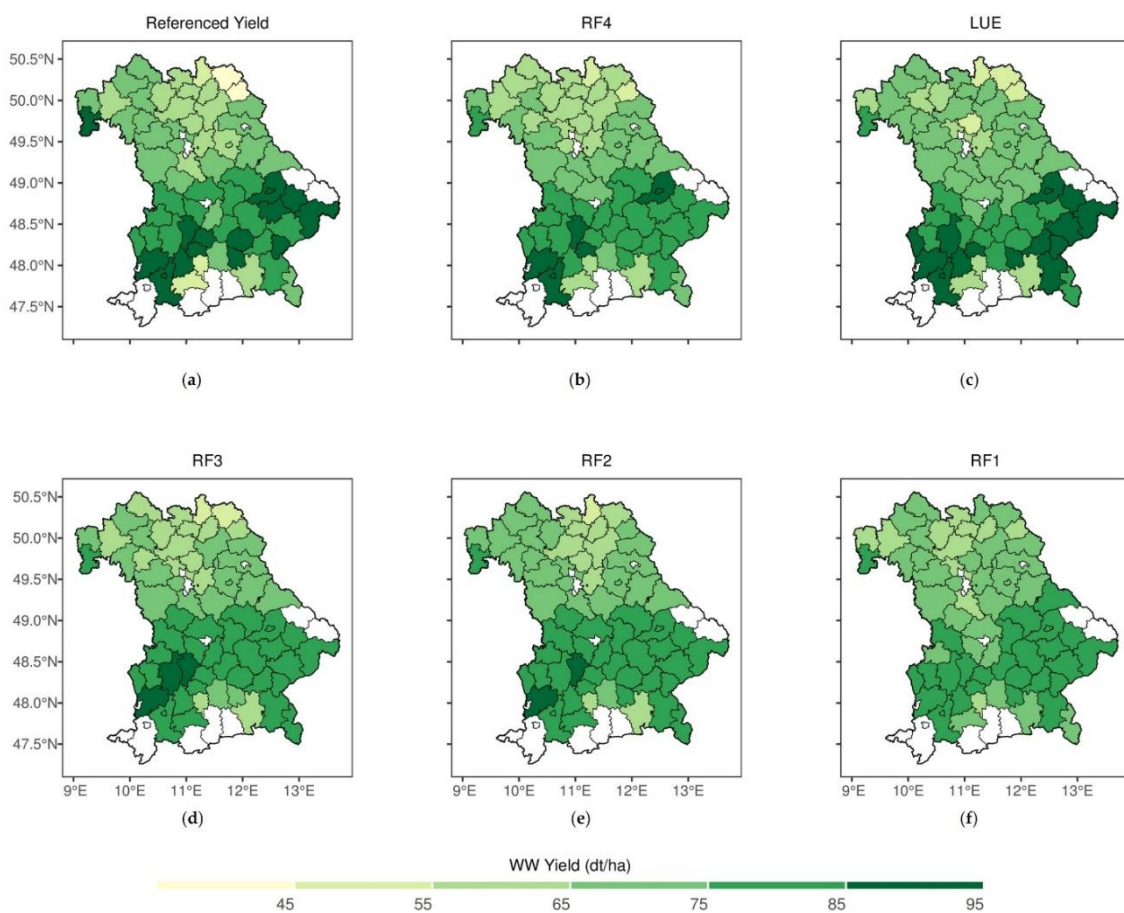


Figure 5.12. Spatial distribution of referenced yield and predicted yield for WW using RF1, RF2, RF3, LUE and RF4 models by inputting S-MOD13Q1 (10 m) for the state of Bavaria in 2019. The white color represents no data available. (a) Referenced Yield (b) RF4 (c) LUE, (d) RF3, (e) RF2, and (f) RF1.

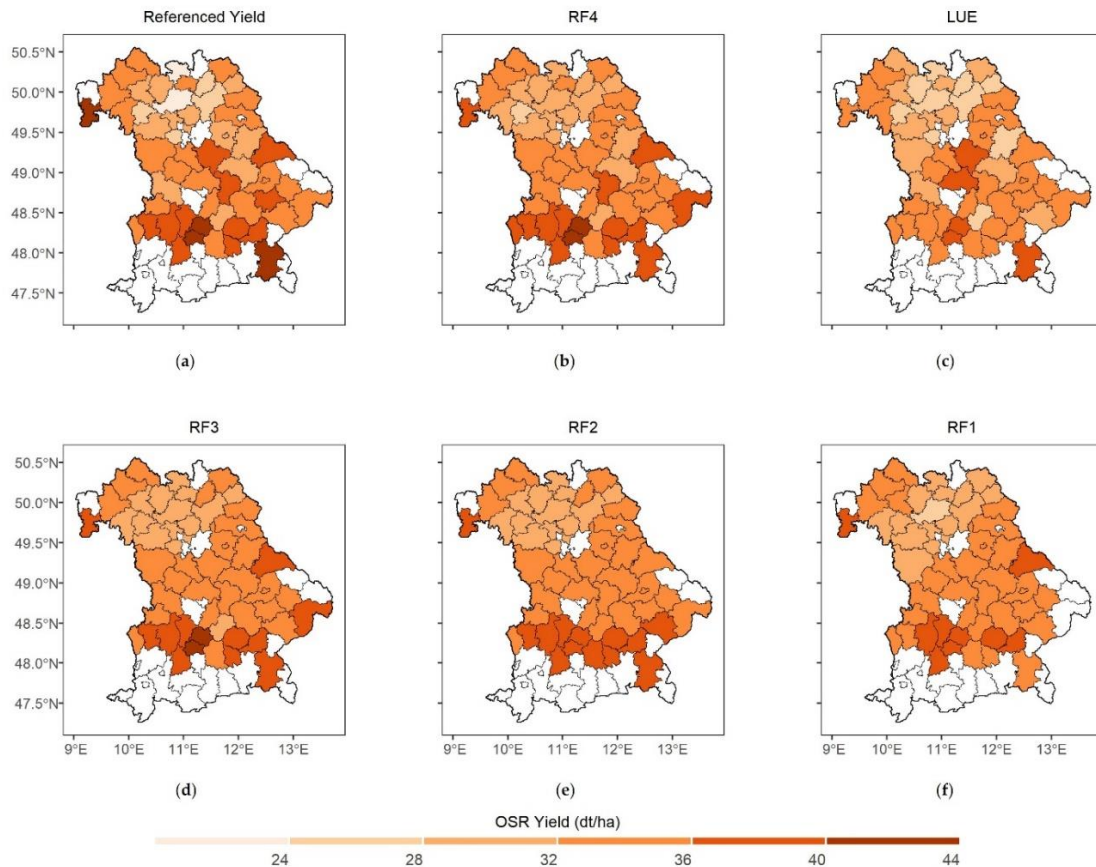


Figure 5.13. Spatial distribution of referenced yield and predicted yield for OSR using RF1, RF2, RF3, LUE and RF4 models by inputting S-MOD13Q1 (10 m) for the state of Bavaria in 2019. The white color represents no data available. (a) Referenced Yield (b) RF4 (c) LUE, (d) RF3, (e) RF2, and (f) RF1.

5.4. Discussion

This study addresses the importance of coupling the RF model with the LUE model to improve the accuracy of crop yield estimation of WW and OSR for Bavaria in 2019. The present study is among the rare other studies that ensemble models to increase crop yield predictability. This study demonstrated that introducing the LUE output spatial biomass plus climate parameters into the RF model (RF4) and utilizing them as inputs to a prediction task on average can decrease the prediction error measure by RMSE from 5.03-4.98 dt/ha (for WW) and 2.14-1.96 dt/ha (for OSR). In addition, the predictions made by the RF4 model show less bias towards the actual regional yields. Similar studies in this area are only limited to coupling the simplest statistical models with crop growth models (Chakraborty, Manjunath, Panigrahy, Kundu, & Parihar, 2005; De Wit & Van

Diepen, 2007; Dente, Satalino, Mattia, & Rinaldi, 2008; Hadria et al., 2006). However, a related study has coupled the Agricultural Production Systems Simulator (APSIM) variables into machine learning models and estimated the decrease of RMSE between 7 and 20% (Shahhosseini et al., 2021).

The cloud and shadow gaps in the optical satellite data can hinder or limit yield prediction algorithms from producing accurate yield results (Gevaert & García-Haro, 2015; David P. Roy et al., 2008). Many studies employing satellite images aimed to compensate the data gaps present in satellite data by fusing it with another data source for various applications of remote sensing (Barbedo, 2022). The research is conducted at different spatial scales where multiple spatial resolution satellite products (two STARFM-derived synthetic NDVI products (L-MOD13Q1 (30 m, 8-days) and S-MOD13Q1 (10 m, 8-days and one real NDVI product (MOD13Q1 (250 m, days))) are inputted to different RF models (Dhillon et al., 2022). The study highlights the importance of high spatial scales in achieving accurate crop yield results. For example, the input products with 10-meter resolutions ($R^2 > 0.75$) resulted in higher accuracy than the 30-meter ($R^2 > 0.72$) and 250-meter ($R^2 > 0.65$) satellite products using RF2, RF3, and RF4 models for WW. Previous studies have also shown that high spatial resolution could significantly improve the accuracy of crop yields (Dhillon et al., 2020; J. Huang et al., 2016; Z.-c. LIU et al., 2021).

Moreover, the results of the study at hand also demonstrate that variable selection plays an important role in achieving more accurate crop predictions. The time series vegetation index (VI) data derived from satellite images are known as a better predictor for many applications of remote sensing (S.-R. Kim et al., 2014; Shen et al., 2015; Wardlow, Egbert, & Kastens, 2007; G. Zhang, Zhang, Dong, & Xiao, 2013; X. Zhang et al., 2003; Zhong, Gong, & Biging, 2012); however, this study highlights that NDVI alone could not be used to achieve accurate crop yield results (WW: $R^2 < 0.65$, OSR: $R^2 < 0.45$). Moreover, the research found that the combined use of NDVI and climate parameters can help to improve the model performance (WW: $R^2 > 0.70$, OSR: $R^2 > 0.60$). The inclusion of relevant climate parameters positively impacted the yield prediction for WW and OSR. For example, extra-terrestrial radiation has higher variable importance

for WW and snow cover for OSR. Furthermore, the crop and phenology-related variables (LUE biomass), solar radiation, soil moisture and temperature are the most influential variables in increasing the yield accuracy for WW and OSR.

This study also compares the performance of LUE when used with and without the random forest model. Similar to other studies, the LUE model resulted precisely and accurately with an average R^2 of 0.78 and 0.76 and an RMSE of 6.10 and 2.47 dt/ha for WW and OSR at different spatial scales, respectively (Dhillon et al., 2020). However, a drastic improvement in the accuracy has been seen when the LUE model was linked with the random forest model by including more climate variables as an input. This coupling has increased the R^2 from 0.78 to 0.85 and 0.76 to 0.81 for WW and OSR using different satellite inputs, respectively.

The simplicity and reliability of the present study conclude that this design needs to be implemented for different periods, locations, and crop types to improve the global yield estimation for developing agricultural policies, improving food security, forecasting, and analysing global trade trends. The study stresses coupling the LUE model with the RF model; however, the applicability of other crop models, such as WOFOST, AquaCrop, or CERES Wheat, on coupling with ML or deep learning (DL) could be tested. Moreover, the study only includes the year 2019 for the state of Bavaria, but the same design could be transferred and tested to other geographical regions at any time scale. Inclusion of climatic variables such as solar radiation, extra-terrestrial radiation, soil moisture, temperature, snow cover (for OSR) and evapotranspiration would be recommended in future studies. Due to the availability of the crop validation data (LfStat) on a regional level, the study integrated the pixel-level information into the district level. This transfer of data (from field to district level) could result in a loss of information, and it might negatively impact the accuracy of the algorithm outcomes. Therefore, to justify the potential of satellite data and machine learning algorithms in crop monitoring, the study recommends testing and validating methodology at the field level. Moreover, as the study validates the accuracy of WW and OSR, the study design might also be tested for different crop types such as Maize, Sugarcane, Rice, etc.

5.5. Conclusions

Conclusively, this study stressed the positive impact of combining crop modelling and machine learning to improve the prediction accuracies for the application of agricultural monitoring. Moreover, the crop and phenology-related inputs (LUE biomass), extra-terrestrial radiation, solar radiation, evapotranspiration, extra-terrestrial radiation, soil moisture, snow cover (for OSR) and temperature are the most influential variables that are needed to be considered for increasing the yield accuracy in future studies. The present research concludes the findings as follows:

- (i) To answer if NDVI or CV is the better predictors of crop yield, the study found that the individual use of NDVI (in RF1) and climate variables (in RF2) would be less accurate in yield prediction than they are used together (in RF3) in machine learning. The accuracy assessment when NDVI is used alone as a crop yield predictor is lower (WW: $R^2 < 0.65$, OSR: $R^2 < 0.45$) than it is used together with the climate variables (WW: $R^2 > 0.70$, OSR: $R^2 > 0.60$).
- (ii) To find if the coupling of ML and CGM results in higher accuracy, the study investigated that linking the LUE model's output with the RF model's input (RF4) would increase the crop yields' accuracy drastically. The coupling has decreased the RMSE by -1.00% (for WW) and -8.4% (for OSR), decreased the RRMSE from -8% (WW) and -1.6% (OSR), and increased the R^2 by 14.3% (for both WW and OSR), compared to results of LUE.
- (iii) To find the impact of high spatial resolution on crop yield estimation, the study concludes that the RS inputs with 10-meter resolutions resulted in higher accuracy than the 30-meter and 250-meter with RF2, RF3, LUE, and RF4 models for WW and OSR.

Moreover, the present study is performed at the regional level; however, the availability of field-level yield information could be useful for implementing a similar methodology and obtaining more accurate outcomes. The study design needs to be implemented for different periods, locations, and crop types to improve the global yield estimation for developing agricultural policies, improving food security, forecasting,

and analysing global trade trends. The accurate validations of WW and OSR broaden the scope of the study. Therefore, the simple and reliable design of the study could be tested for other crop types such as maize, sugarcane, or rice on a global scale.

Chapter 6

Potential and Challenges of Satellite Remote Sensing
in Analysing the Relationship between Land Use
Diversity and Crop Biomass in Bavaria, Germany

Abstract

The importance of agriculture in feeding the world's growing population is undeniable. However, agricultural land productivity is threatened by various factors, including climate change, soil degradation, and water scarcity limiting its potential to achieve sustainability. The diversity of land use patterns in agricultural landscapes has positively impacted agriculture, ecological sustainability, and resilience to climate change. However, the relationship between land use diversity and crop yields is multifaceted and understanding and quantifying this relationship is a significant challenge for researchers and policymakers. Even though satellite remote sensing has emerged as a powerful tool for analysing land use patterns and monitoring changes over time, its potential, or challenges to determine the impact of land use diversity on crop yields/biomass still needs to be explored. This chapter tried to discuss both pros and cons of remote sensing technology while analysing the impact of land use diversity on crop-modelled biomass of winter wheat and oil seed rape in Bavaria 2019. The study has made use of the Shannon Diversity Index calculated (on six land cover classes such as agriculture, forest, grassland, water, urban, and natural-seminatural) for 11 window sizes (150, 250, 350, 450, 850, 950, 1050, 1350, 1750, 2150, and 2650 m) and then, correlated with the modelled crop biomass of both crops at every radius. The study's key finding showed different results for both crop types. The results obtained an increment in a correlation coefficient (R) from 0.24 to 0.27 from 150 to 450 m, which stated that the land use diversity (~0.50) within the radius of 450 m highly influenced the crop biomass of winter wheat. On the other hand, the oil seed rape had an increase in R values from 0.09 to 0.23 (range of Shannon Diversity Index) and 0.03 to 0.29 (standard deviation of Shannon Diversity Index) at 150 to 1050 m, which stated the biomass of OSR was positively impacted by land use diversity till the radius of 1050 m (~0.75). Notably, the study discussed the challenges of remote sensing methodology for excluding some dependent factors (such as the specific crops being grown, the management practices used, soil health, biotic and abiotic stressors, pest management, pollinators, and the local environmental conditions) that might be impactful on positively affecting the accuracy of the analysis. Therefore, the study concluded that including these factors for future

analysis might ensure the reliability and applicability of the findings for researchers, policymakers, and practitioners in agriculture and food security.

6.1. Introduction

Agriculture is vital to human civilization, providing the world's population with food, fibre, and fuel (Heywood, 2013; Swinton, Lupi, Robertson, & Hamilton, 2007). It is the primary user of land, and the diversity of agricultural practices directly affects the health and productivity of the land (Ki-Moon, 2013). Potential farmers adopting various crops, rotations, and land management techniques can lead to more sustainable and productive land use (Branca, Lipper, McCarthy, & Jolejole, 2013; Kovács-Hostyánszki et al., 2017; Wilkins, 2008). For example, crop rotation, intercropping, cover cropping, and agroforestry promote soil health and fertility, reduce erosion, and minimize the need for chemical inputs. Additionally, diversification can help mitigate the effects of climate change by increasing the resilience of agricultural systems to extreme weather events and increasing crop yields (Lin, 2011). Even though the relationship between land use diversity and crop yields is an important area of agriculture research, there is still a research gap in understanding the nuances of this relationship. Remote sensing (RS) can play an essential role in filling this research gap by providing data on land use and crop performance at various spatial and temporal scales (Fegraus et al., 2012); however, its potential or challenges to determine the impact of land use diversity on crop yields/biomass, is still not investigated.

Satellite RS could be a powerful tool for analysing the relationship between land use diversity and crop yields in agricultural landscapes. Satellite and airborne sensors can provide detailed information on crop growth, soil moisture, and vegetation indices, which can help to identify patterns and trends in crop yield about different land use practices (Braun, Damm, Hein, Petchey, & Schaepman, 2018; Nellis, Price, & Rundquist, 2009). Many studies have used several required methods and data sources that can be used to analyse, quantify, and map ecosystem properties and functions using remote sensing (Braun et al., 2018; Palacios-Orueta et al., 2012; Winowiecki, Vågen, & Huising,

2016). These include spectral indices, such as the normalized difference vegetation index (NDVI), which can be used to estimate vegetation productivity and detect changes in land use patterns (Krishnaswamy, Bawa, Ganeshaiah, & Kiran, 2009). Other studies have included high-resolution imagery, which can be used to identify individual crops and estimate crop yields (Dhillon et al., 2020; Dhillon, Dahms, Kuebert-Flock, et al., 2023), and radar and lidar data, which can be used to map terrain and identify land use patterns (Joshi et al., 2016; Madec et al., 2017; McNairn & Shang, 2016). Moreover, some studies have successfully used RS to capture data on the broader landscape context, such as nearby forests, water bodies, and other land uses that may impact agriculture (Swinton et al., 2007).

With advanced sensors and data processing techniques, RS can provide accurate and timely information on land use patterns, crop productivity, and changes in agricultural landscapes over time (Atzberger & Rembold, 2013; D. Lewis, Phinn, & Arroyo, 2013). This information can help researchers and policymakers identify the factors that impact crop yields, support more sustainable and resilient food systems, and ultimately improve the livelihoods of farmers and rural communities worldwide. However, using RS data for this purpose also has significant challenges and limitations. These include data quality and availability, the need for advanced processing and analysis techniques, and agricultural systems' complex and dynamic nature (Mairota et al., 2015). The significant cloud and shadow-generated gaps in the freely available satellite products (such as Landsat (L) and Sentinel-2) hinder the accurate and timely-dense monitoring of RS applications (Gevaert & García-Haro, 2015; David P. Roy et al., 2008). In addition, RS cannot replace the need for on-the-ground field observations and data collection and must be used with other data sources (such as the management practices used, local environmental and market conditions, soil health, pest management and pollination) and analytical approaches (Espinoza-Molina & Datcu, 2013; Mairota et al., 2015; Maniatis & Mollicone, 2010; Persello & Bruzzone, 2009; Richter & Schläpfer, 2005).

Despite these challenges, the potential of RS for analysing the relationship between land use diversity and crop yields can be significant. By providing accurate and timely

information on land use patterns and crop productivity, RS can help to improve agricultural management and support more sustainable and resilient food systems (de Araujo Barbosa, Atkinson, & Dearing, 2015; Muraoka & Koizumi, 2009; Palacios-Orueta et al., 2012). Furthermore, the continued development of RS technology and data processing techniques will likely enhance its potential for monitoring and managing land use diversity in agricultural landscapes. Due to technological advancement, spatial-temporal data fusion algorithms have been made to generate accurate synthetic RS data by filling the observational data gaps in the real satellite data (Dubovik et al., 2021c). They are considered the most effective solution recommended by many studies on vegetation modelling (Cui et al., 2018; Lee et al., 2019; Xie et al., 2016). Moreover, many recent studies have used the synthetic RS data as an input to crop growth models (CGMs) and successfully attempted to estimate crop biomass/yields by covering vast spatial scales and updating the information temporally (Clevers et al., 2002; Dhillon et al., 2020; Dhillon, Dahms, Kuebert-Flock, et al., 2023; Doraiswamy et al., 2004; Jiang et al., 2014; C. Liu et al., 2014; Moriondo et al., 2007; Myneni et al., 1995; J. Wang et al., 2013a).

In this context, this paper explored the potential or challenges of satellite RS in analysing the relationship between land use diversity and crop biomass of WW and OSR in Bavaria 2019. To calculate land use diversity, the study used the Shannon Diversity Index, which is a commonly used measure of biodiversity in ecology (Shannon, 1948; Spellerberg & Fedor, 2003; Wiener, 1948). The diversity index was calculated at 11 window sizes (150, 250, 350, 450, 850, 950, 1050, 1350, 1750, 2150, and 2650 m), and then the values at very window size was correlated with the crop biomass. The present study used the biomass product of L-MOD13Q1 (30 m) generated in chapter 2 and 3. Specifically, the paper will address the following research questions:

- (i) Which is the best satellite product between the synthetic L-MOD13Q1 and real MOD13Q1 (250 m) on field-based validation of OSR's yield at 21 quadrants in Bavaria?
- (ii) What is the impact of land use diversity on the satellite-modelled biomass of OSR and WW in 2019?

- (iii) What is the impact of arable land use between 2018 and 2019 on the biomass of OSR?

By exploring the relationship between land use diversity and crop yields using remote sensing data, the study aimed to provide valuable and transparent insights for researchers, policymakers, and practitioners in agriculture and food security.

6.2. Materials and Methods

The general workflow of the study is shown in Figure 6.1. The flow diagram is divided into three parts: 1) Data fusion, 2) Per pixel crop biomass modelling for 2019 where the field values of WW and OSR were extracted individually with mean, standard deviation and range of biomass per field, and 3) Correlation analysis between the modelled biomass with mean, standard deviation and range of (a) Shannon Diversity Index of WW and OSR, and (b) difference in proportion of OSR by subtracting the landscape metrics of 2018 from 2019. The first and second parts were investigating the suitable synthetic NDVI product (which was L-MOD13Q1) and implementing to model crop biomass for WW and OSR in Bavaria 2019 (completed in the chapters 2 and 3). The modelled biomass of OSR was validated at field level for 21 quadrants of Bavaria; however, the modelled yields of both WW and OSR were validated at regional level in chapter third chapter of the dissertation. The third section is divided in two sets of analysis. In the first analysis, the land cover (LC) map of Bavaria was rescaled at 50 m and then reclassified in six land use classes such as, agriculture, forest, grassland, natural-seminatural, urban, and water. In the next steps, Shannon Diversity Index was calculated. The field values of WW and OSR (obtained from the InVeKos data (source: www.ec.europa.eu/info/index_en)) were extracted with mean, standard deviation, and range values per field. Lastly, the correlation analysis was performed between the mean, standard deviation, and range values of WW and OSR biomass (also extracted using the InVeKos field data from the modelled Biomass rasters of each crop per field) with the extracted field values of Shannon Diversity Index at 11 window sizes (150, 250, 350, 450, 850, 950, 1050, 1350, 1750, 2150, and 2650 m).

In the second analysis, the landscape metrics of OSR for 2018 and 2019 were calculated and then the metrics of 2018 were subtracted from the 2019. In the next steps

the correlation analysis was performed between the mean, standard deviation, and range values of OSR biomass with the extracted landscape metrics (for all statistical parameters) at 11 window sizes (150, 250, 350, 450, 850, 950, 1050, 1350, 1750, 2150, and 2650 m). The satellite data sets were downloaded and preprocessed in Google Earth Engine (GEE), and the analysis is done in R (version 4.0.3) using RStudio and ArcGis.

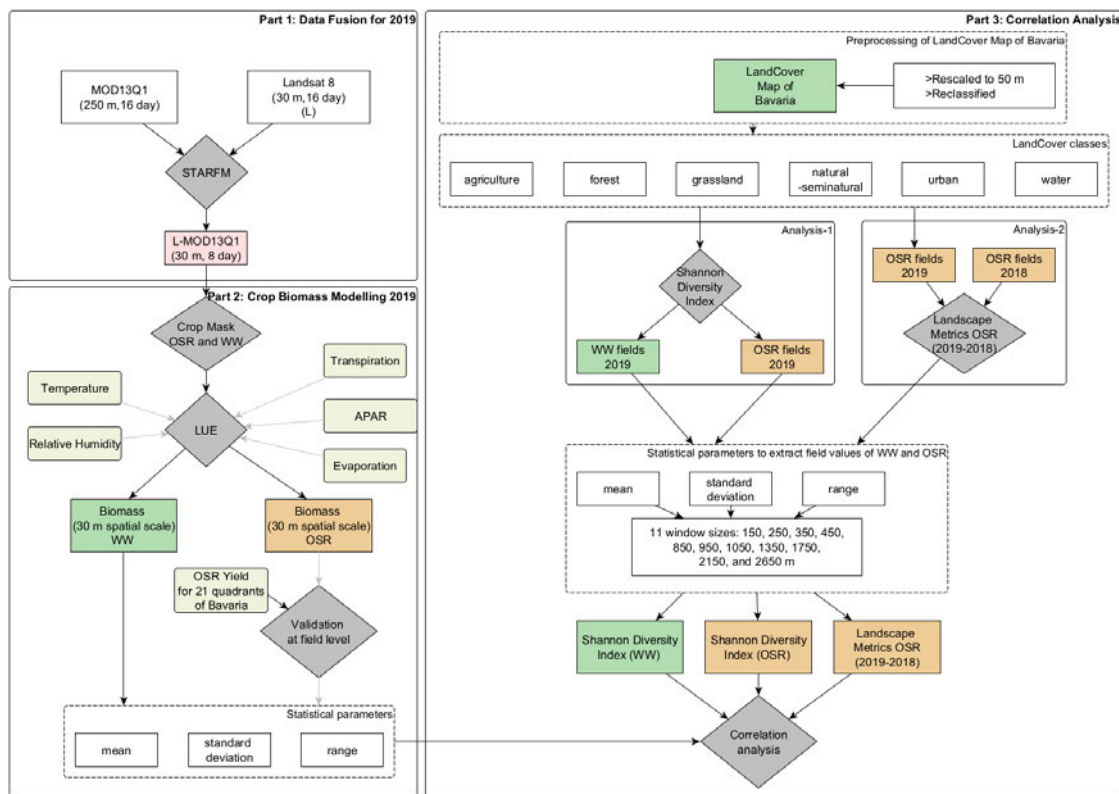


Figure 6.1. The conceptual framework of the study is divided into three parts: Part 1 states the data fusion for 2019 to investigate the best synthetic NDVI time series product (this section is already completed chapter 2); Part 2 states the crop biomass modelling using the Light Use Efficiency model (this section is already completed chapter 3) and Part 3 correlates the modelled crop biomass with mean, standard deviation and range of (i) Shannon Diversity Index of WW and OSR, and (ii) difference in proportion of OSR in two years (i.e., 2019 minus 2018).

6.2.1. Study Area

The federal state of Bavaria is located between 47°N and 50.5°N, and between 9°E and 14°E, in the southeastern part of Germany (Figure 6.2). The region's climate is mainly influenced by the topography, with higher elevations in the south (northern edge of the Alps) and east (Bavarian Forest and Fichtel Mountains). The mean annual temperature ranges from -3.3 to 11°C, but in most of the territory, temperature ranges

Chapter 6

between 8 and 10°C (Dhillon et al., 2022). The mean annual precipitation sums range from approx. 500 to above 3100 mm, with wetter conditions in the southern part of Bavaria. In 2019, the landcover was highly dominated by forest (36.91%) and agriculture (31.67%) (based on LC map of Bavaria, 2019). The agricultural areas are mainly found in the northwest and southwest of Bavaria, while forest cover dominates towards the Alps and the east. The other landcover classes like grassland, urban, natural-semi natural, and water cover approx. 19.16%, 8.97%, 1.84%, and 1.44% for the territory (estimates based on LC map of Bavaria, 2019) (Dhillon et al., 2022). With an area of approx. 70,500 km² Bavaria covers almost one-fifth of Germany. The federal state is divided into 96 counties with 71 rural districts (so called “Landkreise”) and 25 cities districts (so called “Kreisfreie Städte”). Brief description of the regions of Bavaria is shown in Figure A6.

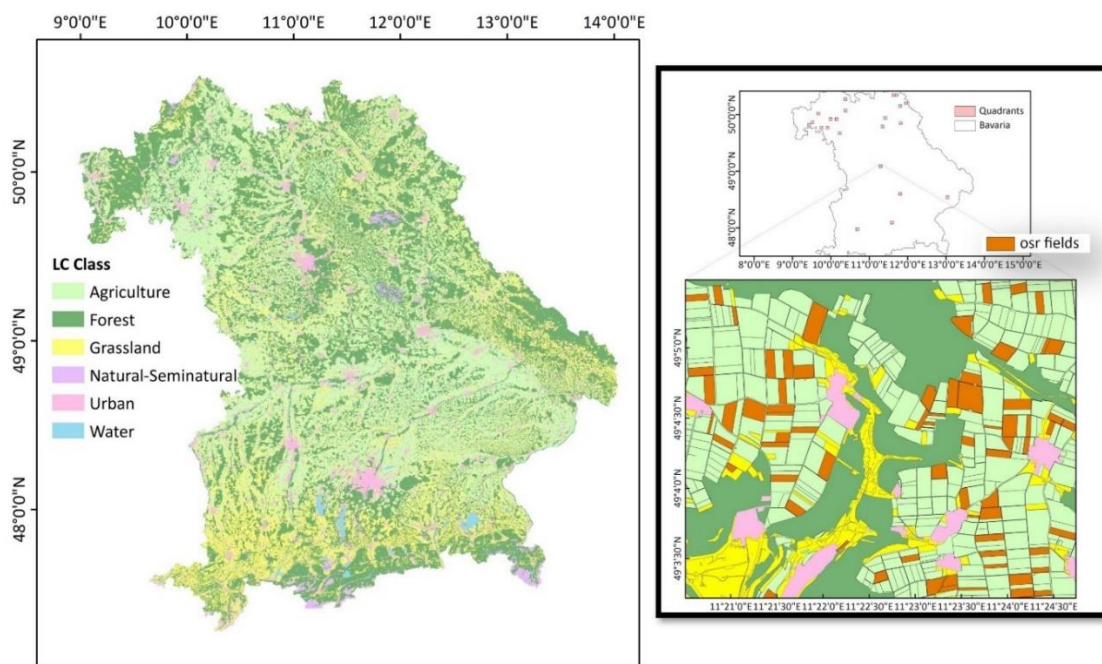


Figure 6.2. Overview of the study region of Bavaria. The left shows the reclassified LC map (1. Agriculture, 2. Forest, 3. Grassland, 4. Natural-Seminatural, 5. Urban and 6. Water) of Bavaria is obtained by combining multiple inputs of Landcover maps such as Amtliche Topographisch-Kartographische Informationssystem, Integrated Administration Control System (provides the crop field information), and Corine LC, into one map. The map on right shows the geographical location of selected 21 quadrants where the crop biomass information for the OSR was available for validation. In zoom, LC classes in one of the selected quadrants are shown with the OSR fields covered in the region.

6.2.2. Data

The study investigated the suitable satellite data with different spatial and temporal resolutions used to predict the crop yields of Bavaria on regional level. Along with the satellite data, several climate parameters were used as an input to the crop models. Further, the updated InVeKos data of 2019 (https://ec.europa.eu/info/index_en) is used to obtain the reference field information of WW and OSR for every district of Bavaria. Table 6.1 provides a brief description of the used data and indicates the spatial and temporal resolutions.

Table 6.1. A summary of the collected datasets for the study. The satellite data used are synthetic L-MOD13Q1; the Land Cover (LC) data is based covers six land use classes of Bavaria: agriculture, forest, urban, water, natural-semi natural, and grassland; InVeKos data provides the fields of WW and OSR for Bavaria for 2019.

| Data | Product Name | Resolution (Spatial-Temporal) | References |
|----------------|---------------------------|-------------------------------|---|
| Satellite data | L-MOD13Q1 | 30 m, 8-days | (Dhillon et al., 2022) |
| Vector data | LC Map of Bavaria | 2019 | www.landklif.biozentrum.uni-wuerzburg.de (accessed on 21 June 2021) |
| | InVeKos | 2019 | www.ec.europa.eu/info/index_en (assessed on 21 June 2021) |
| | In-situ crop yield of OSR | 2019 | www.landklif.biozentrum.uni-wuerzburg.de (accessed on 20 August 2021) |

6.2.2.1. Satellite Data

The study used the synthetic L-MOD13Q1 (30 m, 8-days) NDVI time series generated in chapter 2 to calculate the crop biomass for both WW and OSR. As the STARFM has the potential to fill the cloud and shadow generated gaps in high spatial resolution data, chapter 2 compared the output of a high (Landsat) and a low pair (MODIS) on six LC classes (agriculture, forest, grassland, semi-natural, urban, and water) in 2019 for the entire state of Bavaria. The crop biomass was obtained using the 8-day NDVI time series for the day of the years (DOYs) from the stem elongation phases till the flowering stages of both crops. Four (49, 81, 145, and 177) cloud free DOYs were available for Landsat (Figure 6.3). The accuracy assessments of STARFM generated L-MOD13Q1 NDVI product for different LC classes are shown in Table 6.2.

For OSR, the start of the season was 15th February, and the end of the season was 20th April 2019 (Zamani-Noor & Feistkorn, 2022). And for WW, the start and end of the season period lied between 15th of April to 30th of June 2019 (Harfenmeister et al., 2021).

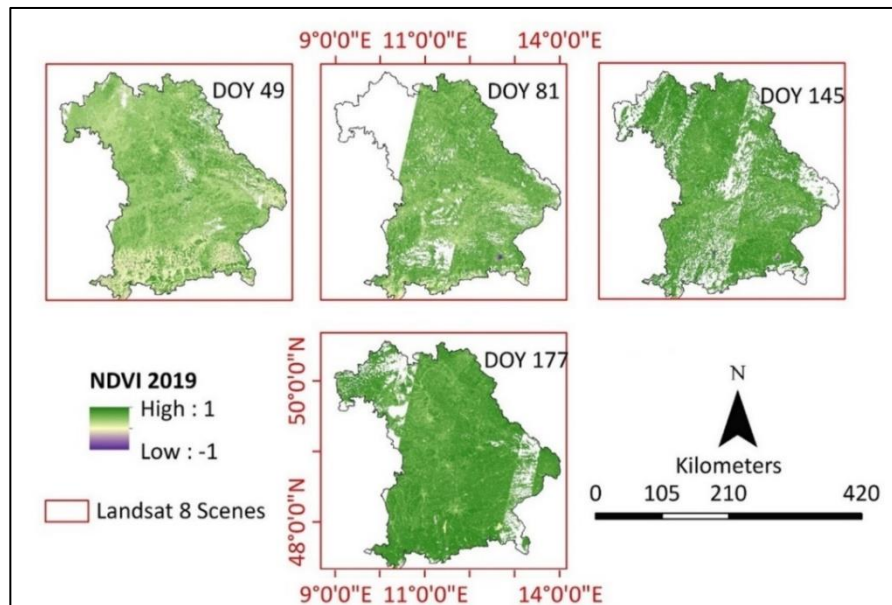


Figure 6.3. The cloud-free scenes are available for Landsat during the seasons of OSR and WW in 2019. Four cloud-free scenes were collected for the Landsat data during the season. The maps show the NDVI values from -1 to 1 for the entire Bavaria during 2019.

Table 6.2. The DOY-based statistical analysis (R^2 and mean RMSE) between the synthetic NDVI (for MOD13Q1 MODIS product) and reference Landsat (L) NDVI in Bavaria for every LC class such as agriculture (31.67%), urban (8.97%), water (1.44%), forest (35.91%), seminatural-natural (1.84%) and grassland (19.16%), in 2019. The percentage represents the number of pixels in each LC class from the total number of pixels ($n = 7,83,48,322$).

| NDVI Product | LC Class | DOY | | | | | | | |
|---------------|---------------------|------|------|------------|-----------|------|------|------------|-----------|
| | | OSR | | | | WW | | | |
| | | 49 | 81 | Mean R^2 | Mean RMSE | 145 | 177 | Mean R^2 | Mean RMSE |
| L-
MOD13Q1 | Agriculture | 0.41 | 0.49 | 0.45 | 0.11 | 0.66 | 0.65 | 0.65 | 0.10 |
| | Urban | 0.35 | 0.46 | 0.41 | 0.10 | 0.67 | 0.81 | 0.74 | 0.07 |
| | Water | 0.44 | 0.55 | 0.50 | 0.15 | 0.64 | 0.72 | 0.68 | 0.13 |
| | Forest | 0.49 | 0.53 | 0.51 | 0.06 | 0.60 | 0.46 | 0.53 | 0.05 |
| | Seminatural-natural | 0.59 | 0.64 | 0.62 | 0.07 | 0.72 | 0.64 | 0.68 | 0.07 |
| | Grassland | 0.30 | 0.35 | 0.33 | 0.12 | 0.35 | 0.45 | 0.40 | 0.11 |
| | Overall | 0.43 | 0.50 | 0.47 | 0.10 | 0.61 | 0.62 | 0.62 | 0.09 |

6.2.2. LC Map of Bavaria 2019

The LC map of Bavaria is generated by combining Amtliche Topographisch-Kartographische Informationssystem (ATKIS), Integrated Administration Control System (IACS), and Corine LC (100m) at ArcGIS pro 2.2.0 (Figure 6.3). The ATKIS data

describes the topographical objects of the landscape in vector format, generated by the official surveying system in Germany, and IACS generates all agricultural plots in European Union (EU) countries by allowing farmers to graphically indicate their agricultural areas. Combining ATKIS, IACS, and Corine LC aims to create an updated LC map of the entire Bavaria for 2019. The features of each dataset are reclassified into pre-defined land use (sub) classes, such as, agriculture (annual crops, perennial crops, and annual crop/managed grassland), forest (deciduous, coniferous, and mixed forest), grassland (managed and permanently managed grassland), urban (settlements and traffic), water, and natural-seminatural (small woody features, wetland, unmanaged grassland, and succession area). Layers with the same land use from different sources are combined into one layer. Selection of every LC class is based on the priority of data sources, for instance, agriculture: IACS > ATKIS, forest: ATKIS, grassland: IACS > ATKIS; urban: ATKIS, water: ATKIS, natural-seminatural: Corine LC > IACS > ATKIS. However, if there are conflicts among the data sources or if there are holes in the area (i.e., no information from both IACS and ATKIS), the gap is filled with Corine LC. This study uses the LC map to mask the high and low pair data fusion inputs into six LC classes before using them for the fusion process.

6.2.3. InVeKos Data

The field-based InVeKos data is used to identify the fields of WW and OSR in 2019 country-wide. InVeKos data is collected through the Integrated Administration Control System (IACS) (www.ec.europa.eu/info/index_en), which is available for all agricultural plots in European Union (EU) countries by allowing farmers to graphically indicate their agricultural areas. In the IACS, European Union countries are responsible for the administration and the control of payments to farmers through a principle called shared management.

6.2.4. In-situ Data

The field-based InVeKos data is used to identify the fields of WW and OSR in 2019 country-wide. InVeKos data is collected through the Integrated Administration Control System (IACS) (www.ec.europa.eu/info/index_en), which is available for all agricultural

plots in European Union (EU) countries by allowing farmers to graphically indicate their agricultural areas. In the IACS, European Union countries are responsible for the administration and the control of payments to farmers through a principle called shared management.

6.2.3. Method

6.2.3.1. Shannon Diversity Index

The study calculates the Shannon Diversity Index (Shannon, 1948; Wiener, 1948) to analyse the impact of land use diversity on crop biomass of WW and OSR in Bavaria 2019. The Shannon-Weiner Species Diversity Index is calculated by taking the number of total land use classes, the proportion of each class is of the total number of individuals and sums the proportion times the natural log of the proportion of each class. As the output obtained is negative, the negative of this negative of this sum was taken (Equation (6.1)). The index ranges from 0 (no diversity) to a maximum value (indicating maximum land use diversity). The equation is as follows:

$$H' = - \sum_{i=1}^s p_i \ln p_i \quad (6.1)$$

where H' is the Shannon Diversity Index, s is the number of LU classes, and p_i is the proportion of individuals of each land use class belonging to the i th class of the total number of individuals. The Shannon Diversity Index was performed at different window sizes such as, 150, 250, 350, 450, 850, 950, 1050, 1350, 1750, 2150, and 2650 m. At every radius, the diversity index values are extracted with mean, standard deviation, and range values for the fields of WW and OSR, respectively. Lastly, the correlation analysis was performed between the extracted values of Shannon diversity Index and the biomass of WW and OSR.

6.2.3.2. Difference in Landscape Metrics for OSR at different Window Sizes

The study correlated the difference (i.e., 2019 minus 2018) in landscape metrics of OSR fields at different window sizes with the modelled biomass of OSR. The landscape

metrics of one year calculates the percentage of pixels containing fields of OSR within a given radius. The calculation is as follows:

$$\text{LM in radius } X_i \text{ for OSR 2019} = \frac{\text{Number of pixels within } X_i}{\text{Number of pixels with OSR fields 2019}} \quad (6.2)$$

$$\text{LM in radius } X_i \text{ for OSR 2018} = \frac{\text{Number of pixels within } X_i}{\text{Number of pixels with OSR fields 2018}} \quad (6.3)$$

$$\text{Difference in LM} = \text{LM in radius } X_i \text{ for OSR 2019} - \text{LM in radius } X_i \text{ for OSR 2018} \quad (6.4)$$

where X_i is the radius of i moving windows (where $X_i = 150, 250, 350, 450, 850, 950, 1050, 1350, 1750, 2150, \text{ and } 2650$ m), LM is for landscape metrics. The size of one pixel is 50 m. The difference in landscape metrics is then correlated (using mean, standard deviation, and range) with the modelled biomass of OSR.

6.2.3.3. Statistical Analysis

The LUE modelled crop yield of OSR were validated using the observed crop yield at field level for 21 quadrants, respectively. The quality (R^2) and the precision (root mean square error (RMSE)) of the obtained results were calculated using the linear regression model (LRM) which aimed to establish a linear relationship between the referenced yield (independent variable) and modelled yield (dependent variable). The statistical parameters used to validate the accuracy of modelled yield are R^2 (Equation (6.5)), Mean Error (ME) (Equation (6.6)) and RMSE (Equation (6.7)). The mean, range, and standard deviation of Shannon Diversity Index of OSR and WW, and land use metrics of OSR, are used to correlate with same statistical parameters of modelled biomass of same crops, respectively. The study used the Pearson correlation coefficient (R) (Equation (6.11), where the R values lie between -1 (strong negative correlation between two variables) to 1 (strong positive correlation between two variables).

$$R^2 = \frac{((\sum P_i - P'))(O_i - O')^2}{(\sum P_i - P')^2 (\sum O_i - O')^2} \quad (6.5)$$

$$\text{ME} = \frac{1}{n} \sum_{i=1}^n (O_i - P_i)^2 \quad (6.6)$$

$$\text{RMSE} = \sqrt{\text{ME}}, \quad (6.7)$$

$$\text{mean}(x') = \frac{1}{n} \sum_{i=1}^n x, \quad (6.8)$$

$$\text{standard deviation} = \sqrt{\frac{1}{n-1} \sum_{i=1}^n (x - x')^2} \quad (6.9)$$

$$\begin{aligned} \text{range} &= \text{Maximum (within a radius of } X_i) \\ &\quad - \text{Minimum (within a radius of } X_i), \end{aligned} \quad (6.10)$$

$$R = \frac{n(\sum A_i * B_i) - (\sum A_i)(\sum B_i)}{\sqrt{((n \sum A_i^2) - (\sum A_i)^2)((n \sum B_i^2) - (\sum B_i)^2)}} \quad (6.11)$$

where P_i is the predicted value, O_i is the observed value, P' is the predicted mean, O' is the observed mean value, n is the total number of observations, x is set of observations, x' mean of observations, A_i are the first observations, B_i are the second observations, A' is the mean of first observations, B' is the mean of second observations. The significance of the obtained results was obtained by observing the probability value (*p-value*) which was calculated using the LRM with a H_0 that there is no correlation between the referenced and the modelled yields, and an H_1 that the correlation exists. The test was performed with at a significance level (or alpha (α)) of 0.05. A *p-value* lower than 0.05 indicated that the model is significant, and it rejected the H_0 that there was no correlation.

6.3. Results

6.3.1. Validation of Modelled and Observed Yield of OSR on 21 Quadrants in Bavaria 2019

For OSR, LUE model performed significantly for MOD13Q1 and L-MOD13Q1 in 2019 (having a *p-value* < 0.05); this rejected the H_0 of the linear regression model that there was no correlation between the referenced and modelled crop yield. After generating the scatter plots, the R^2 , RMSE and ME values of real MOD13Q1 and synthetic L-MOD13Q1 were analysed. From both MOD13Q1 and L-MOD13Q1, the

former resulted in higher accuracy with higher R^2 ($0.80 > 0.31$), lower RMSE ($3.91 < 9.91$ dt/ha) and lower ME ($3.10 < 6.14$ dt/ha), respectively (Figure 6.4).

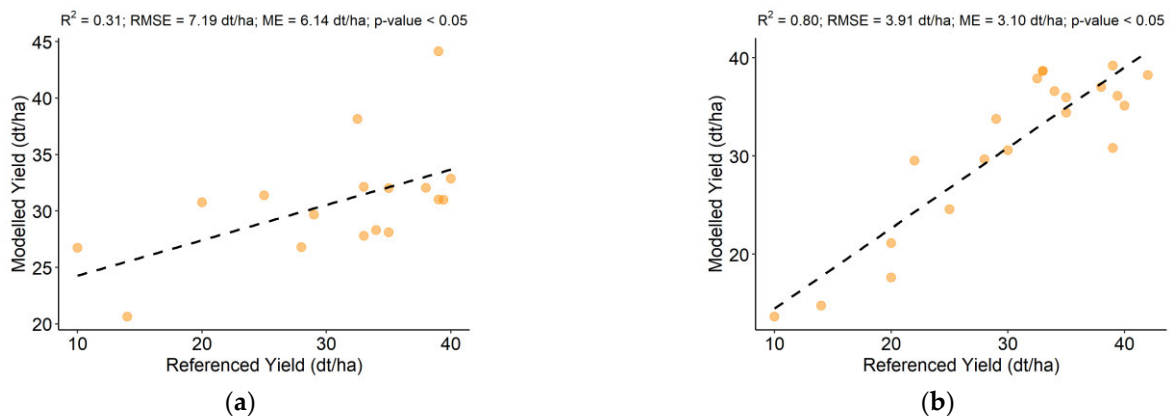


Figure 6.4. The scatter plots compare the accuracies of modelled and referenced yields for 21 quadrants using (a) real MOD13Q1 and (b) synthetic L-MOD13Q1 for OSR in 2019. The values of the statistical parameters such as R^2 , RMSE (dt/ha), and ME (dt/ha) are displayed at the top of each plot. The dashed line represents the regression line.

6.3.2. Visualization of Shannon Diversity Index at different Window Sizes for WW and OSR

The spatial distribution of Shannon Diversity Index in Bavaria is shown in Figure 6.5. The values of the diversity index started increasing from a moving window size of 150 to 2650 m. On comparing the Shannon Diversity Index for WW and OSR, the mean diversity values per field of both crops started increasing with the distance of moving window. For both crops, the mean values of diversity index are lower than 0.5 at 150 m and more than 0.8 at 2650 m (Figure 6.6). The diversity values for range and standard deviation for WW and OSR were inversely proportional to the area of moving windows. More the area, lower was the diversity index. At 150 m, the median range values of the index for both crops were more than 0.5; however, the values were nearly zero at 2650 m (Figure 6.6).

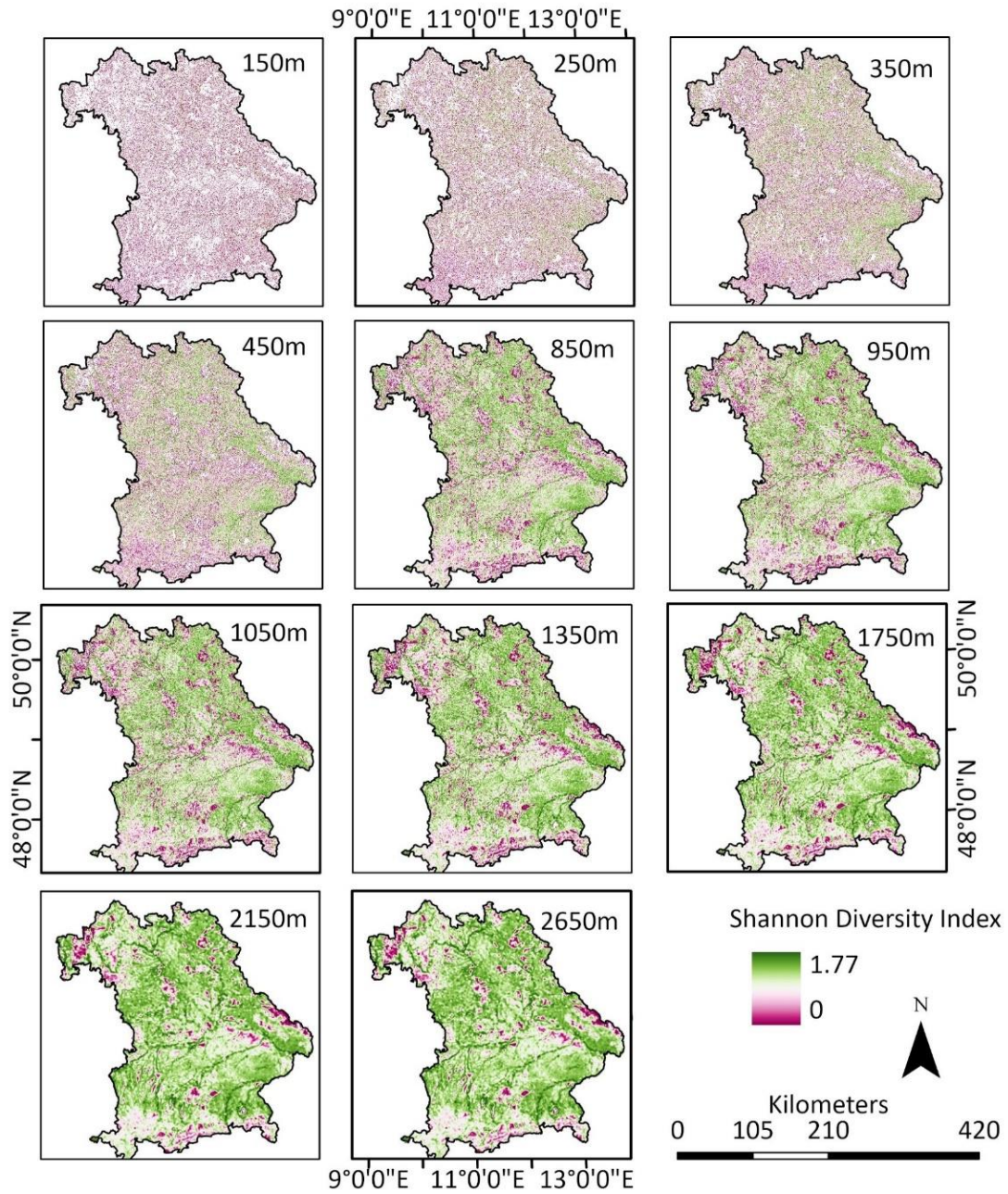


Figure 6.5. Spatial distribution of Shannon Diversity Index in Bavaria with 11 window sizes of 150, 250, 350, 450, 850, 950, 1050, 1350, 1750, 2150 and 2650 m. The lowest value of the index is 0 (dark pink color) and the highest value is 1.77 (dark green color).

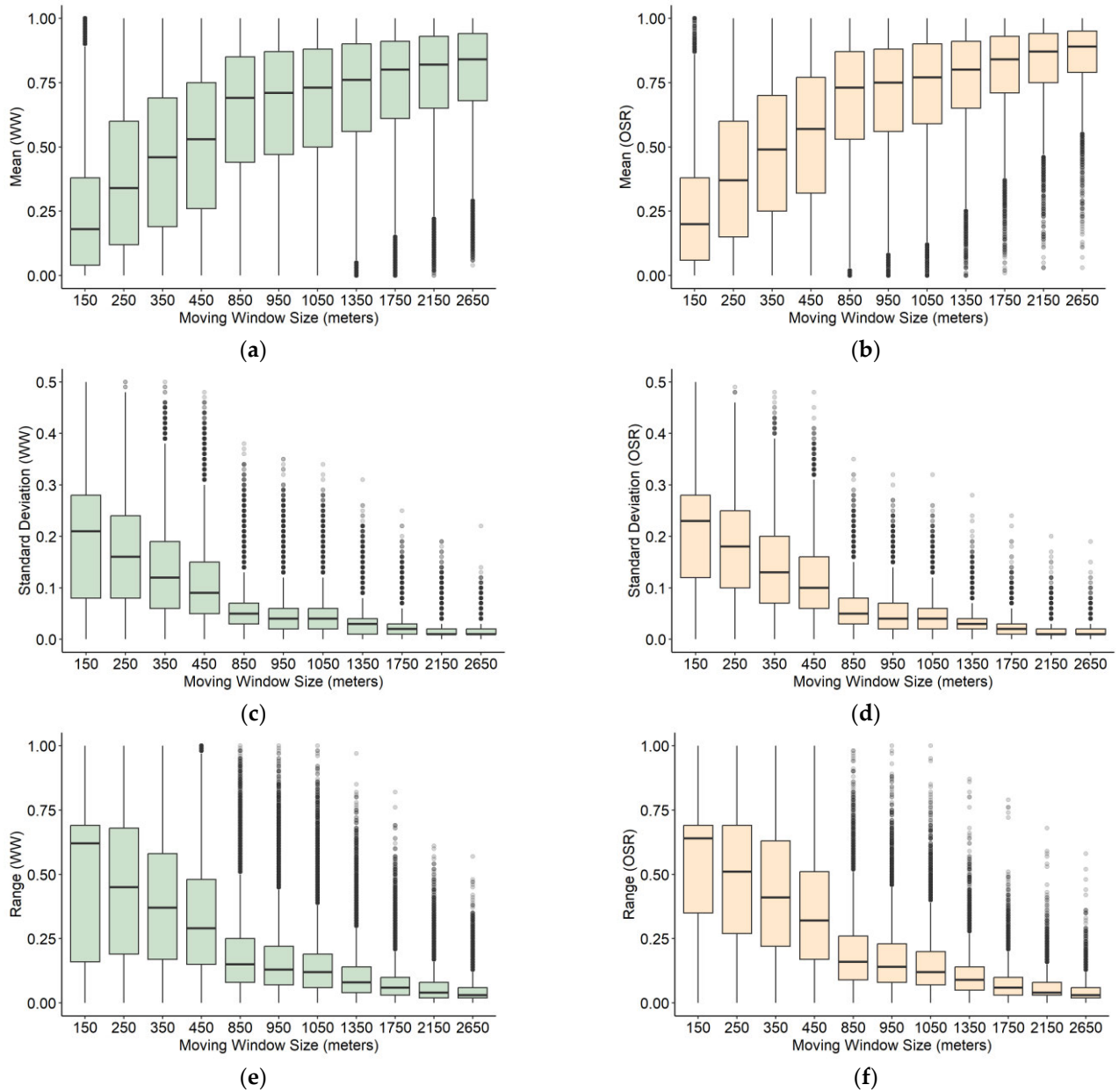


Figure 6.6. The box plots show the distribution of Shannon Diversity Index values of mean (a,b), standard deviation (c,d), and range (e,f) at different window sizes (150, 250, 350, 450, 850, 950, 1050, 1350, 1750, 2150 and 2650 m) of both WW (a,c,e) and OSR (b,d,f), respectively. The green color represents WW and the orange color represents the OSR.

6.3.3. Correlation of Mean, Range and Standard Deviation of Modelled Biomass and Shannon Diversity Index of WW and OSR in 2019

The correlation analysis between the mean of Shannon Diversity Index and the modelled biomass at different window sizes shows an increment in R from 0.24 to 0.27 from 150 to 450 m for WW (Figure 6.7). However, a decrement in R values were observed from 850 to 2650 m. For OSR, the R values increased from 0.09 (150 m) to 0.12 (850 to 1350 m) and then, decreased to 0.10 (from 1350 to 2650 m) (Figure 6.8). Similarly, the correlations between the range and standard deviation of modelled biomass and the diversity index for WW and OSR are shown in Figure A7-A10. The range and standard deviation values of both crops show similar pattern in their correlation values. For WW, the range and standard values showed increase in R values from 0.22 to 0.44, and 0.10 to 0.34 at 150 to 850 m, and decrease from 0.44 to 0.40 and 0.34 to 0.30 at 850 to 2650 m respectively (Figures 6.9a). Similarly, for OSR, the range and standard values showed increase in R values from 0.09 to 0.23, and 0.03 to 0.29 at 150 to 1050 m, and decrease from 0.23 to 0.21 and 0.29 to 0.27 at 1050 to 2650 m respectively (Figures 6.9b).

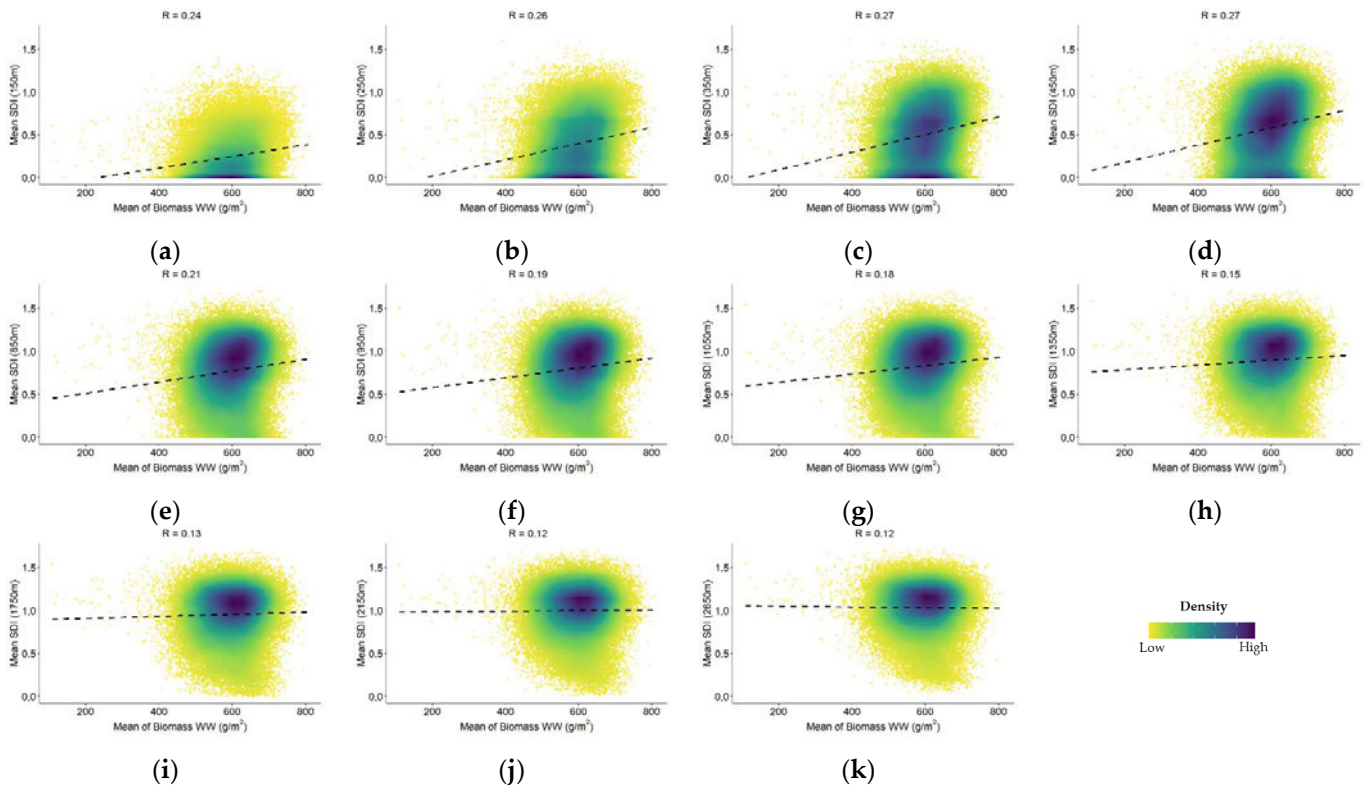


Figure 6.7. The correlation plots (a)-(k) show the relationship between the mean of Shannon Diversity Index and mean of the LUE modelled biomass on every field at different window sizes (150, 250, 350, 450, 850, 950, 1050, 1350, 1750, 2150 and 2650 m) for WW. Every plot contains a dotted line that is used to visualise the correlation of pixels between the Shannon Diversity Index and the biomass values. The blue color shows the highest point density, and the yellow color shows the lowest point density. SDI is for Shannon Diversity Index.

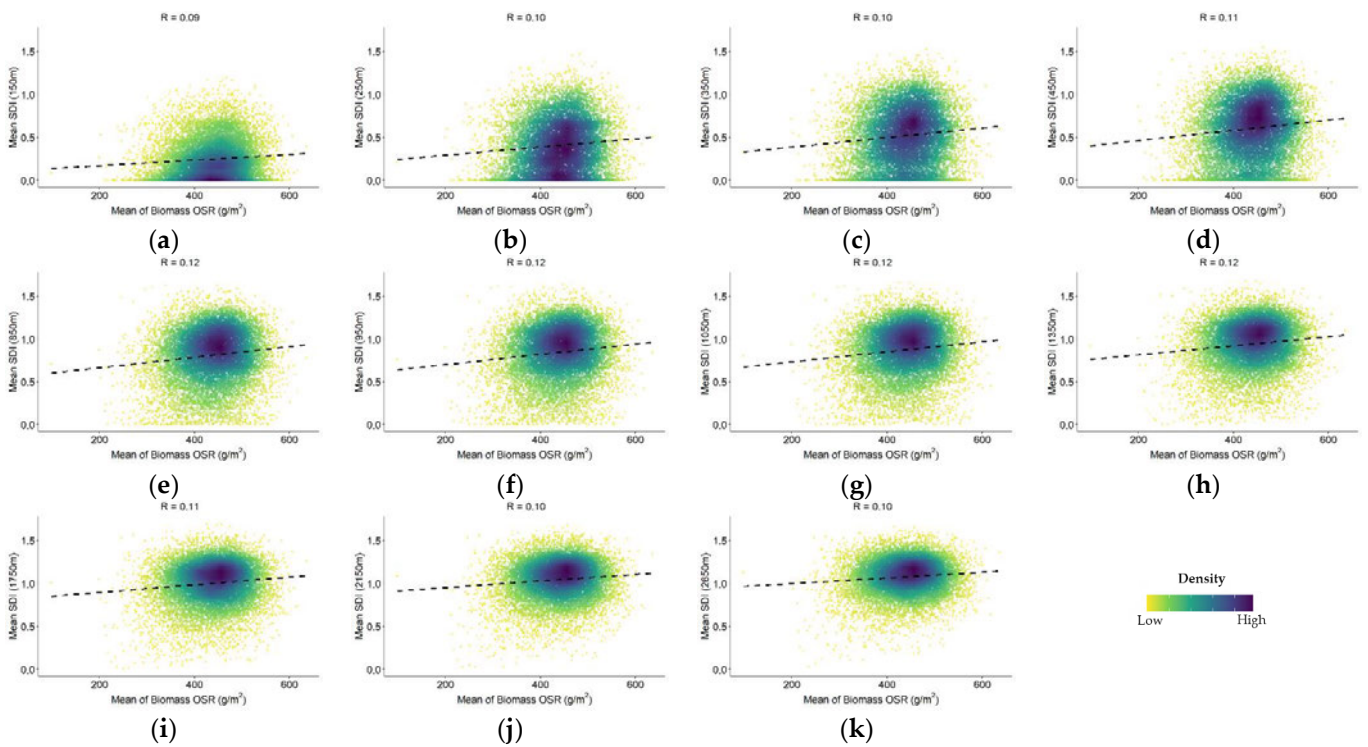


Figure 6.8. The correlation plots (a)-(k) show the relationship between the mean of Shannon Diversity Index and mean of the LUE modelled biomass on every field at different window sizes (150, 250, 350, 450, 850, 950, 1050, 1350, 1750, 2150 and 2650 m) for OSR. Every plot contains a dotted line that is used to visualise the correlation of pixels between the Shannon Diversity Index and the biomass values. The blue color shows the highest point density, and the yellow color shows the lowest point density. SDI is for Shannon Diversity Index.

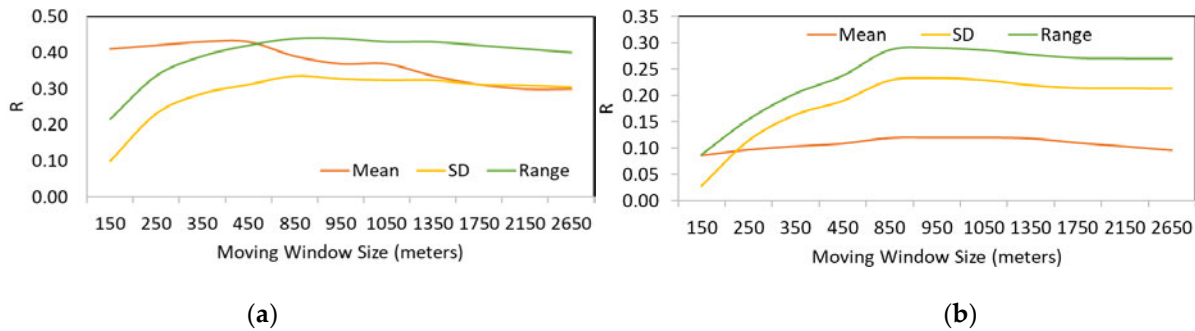


Figure 6.9. The line plots show the correlation coefficient between (the mean, standard deviation, and range of) Shannon Diversity Index and the LUE modelled biomass on every field at different window sizes (150, 250, 350, 450, 850, 950, 1050, 1350, 1750, 2150 and 2650 m) for (a) WW and (b) OSR. SD is for standard deviation.

6.3.4. Visualization of Difference in Landscape Metrics at different Window Sizes for OSR in 2018 and 2019

The spatial distribution of difference in landscape metrics from 2018 to 2019 at 350 m in Bavaria is shown in Figure 6.10. The values of the landscape metrics lied between -1 to 1; where -1 means the OSR rape fields in 2018, 0 means no change in the OSR fields between 2018 and 2019 and 1 means the OSR fields only in 2019. The values of the metrics started decreasing with a moving window size of 150 to 2650 m. On comparing the landscape metrics for OSR, the mean, range, and standard deviation of metrics values per field were inversely proportional to the window size. The mean values of landscape metrics were higher than 0.5 at 150 m and nearly to 0 at 2650 m (Figure 6.11a). At 150 m, the median range values of the metrics were more than 0.5 (range) and 0.18 (standard deviation); however, the values were almost zero at 2650 m (Figure 6.11b,c).

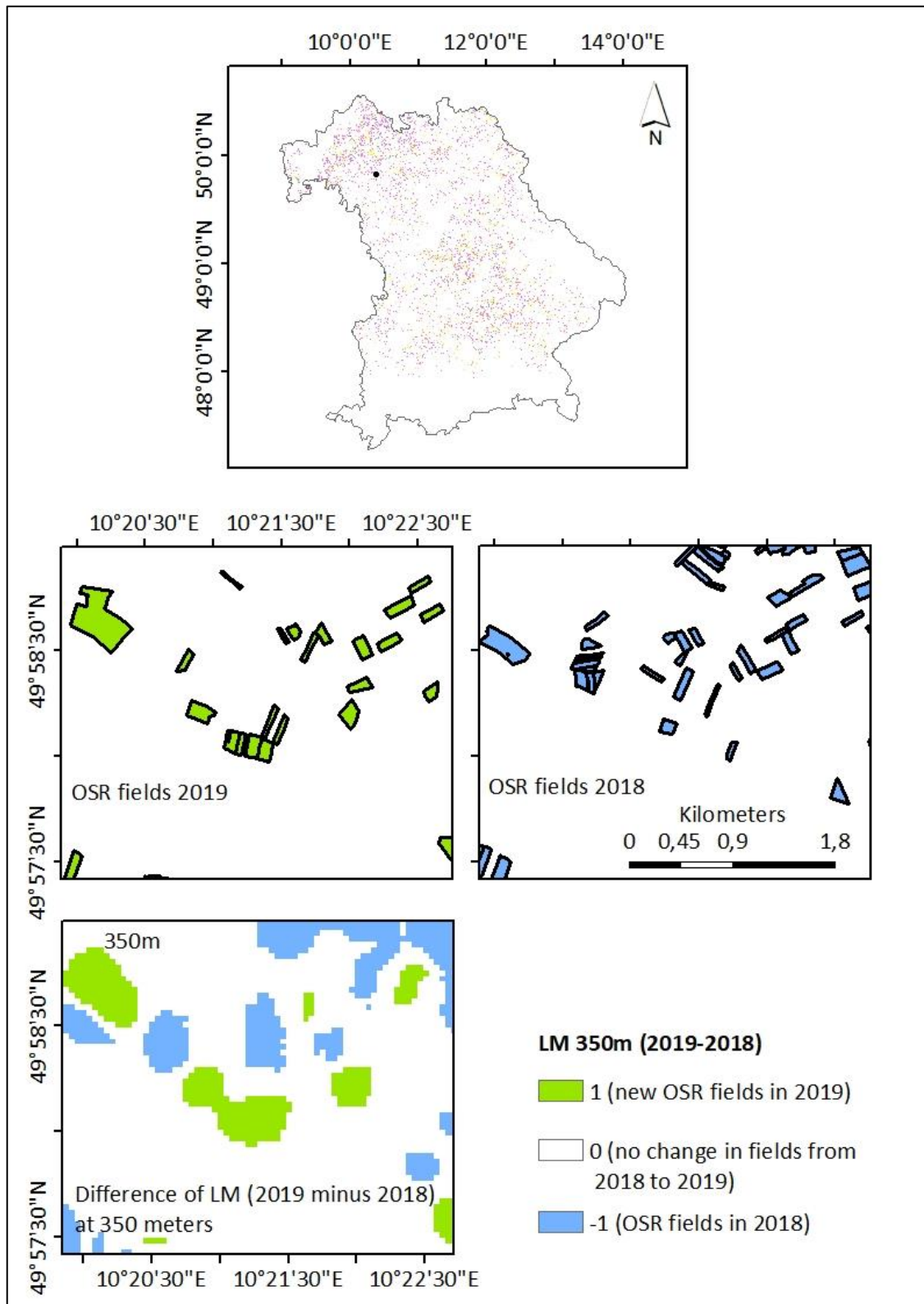


Figure 6.10. Spatial distribution of difference in landscape metrics between 2018 and 2019 in Bavaria at 750 m. The green color of the metrics shows that the new OSR fields of 2019 and blue color shows the OSR fields of 2018. The lowest value of the index is -1 (dark blue color) and the highest value is 1 (dark green color). LM is for landscape metrics.

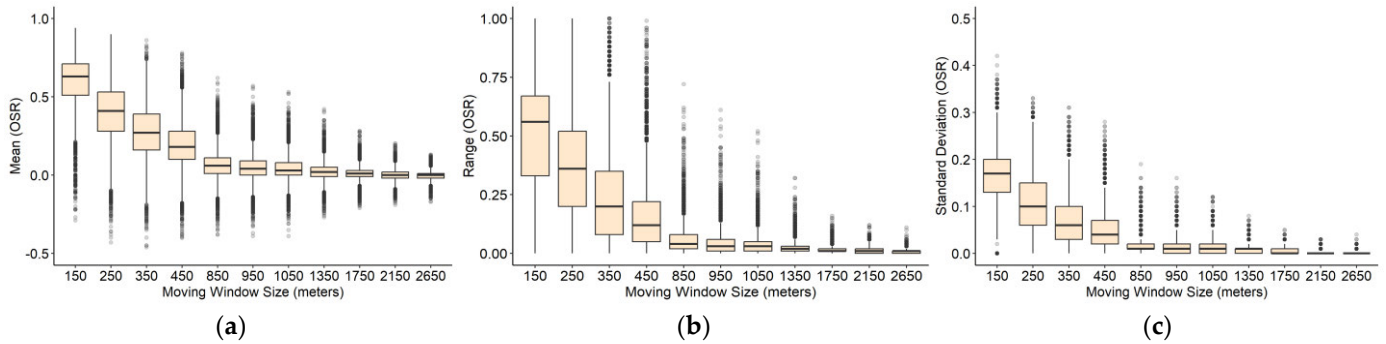


Figure 6.11. The box plots show the distribution of difference in landscape metrics between 2018 to 2019 values of mean (a), standard deviation (b), and range (c) at different window sizes (150, 250, 350, 450, 850, 950, 1050, 1350, 1750, 2150 and 2650 m) for OSR.

6.3.5. Correlation of Mean, Range and Standard Deviation of Modelled Biomass and Difference Landscape Metrics of OSR in 2018 and 2019

The correlation analysis between the mean of difference (between 2019 and 2018) in landscape metrics and the modelled biomass at different window sizes shows an increment in R from 0.13 to 0.14 from 150 to 350 m for OSR (Figure 6.12). However, a decrement in R values were observed at 350 to 2650 m from 0.14 to 0.02. Similarly, the correlations between the range and standard deviation of modelled biomass and the diversity index for WW and OSR are shown in Figure A11,12. The range and standard deviation values of OSR show similar pattern in their correlation values. The range and standard values showed increase in R values from 0.16 to 0.35, and 0.14 to 0.30 at 150 to 450 m, and decrease from 0.35 to 0.20 and 0.30 to 0.16 at 450 to 2650 m respectively (Figures 6.13).

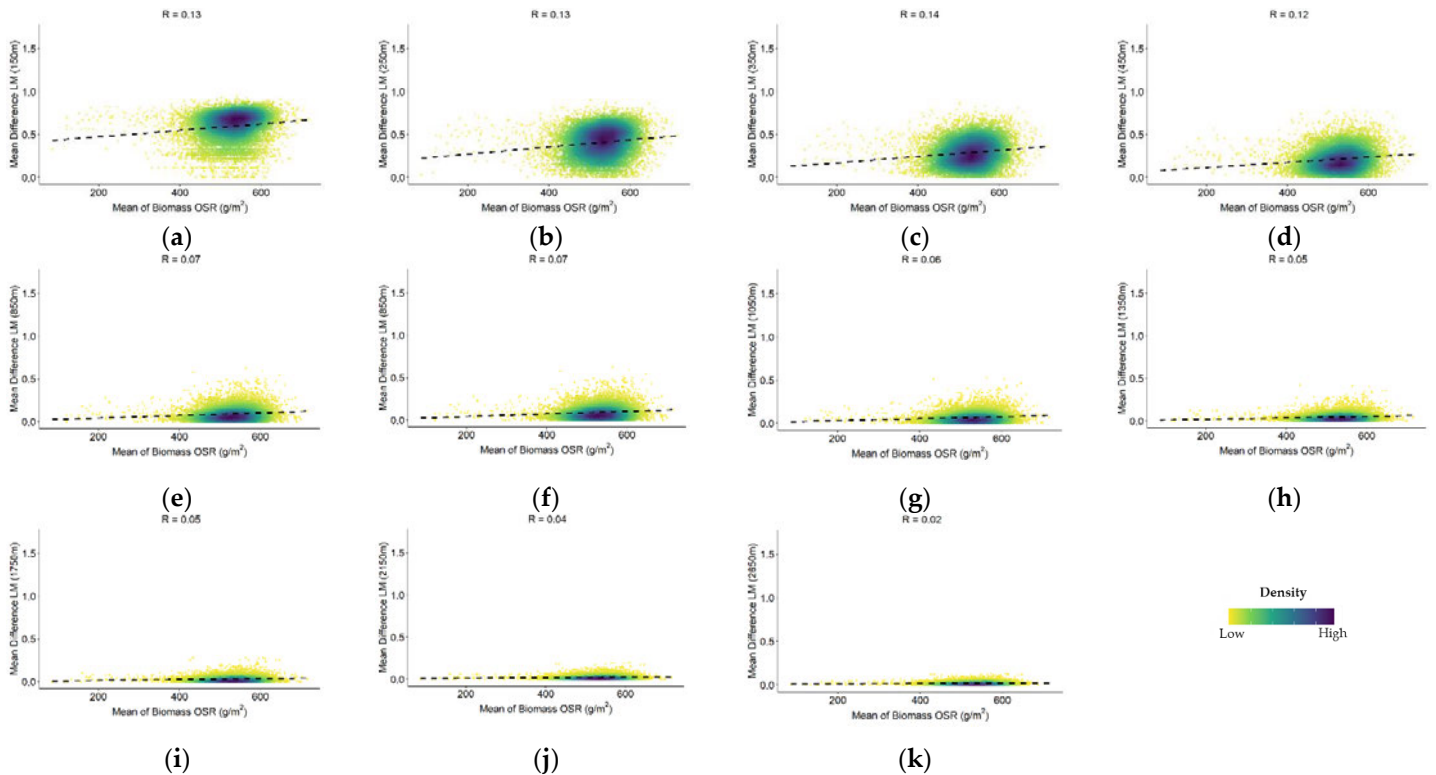


Figure 6.12. The correlation plots (a)-(k) show the relationship between the mean of difference in landscape metrics (i.e., 2019 minus 2018) and mean of the LUE modelled biomass on every field at different window sizes (150, 250, 350, 450, 850, 950, 1050, 1350, 1750, 2150 and 2650 m) for OSR. Every plot contains a dotted line that is used to visualise the correlation of pixels between the difference in landscape metrics and the biomass values. The blue color shows the highest point density, and the yellow color shows the lowest point density. LM is for landscape metrics.

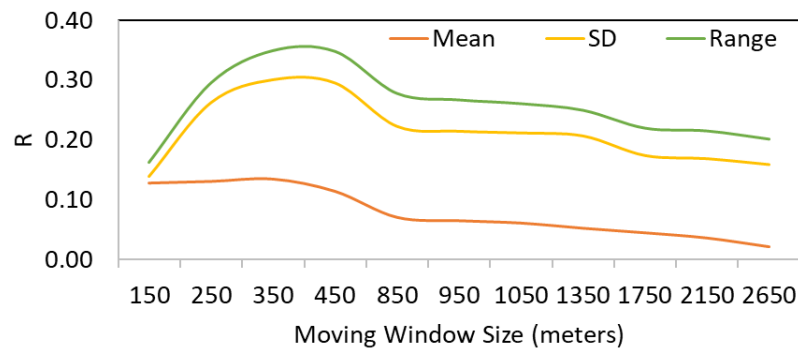


Figure 6.13. The line plot shows the correlation coefficient between (the mean, standard deviation, and range of) the difference in landscape metrics and the LUE modelled biomass on every field at different window sizes (150, 250, 350, 450, 850, 950, 1050, 1350, 1750, 2150 and 2650 m) for OSR. SD is for standard deviation.

6.4. Discussion

Firstly, the study tries to determine the impact of land use diversity on the satellite-modelled biomass of OSR and WW in 2019. For the analysis, the study uses the synthetic

remote sensing product (L-MOD13Q1) obtained after fusing MODIS with Landsat 8. The validation of modelled yield by the synthetic product is compared with the in-situ yield available for 21 quadrants in Bavaria. Secondly, the study correlates the change in arable land of OSR from 2018 to 2019 on the modelled biomass. The following section provides a brief discussion of the points mentioned above.

6.4.1. Validation of the Synthetic Data Used in Correlating Crop Biomass and Land Use Diversity

Satellite RS could be a valuable tool for correlating crop yields with land use diversity; however, it comes with its challenges of cloud and shadow gaps that limit its potential to derive conclusions accurately. The brief discussion on the potential of L-MOD13Q1 in different land use types is explained in chapter 2 (Dhillon et al., 2022). This chapter uses the field biomass calculated using the LUE model by inputting synthetic NDVI time series (L-MOD13Q1) by fusing Landsat 8 and MOD13Q1 in 2019. The chapter compares and validates the LUE calculated crop yield of OSR with the in-situ crop yield for 21 quadrants of Bavaria by the real MOD13Q1 (250 m and 8-days) and synthetic L-MOD13Q1 data (30 m and 8-days). The results prove that the coarse spatial resolution of MOD13Q1 data is insufficient to capture the variability in crop growth to calculate its biomass than the high-resolution L-MOD13Q1. On validation, the synthetic product was more accurate with higher R^2 (0.80) and lower RMSE (3.91 dt/ha) than the real satellite product ($R^2= 0.31$, RMSE = 7.92 dt/ha). However, due to the unavailability of the field-level validation data for WW, the validation results for both L-MOD13Q1 and MOD13Q1 were considered from chapter 3, which performs the validation of WW at the regional level for Bavaria. The regional level validation results for both products stated that L-MOD13Q1 obtained higher R^2 (0.82) and lowered RMSE (5.46 dt/ha) than the MOD13Q1 with lower R^2 (0.73) and higher RMSE (6.52 dt/ha).

6.4.2. Use of Shannon Diversity Index to Determine the Impact of Land Use Diversity on Crop Biomass of WW and OSR

Many studies have previously used the Shannon Diversity Index to measure diversity in ecology (D. Wang, Qiu, Wan, Cao, & Zhang, 2022; Yao et al., 2022). The chapter uses the index to analyse the impact of land use diversity on crop yields at

different window sizes (150, 250, 350, 450, 850, 950, 1050, 1350, 1750, 2150 and 2650 m). The study finds that the mean values of the diversity index are directly proportional to the window size. The larger the window size is, the more land use diversity. A more diverse landscape indicates a greater diversity of beneficial organisms, such as pollinators and natural enemies of pests which might help to improve crop yields by promoting pollination and controlling pests (Estrada-Carmona, Sánchez, Remans, & Jones, 2022). On correlating the Shannon Diversity Index with the modelled crop yields, the study finds different results for the WW (a vital cereal crop) and OSR (a widely grown oilseed crop). Studies found that land use diversity can have several positive impacts on the growth of WW (K. S. Nelson & Burchfield, 2021; K. S. Nelson, Patalee, & Yao, 2022). WW is susceptible to a range of pests and diseases, and monoculture cropping can lead to the buildup of soil-borne pathogens, pests, and weeds (H. Ma, Huang, Dong, Liu, & Guo, 2021; Vitale, Adam, & Vitale, 2020). Incorporating a diverse range of crops and non-crop vegetation in and around crop fields can help to break up pest and disease cycles and reduce pressure on crops (Lazarova, Coyne, Rodriguez, Peteira, & Ciancio, 2021). The study investigates the relationship between the mean diversity index and the modelled biomass of WW, showing an increment in R from 0.24 to 0.27 from 150 to 450 m. It states that the land use diversity (~ 0.50) within the radius of 450 m highly influences the crop yields of WW.

OSR is an insect-pollinated crop, and diverse flowering plants in the surrounding landscape can provide habitat and food resources for pollinators (Perrot, Bretagnolle, & Gaba, 2022). It can lead to increased pollination and improved seed set and yield for OSR crops. In addition, land use diversity can impact OSR growth by providing pollinators (Perrot et al., 2022; Perrot, Gaba, Roncoroni, Gautier, & Bretagnolle, 2018; Woodcock et al., 2016). Unlike the WW, the OSR, the range and standard deviation values showed an increase in R values from 0.09 to 0.23 and 0.03 to 0.29 at 150 to 1050 m, which states that the land use diversity within 1050 m (~ 0.75) for the respective crop highly impacts its yield.

On the other hand, the relationship between land use diversity and crop yields could be complex and depends on various factors, such as the specific crops being grown, the management practices used, and the local environmental conditions. Some studies suggest that moderate levels of biodiversity have the most positive impact on crop yields, while excessively high levels may have negative impacts (Clough et al., 2011; Raudsepp-Hearne et al., 2010). For example, a study found that agricultural landscapes with moderate levels of biodiversity had higher crop yields than monoculture landscapes or landscapes with excessively high levels of biodiversity (DuVal, Mijatovic, & Hodgkin, 2019). Therefore, aiming to improve the correlations and justifications for these impacts using RS, the present study recommends including the management and local environmental data in future studies.

6.4.3. Outlook

The outlook of correlating land use diversity with remote sensing modelled crop biomass can help understand the relationship between crop productivity and the diversity of land use patterns. To accurately correlate land use diversity with RS-modelled crop yields, it is essential to test the accuracy of the obtained data sets. The study suggests including other relevant factors that strongly impact crop yields and accurately interpreting the results of the correlation analysis. For example, a positive correlation between land use diversity and crop yield may indicate that a diverse landscape can support higher levels of productivity due to factors such as improved soil health, pest management, and pollination. However, it is also possible that the relationship is spurious, and other factors such as climate, management practices, and market conditions may be driving the observed patterns (DuVal et al., 2019). Moreover, the insights from correlating land use diversity with crop yield can have practical applications for agricultural management and land-use planning. For example, policymakers could use the results to identify areas where targeted interventions to increase land use diversity led to higher crop yields and more sustainable land use practices. Conclusively, correlating land use diversity with remote sensing modelled crop yield could provide valuable insights into the relationship between crop

productivity and land use patterns, which can inform agricultural management and land-use planning decisions.

6.5. Conclusions

The chapter investigated the potential of satellite remote sensing in defining the impact of land use diversity on crop biomass of winter wheat (WW) and oil seed rape (OSR) in Bavaria 2019. The biomass of WW and OSR was estimated using the synthetic remote sensing product Landsat (L)-MOD13Q1 (30 m) obtained using the Light Use Efficiency model. Secondly, the study correlates the change in arable land of OSR from 2018 to 2019 on the modelled biomass. The research paper concludes the findings as follows:

- (i) On comparing and validating the modelled yield obtained from real MOD13Q1 (250 m) and synthetic L-MOD13Q1 product at 21 quadrants in Bavaria, the results proved that the coarse spatial resolution of the former ($R^2= 0.31$, RMSE = 7.92 dt/ha) is insufficient to capture the variability in crop growth to calculate its biomass than the high-resolution of the latter ($R^2= 0.80$, RMSE = 3.91 dt/ha).
- (ii) On investigating the impact of land use diversity on the satellite-modelled biomass of OSR and WW, the results showed an increment in R from 0.24 to 0.27 from 150 to 450 m which stated that the land use diversity (~0.50) within the radius of 450 m highly influenced the crop yields of WW. Comparably, the OSR, the statistical parameters showed an increase in R values from 0.09 to 0.23 (range) and 0.03 to 0.29 (standard deviation) at 150 to 1050 m, which stated the impact of the land use diversity within 1050 m (~0.75).
- (iii) Lastly, determining the impact of arable land use between 2018 and 2019 on the modelled biomass of OSR, the results concluded that the crop rotation within 350 m in two consecutive years could positively impact the crop biomass or yield.

In conclusion, remote sensing technology has dramatically impacted our understanding of the relationship between land use diversity and satellite-modelled

Chapter 6

crop yields/biomass. It has allowed us to map land use patterns and assess changes in vegetation cover over large areas and at frequent intervals. This information has been critical in understanding the impact of land use diversity on crop productivity and identifying ways to increase crop yields through sustainable land management practices. Conclusively, remote sensing technology holds great promise for analysing land use diversity and crop yields. While the technology has positively revolutionized over the last two decades, still several challenges are needed to be addressed to ensure the accuracy and reliability of its findings. Firstly, the data is limited by its sensors' spatial and temporal resolution, which restricts its ability to detect acceptable changes in heterogeneous landscapes. Therefore, the study recommends including more fine-resolution data for future analysis. Secondly, the relationship between land use diversity and crop yields may be influenced by other factors, including soil properties, climate, management practices, and biotic and abiotic stressors. These factors may vary across different landscapes, and their influence may be difficult to disentangle from the impact of land use diversity alone. Addressing these challenges will ensure the reliability and applicability of the findings for researchers, policymakers, and practitioners in agriculture and food security.

Chapter 7

General Discussion, Outlook, and Conclusion

7.1. Importance of RS in Crop Yield Predictions

Remote sensing (RS) is notable in crop yield estimations by providing valuable insights into crop health, productivity and potential yield to farmers, researchers, and policymakers. This dissertation has effectively offered a reliable and cost-effective solution for crop monitoring over large fields, which could be difficult to perform manually. The dissertation has used different openly accessible satellite datasets, such as MODIS (spatial: 250 or 500 or 1000 m, temporal: daily, 8 or 16-days), Landsat 5,7 and 8 (30 m, 16-days), and Sentinel-2 (10 m, 5 or 16-days), for the crop yield predictions of WW and OSR in Bavaria (Chapters 3-5) (Dhillon, Dahms, Kübert-Flock, et al., 2023; Dhillon, Dahms, Kuebert-Flock, et al., 2023; Dhillon, Kübert-Flock, et al., 2023). Many studies have efficiently made use of very high resolution data such as such as DigitalGlobe (0.30 to 1.5 m, days to weeks) and Planet (3 to 5 m, daily); however these commercialized products come at a high cost (Cadamuro, 2020; Jackson, 2020).

For this dissertation, the RS technology successfully integrated with crop modelling methodologies involving the crop's physical properties, such as vegetation indices, temperature, and soil moisture. These parameters are then used to generate field estimations of crop yield that could be used to make informed decisions about field management practices, including fertilization, irrigation, pest management and harvesting. By analysing the crop yield results generated by RS, farmers could get an overview of their crop's growth patterns and detect early signs of stress and disease. It would help farmers promptly intervene in targeted areas and take informative measures to prevent yield loss and maximize profitability (Figure 7.1). Furthermore, the RS-based methodology of this study has the potential to be analysed in real-time by providing farmers or researchers with up-to-date information about their target crops, which could be used to make quick decisions about their field management practices.

Even though RS technology helps provide valuable insights into crop yield predictions, this dissertation comes out with several challenges associated with the technology (Chapter 2) (Dhillon et al., 2022). For example, the weather conditions, such as cloud and shadow cover, made it difficult for satellite images to provide a complete

picture of the crop's health and productivity and generated substantial data gaps. These data gaps made satellite RS challenging to obtain accurate crop growth information. To avoid the data gaps caused by cloud and shadow covers, the study used the multitemporal data fusion technique discussed in section 7.2.

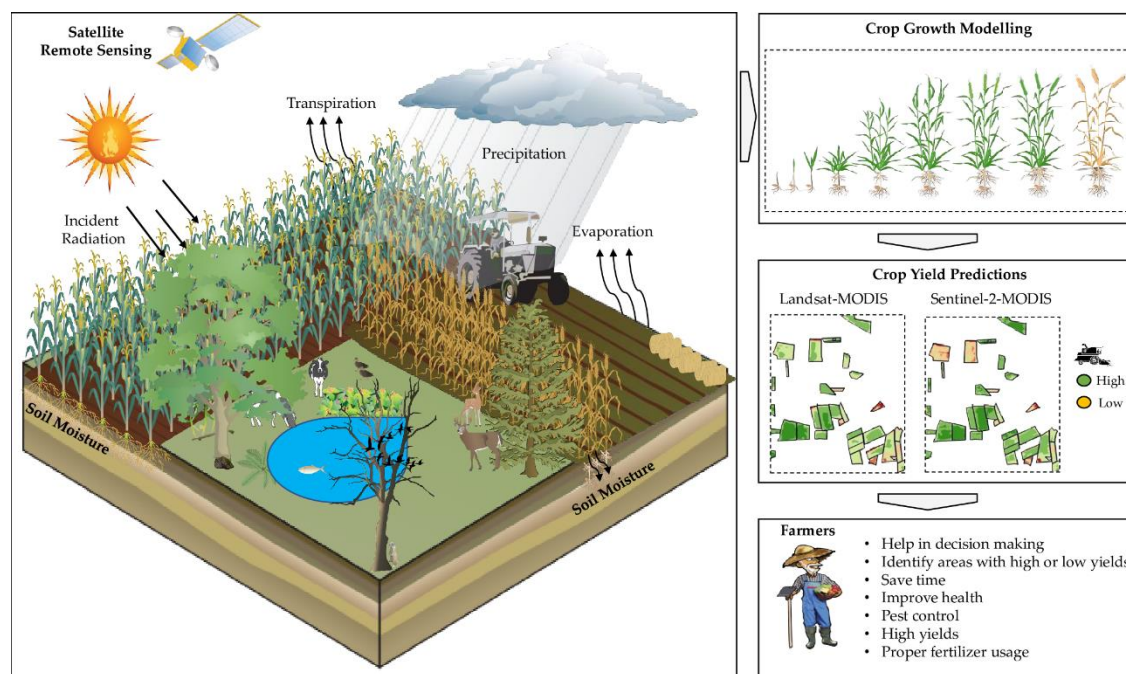


Figure 7.1. An overview stating the importance of satellite RS on predicting accurate crop yield predictions by providing certain field level benefits to farmers. Several symbols, which were used to generate the infographic, were adopted or modified according to courtesy of the Integration and Application Network, University of Maryland Center for Environmental Science (<https://ian.umces.edu/symbols/>, accessed on 20 March 2023).

7.2. Role of the Synthetic NDVI RS Data in Crop Yield Predictions

The Spatial and Temporal Adaptive Reflectance Fusion Model (STARFM)-generated NDVI data (synthetic RS data) is the substantial pillar of the dissertation. It resulted as the most crucial input parameter in crop yield predictions, and its importance was discussed throughout this thesis (Chapters 2-6). The concept of spatiotemporal data fusion using NDVI as the primary input for phenology and yield analysis (Benabdelouahab et al., 2019; Bhandari et al., 2012; Dhillon et al., 2020; Lebrini et al., 2020; Qiu et al., 2021) is not very new; however, its significance, accuracy, and reliability in improving crop yield predictions on such a large scale (for example,

Bavaria, which covers roughly 20% of the total land of Germany) has never been analysed.

Chapter 2 of this dissertation starts the analysis by discussing the primary benefits of generating synthetic data, which allows high-resolution data acquisition over large areas (Dhillon et al., 2022). The chapter also stresses the purpose of synthetic data as helpful in filling cloud and shadow gaps in the real RS data. However, investigating the best high- and low-resolution pair, as multiple RS data sets are available online, is time-consuming and requires high computation power. Chapter 2 addresses this issue by comparing the accuracies of eight NDVI synthetic data-sets obtained from two high (Landsat (L) (16-day, 30 m) and Sentinel-2 (S) (10 m, 5–6 day)) and four low (MOD13Q1 (16-day, 250 m), MCD43A4 (1-day, 500 m), MOD09GQ (1-day, 250 m), and MOD09Q1 (8-day, 250 m)) spatial resolution products (Dhillon et al., 2022). The same chapter runs the accuracy assessment of the STARFM algorithm for eight pairs of synthetic data for six different land use classes such as agriculture, forest, urban, water, grassland, and seminatural-natural, where the accuracy of the agricultural class is used as a benchmark to select the best synthetic data for the following chapters predicting crop yields (Chapters 3-5) (Dhillon, Dahms, Kübert-Flock, et al., 2023; Dhillon, Dahms, Kuebert-Flock, et al., 2023; Dhillon, Kübert-Flock, et al., 2023). For the agriculture class, synthetic products obtained using Sentinel-2 result in higher accuracy than Landsat except for L-MOD13Q1 (16-day, 30 m) ($R^2 = 0.62$, $RMSE = 0.11$), resulting in similar accuracy preciseness as S-MOD13Q1 (16-day, 10 m) ($R^2 = 0.68$, $RMSE = 0.13$). As both L-MOD13Q1 and S-MOD13Q1 result suitable for agricultural class, the study addresses that the spatial resolution of 30 m and low storage capacity makes L-MOD13Q1 more prominent and faster than that of S-MOD13Q1 with the 10-m spatial resolution (Chapter 2) (Dhillon et al., 2022). However, both S-MOD13Q1 and L-MOD13Q1 are further investigated in crop yield predictions in the other chapters (Chapters 3-5) (Dhillon, Dahms, Kübert-Flock, et al., 2023; Dhillon, Dahms, Kuebert-Flock, et al., 2023; Dhillon, Kübert-Flock, et al., 2023).

Previous studies state that the synthetic RS data can help improve the accuracy of crop yield predictions by providing a complete and more accurate picture of the crop

health and growth conditions by filling areas that may be impacted by cloud cover or shadows (B. Huang & Song, 2012; Myneni et al., 1995; J. Zhang, 2010; X. Zhu et al., 2010). Based on that, chapter 3 tests the potential of synthetic RS datasets (obtained in Chapter 2) in crop yield predictions by inputting four different synthetic (L-MOD13Q1 (30 m, 8- and 16-day), and S-MOD13Q1 (10 m, 8- and 16-day)), and two real (MOD13Q1 (250 m, 8- and 16-day)) separately to two widely used CGMs (World Food Studies (WOFOST), and the semi-empiric light use efficiency approach (LUE)) for winter wheat (WW) and oil seed rape (OSR) in Bavaria 2019. To explore the potential of newly generated synthetic data obtained from fusion modelling in crop yield predictions using crop modelling, chapter 4 highlights the importance of high spatial and temporal resolution that could improve the time-series simulation of crop models and increase the models' accuracy. As both L-MOD13Q1 and S-MOD13Q1 are obtained for a 16-day temporal resolution, chapter 4 reduces them to 8-day by using the linear interpolation approach to test and compare the lower (8-day) impact and higher (16-day) temporal resolution on crop yield predictions. The chapter obtains higher crop yield accuracies with the fused products (L- and S-MOD13Q1: $R^2 = 0.72, 0.76$ and $RMSE = 4.91, 4.49$ dt/ha) than the non-fused product (MOD13Q1: $R^2 = 0.63$ and $RMSE = 5.85$ dt/ha) for both WW and OSR irrespective of the crop model (LUE/WOFOST). It proves the importance of synthetic products (or high spatial and temporal resolution) for improving accuracy in crop modelling. It can reduce the problem of mixed pixels and increase the accuracy of different spatial properties at the field scale (Jin et al., 2018). Comparing the yield prediction accuracies of both fused products, S-MOD13Q1 results are more accurate than the L-MOD13Q1.

Moreover, high temporal resolution data also helps improve a crop's accuracy by covering the complete crop stages and measuring climate variables' impact (Waldner et al., 2019). The findings of chapter 4 prove that the 8-day products are more accurate for yield prediction than the 16-day products. Besides the chapter's prominent findings, it is still questionable to prove the stability of yield predictions as only one year of synthetic data is used and compared using simulation methods. To adequately prove the methods' reliability, stability, and preciseness, chapter 4 further investigates the crop yield predictions for two decades, inputting long-term synthetic time series.

Both chapters 2 and 3 are focused on 2019, and S-MOD13Q1 has obtained better accuracy than L-MOD13Q1; however, chapter 4 is a continuation of the previous chapter with a focus on more extended time series for crop yield predictions (Dhillon, Dahms, Kübert-Flock, et al., 2023; Dhillon, Dahms, Kuebert-Flock, et al., 2023; Dhillon, Kübert-Flock, et al., 2023). Therefore, chapter 4 generates and validates Landsat-based synthetic NDVI time series (L-MOD13Q1) due to its continuous availability since 1982 (Dhillon, Dahms, Kübert-Flock, et al., 2023). Chapter 4 discusses how the accuracies of synthetic RS NDVI data inputted to a CGM could impact the final accuracy of crop yield predictions. The chapter generates and validates the NDVI synthetic data by fusing the high spatial resolution (30 m, 16-days) Landsat 5 Thematic Mapper (TM) (2001 to 2012), Landsat 7 Enhanced Thematic Mapper Plus (ETM+) (2002 to 2011), and Landsat 8 Operational Land Imager (OLI) (2013 to 2019) with the coarse resolution of MOD13Q1 (250 m, 16-days) from 2001 to 2019. In the following steps, the chapter discusses various factors responsible for affecting the accuracy of yearly crop yield predictions, for example, the number of cloud and shadow-free Landsat scenes available per year (N), the difference in quality among Landsat 8, 7, and 5 sensors, digital elevation model (discussed in section 7.4), and climate elements (discussed in section 7.3). The chapter finds that the accuracies of the NDVI fusion data have been strongly correlated with the total number of available Landsat scenes every year (N), with a correlation coefficient (R) of +0.83 (between R^2 of yearly synthetic NDVIs and N) and R of -0.84 (between RMSEs and N). The chapter finds that Landsat OLI-based fusion with MOD13Q1 resulted in higher accuracy than Landsat TM (Poursanidis et al., 2015). For instance, the years 2001, 2002, 2004, 2005, and 2012 (Landsat 5 and 7) have low R^2 (<0.60) and high RMSE (>0.12) than the remaining years (using Landsat 8). However, the chapter finds some exceptions in the analysis. For example, 2011 and 2016, with more N (~ 6), result in lower crop yield accuracy than 2007, 2008 and 2011 ($N = \sim 8$). It might result from the impact of climate variables inputted to the LUE model (discussed briefly in section 7.3). Moreover, the chapter observes that the few cloud-free days of the year (DOYs) could create significant gaps between the available Landsat scenes that might affect the accuracy of the fusion product (Dhillon et al., 2022; Dhillon et al., 2020). For example, the DOYs 33 to 97 ($N = \sim 6$) result in low R^2 (0.54) and high RMSE (0.16) as compared to the DOYs 113 to 193 (N

= ~8) with high R^2 (0.64) and low RMSE (0.10). Lastly, the chapter concludes that synthetic RS time series substantially impacted the accuracy of crop yield predictions as the study observes a high positive correlation of $R=0.81$ and $R=0.77$ between the yearly R^2 of synthetic accuracies with modelled yield accuracies for WW and OSR, respectively. Chapter 4 plays a vital role in this dissertation, and its findings show the dependency of crop yield outputs on the synthetic NDVI datasets; however, in the outlook, the chapter states to use the machine learning (ML) algorithms in combination with CGMs inputting synthetic NDVI datasets could even improve the accuracy of the crop yield predictions (Dhillon, Dahms, Kübert-Flock, et al., 2023).

Based on the outlook of previous chapters, the fifth chapter couples random forest (RF) and LUE to improve the yield prediction accuracies of WW and OSR for Bavaria in 2019 (Chapters 3,4) (Dhillon, Dahms, Kübert-Flock, et al., 2023; Dhillon, Kübert-Flock, et al., 2023). The chapter investigates that when the synthetic data is used with the coupling of LUE and ML learning models, it positively impacts the crop yield predictions more than the LUE model. For example, the accuracy of S-MOD13Q1 (8-day) with coupling models ($R^2 = 0.91(\text{WW})/ 0.84(\text{OSR})$; $\text{RRMSE} = 7.29/8.83\%$) is higher than the LUE model ($R^2 = 0.88/0.84$; $\text{RRMSE} = 7.93/9.42\%$) (Dhillon, Dahms, Kuebert-Flock, et al., 2023).

Moreover, synthetic NDVI RS data's significance in improving crop yield predictions could be for many reasons (Chapters 2-5) (Dhillon, Dahms, Kübert-Flock, et al., 2023; Dhillon et al., 2022; Dhillon, Dahms, Kuebert-Flock, et al., 2023; Dhillon, Kübert-Flock, et al., 2023). Integrating data from multiple sources can reduce errors caused by atmospheric conditions, sensor calibration, and other factors, which can lead to more accurate and reliable data. For example, spatiotemporal data fusion can help reduce the noise and errors caused by the different sources (Moreno-Martínez et al., 2020). Significantly, the data fusion methods can help improve crop yield predictions' accuracy by providing a complete and more accurate picture of the crop health and growth conditions. Even though the STARFM method has some limitations (Hilker et al., 2009; David P. Roy et al., 2008; X. Zhu et al., 2010), its public availability of code,

simplicity of design and ability to generate consistent results was the major attraction of including it in the study (Chapters 2-4).

7.3. Comparison of Crop Yield Prediction Models

The dissertation compares several crop yield prediction models intending to improve yield accuracy (Chapters 3,4) (Dhillon, Dahms, Kübert-Flock, et al., 2023; Dhillon, Kübert-Flock, et al., 2023). Chapter 3 uses the conventional technique of CGMs to monitor Bavarian WW and OSR yields by integrating STARFM-generated S-MOD13Q1 (10 m, 8- or 16-day) and L-MOD13Q1 (30 m, 8- or 16-day) and real MOD13Q1 (250 m, 8- or 16-day) products in the two CGMs: WOFOST and LUE. Like other studies, the chapter finds that the WOFOST model, which requires more input parameters, is complex in its design and needs more processing time to generate the output (Dhillon et al., 2020). The WOFOST model results for WW in R^2 of 0.71 and RMSE of 7.75 dt/ha, while the LUE model results in R^2 of 0.81 and RMSE of 5.17 dt/ha. Overall, irrespective of the crop type and satellite spatial scale, the LUE model (average $R^2 = 0.77$, RMSE = 4.45 dt/ha) performs more accurately than the WOFOST model (average $R^2 = 0.66$, RMSE = 7.75 dt/ha). Comparing the performance of both models based on different crop types, the LUE model performs consistently for WW and OSR models with an R^2 of 0.76 (for both crops) and RMSE of 6.34 (WW)/2.84 (OSR) dt/ha. In contrast, the WOFOST model performs better for WW than the OSR with an accuracy of 0.71/0.63 (R^2) and 7.75/3.78 dt/ha (RMSE). The chapter concludes that the model requiring fewer input parameters (LUE) to simulate crop biomass is highly applicable and precise. At the same time, LUE is more accessible to implement than models which needed more input parameters, such as WOFOST (Dhillon et al., 2020). However, many past studies have preferred the WOFOST model for accurate yield predictions (J. Huang, Tian, et al., 2015; G. Ma et al., 2013; Zhuo et al., 2022). The management data requirement is a critical variable affecting the WOFOST model's accuracy of WW and OSR. The accuracy of both models is also influenced by the spatial and temporal resolution of the RS input used. For example, both models obtain higher accuracy with the synthetic RS products (particularly the S-MOD13Q1 (10 m, 8-day)) than the coarse MOD13Q1.

Based on the best model output of chapter 3, chapters 4 and 5 analysed crop yield predictions using the LUE model. Even though the crop yield results obtained by chapter 3 using the LUE model are accurate, it would be hard to justify the stability and preciseness of the model as the chapter is only focused on one year of analysis (Dhillon, Kübert-Flock, et al., 2023). Based on this shortcoming, chapter 4 continues the study and predicts crop yields using the LUE for two decades (2001 to 2019) (Dhillon, Dahms, Kübert-Flock, et al., 2023). The model performs significantly for both WW and OSR; however, some years obtain higher accuracy than others. For example, 2007, 2018, and 2019 are the most accurate years, with R^2 of more than 0.79 for both crop types. However, as discussed in the last section (7.1), the model results are highly influenced by the quality of the synthetic RS input used. Moreover, the climate elements and elevation of the crops grown also affect the model results. Section 7.3 discusses the impact of climate elements on the accuracy of modelled yields for both chapter 3 and chapter 4.

7.4. Influence of Climate Elements in Crop Yield Predictions

Besides the synthetic NDVI input, climate data played an essential role in impacting the accuracy of crop yield predictions (Chapters 3-5) (Cabas et al., 2010; Dhillon, Dahms, Kübert-Flock, et al., 2023; Dhillon, Dahms, Kuebert-Flock, et al., 2023; Dhillon, Kübert-Flock, et al., 2023; Sidhu et al., 2023). Both chapters 3 and 4 perform sensitivity analysis by removing the impact of climate elements from crop modelling. Chapter 3 investigates that including climate stress indices in CGMs improves the performance of both models by decreasing the RMSE by -38% (LUE) and -11% (WOFOST) and increasing the R^2 from 19% and 12%, respectively. Similarly, chapter 4 performs the sensitivity analysis from 2001 to 2019 and finds an increase in R^2 (0.79/0.86) and a decrease in RMSE (4.51/2.57 dt/ha) by including the effect of climate elements in the LUE model. The reason for better yield prediction accuracy could be that the climate had already influenced the referenced or the validation yield.

Moreover, the relationship between climate and crop yield undergoes significant shifts, which might be the reason that some years (2011 and 2016) with higher N (8) obtained lower crop yield accuracy than years (2007, 2018 and 2019) with comparably

lower N (6) (Chapter 4) (Dhillon, Dahms, Kübert-Flock, et al., 2023). Chapter 5 further illustrates that the crop and phenology-related variables (LUE biomass), solar radiation, soil moisture, extra-terrestrial radiation and temperature are the most influential variables in increasing the yield accuracy for WW and OSR (Dhillon, Dahms, Kuebert-Flock, et al., 2023). In summary, climate data is critical in accurate crop yield predictions by providing information on weather patterns and other climatic factors that affect crop growth and development. Farmers and agricultural experts can make better-informed decisions to optimize crop yields and adapt to changing climate conditions by incorporating climate data into yield prediction models and decision-making processes (Lezoche, Hernandez, Díaz, Panetto, & Kacprzyk, 2020; Stone & Meinke, 2006).

7.5. Spatial Analysis of Yield Variation in Bavaria

As the dissertation predicts the crop yield for the 96 counties of the Free State of Bavaria, the crop models spatially resulted in different prediction results (Chapters 3-5) (Dhillon, Dahms, Kübert-Flock, et al., 2023; Dhillon, Dahms, Kuebert-Flock, et al., 2023; Dhillon, Kübert-Flock, et al., 2023). For both chapters 3 and 4, the LUE were precarious in specific regions, especially the districts at higher elevations in the south (Bavarian Alps) and east (Bavarian Forest and Fichtel Mountains) of Bavaria for both WW and OSR. The model highly overestimates the crop yield in regions such as Regen, Freyung-Grafenau, Bad Tölz-Wolfratshausen, Garmisch-Partenkirchen, Oberallgäu, Miltenberg, Deggendorf and Dachau; it underestimates the yield as compared to the referenced yield for WW. Based on the results of previous studies, which found that the elevation significantly impacted the regional crop yield, chapter 4 analyses the impact of elevation on comparing the crop yields at the regional level (Bhatt et al., 2014; Dhillon, Dahms, Kübert-Flock, et al., 2023; Thomson et al., 2002). The survey finds negative correlations between the mean regional elevations and the crop yields of WW (-0.30) and OSR (-0.38).

Similarly, many studies found lower crop productivity at higher elevations due to complex topography and different climate and management practices (Anderson et al., 2016; Semwal & Maikhuri, 1996). Moreover, the cropping intensity at lower elevations was higher than at higher elevations. Chapter 4 calculates the county-wise mean yield difference from 2001 to 2019 and results that the model performed relatively stable for

48 districts (out of 71) for WW with a slight change between -2% to $+2\%$. However, only 27 (out of 65) districts performed stably for OSR (Dhillon, Dahms, Kübert-Flock, et al., 2023). The reason could be linked with the DOYs 33 to 97 ($N = \sim 6$) needed for the analysis of OSR result in low R^2 (0.54) and high RMSE (0.16) as compared to the DOYs 113 to 193 ($N = \sim 8$) needed for WW with high R^2 (0.64) and low RMSE (0.10).

Moreover, other reasons for the model's instability could be either higher elevations or the bad quality of the synthetic NDVI products for specific regions. As the crop yield predictions are strongly dependent on the quality of the synthetic products, it could be that these regions have no horizontal or vertical overlay of Landsat scenes within the path row, which limits their coverage frequency. Moreover, chapter 3 compares the performance of both models based on the synthetic data inputted and finds the LUE model with S-MOD13Q1 8-day showing higher regional accuracy than the WOFOST model (Dhillon, Kübert-Flock, et al., 2023).

7.6. Potentials and Limitations of the Research

Despite certain advantages, chapters 3 and 4 discuss certain limitations and disadvantages of the CGMs (Dhillon, Dahms, Kübert-Flock, et al., 2023; Dhillon, Kübert-Flock, et al., 2023). They can require a detailed understanding of crop physiology and environmental factors. Due to the need for more detailed information about a crop, CGMs are very dependent on the quality of the RS product inputted. The poor quality of the input products can make CGMs challenging for farmers and others without specialized knowledge or training. Calibration and validation of the models can be time-consuming and expensive. Despite their complexity, CGMs could still be limited in their accuracy, mainly when predicting yields at the plant level (Drummond et al., 2003; Puntel et al., 2016; Shahhosseini et al., 2019).

Similarly, many studies have used ML approaches to predict crop yields in different parts of the world (Champaneri, Chachpara, Chandvidkar, & Rathod, 2016; Kale & Patil, 2019; Shahhosseini et al., 2021; Q. Zhou & Ismaeel, 2021). Even though ML has become a popular technique for predicting crop yields, several challenges must be overcome to ensure accurate and reliable predictions. Firstly, the algorithms require high-quality data to learn patterns and make accurate predictions. However, data availability for

crop yield predictions is often limited, particularly in developing countries, where data collection and management could be more advanced (Breiman, 2001; Segal, 2004). Secondly, models can be difficult to interpret, making it challenging to understand why specific predictions are made (Murdoch, Singh, Kumbier, Abbasi-Asl, & Yu, 2019). It can be a problem for stakeholders who must understand the factors contributing to crop yield predictions. Chapters 3 and 4 advised investigating the potential of integrating CGMs with ML algorithms for accurate crop yield predictions to make the prediction process transparent (Dhillon, Dahms, Kübert-Flock, et al., 2023; Dhillon, Kübert-Flock, et al., 2023). Therefore, chapter 5 hypothesizes that integrating crop modelling with ML would improve the accuracy of crop yield predictions (Dhillon, Dahms, Kuebert-Flock, et al., 2023).

Both LUE and RF models were combined to analyse the accuracy of both WW and OSR for Bavaria. The chapter found that with the individual use of both RF and LUE models, the performance results were between 0.70-0.78 (WW)/ 0.60-0.76 (OSR) (R^2) (Dhillon et al., 2020). However, a drastic improvement in the accuracy was seen when the LUE model was linked with the random forest model by including more climate variables as input. This coupling has increased the R^2 from 0.78 to 0.85 and 0.76 to 0.81 for WW and OSR respectively using different satellite inputs.

Chapters 3, 4, and 5 discuss the imbalance in the availability of the crop yield validation data at the regional level and the crop-modelled results obtained at the pixel level for Bavaria (Dhillon, Dahms, Kübert-Flock, et al., 2023; Dhillon, Dahms, Kuebert-Flock, et al., 2023; Dhillon, Kübert-Flock, et al., 2023). Even though this uncertainty was less problematic for the outcomes of this dissertation, still bringing pixel-based modelled results to the regional level might affect the validation results negatively. Moreover, there are some limitations found in the validation data. The regions of southern Bavaria (Bad Tölz-Wolfratshausen, Garmisch-Partenkirchen, Traunstein, Unterallgäu, and Oberallgäu) had fewer fields of WW and OSR; however, the validation data records higher yields for the respective regions which are inversely proportional to the crop modelled results. For all the analyses done for 2019, these regions were removed. Therefore, for future research, it is advisable to include field-based crop yield

results to secure the accurate validation of crop yields obtained using satellite products. Additionally, crop-related parameters, such as crop management practices, the amount of fertilizer used, soil information, and seed type, could be included as input to the CGMs with a hypothesis to improve their crop prediction accuracy.

7.7. Broader Implications of this Research: Outlook of the Study

The implications of the dissertation extend beyond the immediate scope of the research and could contribute to a broader understanding of including, developing, and implementing new data and methods for improving the accuracies of crop yield predictions using RS. Future studies could explore using Sentinel-1 SAR data, hyperspectral or other sensors, and Landsat, MODIS, and Sentinel-2 for better future accuracies. It could provide a more comprehensive understanding of the relationship between RS and crop yield predictions. The dissertation could suggest using UAVs or drones, in addition to satellite remote sensing, which could provide higher-resolution data and enable a more precise analysis of yield forecasting for precision agriculture. The study could propose integrating DL models with crop modelling to provide more accurate predictions and potentially help overcome existing models' limitations. For a more global understanding of the potential of the dissertation, the study methodology could be transferred to other regions of the world to explore how the findings can be applied in different contexts. Also, the study methods could be used for different crop types (such as maize, rice, and cotton) worldwide beyond WW and OSR. Doing so could lead to a more comprehensive understanding of how synthetic RS can predict crop yields across various crops and regions. The dissertation also suggests validating the crop yield outputs of CGMs at the field level, which could help improve models' performance and promote sustainable and precision farming.

Moreover, the dissertation suggests covering the limitations of chapter 6, which investigates the pros and cons of RS and analyses the relationship between the land use diversity and modelled crop biomass of WW and OSR in Bavaria 2019. Chapter 6 states that the biomass of WW and OSR were positively impacted by land use diversity to the radius of 450 (Shannon Diversity Index ~ 0.75) and 1050 m (~ 0.75) from the respective

crop fields. However, the results achieved a weak correlation between the modelled biomass and land use diversity. Further, the chapter discusses the importance of dependent factors such as the specific crops being grown, the management practices used, soil health, biotic and abiotic stressors, pest management, pollinators, and the local environmental conditions that might be impactful on positively affecting the accuracy of the analysis (Clough et al., 2011; Raudsepp-Hearne et al., 2010). Considering the factors mentioned above, this study can stimulate future research on the relationship between crop yields and land use diversity, resulting in more reliable and applicable findings for researchers, policymakers, and practitioners in agriculture and food security. It could aid in maximizing yields while also promoting biodiversity conservation.

7.8. Conclusions

With its ability to collect data on a large scale and with a high level of precision, remote sensing (RS) has enabled researchers to analyse and monitor crop growth and yield patterns in real-time. The thesis aims to provide a comprehensive overview of the potential of remote sensing in addressing one of the most pressing challenges of our time - how to increase agricultural productivity and sustainability in the face of a changing climate and growing demand for food. Having fulfilled its objectives, this dissertation yields the following general conclusions.

- (i) The dissertation compares the performance of eight NDVI synthetic products (including two high pairs: Landsat (L) and Sentinel-2 (S) and four low pairs: MODIS) generated using the STARFM for the entire state of Bavaria in 2019. The thesis states that the synthetic products obtained using Sentinel-2 are more accurate than products obtained using Landsat. Therefore, Sentinel-2 could be used as an input high-pair product for the STARFM. MOD13Q1 is deemed the most fitting among the low-pair products for this purpose. The synthetic NDVI products L-MOD13Q1 (30 m) and S-MOD13Q1 (10 m) are considered the most appropriate for six distinct land use categories (agriculture, forest, grassland, semi-natural, urban, and water), owing to their superior quality. However, the spatial

resolution of 30 m and low storage capacity makes L-MOD13Q1 more prominent and faster in pre-processing than S-MOD13Q1 with the 10-m spatial resolution.

- (ii) On comparing the performance of six different remote sensing products (synthetic: L-MOD13Q1 (8- and 16-days) and S-MOD13Q1 (8- and 16-days), real: MOD13Q1 (8- and 16-days)) when inputted to crop growth models (CGMs) to estimate crop yields of winter wheat (WW) and oil seed rape (OSR), the synthetic products result in higher accuracy than the real products. The observations of high temporal resolution (8-day) products of both S-MOD13Q1 and L-MOD13Q1 played a significant role in accurately measuring the yield of both crop types with the light use efficiency (LUE) model (proven to be a simpler, more precise, and accurate model than the WOFOST), respectively. The dissertation recommends using S-MOD13Q1 as the optimal spatial resolution for precise crop yield predictions. It is due to its ability to reduce uncertainties related to mixed pixel information, thereby increasing the accuracy and precision of the yield model. In contrast, using the L-MOD13Q1 product is better suited for generating and analysing long-term yield time series. It is attributed to the availability of Landsat data dating back to 1982, with a maximum resolution of 30 m, making it more advantageous. The study explores the importance of climate variables while validating crop yields with the referenced yields, which the impact of climate parameters had already influenced. It results in an improvement in the performance of CGMs when the climate stress indices are incorporated.
- (iii) When assessing the crop yield accuracy of the LUE model from 2001 to 2019, the dissertation investigates the impact of input data fusion. Specifically, when plotting the accuracy of synthetic NDVI time series against the accuracy of the modelled crop yield for WW and OSR, strong positive correlations are found, with correlation coefficient (R) values of 0.81 and 0.77, respectively. Negative correlations are found between mean regional

elevations and crop yields of WW (-0.30) and OSR (-0.38). Additionally, the thesis reveals that the cropping intensity tends to be higher at lower elevations than at higher elevations. Therefore, the study finds that the accuracy of the LUE is less reliable in certain regions, particularly in districts located at higher elevations in the south (Bavarian Alps) and east (Bavarian Forest and Fichtel Mountains) of Bavaria, where the referenced crop yields were observed to be higher than the modelled yields. Moreover, the study observes that the relationship between climate and crop yield experiences significant variations, which is why specific years (2011 and 2016) showed lower crop yield accuracy than others (2007, 2018, and 2019).

- (iv) The dissertation highlights the benefits of integrating crop modelling (LUE model) and machine learning (ML) (random forest (RF)) to enhance prediction accuracy in agricultural monitoring. The crucial variables, such as LUE biomass, phenology-related inputs, extra-terrestrial radiation, solar radiation, evapotranspiration, soil moisture, snow cover (for OSR), and temperature, play a crucial role in improving the crop yield accuracy using the RF. Moreover, using NDVI or climate variables alone as predictors of crop yield would result in less accuracy in yield prediction compared to their combined use in RF.
- (v) After examining the effect of land use diversity on the satellite-modelled biomass of OSR and WW, the dissertation suggests that the crop yields of WW and OSR are highly influenced by land use diversity (~0.50) within a radius of 450 and 1050 m. The dissertation aims to investigate the impact of arable land use on the modelled biomass of OSR between 2018 and 2019. The results indicate that crop rotation within 350 m in two consecutive years could positively impact OSR's crop biomass or yield. The dissertation opens a broader question of accurately establishing satellite-based crop modelling relationship with biodiversity by involving dependent factors such as the specific crops grown on a field, the management practices used, soil health,

biotic and abiotic stressors, pest management, pollinators, and the local environmental conditions in the future research analysis.

As crop yields are an important agricultural agroecosystem service, it is essential to carefully monitor and predict them to ensure food security and sustainable agricultural practices and mitigate climate change's potential impacts on crop production. Thus, the dissertation results highlight the importance of closely examining crop yields and their relationship with land use diversity. Lastly, this dissertation ends with an aim and hopes to extend this research by further developing, testing, and refining crop yield prediction methods and including new data essential for promoting sustainable agriculture and ensuring the long-term health of our planet.

Appendices

Appendix 1: Figures and Tables



Figure A1. Detailed map of administrative regions of Bavaria (Landkreise und kreisfreie Städte in Bayern). The names of the districts are translated from German to English as: Unterfranken as Lower Franconia, Mittelfranken as Middle Franconia, Oberfranken as Upper Franconia, Oberpfalz as Upper Palatinate, Oberbayern as Upper Bavaria, and Niederbayern as Lower Bavaria. (Source: <https://www.gifex.com/>)

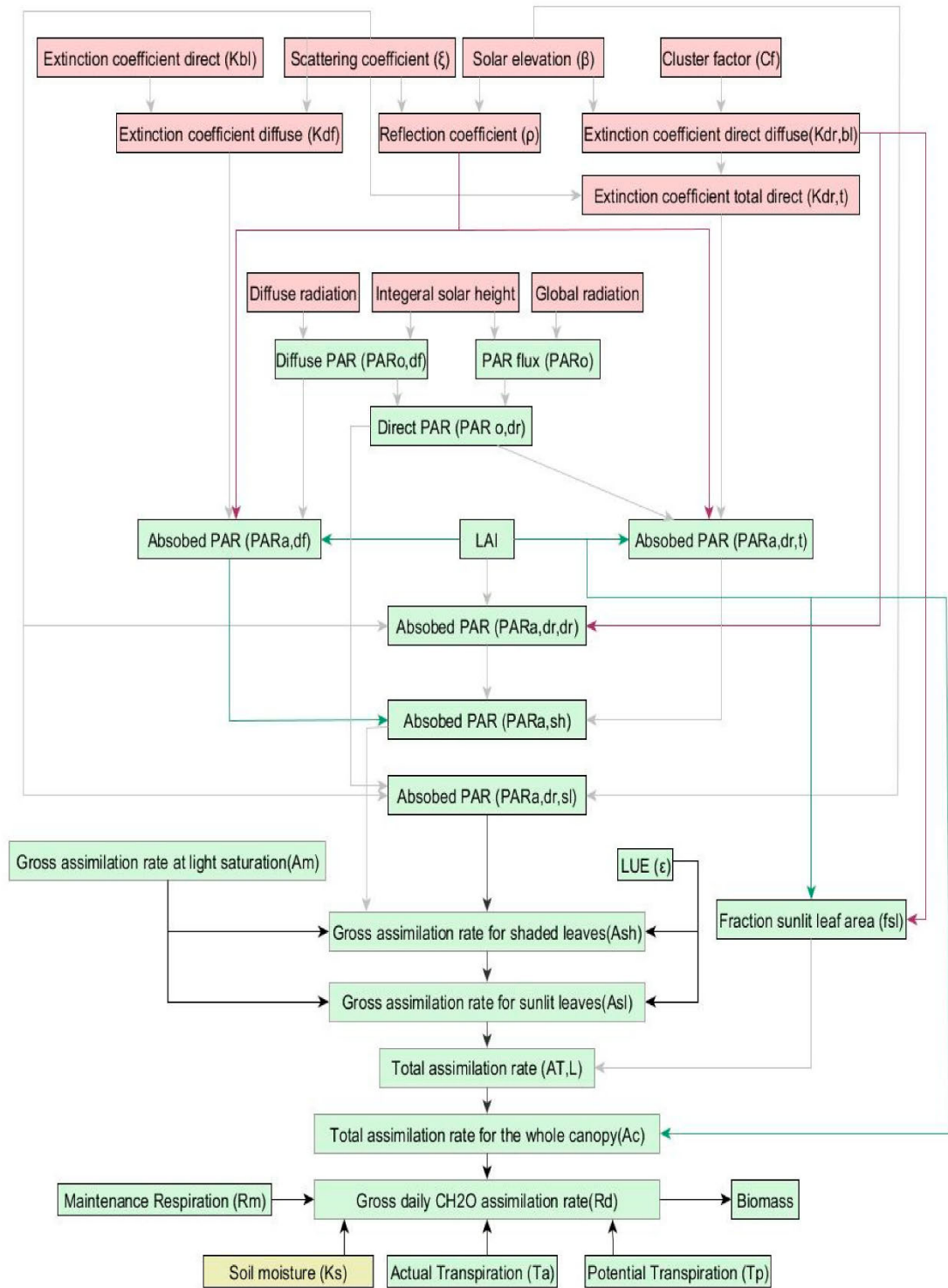


Figure A2: Flowchart of the WOFOST model. (source : (Dhillon et al., 2020))

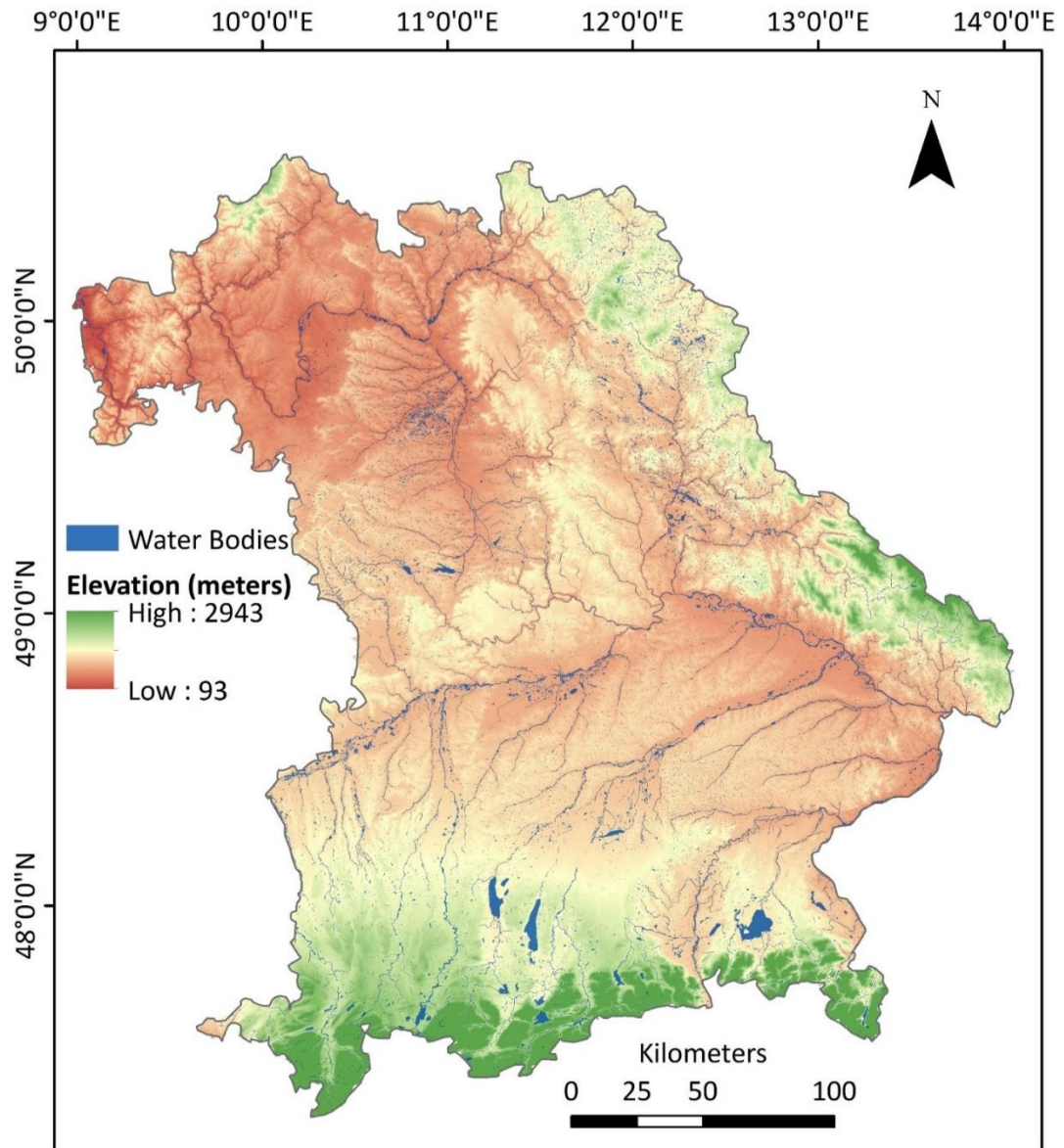
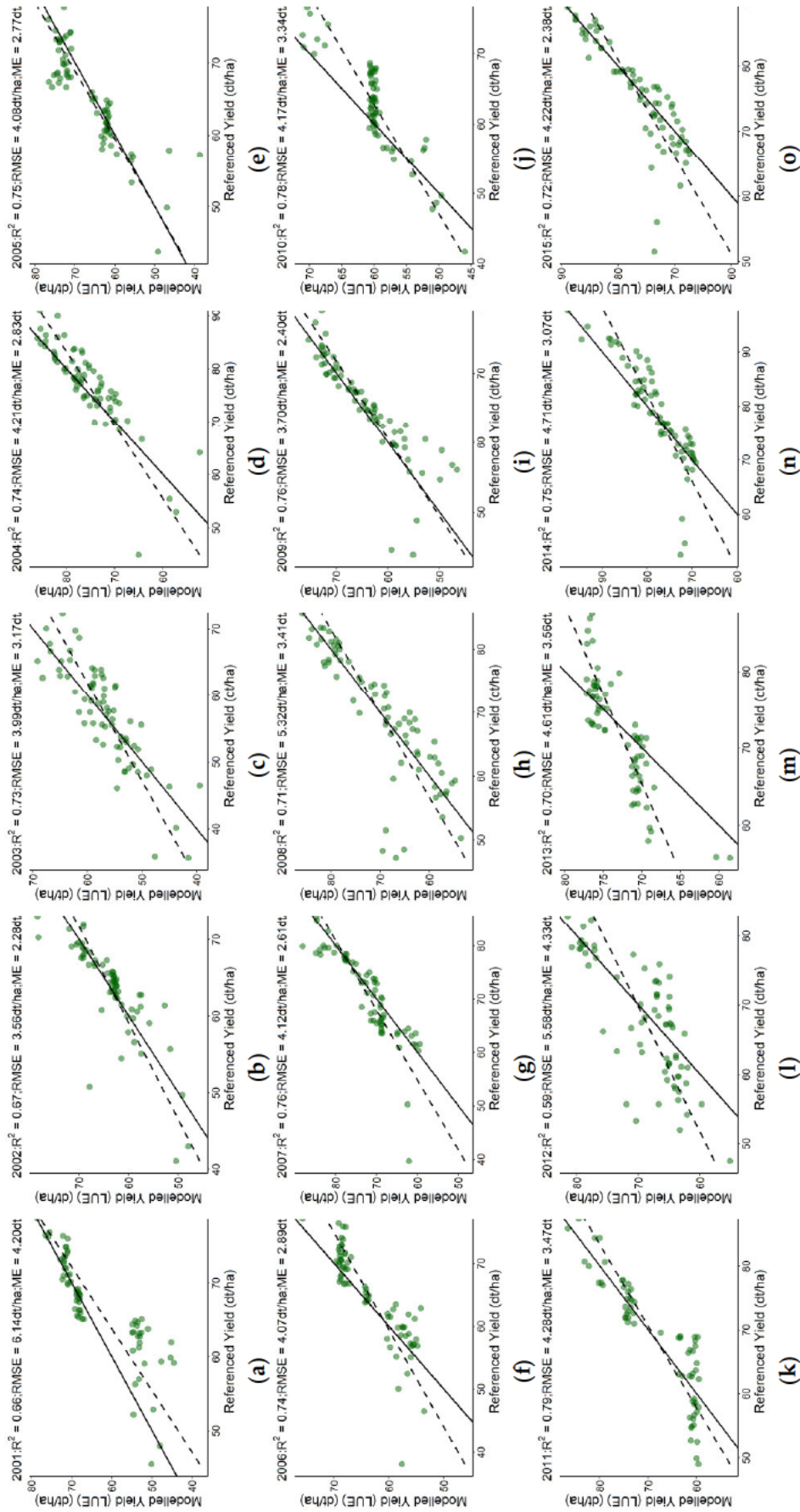


Figure A3. The digital elevation map of Bavaria. The map is generated from Shuttle Radar Topography Mission (SRTM) digital elevation data. The elevation ranges from 93 m to 2943 m.



Appendices

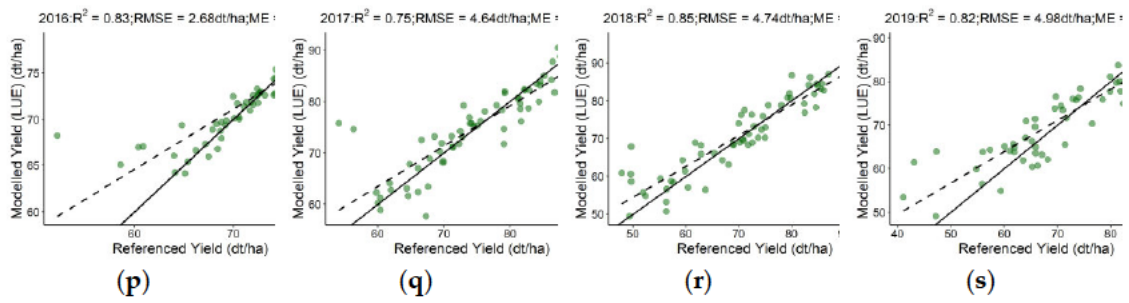
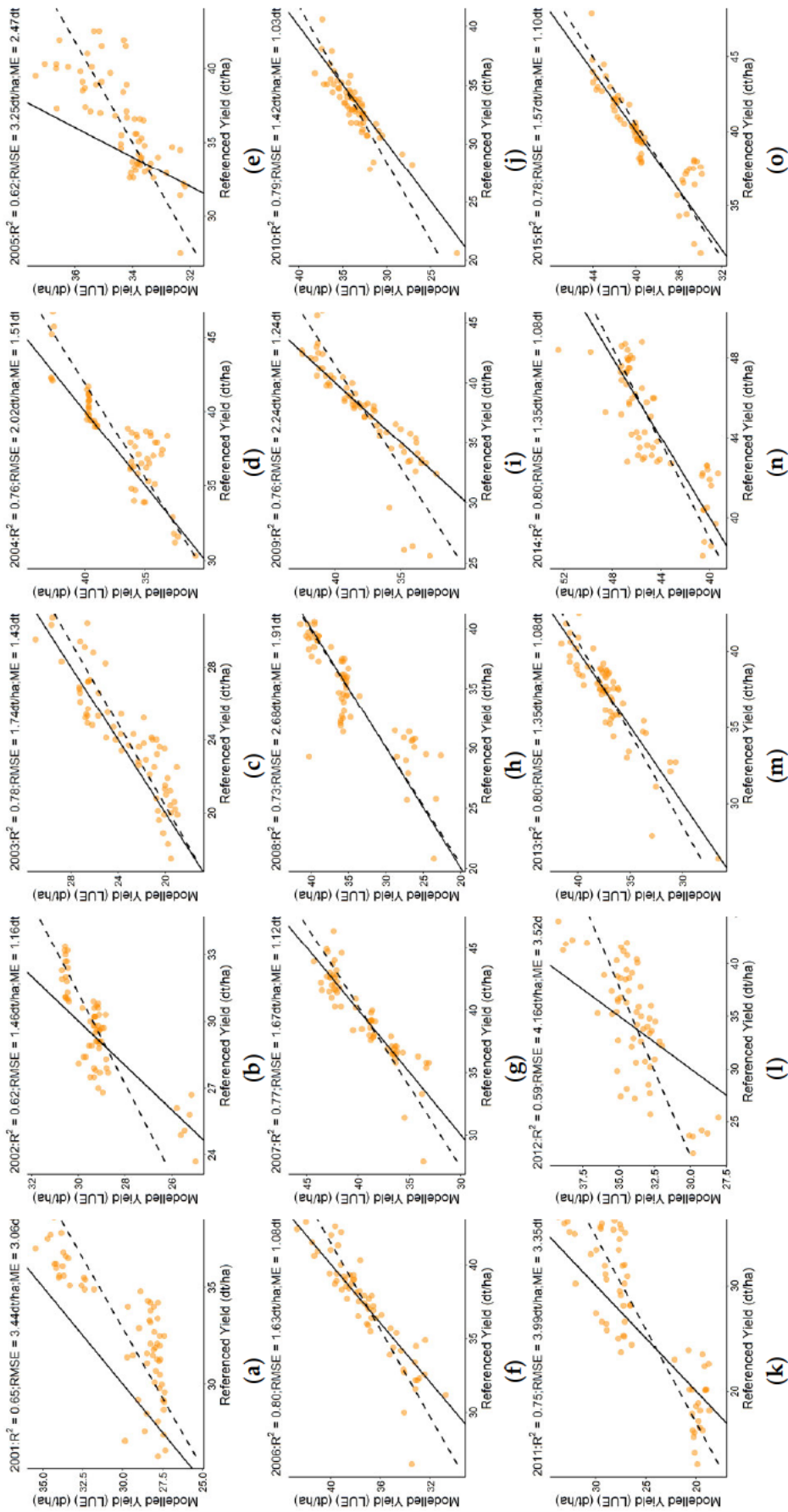


Figure A4. The scatter plots (a)-(s) compare the accuracies of modelled and referenced yields of WW for 2001 to 2019. The values of the statistical parameters such as R^2 , RMSE (dt/ha), and ME (dt/ha) are displayed at the top of each plot. Every plot contains a solid line (1:1 line) that is used to visualise the correlation of pixels between the modelled and referenced yield values. The green color of scatter plots represents WW.



Appendices

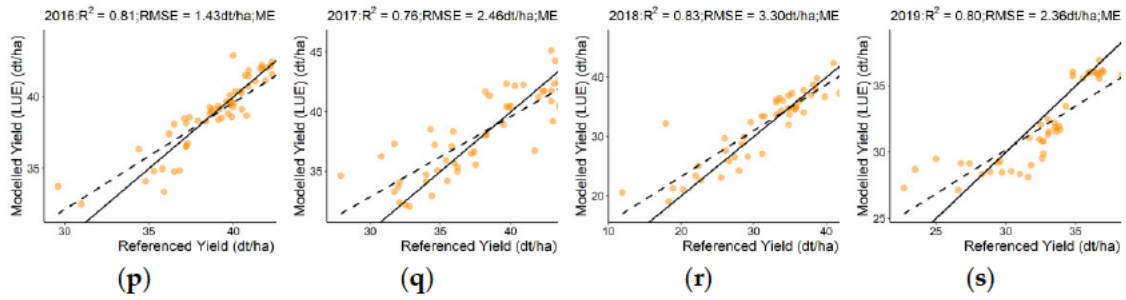


Figure A5. The scatter plots (a)-(s) compare the accuracies of modelled and referenced yields of OSR for 2001 to 2019. The values of the statistical parameters such as R^2 , RMSE (dt/ha), and ME (dt/ha) are displayed at the top of each plot. Every plot contains a solid line (1:1 line) that is used to visualise the correlation of pixels between the modelled and referenced yield values. The orange color of scatter plots represents OSR.

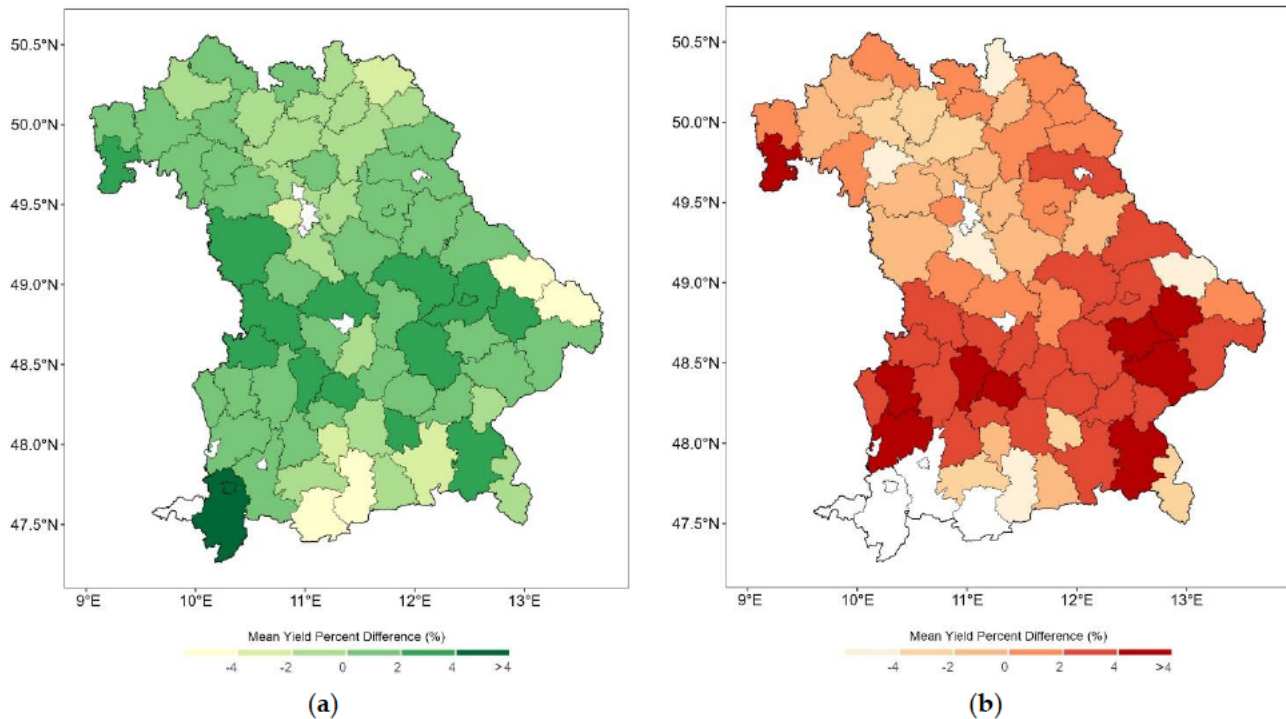


Figure A6. The regional scale average yield percent difference between the referenced and the modelled yield from 2001 to 2019 (a) WW, (b) OSR. The yield percent difference is calculated in Equation (9).

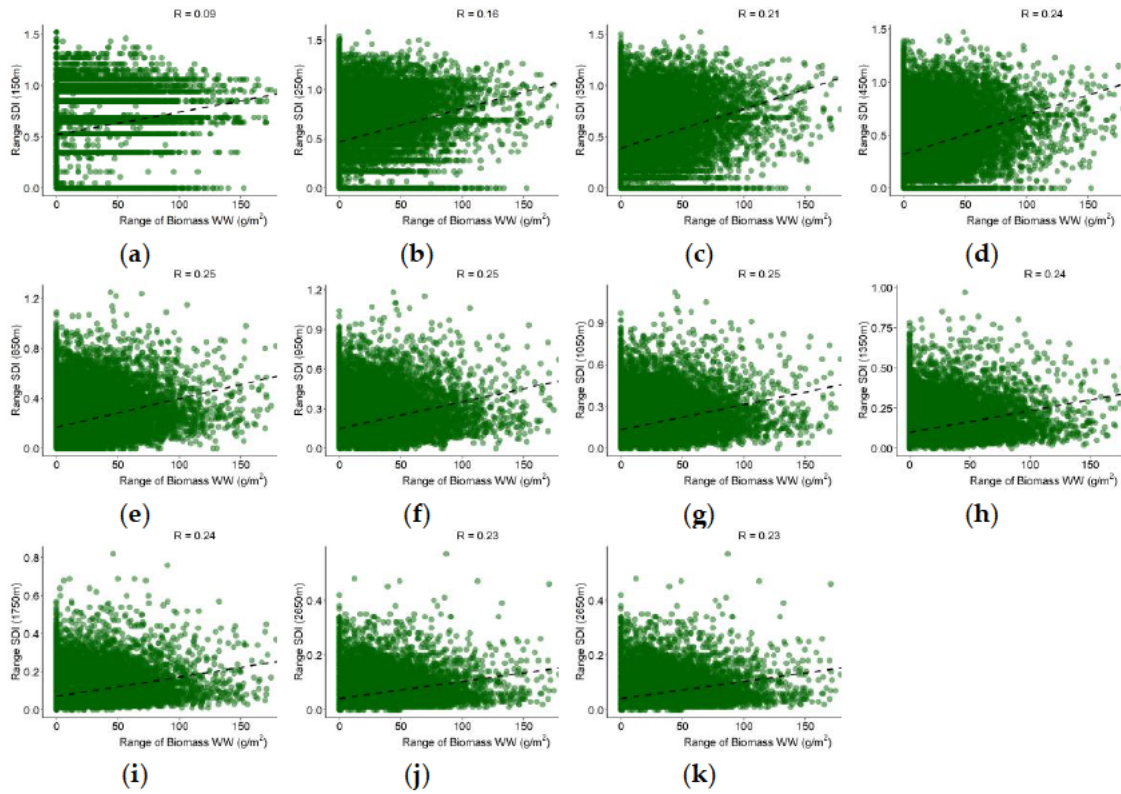


Figure A7. The correlation plots (a)-(k) show the relationship between the range of Shannon Diversity Index and range of the LUE modelled biomass on every field at different window sizes (150, 250, 350, 450, 850, 950, 1050, 1350, 1750, 2150 and 2650 m) for WW. Every plot contains a dotted line that is used to visualise the correlation of pixels between the Shannon Diversity Index and the biomass values. The green color represents to WW. SDI is for Shannon Diversity Index.

Appendices

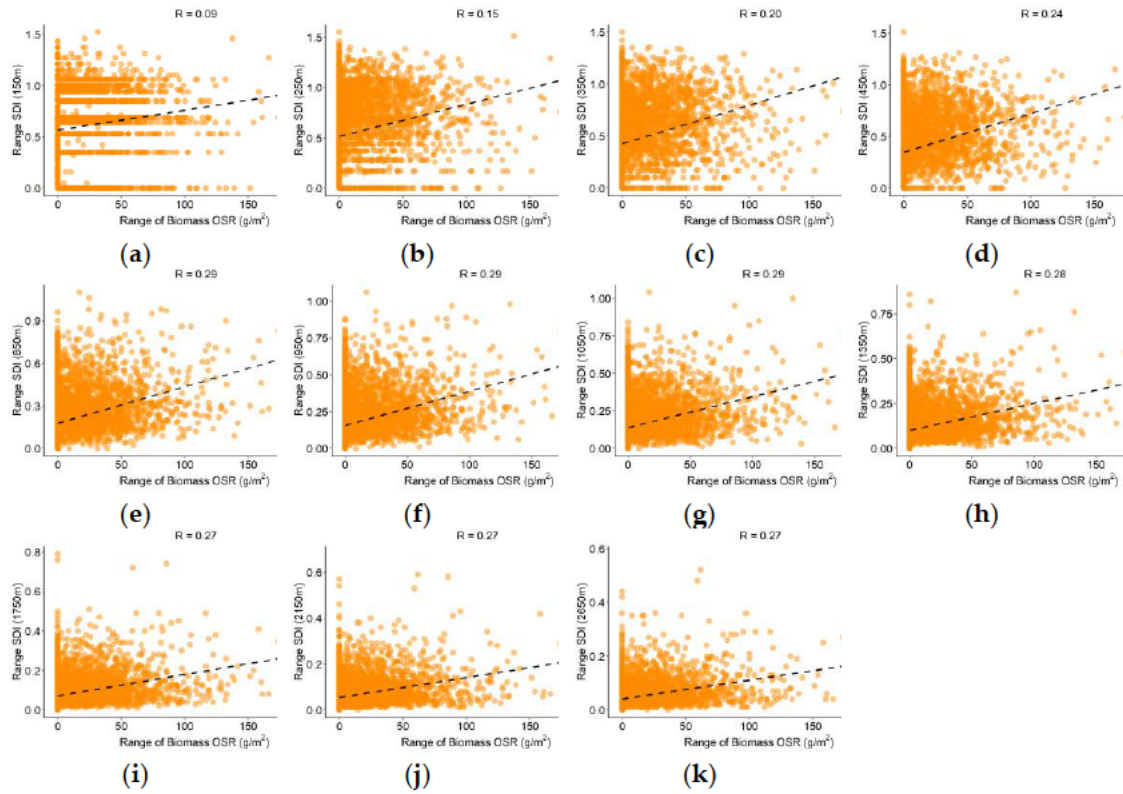


Figure A8. The correlation plots (a)-(k) show the relationship between the range of Shannon Diversity Index and range of the LUE modelled biomass on every field at different window sizes (150, 250, 350, 450, 850, 950, 1050, 1350, 1750, 2150 and 2650 m) for OSR. Every plot contains a dotted line that is used to visualise the correlation of pixels between the Shannon Diversity Index and the biomass values. The orange color represents to OSR. SDI is for Shannon Diversity Index.

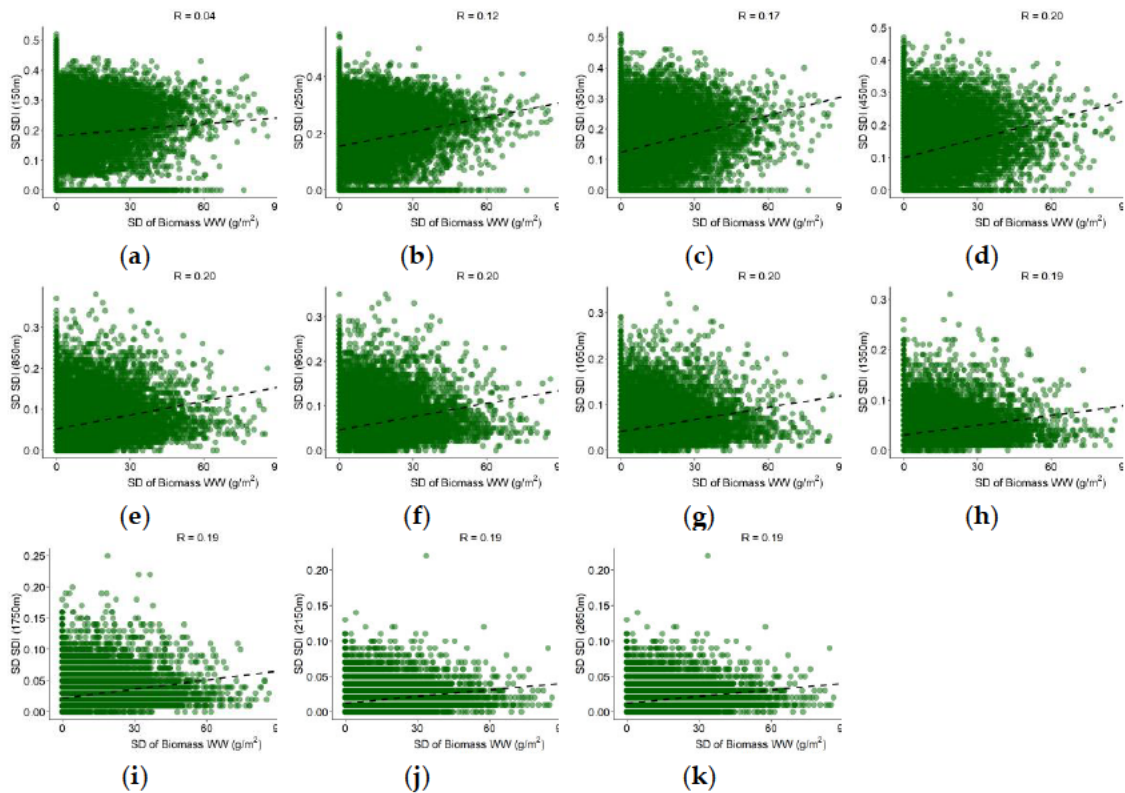


Figure A9. The correlation plots (a)-(k) show the relationship between the standard deviation of Shannon Diversity Index and standard deviation of the LUE modelled biomass on every field at different window sizes (150, 250, 350, 450, 850, 950, 1050, 1350, 1750, 2150 and 2650 m) for WW. Every plot contains a dotted line that is used to visualise the correlation of pixels between the Shannon Diversity Index and the biomass values. The green color represents to WW. SD is for standard deviation and SDI is for Shannon Diversity Index.

Appendices

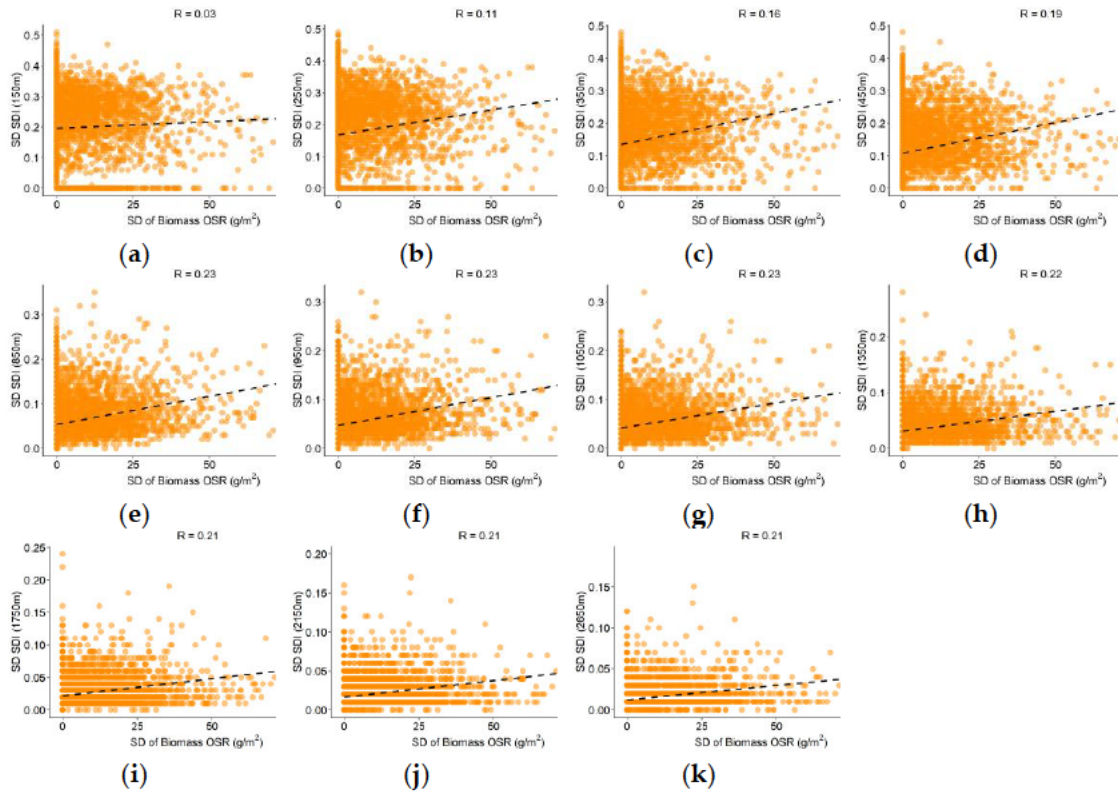


Figure A10. The correlation plots (a)-(k) show the relationship between the standard deviation of Shannon Diversity Index and standard deviation of the LUE modelled biomass on every field at different window sizes (150, 250, 350, 450, 850, 950, 1050, 1350, 1750, 2150 and 2650 m) for OSR. Every plot contains a dotted line that is used to visualise the correlation of pixels between the Shannon Diversity Index and the biomass values. The orange color represents to OSR. SD is for standard deviation and SDI is for Shannon Diversity Index.

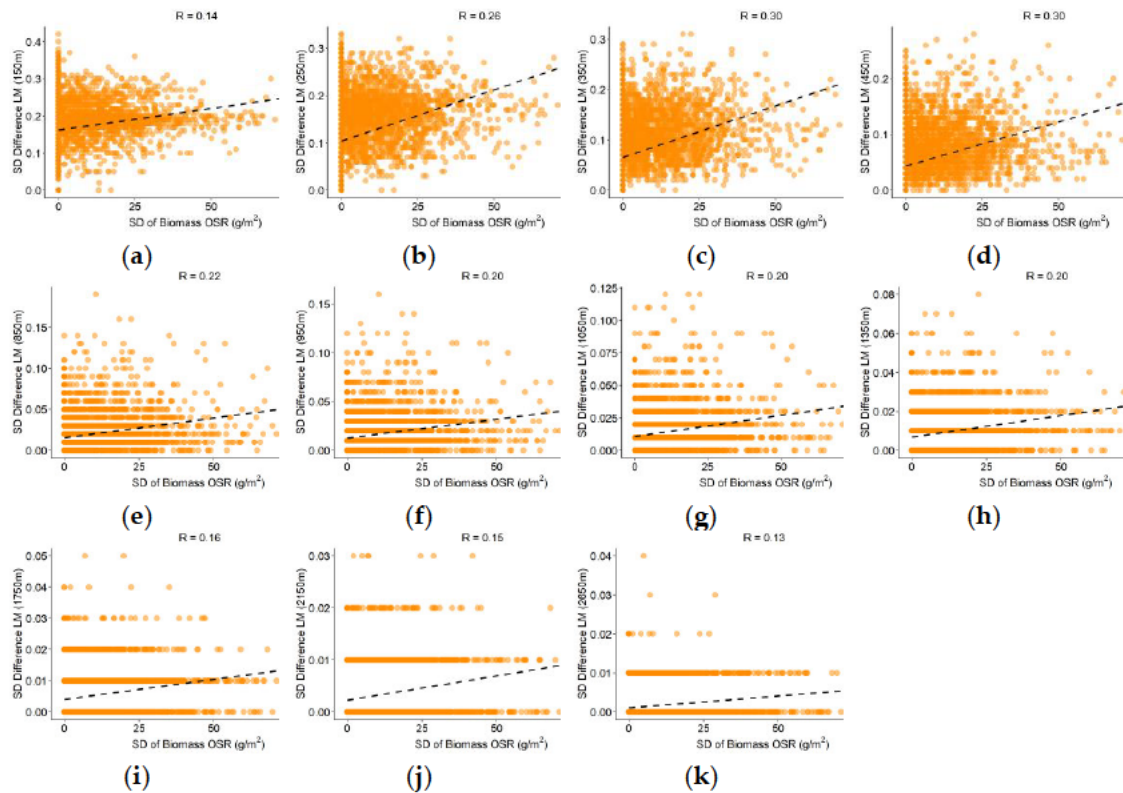


Figure A11. The correlation plots (a)-(k) show the relationship between the standard deviation of difference in landscape metrics (i.e., 2019 minus 2018) and standard deviation of the LUE modelled biomass on every field at different window sizes (150, 250, 350, 450, 850, 950, 1050, 1350, 1750, 2150 and 2650 m) for OSR. Every plot contains a dotted line that is used to visualise the correlation of pixels between the difference in landscape metrics and the biomass values. The orange color represents the OSR. LM is for landscape metrics.

Appendices

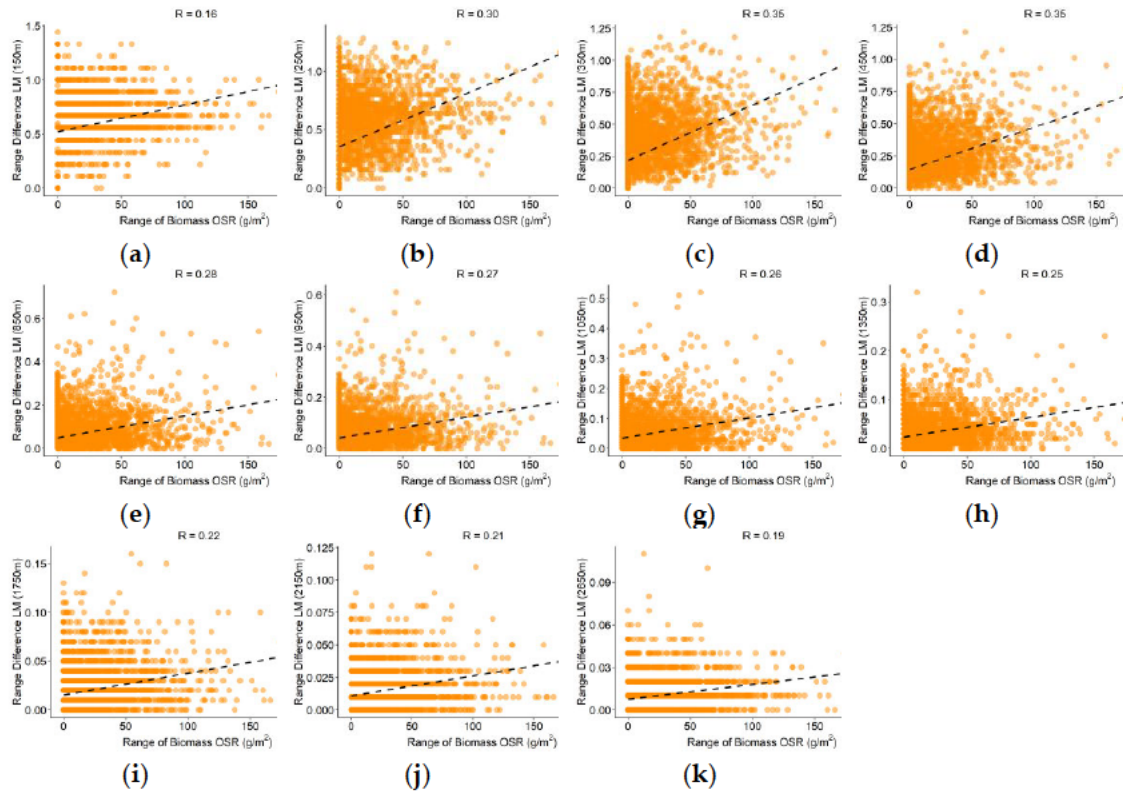


Figure A12. The correlation plots (a)-(k) show the relationship between the range of difference in landscape metrics (i.e., 2019 minus 2018) and range of the LUE modelled biomass on every field at different window sizes (150, 250, 350, 450, 850, 950, 1050, 1350, 1750, 2150 and 2650 m) for OSR. Every plot contains a dotted line that is used to visualise the correlation of pixels between the difference in landscape metrics and the biomass values. The orange color represents the OSR. LM is for landscape metrics.

Table A1. A summary of linear regression equations used to calculate crop yield from biomass obtained from different satellite products (MOD13Q1, Landsat (L)-MOD13Q1 and Sentinel-2 (S)-MOD13Q1) for WW and OSR using LUE and WOFOST models. The yield obtained is in dt/ha.

| Crop Type | Crop Model | Equation | R ² |
|-----------|------------|---|----------------|
| WW | LUE | $\text{Yield}_{\text{MOD13Q1}} = -56.549 + 0.2231 * \text{Biomass}_{\text{MOD13Q1}}$ | 0.73 |
| WW | LUE | $\text{Yield}_{\text{L-MOD13Q1}} = 22.278 + 0.0743 * \text{Biomass}_{\text{L-MOD13Q1}}$ | 0.82 |
| WW | LUE | $\text{Yield}_{\text{S-MOD13Q1}} = -14.377 + 0.147 * \text{Biomass}_{\text{S-MOD13Q1}}$ | 0.85 |
| WW | WOFOST | $\text{Yield}_{\text{MOD13Q1}} = 52.533 + 0.0599 * \text{Biomass}_{\text{MOD13Q1}}$ | 0.69 |
| WW | WOFOST | $\text{Yield}_{\text{L-MOD13Q1}} = 58.027 + 0.0537 * \text{Biomass}_{\text{L-MOD13Q1}}$ | 0.75 |
| WW | WOFOST | $\text{Yield}_{\text{S-MOD13Q1}} = 58.670 + 0.0573 * \text{Biomass}_{\text{S-MOD13Q1}}$ | 0.78 |
| OSR | LUE | $\text{Yield}_{\text{MOD13Q1}} = -25.192 + 0.1158 * \text{Biomass}_{\text{MOD13Q1}}$ | 0.67 |
| OSR | LUE | $\text{Yield}_{\text{L-MOD13Q1}} = -5.823 + 0.0807 * \text{Biomass}_{\text{L-MOD13Q1}}$ | 0.80 |
| OSR | LUE | $\text{Yield}_{\text{S-MOD13Q1}} = -6.035 + 0.0816 * \text{Biomass}_{\text{S-MOD13Q1}}$ | 0.82 |
| OSR | WOFOST | $\text{Yield}_{\text{MOD13Q1}} = -4.4375 + 0.0721 * \text{Biomass}_{\text{MOD13Q1}}$ | 0.62 |
| OSR | WOFOST | $\text{Yield}_{\text{L-MOD13Q1}} = -16.345 + 0.089 * \text{Biomass}_{\text{L-MOD13Q1}}$ | 0.63 |
| OSR | WOFOST | $\text{Yield}_{\text{S-MOD13Q1}} = -8.592 + 0.815 * \text{Biomass}_{\text{S-MOD13Q1}}$ | 0.64 |

Appendix 2: Author Contributions

Chapter 2 has been published in MDPI Remote Sensing as: Dhillon, M.S.; Dahms, T.; Kübert-Flock, C.; Steffan-Dewenter, I.; Zhang, J.; Ullmann, T. Spatiotemporal Fusion Modelling Using STARFM: Examples of Landsat 8 and Sentinel-2 NDVI in Bavaria. *Remote Sens.* **2022**, *14*, 677. <https://doi.org/10.3390/rs14030677>

Author Contributions

Conceptualization, M.S.D., T.D. and T.U.; Methodology, M.S.D.; Software, M.S.D.; Validation, M.S.D.; Formal Analysis, M.S.D. and T.U.; Investigation, M.S.D.; Resources, M.S.D., T.D., C.K.-F., J.Z., I.S.-D. and T.U.; Data Curation, M.S.D., C.K.-F. and J.Z.; Writing—original draft preparation, M.S.D.; Writing—review and editing, M.S.D. and T.U.; Visualization, M.S.D., and T.U.; Supervision, T.U.; Project Administration, C.K.-F. and T.D.; Funding Acquisition, I.S.-D. All authors have read and agreed to the published version of the manuscript.

Contribution of the Candidate

| <i>Publication Details</i> | <i>Description of the Own Contribution</i> |
|--|---|
| Writing of the article: Which parts of the article have been written to which extent by the candidate? | The writing of the article was led by Maninder Singh Dhillon including the writing of the first draft and the implementation of comments from co-authors, and reviewers of the MDPI Remote Sensing. |
| Performed research: Which experimental procedures have been conducted by the candidate? | All needed experiments for the manuscript were performed by Maninder Singh Dhillon. |
| Conceptual design of the research: To which extent did the candidate contribute to the conceptual design of the research project? | Under the supervision of Prof. Dr. Tobias Ullmann, the conceptual design was developed by Maninder Singh Dhillon |
| Data analysis: To which extent did the candidate contribute to the data analysis? | Data were analysed by Maninder Singh Dhillon |
| Overall contribution of the candidate (in%) | 90% |

Appendices

Confirmation by Co-Authors

| Name Co-author | Signature | Date |
|-------------------------|------------------|-------------|
| Thorsten Dahms | | |
| Carina Kübert-Flock | | |
| Ingolf Steffan-Dewenter | | |
| Jie Zhang | | |
| Tobias Ullmann | | |

Chapter 3 has been published in MDPI Remote Sensing as: Dhillon, M.S.; Kübert-Flock, C.; Dahms, T.; Rummler, T.; Arnault, J.; Steffan-Dewenter, I.; Ullmann, T. Suitable Spatiotemporal Data for Crop Yield Predictions: Inputting STARFM NDVIs to Crop Models in Bavaria Germany. Remote Sens. **2023**

Author Contributions

Conceptualization, M.S.D. and T.U.; Methodology, M.S.D.; Software, M.S.D.; Validation, M.S.D.; Formal Analysis, M.S.D. and T.U.; Investigation, M.S.D.; Resources, M.S.D., C.K.-F., T.R., J.A., I.S.-D. and T.U.; Data Curation, M.S.D., C.K.-F., T.R. and J.A.; Writing—original draft preparation, M.S.D.; Writing—review and editing, M.S.D. and T.U.; Visualization, M.S.D. and T.U.; Supervision, T.U. and I.S.-D.; Project Administration, M.S.D., C.K.-F. and T.D.; Funding Acquisition, T.U. and I.S.-D. All authors have read and agreed to the published version of the manuscript.

Contribution of the Candidate

| <i>Publication Details</i> | <i>Description of the Own Contribution</i> |
|--|---|
| Writing of the article: Which parts of the article have been written to which extent by the candidate? | The writing of the article was led by Maninder Singh Dhillon including the writing of the first draft and the implementation of comments from co-authors, and reviewers of the MDPI Remote Sensing. |
| Performed research: Which experimental procedures have been conducted by the candidate? | All needed experiments for the manuscript were performed by Maninder Singh Dhillon. |
| Conceptual design of the research: To which extent did the candidate contribute to the conceptual design of the research project? | Under the supervision of Prof. Dr. Tobias Ullmann, the conceptual design was developed by Maninder Singh Dhillon |
| Data analysis: To which extent did the candidate contribute to the data analysis? | Data were analysed by Maninder Singh Dhillon |
| Overall contribution of the candidate (in%) | 90% |

Appendices

Confirmation by Co-Authors

| Name Co-author | Signature | Date |
|-------------------------|------------------|-------------|
| Thorsten Dahms | | |
| Carina Kübert-Flock | | |
| Thomas Rummler | | |
| Joel Arnault | | |
| Ingolf Steffan-Dewenter | | |
| Tobias Ullmann | | |

Chapter 4 has been published in MDPI Remote Sensing as: Dhillon, M.S.; Dahms, T.; Kübert-Flock, C.; Liepa, A.; Rummler, T.; Arnault, J.; Steffan-Dewenter, I.; Ullmann, T. Impact of STARFM on Crop Yield Predictions: Fusing MODIS with Landsat 5, 7, and 8 NDVIs in Bavaria Germany. Remote Sens. **2023**

Author Contributions

Conceptualization, M.S.D. and T.U.; Methodology, M.S.D.; Software, M.S.D.; Validation, M.S.D.; Formal Analysis, M.S.D. and T.U.; Investigation, M.S.D.; Resources, M.S.D., C.K.-F., T.R., J.A., I.S.-D. and T.U.; Data Curation, M.S.D., C.K.-F., T.R. and J.A.; Writing—original draft preparation, M.S.D.; Writing—M.S.D. and T.U.; Visualization, M.S.D. and T.U.; Supervision, T.U.; Project Administration, M.S.D., C.K.-F. and T.D.; Funding Acquisition, T.U. and I.S.-D. All authors have read and agreed to the published version of the manuscript.

Contribution of the Candidate

| <i>Publication Details</i> | <i>Description of the Own Contribution</i> |
|--|---|
| Writing of the article: Which parts of the article have been written to which extent by the candidate? | The writing of the article was led by Maninder Singh Dhillon including the writing of the first draft and the implementation of comments from co-authors, and reviewers of the MDPI Remote Sensing. |
| Performed research: Which experimental procedures have been conducted by the candidate? | All needed experiments for the manuscript were performed by Maninder Singh Dhillon. |
| Conceptual design of the research: To which extent did the candidate contribute to the conceptual design of the research project? | Under the supervision of Prof. Dr. Tobias Ullmann, the conceptual design was developed by Maninder Singh Dhillon |
| Data analysis: To which extent did the candidate contribute to the data analysis? | Data were analysed by Maninder Singh Dhillon |
| Overall contribution of the candidate (in%) | 90% |

Appendices

Confirmation by Co-Authors

| Name Co-author | Signature | Date |
|-------------------------|------------------|-------------|
| Thorsten Dahms | | |
| Carina Kübert-Flock | | |
| Adomas Liepa | | |
| Thomas Rummeler | | |
| Joel Arnault | | |
| Ingolf Steffan-Dewenter | | |
| Tobias Ullmann | | |

Chapter 5 has been published in *Frontiers in Remote Sensing* as: Dhillon, M.S.; Dahms, T.; Kuebert-Flock, C.; Rummler, T.; Arnault, J.; Stefan-Dewenter, I.; Ullmann, T. Integrating random forest and crop modelling improves the crop yield prediction of winter wheat and oil seed rape. *Frontiers in Remote Sensing* **2023**, *3*, 109.

Author Contributions

Conceptualization, M.S.D. and T.U.; Methodology, M.S.D.; Software, M.S.D.; Validation, M.S.D.; Formal Analysis, M.S.D, and T.U.; Investigation, M.S.D.; Resources, M.S.D., C.K.-F., T.R., J.A., I.S.-D. and T.U.; Data Curation, M.S.D., C.K.-F., T.R. and J.A.; Writing—original draft preparation, M.S.D.; Writing—M.S.D. and T.U.; Visualization, M.S.D. and T.U.; Supervision, T.U.; Project Administration, M.S.D., C.K.-F. and T.D.; Funding Acquisition, T.U. and I.S.-D. All authors have read and agreed to the published version of the manuscript.

Contribution of the Candidate

| <i>Publication Details</i> | <i>Description of the Own Contribution</i> |
|--|---|
| Writing of the article: Which parts of the article have been written to which extent by the candidate? | The writing of the article was led by Maninder Singh Dhillon including the writing of the first draft and the implementation of comments from co-authors, and reviewers of the MDPI Remote Sensing. |
| Performed research: Which experimental procedures have been conducted by the candidate? | All needed experiments for the manuscript were performed by Maninder Singh Dhillon. |
| Conceptual design of the research: To which extent did the candidate contribute to the conceptual design of the research project? | Under the supervision of Prof. Dr. Tobias Ullmann, the conceptual design was developed by Maninder Singh Dhillon |
| Data analysis: To which extent did the candidate contribute to the data analysis? | Data were analysed by Maninder Singh Dhillon |
| Overall contribution of the candidate (in%) | 890% |

Appendices

Confirmation by Co-Authors

| Name Co-author | Signature | Date |
|-------------------------|------------------|-------------|
| Thorsten Dahms | | |
| Carina Kübert-Flock | | |
| Thomas Rummler | | |
| Joel Arnault | | |
| Ingolf Steffan-Dewenter | | |
| Tobias Ullmann | | |

References

- Ahmad, I., Ghafoor, A., Bhatti, M. I., Akhtar, I.-u. H., & Ibrahim, M. (2014). Satellite remote sensing and GIS-based crops forecasting & estimation system in Pakistan. *Crop monitoring for improved food security*.
- Alarcón-Segura, V., Grass, I., Breustedt, G., Rohlf, M., & Tschardt, T. (2022). Strip intercropping of wheat and oilseed rape enhances biodiversity and biological pest control in a conventionally managed farm scenario. *Journal of applied ecology*.
- Ali, A. M., Abouelghar, M. A., Belal, A.-A., Saleh, N., Younes, M., Selim, A., . . . Maignan, S. (2022). Crop Yield Prediction Using Multi Sensors Remote Sensing. *The Egyptian Journal of Remote Sensing and Space Science*.
- Allen, R. G., Pereira, L. S., Raes, D., & Smith, M. (1998). Crop evapotranspiration-Guidelines for computing crop water requirements-FAO Irrigation and drainage paper 56. *Fao, Rome, 300(9)*, D05109.
- Altieri, M. A., & Toledo, V. M. (2005). Natural resource management among small-scale farmers in semi-arid lands: building on traditional knowledge and agroecology. *Annals of Arid zone, 44(3/4)*, 365.
- Altman, A., & Hasegawa, P. M. (2011). *Plant biotechnology and agriculture: prospects for the 21st century*: Academic press.
- Anderson, M. C., Hain, C. R., Jurecka, F., Trnka, M., Hlavinka, P., Dulaney, W., . . . Gao, F. (2016). Relationships between the evaporative stress index and winter wheat and spring barley yield anomalies in the Czech Republic. *Climate Research, 70(2-3)*, 215-230.
- Anderson, M. C., Kustas, W. P., Norman, J. M., Hain, C. R., Mecikalski, J. R., Schultz, L., . . . Pimstein, A. (2011). Mapping daily evapotranspiration at field to continental scales using geostationary and polar orbiting satellite imagery. *Hydrology and Earth System Sciences, 15(1)*, 223-239.
- Arai, E., Shimabukuro, Y. E., Pereira, G., & Vijaykumar, N. L. (2011). A Multi-Resolution Multi-Temporal Technique for Detecting and Mapping Deforestation in the Brazilian Amazon Rainforest. *Remote Sensing, 3(9)*, 1943-1956. doi:10.3390/rs3091943
- Archontoulis, S. V., Castellano, M. J., Licht, M. A., Nichols, V., Baum, M., Huber, I., . . . Iqbal, J. (2020). Predicting crop yields and soil-plant nitrogen dynamics in the US Corn Belt. *Crop Science, 60(2)*, 721-738.
- Arcipowska, A., Mangan, E., Lyu, Y., & Waite, R. 5 Questions About Agricultural Emissions, Answered.
- Arnault, J., Rummeler, T., Baur, F., Lerch, S., Wagner, S., Fersch, B., . . . Kunstmann, H. (2018). Precipitation sensitivity to the uncertainty of terrestrial water flow in WRF-Hydro: An ensemble analysis for central Europe. *Journal of Hydrometeorology, 19(6)*, 1007-1025.
- Asrar, G., Myneni, R., & Choudhury, B. (1992). Spatial heterogeneity in vegetation canopies and remote sensing of absorbed photosynthetically active radiation: a modeling study. *Remote Sensing of Environment, 41(2-3)*, 85-103.
- Atamanyuk, I., Kondratenko, Y., Shebanin, V., Sirenko, N., Poltorak, A., Baryshevska, I., & Atamaniuk, V. (2019). Forecasting of cereal crop harvest on the basis of an extrapolation canonical model of a vector random sequence.
- Atzberger, C., & Rembold, F. (2013). Mapping the spatial distribution of winter crops at sub-pixel level using AVHRR NDVI time series and neural nets. *Remote Sensing, 5(3)*, 1335-1354.
- Barbedo, J. G. A. (2022). Data Fusion in Agriculture: Resolving Ambiguities and Closing Data Gaps. *Sensors, 22(6)*, 2285.
- Basiago, A. D. (1995). Methods of defining 'sustainability'. *Sustainable development, 3(3)*, 109-119.
- Basso, B., & Liu, L. (2019). Seasonal crop yield forecast: Methods, applications, and accuracies. *advances in agronomy, 154*, 201-255.
- Battude, M., Al Bitar, A., Morin, D., Cros, J., Huc, M., Sicre, C. M., . . . Demarez, V. (2016). Estimating maize biomass and yield over large areas using high spatial and temporal resolution Sentinel-2 like remote sensing data. *Remote Sensing of Environment, 184*, 668-681.
- Bebbington, J., & Unerman, J. (2018). Achieving the United Nations Sustainable Development Goals: an enabling role for accounting research. *Accounting, Auditing & Accountability Journal*.
- Belgiu, M., & Csillik, O. (2018). Sentinel-2 cropland mapping using pixel-based and object-based time-weighted dynamic time warping analysis. *Remote Sensing of Environment, 204*, 509-523.
- Belgiu, M., & Stein, A. (2019). Spatiotemporal image fusion in remote sensing. *Remote Sensing, 11(7)*, 818.

References

- Benabdelouahab, T., Lebrini, Y., Boudhar, A., Hadria, R., Htitiou, A., & Lionboui, H. (2019). Monitoring spatial variability and trends of wheat grain yield over the main cereal regions in Morocco: a remote-based tool for planning and adjusting policies. *Geocarto International*, 1-20.
- Bexell, M., & Jönsson, K. (2017). *Responsibility and the United Nations' sustainable development goals*. Paper presented at the Forum for development studies.
- Bhandari, S., Phinn, S., & Gill, T. (2012). Preparing Landsat Image Time Series (LITS) for Monitoring Changes in Vegetation Phenology in Queensland, Australia. *Remote Sensing*, 4(6), 1856-1886. doi:10.3390/rs4061856
- Bhatt, D., Maskey, S., Babel, M. S., Uhlenbrook, S., & Prasad, K. C. (2014). Climate trends and impacts on crop production in the Koshi River basin of Nepal. *Regional Environmental Change*, 14, 1291-1301.
- Bian, C., Shi, H., Wu, S., Zhang, K., Wei, M., Zhao, Y., . . . Chen, S. (2022). Prediction of Field-Scale Wheat Yield Using Machine Learning Method and Multi-Spectral UAV Data. *Remote Sensing*, 14(6), 1474.
- Boelens, R., & Vos, J. (2012). The danger of naturalizing water policy concepts: Water productivity and efficiency discourses from field irrigation to virtual water trade. *Agricultural water management*, 108, 16-26.
- Bogard, M., Biddulph, B., Zheng, B., Hayden, M., Kuchel, H., Mullan, D., . . . Chapman, S. C. (2020). Linking genetic maps and simulation to optimize breeding for wheat flowering time in current and future climates. *Crop Science*, 60(2), 678-699.
- Bolton, D. K., & Friedl, M. A. (2013). Forecasting crop yield using remotely sensed vegetation indices and crop phenology metrics. *Agricultural and Forest Meteorology*, 173, 74-84.
- Bolton, D. K., Gray, J. M., Melaas, E. K., Moon, M., Eklundh, L., & Friedl, M. A. (2020). Continental-scale land surface phenology from harmonized Landsat 8 and Sentinel-2 imagery. *Remote Sensing of Environment*, 240, 111685.
- Boogaard, H., De Wit, A., Te Roller, J., & Van Diepen, C. (2011). User's guide for the WOFOST Control Center 1.8 and WOFOST 7.1. 3 crop growth simulation model. *Alterra Wageningen University*.
- Borak, J. S., & Jasinski, M. F. (2009). Effective interpolation of incomplete satellite-derived leaf-area index time series for the continental United States. *Agricultural and Forest Meteorology*, 149(2), 320-332.
- Branca, G., Lipper, L., McCarthy, N., & Jolejole, M. C. (2013). Food security, climate change, and sustainable land management. A review. *Agronomy for sustainable development*, 33, 635-650.
- Braun, D., Damm, A., Hein, L., Petchey, O. L., & Schaepman, M. E. (2018). Spatio-temporal trends and trade-offs in ecosystem services: An Earth observation based assessment for Switzerland between 2004 and 2014. *Ecological Indicators*, 89, 828-839.
- Breiman, L. (2001). Random forests. *Machine learning*, 45(1), 5-32.
- Brisson, N., Gary, C., Justes, E., Roche, R., Mary, B., Ripoche, D., . . . Burger, P. (2003). An overview of the crop model STICS. *European journal of agronomy*, 18(3-4), 309-332.
- Brown, J. C. (1989). Prosperity or Hard Times in Renaissance Italy? *Renaissance Quarterly*, 42(4), 761-780.
- Bryan, E., Deressa, T. T., Gbetibouo, G. A., & Ringler, C. (2009). Adaptation to climate change in Ethiopia and South Africa: options and constraints. *Environmental science & policy*, 12(4), 413-426.
- Bryer, R. (2004). The roots of modern capitalism: A Marxist accounting history of the origins and consequences of capitalist landlords in England. *Accounting Historians Journal*, 31(1), 1-56.
- Butzer, K. W. (1992). The Americas before and after 1492: An introduction to current geographical research. *Annals of the Association of American Geographers*, 82(3), 345-368.
- Cabas, J., Weersink, A., & Olale, E. (2010). Crop yield response to economic, site and climatic variables. *Climatic change*, 101(3-4), 599-616.
- Cadamuro, G. (2020). *Prediction and Inference on Big Data in Development*: University of Washington.
- Casa, R., Varella, H., Buis, S., Guérif, M., De Solan, B., & Baret, F. (2012). Forcing a wheat crop model with LAI data to access agronomic variables: Evaluation of the impact of model and LAI uncertainties and comparison with an empirical approach. *European journal of agronomy*, 37(1), 1-10.
- Cauvin, J. (2000). *The Birth of the Gods and the Origins of Agriculture*: Cambridge University Press.
- Chakraborty, M., Manjunath, K., Panigrahy, S., Kundu, N., & Parihar, J. (2005). Rice crop parameter retrieval using multi-temporal, multi-incidence angle Radarsat SAR data. *ISPRS Journal of Photogrammetry and Remote Sensing*, 59(5), 310-322.
- Champaneri, M., Chachpara, D., Chandvidkar, C., & Rathod, M. (2016). Crop yield prediction using machine learning. *Technology*, 9, 38.
- Chen, B., Huang, B., & Xu, B. (2015). Comparison of spatiotemporal fusion models: A review. *Remote Sensing*, 7(2), 1798-1835.

- Chen, X., Liu, M., Zhu, X., Chen, J., Zhong, Y., & Cao, X. (2018). "Blend-then-Index" or "Index-then-Blend": A theoretical analysis for generating high-resolution NDVI time series by STARFM. *Photogrammetric Engineering & Remote Sensing*, 84(2), 65-73.
- Claverie, M., Ju, J., Masek, J. G., Dungan, J. L., Vermote, E. F., Roger, J.-C., . . . Justice, C. (2018). The Harmonized Landsat and Sentinel-2 surface reflectance data set. *Remote Sensing of Environment*, 219, 145-161.
- Cleaver, H. M. (1972). The contradictions of the Green Revolution. *The American economic review*, 62(1/2), 177-186.
- Clevers, J. G. P. W., Vonder, O. W., Jongschaap, R. E. E., Desprats, J. F., King, C., Prevoit, L., & Bruguier, N. (2002). Using SPOT data for calibrating a wheat growth model under mediterranean conditions. *Agronomie*, 22(6), 687-694. doi:10.1051/agro:2002038
- Clough, Y., Barkmann, J., Jührbandt, J., Kessler, M., Wanger, T. C., Anshary, A., . . . Putra, D. D. (2011). Combining high biodiversity with high yields in tropical agroforests. *Proceedings of the National Academy of Sciences*, 108(20), 8311-8316.
- Confalonieri, R., Orlando, F., Paleari, L., Stella, T., Gilardelli, C., Movedi, E., . . . Alberti, L. (2016). Uncertainty in crop model predictions: what is the role of users? *Environmental Modelling & Software*, 81, 165-173.
- Cui, J., Zhang, X., & Luo, M. (2018). Combining Linear pixel unmixing and STARFM for spatiotemporal fusion of Gaofen-1 wide field of view imagery and MODIS imagery. *Remote Sensing*, 10(7), 1047.
- Dariane, A. B., Khoramian, A., & Santi, E. (2017). Investigating spatiotemporal snow cover variability via cloud-free MODIS snow cover product in Central Alborz Region. *Remote Sensing of Environment*, 202, 152-165.
- Dasgupta, I., Saha, J., Venkatasubbu, P., & Ramasubramanian, P. (2020). AI crop predictor and weed detector using wireless technologies: a smart application for farmers. *Arabian Journal for Science and Engineering*, 45, 11115-11127.
- Daw, A., Karpatne, A., Watkins, W. D., Read, J. S., & Kumar, V. (2017). Physics-guided neural networks (pgnn): An application in lake temperature modeling. In *Knowledge-Guided Machine Learning* (pp. 353-372): Chapman and Hall/CRC.
- De'ath, G., & Fabricius, K. E. (2000). Classification and regression trees: a powerful yet simple technique for ecological data analysis. *Ecology*, 81(11), 3178-3192.
- de Araujo Barbosa, C. C., Atkinson, P. M., & Dearing, J. A. (2015). Remote sensing of ecosystem services: A systematic review. *Ecological Indicators*, 52, 430-443.
- de Sousa, K., van Etten, J., Poland, J., Fadda, C., Jannink, J.-L., Kidane, Y. G., . . . Solberg, S. Ø. (2021). Data-driven decentralized breeding increases prediction accuracy in a challenging crop production environment. *Communications biology*, 4(1), 944.
- De Wit, A. d., & Van Diepen, C. (2007). Crop model data assimilation with the Ensemble Kalman filter for improving regional crop yield forecasts. *Agricultural and Forest Meteorology*, 146(1-2), 38-56.
- Dente, L., Satalino, G., Mattia, F., & Rinaldi, M. (2008). Assimilation of leaf area index derived from ASAR and MERIS data into CERES-Wheat model to map wheat yield. *Remote Sensing of Environment*, 112(4), 1395-1407.
- Dhillon, M. S., Dahms, T., Kübert-Flock, C., Liepa, A., Rummler, T., Arnault, J., . . . Ullmann, T. (2023). Impact of STARFM on Crop Yield Predictions: Fusing MODIS with Landsat 5, 7, and 8 NDVIs in Bavaria Germany. *Remote Sensing*, 15(6), 1651.
- Dhillon, M. S., Dahms, T., Kübert-Flock, C., Steffan-Dewenter, I., Zhang, J., & Ullmann, T. (2022). Spatiotemporal Fusion Modelling Using STARFM: Examples of Landsat 8 and Sentinel-2 NDVI in Bavaria. *Remote Sensing*, 14(3), 677.
- Dhillon, M. S., Dahms, T., Kuebert-Flock, C., Borg, E., Conrad, C., & Ullmann, T. (2020). Modelling Crop Biomass from Synthetic Remote Sensing Time Series: Example for the DEMMIN Test Site, Germany. *Remote Sensing*, 12(11), 1819.
- Dhillon, M. S., Dahms, T., Kuebert-Flock, C., Rummler, T., Arnault, J., Stefan-Dewenter, I., & Ullmann, T. (2023). Integrating random forest and crop modeling improves the crop yield prediction of winter wheat and oil seed rape. *Frontiers in Remote Sensing*, 3, 109.
- Dhillon, M. S., Kübert-Flock, C., Dahms, T., Rummler, T., Arnault, J., Steffan-Dewenter, I., & Ullmann, T. (2023). Evaluation of MODIS, Landsat 8 and Sentinel-2 Data for Accurate Crop Yield Predictions: A Case Study Using STARFM NDVI in Bavaria, Germany. *Remote Sensing*, 15(7), 1830. Retrieved from <https://www.mdpi.com/2072-4292/15/7/1830>

References

- Didan, K., Munoz, A. B., Solano, R., & Huete, A. (2015). MODIS vegetation index user's guide (MOD13 series). *University of Arizona: Vegetation Index and Phenology Lab*.
- Djumaniyazova, Y., Sommer, R., Ibragimov, N., Ruzimov, J., Lamers, J., & Vlek, P. (2010). Simulating water use and N response of winter wheat in the irrigated floodplains of Northwest Uzbekistan. *Field Crops Research*, 116(3), 239-251.
- Dong, C., & Menzel, L. (2016). Improving the accuracy of MODIS 8-day snow products with in situ temperature and precipitation data. *Journal of Hydrology*, 534, 466-477.
- Dong, T., Liu, J., Qian, B., Jing, Q., Croft, H., Chen, J., . . . Chen, P. (2016). Deriving maximum light use efficiency from crop growth model and satellite data to improve crop biomass estimation. *IEEE Journal of Selected Topics in Applied Earth Observations and Remote Sensing*, 10(1), 104-117.
- Dong, T., Liu, J., Qian, B., Zhao, T., Jing, Q., Geng, X., . . . Shang, J. (2016). Estimating winter wheat biomass by assimilating leaf area index derived from fusion of Landsat-8 and MODIS data. *International Journal of Applied Earth Observation and Geoinformation*, 49, 63-74.
- Doraiswamy, P. C., Hatfield, J. L., Jackson, T. J., Akhmedov, B., Prueger, J., & Stern, A. (2004). Crop condition and yield simulations using Landsat and MODIS. *Remote Sensing of Environment*, 92(4), 548-559.
- Drummond, S. T., Sudduth, K. A., Joshi, A., Birrell, S. J., & Kitchen, N. R. (2003). Statistical and neural methods for site-specific yield prediction. *Transactions of the ASAE*, 46(1), 5.
- Du Pisani, J. A. (2006). Sustainable development-historical roots of the concept. *Environmental sciences*, 3(2), 83-96.
- Dubovik, O., Schuster, G. L., Xu, F., Hu, Y., Bösch, H., Landgraf, J., & Li, Z. (2021a). Grand challenges in satellite remote sensing. *Frontiers in Remote Sensing*, 1.
- Dubovik, O., Schuster, G. L., Xu, F., Hu, Y., Bösch, H., Landgraf, J., & Li, Z. (2021b). Grand Challenges in Satellite Remote Sensing. *Frontiers in Remote Sensing*, 2. doi:10.3389/frsen.2021.619818
- Dubovik, O., Schuster, G. L., Xu, F., Hu, Y., Bösch, H., Landgraf, J., & Li, Z. (2021c). Grand challenges in satellite remote sensing. In (Vol. 2, pp. 619818): Frontiers Media SA.
- Duchemin, B., Maisongrande, P., Boulet, G., & Benhadj, I. (2008). A simple algorithm for yield estimates: Evaluation for semi-arid irrigated winter wheat monitored with green leaf area index. *Environmental Modelling & Software*, 23(7), 876-892.
- DuVal, A., Mijatovic, D., & Hodgkin, T. (2019). contribution of biodiversity for food and agriculture to the resilience of production systems: thematic study for The State of the World's Biodiversity for Food and Agriculture.
- Economics, V. U. o. E. a. B. W. I. f. E., Stephan Lutter, S. G., Burcu Gözet, Hanspeter Wieland, (UBA);, F. E. A., & Manstein, C. (2018). *The Use of Natural Resources: Report for Germany 2018*. 06844 Dessau-Roßlau: Federal Environment Agency Retrieved from <https://www.umweltbundesamt.de/en/publikationen/the-use-of-natural-resources-report-for-germany>
- Eitzinger, J., Trnka, M., Hösch, J., Žalud, Z., & Dubrovský, M. (2004). Comparison of CERES, WOFOST and SWAP models in simulating soil water content during growing season under different soil conditions. *Ecological Modelling*, 171(3), 223-246.
- Elavarasan, D., & Vincent, P. D. (2020). Crop yield prediction using deep reinforcement learning model for sustainable agrarian applications. *IEEE access*, 8, 86886-86901.
- Emelyanova, I. V., McVicar, T. R., Van Niel, T. G., Li, L. T., & Van Dijk, A. I. J. M. (2013). Assessing the accuracy of blending Landsat-MODIS surface reflectances in two landscapes with contrasting spatial and temporal dynamics: A framework for algorithm selection. *Remote Sensing of Environment*, 133, 193-209.
- Ersoz, E. S., Martin, N. F., & Stapleton, A. E. (2020). On to the next chapter for crop breeding: convergence with data science. *Crop Science*, 60(2), 639-655.
- Espinoza-Molina, D., & Datcu, M. (2013). Earth-observation image retrieval based on content, semantics, and metadata. *IEEE Transactions on Geoscience and Remote sensing*, 51(11), 5145-5159.
- Estrada-Carmona, N., Sánchez, A. C., Remans, R., & Jones, S. K. (2022). Complex agricultural landscapes host more biodiversity than simple ones: A global meta-analysis. *Proceedings of the National Academy of Sciences*, 119(38), e2203385119.
- Eurostat, W. S. (2019). Available online: https://ec.europa.eu/eurostat/statistics-explained/index.php/Waste_statistics_-_electrical_and_electronic_equipment (accessed on 7 August 2020).
- FAO, F. (2017). The future of food and agriculture-Trends and challenges. *Annual Report*, 296, 1-180.

- Farr, T. G., Rosen, P. A., Caro, E., Crippen, R., Duren, R., Hensley, S., . . . Roth, L. (2007). The shuttle radar topography mission. *Reviews of geophysics*, 45(2).
- Fegraus, E. H., Zaslavsky, I., Whitenack, T., Dempewolf, J., Ahumada, J. A., Lin, K., & Andelman, S. J. (2012). Interdisciplinary decision support dashboard: A new framework for a tanzanian agricultural and ecosystem service monitoring system pilot. *IEEE Journal of Selected Topics in Applied Earth Observations and Remote Sensing*, 5(6), 1700-1708.
- Franko, U., Puhmann, M., Kuka, K., Böhme, F., & Merbach, I. (2007). Dynamics of water, carbon and nitrogen in an agricultural used Chernozem soil in Central Germany. In *Modelling water and nutrient dynamics in soil-crop systems* (pp. 245-258): Springer.
- Friedl, M. A., Sulla-Menashe, D., Tan, B., Schneider, A., Ramankutty, N., Sibley, A., & Huang, X. (2010). MODIS Collection 5 global land cover: Algorithm refinements and characterization of new datasets. *Remote Sensing of Environment*, 114(1), 168-182.
- Fritz, S., See, L., Bayas, J. C. L., Waldner, F., Jacques, D., Becker-Reshef, I., . . . Crutchfield, J. (2019). A comparison of global agricultural monitoring systems and current gaps. *Agricultural Systems*, 168, 258-272.
- Fukuda, S., Spreer, W., Yasunaga, E., Yuge, K., Sardud, V., & Müller, J. (2013). Random Forests modelling for the estimation of mango (*Mangifera indica* L. cv. Chok Anan) fruit yields under different irrigation regimes. *Agricultural water management*, 116, 142-150.
- Gao, B.-C. (1996). NDWI—A normalized difference water index for remote sensing of vegetation liquid water from space. *Remote Sensing of Environment*, 58(3), 257-266.
- Gao, F., Anderson, M. C., Kustas, W. P., & Wang, Y. (2012). Simple method for retrieving leaf area index from Landsat using MODIS leaf area index products as reference. *Journal of Applied Remote Sensing*, 6(1), 063554.
- Gao, F., Masek, J., Schwaller, M., & Hall, F. (2006). On the blending of the Landsat and MODIS surface reflectance: Predicting daily Landsat surface reflectance. *IEEE Transactions on Geoscience and Remote Sensing*, 44(8), 2207-2218.
- Gao, F., Morisette, J. T., Wolfe, R. E., Ederer, G., Pedelty, J., Masuoka, E., . . . Nightingale, J. (2008). An algorithm to produce temporally and spatially continuous MODIS-LAI time series. *IEEE Geoscience and Remote Sensing Letters*, 5(1), 60-64.
- Gevaert, C. M., & García-Haro, F. J. (2015). A comparison of STARFM and an unmixing-based algorithm for Landsat and MODIS data fusion. *Remote Sensing of Environment*, 156, 34-44. doi:10.1016/j.rse.2014.09.012
- Ghadge, R., Kulkarni, J., More, P., Nene, S., & Priya, R. (2018). Prediction of crop yield using machine learning. *Int. Res. J. Eng. Technol.(IRJET)*, 5.
- Ghosh, R., Gupta, P. K., Tolpekin, V., & Srivastav, S. (2020). An enhanced spatiotemporal fusion method—Implications for coal fire monitoring using satellite imagery. *International Journal of Applied Earth Observation and Geoinformation*, 88, 102056.
- Gitelson, A. A., Peng, Y., Masek, J. G., Rundquist, D. C., Verma, S., Suyker, A., . . . Meyers, T. (2012). Remote estimation of crop gross primary production with Landsat data. *Remote Sensing of Environment*, 121, 404-414.
- Gochis, D., Barlage, M., Dugger, A., FitzGerald, K., Karsten, L., McAllister, M., . . . Read, L. (2018). The WRF-Hydro modeling system technical description,(Version 5.0). *NCAR Technical Note*, 107.
- Gorelick, N., Hancher, M., Dixon, M., Ilyushchenko, S., Thau, D., & Moore, R. (2017). Google Earth Engine: Planetary-scale geospatial analysis for everyone. *Remote Sensing of Environment*, 202, 18-27.
- Gorlinski, G. (2012). *The history of agriculture*: Britannica Educational Publishing.
- Goudriaan, J. (1977). Crop micrometeorology: a simulation study.
- Grace, J. (1988). *Temperature as a determinant of plant productivity*.
- Grigg, D. B. (1980). *Population growth and agrarian change: an historical perspective* (Vol. 13): Cambridge University Press.
- Groten, S. (1993). NDVI—crop monitoring and early yield assessment of Burkina Faso. *Remote Sensing of Environment*, 14(8), 1495-1515.
- Guo, Y., Wang, C., Lei, S., Yang, J., & Zhao, Y. (2020). A framework of spatio-temporal fusion algorithm selection for landsat NDVI time series construction. *ISPRS International Journal of Geo-Information*, 9(11), 665.
- Habekotté, B. (1997). A model of the phenological development of winter oilseed rape (*Brassica napus* L.). *Field Crops Research*, 54(2-3), 127-136.

References

- Hadria, R., Duchemin, B., Lahrouni, A., Khabba, S., Er-Raki, S., Dedieu, G., . . . Oliso, S. A. (2006). Monitoring of irrigated wheat in a semi-arid climate using crop modelling and remote sensing data: Impact of satellite revisit time frequency. *International journal of remote sensing*, 27(6), 1093-1117.
- Hansen, J., & Jones, J. (2000). Scaling-up crop models for climate variability applications. *Agricultural Systems*, 65(1), 43-72.
- Haque, F. F., Abdelgawad, A., Yanambaka, V. P., & Yelamarthi, K. (2020). *Crop Yield Prediction Using Deep Neural Network*. Paper presented at the 2020 IEEE 6th World Forum on Internet of Things (WF-IoT).
- Harfenmeister, K., Itzerott, S., Weltzien, C., & Spengler, D. (2021). Detecting phenological development of winter wheat and winter barley using time series of Sentinel-1 and Sentinel-2. *Remote Sensing*, 13(24), 5036.
- Harlan, J. R. (1975). Our Vanishing Genetic Resources: Modern varieties replace ancient populations that have provided genetic variability for plant breeding programs. *Science*, 188(4188), 618-621.
- Heinzl, V., Waske, B., Braun, M., & Menz, G. (2005). *The potential of multitemporal and multisensoral remote sensing data for the extraction of biophysical parameters of wheat*. Paper presented at the Remote Sensing for Agriculture, Ecosystems, and Hydrology VII.
- Hersbach, H., Bell, B., Berrisford, P., Hirahara, S., Horányi, A., Muñoz-Sabater, J., & Simmons, A. (2020). The ERA5 global reanalysis. *Quarterly Journal of the Royal Meteorological Society*. (In print).
- Heywood, V. H. (2013). Overview of agricultural biodiversity and its contribution to nutrition and health. In *Diversifying food and diets* (pp. 67-99): Routledge.
- Hilker, T., Wulder, M. A., Coops, N. C., Linke, J., McDermid, G., Masek, J. G., . . . White, J. C. (2009). A new data fusion model for high spatial-and temporal-resolution mapping of forest disturbance based on Landsat and MODIS. *Remote Sensing of Environment*, 113(8), 1613-1627.
- Hodgson, A. (1978). Repeseed adaptation in Northern New South Wales. II.* Predicting plant development of Brassica campestris L. and Brassica napus L. and its implications for planting time, designed to avoid water deficit and frost. *Australian Journal of Agricultural Research*, 29(4), 711-726.
- Hoogenboom, G. (2000). Contribution of agrometeorology to the simulation of crop production and its applications. *Agricultural and Forest Meteorology*, 103(1-2), 137-157.
- Howden, S. M., Soussana, J.-F., Tubiello, F. N., Chhetri, N., Dunlop, M., & Meinke, H. (2007). Adapting agriculture to climate change. *Proceedings of the National Academy of Sciences*, 104(50), 19691-19696.
- Htitiou, A., Boudhar, A., & Benabdelouahab, T. (2021). Deep Learning-Based Spatiotemporal Fusion Approach for Producing High-Resolution NDVI Time-Series Datasets. *Canadian Journal of Remote Sensing*, 47(2), 182-197. doi:10.1080/07038992.2020.1865141
- Htitiou, A., Boudhar, A., Lebrini, Y., Hadria, R., Lionboui, H., Elmansouri, L., . . . Benabdelouahab, T. (2019). The performance of random forest classification based on phenological metrics derived from Sentinel-2 and Landsat 8 to map crop cover in an irrigated semi-arid region. *Remote Sensing in Earth Systems Sciences*, 2(4), 208-224.
- Huang, B., & Song, H. (2012). Spatiotemporal reflectance fusion via sparse representation. *IEEE Transactions on Geoscience and Remote sensing*, 50(10), 3707-3716.
- Huang, J., Gómez-Dans, J. L., Huang, H., Ma, H., Wu, Q., Lewis, P. E., . . . Wu, Y. (2019). Assimilation of remote sensing into crop growth models: Current status and perspectives. *Agricultural and Forest Meteorology*, 276, 107609.
- Huang, J., Ma, H., Su, W., Zhang, X., Huang, Y., Fan, J., & Wu, W. (2015). Jointly assimilating MODIS LAI and ET products into the SWAP model for winter wheat yield estimation. *IEEE Journal of Selected Topics in Applied Earth Observations and Remote Sensing*, 8(8), 4060-4071.
- Huang, J., Sedano, F., Huang, Y., Ma, H., Li, X., Liang, S., . . . Wu, W. (2016). Assimilating a synthetic Kalman filter leaf area index series into the WOFOST model to improve regional winter wheat yield estimation. *Agricultural and Forest Meteorology*, 216, 188-202.
- Huang, J., Tian, L., Liang, S., Ma, H., Becker-Reshef, I., Huang, Y., . . . Wu, W. (2015). Improving winter wheat yield estimation by assimilation of the leaf area index from Landsat TM and MODIS data into the WOFOST model. *Agricultural and Forest Meteorology*, 204, 106-121.
- Huang, J., Zhuo, W., Li, Y., Huang, R., Sedano, F., Su, W., . . . Zhu, D. (2020). Comparison of three remotely sensed drought indices for assessing the impact of drought on winter wheat yield. *International Journal of Digital Earth*, 13(4), 504-526.
- Hurt, R. D. (1987). *Indian agriculture in America: Prehistory to the present*: University Press of Kansas.

- Hwang, T., Song, C., Bolstad, P. V., & Band, L. E. (2011). Downscaling real-time vegetation dynamics by fusing multi-temporal MODIS and Landsat NDVI in topographically complex terrain. *Remote Sensing of Environment*, 115(10), 2499-2512.
- Index, G. H. (2022). 2022-G LOBAL HUNGER INDEX-FOOD SYSTEMS TRANSFORMATION AND LOCAL GOVERNANCE.
- Ines, A. V., Hansen, J. W., & Robertson, A. W. (2011). Enhancing the utility of daily GCM rainfall for crop yield prediction. *International Journal of Climatology*, 31(14), 2168-2182.
- IPCC, C. C. (2007). The physical science basis; summary for policymakers. *Contribution of working group I to the fourth assessment report of the intergovernmental panel on climate change*.
- Iqbal, M. A., Shen, Y., Stricevic, R., Pei, H., Sun, H., Amiri, E., . . . del Rio, S. (2014). Evaluation of the FAO AquaCrop model for winter wheat on the North China Plain under deficit irrigation from field experiment to regional yield simulation. *Agricultural water management*, 135, 61-72.
- Jabal, Z. K., Khayyun, T. S., & Alwan, I. A. (2022). Impact of climate change on crops productivity using MODIS-NDVI time series. *Civil Engineering Journal*, 8(06).
- Jackson, B. (2020). *Slavery from space: an analysis of the modern slavery-environmental degradation nexus using remote sensing data*. University of Nottingham,
- Jarihani, A., McVicar, T., Van Niel, T., Emelyanova, I., Callow, J., & Johansen, K. (2014). Blending Landsat and MODIS Data to Generate Multispectral Indices: A Comparison of "Index-then-Blend" and "Blend-then-Index" Approaches. *Remote Sensing*, 6(10), 9213-9238. doi:10.3390/rs6109213
- Jeong, J. H., Resop, J. P., Mueller, N. D., Fleisher, D. H., Yun, K., Butler, E. E., . . . Reddy, V. R. (2016). Random forests for global and regional crop yield predictions. *PLoS one*, 11(6), e0156571.
- Jiang, Z., Chen, Z., Chen, J., Liu, J., Ren, J., Li, Z., . . . Li, H. (2014). Application of crop model data assimilation with a particle filter for estimating regional winter wheat yields. *IEEE Journal of Selected Topics in Applied Earth Observations and Remote Sensing*, 7(11), 4422-4431.
- Jin, X., Kumar, L., Li, Z., Feng, H., Xu, X., Yang, G., & Wang, J. (2018). A review of data assimilation of remote sensing and crop models. *European journal of agronomy*, 92, 141-152.
- Johnson, M. D., Hsieh, W. W., Cannon, A. J., Davidson, A., & Bédard, F. (2016). Crop yield forecasting on the Canadian Prairies by remotely sensed vegetation indices and machine learning methods. *Agricultural and Forest Meteorology*, 218, 74-84.
- Jones, J. W., Hoogenboom, G., Porter, C. H., Boote, K. J., Batchelor, W. D., Hunt, L., . . . Ritchie, J. T. (2003). The DSSAT cropping system model. *European journal of agronomy*, 18(3-4), 235-265.
- Joshi, N., Baumann, M., Ehammer, A., Fensholt, R., Grogan, K., Hostert, P., . . . Mitchard, E. T. (2016). A review of the application of optical and radar remote sensing data fusion to land use mapping and monitoring. *Remote Sensing*, 8(1), 70.
- Justice, C., Townshend, J., Vermote, E., Masuoka, E., Wolfe, R., Saleous, N., . . . Morisette, J. (2002). An overview of MODIS Land data processing and product status. *Remote Sensing of Environment*, 83(1-2), 3-15.
- Kale, S. S., & Patil, P. S. (2019). *A machine learning approach to predict crop yield and success rate*. Paper presented at the 2019 IEEE Pune Section International Conference (PuneCon).
- Kandasamy, S., Baret, F., Verger, A., Neveux, P., & Weiss, M. (2013). A comparison of methods for smoothing and gap filling time series of remote sensing observations & application to MODIS LAI products. *Biogeosciences*, 10(6), 4055-4071. doi:10.5194/bg-10-4055-2013
- Karila, K., Nevalainen, O., Krooks, A., Karjalainen, M., & Kaasalainen, S. (2014). Monitoring changes in rice cultivated area from SAR and optical satellite images in Ben Tre and Tra Vinh Provinces in Mekong Delta, Vietnam. *Remote Sensing*, 6(5), 4090-4108.
- Kasampalis, D. A., Alexandridis, T. K., Deva, C., Challinor, A., Moshou, D., & Zalidis, G. (2018). Contribution of remote sensing on crop models: a review. *Journal of Imaging*, 4(4), 52.
- Kassam, A., & Kassam, L. (2020). The need for conservation agriculture. In *Advances in Conservation Agriculture* (pp. 1-30): Burleigh Dodds Science Publishing.
- Keating, B. A., Carberry, P. S., Hammer, G. L., Probert, M. E., Robertson, M. J., Holzworth, D., . . . Hochman, Z. (2003). An overview of APSIM, a model designed for farming systems simulation. *European journal of agronomy*, 18(3-4), 267-288.
- Kephe, P. N., Ayisi, K. K., & Petja, B. M. (2021). Challenges and opportunities in crop simulation modelling under seasonal and projected climate change scenarios for crop production in South Africa. *Agriculture & Food Security*, 10(1), 1-24.

References

- Kern, A., Barcza, Z., Marjanović, H., Árendás, T., Fodor, N., Bónis, P., . . . Lichtenberger, J. (2018). Statistical modelling of crop yield in Central Europe using climate data and remote sensing vegetation indices. *Agricultural and Forest Meteorology*, 260, 300-320.
- Khaki, S., & Wang, L. (2019). Crop yield prediction using deep neural networks. *Frontiers in plant science*, 10, 621.
- Khaki, S., Wang, L., & Archontoulis, S. V. (2020). A cnn-rnn framework for crop yield prediction. *Frontiers in plant science*, 10, 1750.
- Ki-Moon, B. (2013). The millennium development goals report 2013. *United Nations Pubns*, 365, 366.
- Kim, N., Ha, K.-J., Park, N.-W., Cho, J., Hong, S., & Lee, Y.-W. (2019). A comparison between major artificial intelligence models for crop yield prediction: Case study of the midwestern United States, 2006–2015. *ISPRS International Journal of Geo-Information*, 8(5), 240.
- Kim, S.-R., Prasad, A. K., El-Askary, H., Lee, W.-K., Kwak, D.-A., Lee, S.-H., & Kafatos, M. (2014). Application of the Savitzky-Golay filter to land cover classification using temporal MODIS vegetation indices. *Photogrammetric Engineering & Remote Sensing*, 80(7), 675-685.
- Kloos, S., Yuan, Y., Castelli, M., & Menzel, A. (2021). Agricultural Drought Detection with MODIS Based Vegetation Health Indices in Southeast Germany. *Remote Sensing*, 13(19). doi:10.3390/rs13193907
- Koohafkan, P., & Altieri, M. A. (2011). *Globally important agricultural heritage systems: a legacy for the future*. Food and Agriculture Organization of the United Nations Rome.
- Kovács-Hostyánszki, A., Espíndola, A., Vanbergen, A. J., Settele, J., Kremen, C., & Dicks, L. V. (2017). Ecological intensification to mitigate impacts of conventional intensive land use on pollinators and pollination. *Ecology Letters*, 20(5), 673-689.
- Krishnaswamy, J., Bawa, K. S., Ganeshiah, K., & Kiran, M. (2009). Quantifying and mapping biodiversity and ecosystem services: Utility of a multi-season NDVI based Mahalanobis distance surrogate. *Remote Sensing of Environment*, 113(4), 857-867.
- Kuebert, C. (2018a). *Fernerkundung für das Phänologiemonitoring: Optimierung und Analyse des Ergrünungsbeginns mittels MODIS-Zeitreihen für Deutschland*. (Doctorate). University of Wuerzburg, Wuerzburg.
- Kuebert, C. (2018b). *Fernerkundung für das Phänologiemonitoring: Optimierung und Analyse des Ergrünungsbeginns mittels MODIS-Zeitreihen für Deutschland*. (PhD Thesis). University of Wuerzburg, Wuerzburg, Germany.
- Kumar, S., & Arya, S. (2021). Change detection techniques for land cover change analysis using spatial datasets: A review. *Remote Sensing in Earth Systems Sciences*, 4(3), 172-185.
- Kuwata, K., & Shibasaki, R. (2015). *Estimating crop yields with deep learning and remotely sensed data*. Paper presented at the 2015 IEEE International Geoscience and Remote Sensing Symposium (IGARSS).
- Lasaponara, R., Abate, N., Fattore, C., Aromando, A., Cardettini, G., & Di Fonzo, M. (2022). On the Use of Sentinel-2 NDVI Time Series and Google Earth Engine to Detect Land-Use/Land-Cover Changes in Fire-Affected Areas. *Remote Sensing*, 14(19), 4723.
- Laurance, W. F., & Engert, J. (2022). Sprawling cities are rapidly encroaching on Earth's biodiversity. *Proceedings of the National Academy of Sciences*, 119(16), e2202244119.
- Lazarova, S., Coyne, D., Rodriguez, M. G., Peteira, B., & Ciancio, A. (2021). Functional diversity of soil nematodes in relation to the impact of agriculture—a review. *Diversity*, 13(2), 64.
- Lebrini, Y., Boudhar, A., Htitiou, A., Hadria, R., Lionbouï, H., Bounoua, L., & Benabdelouahab, T. (2020). Remote monitoring of agricultural systems using NDVI time series and machine learning methods: a tool for an adaptive agricultural policy. *Arabian Journal of Geosciences*, 13(16), 1-14.
- Lee, M. H., Cheon, E. J., & Eo, Y. D. (2019). Cloud Detection and Restoration of Landsat-8 using STARFM. *Korean Journal of Remote Sensing*, 35(5_2), 861-871.
- Levy, B. S. (2006). *Occupational and environmental health: recognizing and preventing disease and injury*: Lippincott Williams & Wilkins.
- Lewis, D., Phinn, S., & Arroyo, L. (2013). Cost-effectiveness of seven approaches to map vegetation communities—A case study from Northern Australia's tropical savannas. *Remote Sensing*, 5(1), 377-414.
- Lewis, P., Gómez-Dans, J., Kaminski, T., Settle, J., Quaife, T., Gobron, N., . . . Berger, M. (2012). An earth observation land data assimilation system (EO-LDAS). *Remote Sensing of Environment*, 120, 219-235.
- Lezoche, M., Hernandez, J. E., Díaz, M. d. M. E. A., Panetto, H., & Kacprzyk, J. (2020). Agri-food 4.0: A survey of the supply chains and technologies for the future agriculture. *Computers in industry*, 117, 103187.

- Li, Y., Ren, Y. Z., Gao, W. L., Tao, S., Jia, J. D., & Liu, X. L. (2021). Analysis of influencing factors on winter wheat yield estimations based on a multisource remote sensing data fusion. *Applied Engineering in Agriculture*, 37(5), 991-1003.
- Liao, C., Wang, J., Pritchard, I., Liu, J., & Shang, J. (2017). A Spatio-Temporal Data Fusion Model for Generating NDVI Time Series in Heterogeneous Regions. *Remote Sensing*, 9(11). doi:10.3390/rs9111125
- Liaw, A., & Wiener, M. (2002). Classification and regression by randomForest. *R news*, 2(3), 18-22.
- Lin, B. B. (2011). Resilience in agriculture through crop diversification: adaptive management for environmental change. *BioScience*, 61(3), 183-193.
- Liu, C., Gao, W., Liu, P., & Sun, Z. (2014). *Assimilation of remote sensing data into crop growth model to improve the estimation of regional winter wheat yield*. Paper presented at the Remote Sensing and Modeling of Ecosystems for Sustainability XI.
- Liu, J., Pattey, E., Miller, J. R., McNairn, H., Smith, A., & Hu, B. (2010). Estimating crop stresses, aboveground dry biomass and yield of corn using multi-temporal optical data combined with a radiation use efficiency model. *Remote Sensing of Environment*, 114(6), 1167-1177.
- Liu, M., Ke, Y., Yin, Q., Chen, X., & Im, J. (2019). Comparison of five spatio-temporal satellite image fusion models over landscapes with various spatial heterogeneity and temporal variation. *Remote Sensing*, 11(22), 2612.
- Liu, Y., Pan, X., & Li, J. (2015). Current agricultural practices threaten future global food production. *Journal of Agricultural and Environmental Ethics*, 28, 203-216.
- LIU, Z.-c., Chao, W., BI, R.-t., ZHU, H.-f., Peng, H., JING, Y.-d., & YANG, W.-d. (2021). Winter wheat yield estimation based on assimilated Sentinel-2 images with the CERES-Wheat model. *Journal of Integrative Agriculture*, 20(7), 1958-1968.
- Lobell, D. B. (2013). The use of satellite data for crop yield gap analysis. *Field Crops Research*, 143, 56-64.
- Lobell, D. B., Asner, G. P., Ortiz-Monasterio, J. I., & Benning, T. L. (2003). Remote sensing of regional crop production in the Yaqui Valley, Mexico: estimates and uncertainties. *Agriculture, Ecosystems & Environment*, 94(2), 205-220.
- Lunetta, R. S., Lyon, J. G., Guindon, B., & Elvidge, C. D. (1998). North American landscape characterization dataset development and data fusion issues. *Photogrammetric Engineering and Remote Sensing*, 64, 821-828.
- Luo, Y., Guan, K., & Peng, J. (2018). STAIR: A generic and fully-automated method to fuse multiple sources of optical satellite data to generate a high-resolution, daily and cloud-/gap-free surface reflectance product. *Remote Sensing of Environment*, 214, 87-99.
- Ma, G., Huang, J., Wu, W., Fan, J., Zou, J., & Wu, S. (2013). Assimilation of MODIS-LAI into the WOFOST model for forecasting regional winter wheat yield. *Mathematical and Computer Modelling*, 58(3-4), 634-643.
- Ma, H., Huang, W., Dong, Y., Liu, L., & Guo, A. (2021). Using UAV-based hyperspectral imagery to detect winter wheat fusarium head blight. *Remote Sensing*, 13(15), 3024.
- Macholdt, J., & Honermeier, B. (2017). Yield stability in winter wheat production: a survey on German farmers' and advisors' views. *Agronomy*, 7(3), 45.
- Madec, S., Baret, F., De Solan, B., Thomas, S., Dutartre, D., Jezequel, S., . . . Comar, A. (2017). High-throughput phenotyping of plant height: comparing unmanned aerial vehicles and ground LiDAR estimates. *Frontiers in plant science*, 8, 2002.
- Mairota, P., Cafarelli, B., Didham, R. K., Lovergine, F. P., Lucas, R. M., Nagendra, H., . . . Tarantino, C. (2015). Challenges and opportunities in harnessing satellite remote-sensing for biodiversity monitoring. *Ecological Informatics*, 30, 207-214.
- Maitima, J. M., Mugatha, S. M., Reid, R. S., Gachimbi, L. N., Majule, A., Lyaruu, H., . . . Mugisha, S. (2009). The linkages between land use change, land degradation and biodiversity across East Africa. *African Journal of Environmental Science and Technology*, 3(10).
- Maniatis, D., & Mollicone, D. (2010). Options for sampling and stratification for national forest inventories to implement REDD+ under the UNFCCC. *Carbon balance and management*, 5, 1-14.
- Mariano, C., & Monica, B. (2021). A random forest-based algorithm for data-intensive spatial interpolation in crop yield mapping. *Computers and Electronics in Agriculture*, 184, 106094.
- McNairn, H., & Shang, J. (2016). A review of multitemporal synthetic aperture radar (SAR) for crop monitoring. *Multitemporal Remote Sensing: Methods and Applications*, 317-340.

References

- McNeely, J. A., & Scherr, S. J. (2003). *Ecoagriculture: strategies to feed the world and save wild biodiversity*: Island press.
- Meier, U., Bleiholder, H., Buhr, L., Feller, C., Hack, H., Heß, M., . . . Van Den Boom, T. (2009). The BBCH system to coding the phenological growth stages of plants—history and publications. *Journal für Kulturpflanzen*, 61(2), 41-52.
- Miller, J. (2002). *Agriculture and Forestry in Bavaria: Facts and Figures 2002*. Postfach 22 00 12, 80535 München, Germany: Bayerisches Staatsministerium für Landwirtschaft und Forsten Retrieved from www.landwirtschaft.bayern.de
- Mirschel, W., Schultz, A., Wenkel, K. O., Wieland, R., & Poluektov, R. A. (2004). Crop growth modelling on different spatial scales—A wide spectrum of approaches. *Archives of Agronomy and Soil Science*, 50(3), 329-343.
- Miskimin, H. A. (1975). *The economy of early Renaissance Europe, 1300-1460*: Cambridge University Press.
- Miskimin, H. A. (1977). *The economy of later Renaissance Europe 1460-1600*: Cambridge University Press.
- Mo, X., Liu, S., Lin, Z., Xu, Y., Xiang, Y., & McVicar, T. (2005). Prediction of crop yield, water consumption and water use efficiency with a SVAT-crop growth model using remotely sensed data on the North China Plain. *Ecological Modelling*, 183(2-3), 301-322.
- Monteith, J. L. (1972). Solar radiation and productivity in tropical ecosystems. *Journal of applied ecology*, 9(3), 747-766.
- Monteith, J. L. (1977). Climate and the efficiency of crop production in Britain. *Philosophical Transactions of the Royal Society of London. B, Biological Sciences*, 281(980), 277-294.
- Moon, M., Richardson, A. D., & Friedl, M. A. (2021). Multiscale assessment of land surface phenology from harmonized Landsat 8 and Sentinel-2, PlanetScope, and PhenoCam imagery. *Remote Sensing of Environment*, 266, 112716.
- Moreno-Martínez, Á., Izquierdo-Verdiguier, E., Maneta, M. P., Camps-Valls, G., Robinson, N., Muñoz-Mari, J., . . . Running, S. W. (2020). Multispectral high resolution sensor fusion for smoothing and gap-filling in the cloud. *Remote Sensing of Environment*, 247, 111901.
- Moriondo, M., Maselli, F., & Bindi, M. (2007). A simple model of regional wheat yield based on NDVI data. *European journal of agronomy*, 26(3), 266-274.
- Mueller, N. D., Gerber, J. S., Johnston, M., Ray, D. K., Ramankutty, N., & Foley, J. A. (2012). Closing yield gaps through nutrient and water management. *Nature*, 490(7419), 254-257.
- Muraoka, H., & Koizumi, H. (2009). Satellite Ecology (SATECO)—linking ecology, remote sensing and micrometeorology, from plot to regional scale, for the study of ecosystem structure and function. *Journal of plant research*, 122, 3-20.
- Murdoch, W. J., Singh, C., Kumbier, K., Abbasi-Asl, R., & Yu, B. (2019). Definitions, methods, and applications in interpretable machine learning. *Proceedings of the National Academy of Sciences*, 116(44), 22071-22080.
- Murthy, V. R. K. (2004). Crop growth modeling and its applications in agricultural meteorology. *Satellite remote sensing and GIS applications in agricultural meteorology*, 235.
- Mutanga, O., Adam, E., & Cho, M. A. (2012). High density biomass estimation for wetland vegetation using WorldView-2 imagery and random forest regression algorithm. *International Journal of Applied Earth Observation and Geoinformation*, 18, 399-406.
- Myneni, R. B., Hall, F. G., Sellers, P. J., & Marshak, A. L. (1995). The interpretation of spectral vegetation indexes. *IEEE Transactions on Geoscience and Remote sensing*, 33(2), 481-486.
- Nellis, M. D., Price, K. P., & Rundquist, D. (2009). Remote sensing of cropland agriculture. *The SAGE handbook of remote sensing*, 1, 368-380.
- Nelson, G. C., Rosegrant, M. W., Palazzo, A., Gray, I., Ingersoll, C., Robertson, R., . . . Ringler, C. (2010). *Food security, farming, and climate change to 2050: scenarios, results, policy options* (Vol. 172): Intl Food Policy Res Inst.
- Nelson, K. S., & Burchfield, E. K. (2021). Landscape complexity and US crop production. *Nature Food*, 2(5), 330-338.
- Nelson, K. S., Patalee, B., & Yao, B. (2022). Higher landscape diversity associated with improved crop production resilience in Kansas-USA. *Environmental Research Letters*, 17(8), 084011.
- Nemecek, T., Weiler, K., Plassmann, K., Schnetzer, J., Gaillard, G., Jefferies, D., . . . i Canals, L. M. (2012). Estimation of the variability in global warming potential of worldwide crop production using a modular extrapolation approach. *Journal of Cleaner Production*, 31, 106-117.

- Nendel, C., Berg, M., Kersebaum, K. C., Mirschel, W., Specka, X., Wegehenkel, M., . . . Wieland, R. (2011). The MONICA model: Testing predictability for crop growth, soil moisture and nitrogen dynamics. *Ecological Modelling*, 222(9), 1614-1625.
- Noaman, M., & El Quosy, D. (2017). Hydrology of the Nile and ancient agriculture. *Irrigated Agriculture in Egypt: Past, Present and Future*, 9-28.
- Ogutu, B. O., & Dash, J. (2013). An algorithm to derive the fraction of photosynthetically active radiation absorbed by photosynthetic elements of the canopy (FAPAR ps) from eddy covariance flux tower data. *New Phytologist*, 197(2), 511-523.
- Olesen, J. E., Trnka, M., Kersebaum, K. C., Skjelvåg, A. O., Seguin, B., Peltonen-Sainio, P., . . . Micale, F. (2011). Impacts and adaptation of European crop production systems to climate change. *European journal of agronomy*, 34(2), 96-112.
- Olexa, E. M., & Lawrence, R. L. (2014). Performance and effects of land cover type on synthetic surface reflectance data and NDVI estimates for assessment and monitoring of semi-arid rangeland. *International Journal of Applied Earth Observation and Geoinformation*, 30, 30-41. doi:10.1016/j.jag.2014.01.008
- Pahlevan, N., Chittimalli, S. K., Balasubramanian, S. V., & Vellucci, V. (2019). Sentinel-2/Landsat-8 product consistency and implications for monitoring aquatic systems. *Remote Sensing of Environment*, 220, 19-29.
- Palacios-Orueta, A., Huesca, M., Whiting, M. L., Litago, J., Khanna, S., Garcia, M., & Ustin, S. L. (2012). Derivation of phenological metrics by function fitting to time-series of Spectral Shape Indexes AS1 and AS2: Mapping cotton phenological stages using MODIS time series. *Remote Sensing of Environment*, 126, 148-159.
- Parajka, J., & Blöschl, G. (2008). Spatio-temporal combination of MODIS images - potential for snow cover mapping. *Water Resources Research*, 44(3). doi:10.1029/2007wr006204
- Patnaik, S., Sen, S., & Mahmoud, M. S. (2020). *Smart Village Technology: Concepts and Developments*: Springer.
- Pellegrini, P., & Fernández, R. J. (2018). Crop intensification, land use, and on-farm energy-use efficiency during the worldwide spread of the green revolution. *Proceedings of the National Academy of Sciences*, 115(10), 2335-2340.
- Perrot, T., Bretagnolle, V., & Gaba, S. (2022). Environmentally friendly landscape management improves oilseed rape yields by increasing pollinators and reducing pests. *Journal of applied ecology*, 59(7), 1825-1836.
- Perrot, T., Gaba, S., Roncoroni, M., Gautier, J.-L., & Bretagnolle, V. (2018). Bees increase oilseed rape yield under real field conditions. *Agriculture, Ecosystems & Environment*, 266, 39-48.
- Persello, C., & Bruzzone, L. (2009). A novel protocol for accuracy assessment in classification of very high resolution images. *IEEE Transactions on Geoscience and Remote sensing*, 48(3), 1232-1244.
- Pinter Jr, P. J., Hatfield, J. L., Schepers, J. S., Barnes, E. M., Moran, M. S., Daughtry, C. S., & Upchurch, D. R. (2003). Remote sensing for crop management.
- Pohl, C., & van Genderen, J. (1998). Multisensor image fusion in remote sensing: Concepts, methods and applications: *International Journal of Remote Sensing*.
- Porter, J. R., & Gawith, M. (1999). Temperatures and the growth and development of wheat: a review. *European journal of agronomy*, 10(1), 23-36.
- Porter, J. R., & Moot, D. J. (1998). *Research beyond the means: climatic variability and plant growth*.
- Potter, C. S., Randerson, J. T., Field, C. B., Matson, P. A., Vitousek, P. M., Mooney, H. A., & Klooster, S. A. (1993). Terrestrial ecosystem production: a process model based on global satellite and surface data. *Global Biogeochemical Cycles*, 7(4), 811-841.
- Potts, S. G., Biesmeijer, J. C., Kremen, C., Neumann, P., Schweiger, O., & Kunin, W. E. (2010). Global pollinator declines: trends, impacts and drivers. *Trends in ecology & evolution*, 25(6), 345-353.
- Poursanidis, D., Chrysoulakis, N., & Mitrika, Z. (2015). Landsat 8 vs. Landsat 5: A comparison based on urban and peri-urban land cover mapping. *International Journal of Applied Earth Observation and Geoinformation*, 35, 259-269.
- Pringle, H. (1998). The slow birth of agriculture. In: American Association for the Advancement of Science.
- Puntel, L. A., Sawyer, J. E., Barker, D. W., Dietzel, R., Poffenbarger, H., Castellano, M. J., . . . Archontoulis, S. V. (2016). Modeling long-term corn yield response to nitrogen rate and crop rotation. *Frontiers in plant science*, 7, 1630.

References

- Qiu, Y., Zhou, J., Chen, J., & Chen, X. (2021). Spatiotemporal fusion method to simultaneously generate full-length normalized difference vegetation index time series (SSFIT). *International Journal of Applied Earth Observation and Geoinformation*, 100, 102333.
- Quintano, C., Fernández-Manso, A., & Fernández-Manso, O. (2018). Combination of Landsat and Sentinel-2 MSI data for initial assessing of burn severity. *International Journal of Applied Earth Observation and Geoinformation*, 64, 221-225.
- Ramesh, D., & Vardhan, B. V. (2015). Analysis of crop yield prediction using data mining techniques. *International Journal of research in engineering and technology*, 4(1), 47-473.
- Rao, Y., Zhu, X., Chen, J., & Wang, J. (2015). An Improved Method for Producing High Spatial-Resolution NDVI Time Series Datasets with Multi-Temporal MODIS NDVI Data and Landsat TM/ETM+ Images. *Remote Sensing*, 7(6), 7865-7891. doi:10.3390/rs70607865
- Raudsepp-Hearne, C., Peterson, G. D., Tengö, M., Bennett, E. M., Holland, T., Benessaiah, K., . . . Pfeifer, L. (2010). Untangling the environmentalist's paradox: why is human well-being increasing as ecosystem services degrade? *BioScience*, 60(8), 576-589.
- Raven, P. H., & Wagner, D. L. (2021). Agricultural intensification and climate change are rapidly decreasing insect biodiversity. *Proceedings of the National Academy of Sciences*, 118(2), e2002548117.
- Ray, J. D., Gesch, R. W., Sinclair, T. R., & Allen, L. H. (2002). The effect of vapor pressure deficit on maize transpiration response to a drying soil. *Plant and soil*, 239(1), 113-121.
- Richter, R., & Schläpfer, D. (2005). Atmospheric/topographic correction for satellite imagery. *DLR report DLR-IB*, 565.
- Ritchie, H., Roser, M., & Pablo, R. (2022). Crop Yields. *Our World in Data*.
- Robinson, N. P., Allred, B. W., Jones, M. O., Moreno, A., Kimball, J. S., Naugle, D. E., . . . Richardson, A. D. (2017). A dynamic Landsat derived normalized difference vegetation index (NDVI) product for the conterminous United States. *Remote Sensing*, 9(8), 863.
- Rosenzweig, C., Iglesias, A., Yang, X.-B., Epstein, P. R., & Chivian, E. (2001). Climate change and extreme weather events-Implications for food production, plant diseases, and pests.
- Rouse, J. W., Haas, R. H., Schell, J. A., Deering, D. W., & Harlan, J. C. (1974). Monitoring the vernal advancement and retrogradation (green wave effect) of natural vegetation. *NASA/GSFC Type III Final Report, Greenbelt, Md*, 371.
- Roy, D. P., Ju, J., Lewis, P., Schaaf, C., Gao, F., Hansen, M., & Lindquist, E. (2008). Multi-temporal MODIS-Landsat data fusion for relative radiometric normalization, gap filling, and prediction of Landsat data. *Remote Sensing of Environment*, 112(6), 3112-3130.
- Roy, D. P., Kovalsky, V., Zhang, H., Vermote, E. F., Yan, L., Kumar, S., & Egorov, A. (2016). Characterization of Landsat-7 to Landsat-8 reflective wavelength and normalized difference vegetation index continuity. *Remote Sensing of Environment*, 185, 57-70.
- Rummler, T., Arnault, J., Gochis, D., & Kunstmann, H. (2019). Role of lateral terrestrial water flow on the regional water cycle in a complex terrain region: Investigation with a fully coupled model system. *Journal of Geophysical Research: Atmospheres*, 124(2), 507-529.
- Russell, G., & Wilson, G. W. (1994). An agro-pedo-climatological knowledge-base of wheat in Europe.
- Schwalbert, R. A., Amado, T., Corassa, G., Pott, L. P., Prasad, P. V., & Ciampitti, I. A. (2020). Satellite-based soybean yield forecast: Integrating machine learning and weather data for improving crop yield prediction in southern Brazil. *Agricultural and Forest Meteorology*, 284, 107886.
- Segal, M. R. (2004). Machine learning benchmarks and random forest regression.
- Semwal, R., & Maikhuri, R. (1996). Structure and functioning of traditional hill agroecosystems of Garhwal Himalaya. *Biological Agriculture & Horticulture*, 13(3), 267-289.
- Shahhosseini, M., Hu, G., & Archontoulis, S. V. (2020). Forecasting corn yield with machine learning ensembles. *Frontiers in plant science*, 11, 1120.
- Shahhosseini, M., Hu, G., Huber, I., & Archontoulis, S. V. (2021). Coupling machine learning and crop modeling improves crop yield prediction in the US Corn Belt. *Scientific reports*, 11(1), 1-15.
- Shahhosseini, M., Martinez-Feria, R. A., Hu, G., & Archontoulis, S. V. (2019). Maize yield and nitrate loss prediction with machine learning algorithms. *Environmental Research Letters*, 14(12), 124026.
- Shammi, S. A., & Meng, Q. (2021). Use time series NDVI and EVI to develop dynamic crop growth metrics for yield modeling. *Ecological Indicators*, 121, 107124.
- Shannon, C. E. (1948). A mathematical theory of communication. *The Bell system technical journal*, 27(3), 379-423.

- Sharifi, A. (2020). Flood mapping using relevance vector machine and SAR data: A case study from Aqqala, Iran. *Journal of the Indian Society of Remote Sensing*, 48(9), 1289-1296.
- Sharifi, A. (2021). Development of a method for flood detection based on Sentinel-1 images and classifier algorithms. *Water and Environment Journal*, 35(3), 924-929.
- Shelia, V., Hansen, J., Sharda, V., Porter, C., Aggarwal, P., Wilkerson, C. J., & Hoogenboom, G. (2019). A multi-scale and multi-model gridded framework for forecasting crop production, risk analysis, and climate change impact studies. *Environmental Modelling & Software*, 115, 144-154.
- Shen, M., Piao, S., Jeong, S.-J., Zhou, L., Zeng, Z., Ciais, P., . . . Li, L. Z. (2015). Evaporative cooling over the Tibetan Plateau induced by vegetation growth. *Proceedings of the National Academy of Sciences*, 112(30), 9299-9304.
- Shi, Z., Ruecker, G. R., Mueller, M., Conrad, C., Ibragimov, N., Lamers, J., . . . Vlek, P. L. G. (2007). Modeling of cotton yields in the amu darya river floodplains of Uzbekistan integrating multitemporal remote sensing and minimum field data. *Agronomy Journal*, 99(5), 1317-1326.
- Sidhu, B. S., Mehrabi, Z., Ramankutty, N., & Kandlikar, M. (2023). How can machine learning help in understanding the impact of climate change on crop yields? *Environmental Research Letters*.
- Singh, D. (2011). Generation and evaluation of gross primary productivity using Landsat data through blending with MODIS data. *International Journal of Applied Earth Observation and Geoinformation*, 13(1), 59-69.
- Single, W. V. (1985). Frost injury and the physiology of the wheat plant. *Journal of the Australian Institute of Agricultural Science*.
- Sivakumar, M., Gommers, R., & Baier, W. (2000). Agrometeorology and sustainable agriculture. *Agricultural and Forest Meteorology*, 103(1-2), 11-26.
- Skamarock, W. C., Klemp, J. B., Dudhia, J., Gill, D. O., Liu, Z., Berner, J., . . . Barker, D. M. (2019). A description of the advanced research WRF model version 4. *National Center for Atmospheric Research: Boulder, CO, USA*, 145, 145.
- Skendžić, S., Zovko, M., Živković, I. P., Lešić, V., & Lemić, D. (2021). The impact of climate change on agricultural insect pests. *Insects*, 12(5), 440.
- Slattery, R. A., & Ort, D. R. (2015). Photosynthetic energy conversion efficiency: setting a baseline for gauging future improvements in important food and biofuel crops. *Plant Physiology*, 168(2), 383-392.
- Solano, R., Didan, K., Jacobson, A., & Huete, A. MODIS vegetation index user's guide (MOD13 series).
- Souza, E., Bazzi, C., Khosla, R., Uribe-Opazo, M., & Reich, R. M. (2016). Interpolation type and data computation of crop yield maps is important for precision crop production. *Journal of Plant Nutrition*, 39(4), 531-538.
- Spellerberg, I. F., & Fedor, P. J. (2003). A tribute to Claude Shannon (1916–2001) and a plea for more rigorous use of species richness, species diversity and the 'Shannon–Wiener' Index. *Global ecology and biogeography*, 12(3), 177-179.
- Spitters, C., Van Keulen, H., & Van Kraalingen, D. (1989). A simple and universal crop growth simulator: SUCRO87. In *Simulation and systems management in crop protection* (pp. 147-181): Pudoc.
- Spitters, C. J. T., & Kramer, T. H. (1986). Differences between spring wheat cultivars in early growth. *Euphytica*, 35(1), 273-292.
- Steduto, P., Hsiao, T. C., Raes, D., & Fereres, E. (2009). AquaCrop – The FAO crop model to simulate yield response to water: I. Concepts and underlying principles. *Agronomy Journal*, 101(3), 426-437.
- Stöckle, C. O., Donatelli, M., & Nelson, R. (2003). CropSyst, a cropping systems simulation model. *European journal of agronomy*, 18(3-4), 289-307.
- Stone, R. C., & Meinke, H. (2006). Weather, climate, and farmers: an overview. *Meteorological Applications*, 13(S1), 7-20.
- Sulik, J. J., & Long, D. S. (2015). Spectral indices for yellow canola flowers. *International journal of remote sensing*, 36(10), 2751-2765.
- Supit, I. (1994). System description of the WOFOST 6.0 crop simulation model implemented in CGMS. *Theory and algorithms*, 1, 146.
- Swinton, S. M., Lupi, F., Robertson, G. P., & Hamilton, S. K. (2007). Ecosystem services and agriculture: cultivating agricultural ecosystems for diverse benefits. In (Vol. 64, pp. 245-252): Elsevier.
- Tang, W., Tang, R., Guo, T., & Wei, J. (2022). Remote Prediction of Oilseed Rape Yield via Gaofen-1 Images and a Crop Model. *Remote Sensing*, 14(9), 2041.

References

- Tao, G., Jia, K., Wei, X., Xia, M., Wang, B., Xie, X., . . . Zhang, X. (2021). Improving the spatiotemporal fusion accuracy of fractional vegetation cover in agricultural regions by combining vegetation growth models. *International Journal of Applied Earth Observation and Geoinformation*, 101, 102362.
- Team, R. C. (2013). R: A language and environment for statistical computing.
- Tewes, A., Thonfeld, F., Schmidt, M., Oomen, R. J., Zhu, X., Dubovyk, O., . . . Schellberg, J. (2015). Using RapidEye and MODIS data fusion to monitor vegetation dynamics in semi-arid rangelands in South Africa. *Remote Sensing*, 7(6), 6510-6534.
- Thomson, A. M., Brown, R. A., Ghan, S. J., Izaurralde, R. C., Rosenberg, N. J., & Leung, L. R. (2002). Elevation dependence of winter wheat production in eastern Washington State with climate change: A methodological study. *Climatic change*, 54, 141-164.
- Thorsten, D., Christopher, C., Babu, D. K., Marco, S., & Erik, B. (2017). *Derivation of biophysical parameters from fused remote sensing data*.
- Thrupp, L. A. (2000). Linking agricultural biodiversity and food security: the valuable role of agrobiodiversity for sustainable agriculture. *International affairs*, 76(2), 265-281.
- Tilman, D. (2001). Functional diversity. *Encyclopedia of biodiversity*, 3(1), 109-120.
- Timmer, C. P. (1988). The agricultural transformation. *Handbook of development economics*, 1, 275-331.
- Tucker, C. J. (1979). Red and photographic infrared linear combinations for monitoring vegetation. *Remote Sensing of Environment*, 8(2), 127-150.
- UFOP. (2019). Union zur förderung von oel-und proteinpflanzen E.V. Retrieved from <https://www.ufop.de/>
- Van Dam, J. C., Huygen, J., Wesseling, J., Feddes, R., Kabat, P., Van Walsum, P., . . . Van Diepen, C. (1997). *Theory of SWAP version 2.0; Simulation of water flow, solute transport and plant growth in the soil-water-atmosphere-plant environment*. Retrieved from
- Van Diepen, C. A. v., Wolf, J., Van Keulen, H., & Rappoldt, C. (1989). WOFOST: a simulation model of crop production. *Soil use and management*, 5(1), 16-24.
- Van Klompenburg, T., Kassahun, A., & Catal, C. (2020). Crop yield prediction using machine learning: A systematic literature review. *Computers and Electronics in Agriculture*, 177, 105709.
- Vasey, D. E. (1992). *An ecological history of agriculture, 10,000 BC-AD 10,000*: Purdue University Press.
- Verger, A., Baret, F., & Weiss, M. (2011). A multisensor fusion approach to improve LAI time series. *Remote Sensing of Environment*, 115(10), 2460-2470.
- Vigne, J.-D., Peters, J., & Helmer, D. (2005). The first steps of animal domestication. *New archaeozoological approaches*.
- Vincenzi, S., Zucchetta, M., Franzoi, P., Pellizzato, M., Pranovi, F., De Leo, G. A., & Torricelli, P. (2011). Application of a Random Forest algorithm to predict spatial distribution of the potential yield of *Ruditapes philippinarum* in the Venice lagoon, Italy. *Ecological Modelling*, 222(8), 1471-1478.
- Vitale, J., Adam, B., & Vitale, P. (2020). Economics of wheat breeding strategies: focusing on Oklahoma hard red winter wheat. *Agronomy*, 10(2), 238.
- Waldner, F., Horan, H., Chen, Y., & Hochman, Z. (2019). High temporal resolution of leaf area data improves empirical estimation of grain yield. *Scientific reports*, 9(1), 1-14.
- Walker, J., De Beurs, K., Wynne, R., & Gao, F. (2012). Evaluation of Landsat and MODIS data fusion products for analysis of dryland forest phenology. *Remote Sensing of Environment*, 117, 381-393.
- Walker, J. J., De Beurs, K. M., Wynne, R. H., & Gao, F. (2012). Evaluation of Landsat and MODIS data fusion products for analysis of dryland forest phenology. *Remote Sensing of Environment*, 117, 381-393.
- Wang, D., Qiu, P., Wan, B., Cao, Z., & Zhang, Q. (2022). Mapping α - and β -diversity of mangrove forests with multispectral and hyperspectral images. *Remote Sensing of Environment*, 275, 113021.
- Wang, E., Robertson, M., Hammer, G., Carberry, P. S., Holzworth, D., Meinke, H., . . . McLean, G. (2002). Development of a generic crop model template in the cropping system model APSIM. *European journal of agronomy*, 18(1-2), 121-140.
- Wang, J., Li, X., Lu, L., & Fang, F. (2013a). Estimating near future regional corn yields by integrating multi-source observations into a crop growth model. *European journal of agronomy*, 49, 126-140.
- Wang, J., Li, X., Lu, L., & Fang, F. (2013b). Parameter sensitivity analysis of crop growth models based on the extended Fourier Amplitude Sensitivity Test method. *Environmental Modelling & Software*, 48, 171-182.
- Wang, L., Wang, P., Liang, S., Zhu, Y., Khan, J., & Fang, S. (2020). Monitoring maize growth on the North China Plain using a hybrid genetic algorithm-based back-propagation neural network model. *Computers and Electronics in Agriculture*, 170, 105238.

- Wardlow, B. D., Egbert, S. L., & Kastens, J. H. (2007). Analysis of time-series MODIS 250 m vegetation index data for crop classification in the US Central Great Plains. *Remote Sensing of Environment*, 108(3), 290-310.
- Washburn, J. D., Burch, M. B., & Franco, J. A. V. (2020). Predictive breeding for maize: Making use of molecular phenotypes, machine learning, and physiological crop models. *Crop Science*, 60(2), 622-638.
- Wei, C., Huang, J., Mansaray, L. R., Li, Z., Liu, W., & Han, J. (2017). Estimation and mapping of winter oilseed rape LAI from high spatial resolution satellite data based on a hybrid method. *Remote Sensing*, 9(5), 488.
- Whitcraft, A. K., Vermote, E. F., Becker-Reshef, I., & Justice, C. O. (2015). Cloud cover throughout the agricultural growing season: Impacts on passive optical earth observations. *Remote Sensing of Environment*, 156, 438-447.
- White, K. D. (1970). Fallowing, crop rotation, and crop yields in Roman times. *Agricultural History*, 44(3), 281-290.
- Wiener, N. (1948). *Cybernetics or control and communication in the animal and the machine*. Cambridge, Massachusetts, MIT Press.
- Wilkins, R. J. (2008). Eco-efficient approaches to land management: a case for increased integration of crop and animal production systems. *Philosophical Transactions of the Royal Society B: Biological Sciences*, 363(1491), 517-525.
- Winowiecki, L., Vågen, T.-G., & Huising, J. (2016). Effects of land cover on ecosystem services in Tanzania: A spatial assessment of soil organic carbon. *Geoderma*, 263, 274-283.
- Wiseman, G., McNairn, H., Homayouni, S., & Shang, J. (2014). RADARSAT-2 polarimetric SAR response to crop biomass for agricultural production monitoring. *IEEE Journal of Selected Topics in Applied Earth Observations and Remote Sensing*, 7(11), 4461-4471.
- Woodcock, B., Bullock, J., McCracken, M., Chapman, R., Ball, S., Edwards, M., . . . Pywell, R. (2016). Spillover of pest control and pollination services into arable crops. *Agriculture, Ecosystems & Environment*, 231, 15-23.
- Wu, F., & Butz, W. (2004). *The future of genetically modified crops: Lessons from the Green Revolution*: Rand Corporation.
- Wu, M., Niu, Z., Wang, C., Wu, C., & Wang, L. (2012). Use of MODIS and Landsat time series data to generate high-resolution temporal synthetic Landsat data using a spatial and temporal reflectance fusion model. *Journal of Applied Remote Sensing*, 6(1), 063507.
- Wulder, M. A., Loveland, T. R., Roy, D. P., Crawford, C. J., Masek, J. G., Woodcock, C. E., . . . Cohen, W. B. (2019). Current status of Landsat program, science, and applications. *Remote Sensing of Environment*, 225, 127-147.
- Wulder, M. A., Masek, J. G., Cohen, W. B., Loveland, T. R., & Woodcock, C. E. (2012). Opening the archive: How free data has enabled the science and monitoring promise of Landsat. *Remote Sensing of Environment*, 122, 2-10.
- Wulder, M. A., White, J. C., Loveland, T. R., Woodcock, C. E., Belward, A. S., Cohen, W. B., . . . Roy, D. P. (2016). The global Landsat archive: Status, consolidation, and direction. *Remote Sensing of Environment*, 185, 271-283.
- Xie, D., Zhang, J., Zhu, X., Pan, Y., Liu, H., Yuan, Z., & Yun, Y. (2016). An improved STARFM with help of an unmixing-based method to generate high spatial and temporal resolution remote sensing data in complex heterogeneous regions. *Sensors*, 16(2), 207.
- Xin, Q., Olofsson, P., Zhu, Z., Tan, B., & Woodcock, C. E. (2013). Toward near real-time monitoring of forest disturbance by fusion of MODIS and Landsat data. *Remote Sensing of Environment*, 135, 234-247.
- Xue, J., Leung, Y., & Fung, T. (2017). A Bayesian data fusion approach to spatio-temporal fusion of remotely sensed images. *Remote Sensing*, 9(12), 1310.
- Xue, Q., Weiss, A., Arkebauer, T. J., & Baenziger, P. S. (2004). Influence of soil water status and atmospheric vapor pressure deficit on leaf gas exchange in field-grown winter wheat. *Environmental and experimental botany*, 51(2), 167-179.
- Yang, J., Yang, J.-Y., Liu, S., & Hoogenboom, G. (2014). An evaluation of the statistical methods for testing the performance of crop models with observed data. *Agricultural Systems*, 127, 81-89.
- Yao, X., Liu, Y., Liu, X., Qiao, Z., Sun, S., Li, X., . . . Jiang, X. (2022). Effects of thifluzamide on soil fungal microbial ecology. *Journal of Hazardous Materials*, 431, 128626.

References

- Yuan, W., Chen, Y., Xia, J., Dong, W., Magliulo, V., Moors, E., . . . Zhang, H. (2016). Estimating crop yield using a satellite-based light use efficiency model. *Ecological Indicators*, *60*, 702-709.
- Yuan, W., Liu, S., Zhou, G., Zhou, G., Tieszen, L. L., Baldocchi, D., . . . Goulden, M. L. (2007). Deriving a light use efficiency model from eddy covariance flux data for predicting daily gross primary production across biomes. *Agricultural and Forest Meteorology*, *143*(3-4), 189-207.
- Zamani-Noor, N., & Feistkorn, D. (2022). Monitoring Growth Status of Winter Oilseed Rape by NDVI and NDYI Derived from UAV-Based Red-Green-Blue Imagery. *Agronomy*, *12*(9), 2212.
- Zha, Y., Gao, J., & Ni, S. (2003). Use of normalized difference built-up index in automatically mapping urban areas from TM imagery. *International journal of remote sensing*, *24*(3), 583-594.
- Zhang, G., Zhang, Y., Dong, J., & Xiao, X. (2013). Green-up dates in the Tibetan Plateau have continuously advanced from 1982 to 2011. *Proceedings of the National Academy of Sciences*, *110*(11), 4309-4314.
- Zhang, J. (2010). Multi-source remote sensing data fusion: status and trends. *International Journal of Image and Data Fusion*, *1*(1), 5-24.
- Zhang, X., Friedl, M. A., Schaaf, C. B., Strahler, A. H., Hodges, J. C., Gao, F., . . . Huete, A. (2003). Monitoring vegetation phenology using MODIS. *Remote Sensing of Environment*, *84*(3), 471-475.
- Zhang, Y., Ling, F., Wang, X., Foody, G. M., Boyd, D. S., Li, X., . . . Atkinson, P. M. (2021). Tracking small-scale tropical forest disturbances: Fusing the Landsat and Sentinel-2 data record. *Remote Sensing of Environment*, *261*, 112470.
- Zhao, Y., Chen, S., & Shen, S. (2013). Assimilating remote sensing information with crop model using Ensemble Kalman Filter for improving LAI monitoring and yield estimation. *Ecological Modelling*, *270*, 30-42.
- Zhong, L., Gong, P., & Biging, G. S. (2012). Phenology-based crop classification algorithm and its implications on agricultural water use assessments in California's Central Valley. *Photogrammetric Engineering & Remote Sensing*, *78*(8), 799-813.
- Zhou, Q., & Ismaeel, A. (2021). Integration of maximum crop response with machine learning regression model to timely estimate crop yield. *Geo-Spatial Information Science*, *24*(3), 474-483.
- Zhou, W., Liu, Y., Ata-Ul-Karim, S. T., Ge, Q., Li, X., & Xiao, J. (2022). Integrating climate and satellite remote sensing data for predicting county-level wheat yield in China using machine learning methods. *International Journal of Applied Earth Observation and Geoinformation*, *111*, 102861.
- Zhu, L., Radeloff, V. C., & Ives, A. R. (2017). Improving the mapping of crop types in the Midwestern US by fusing Landsat and MODIS satellite data. *International Journal of Applied Earth Observation and Geoinformation*, *58*, 1-11.
- Zhu, X., Cai, F., Tian, J., & Williams, T. K.-A. (2018). Spatiotemporal fusion of multisource remote sensing data: literature survey, taxonomy, principles, applications, and future directions. *Remote Sensing*, *10*(4), 527.
- Zhu, X., Chen, J., Gao, F., Chen, X., & Masek, J. G. (2010). An enhanced spatial and temporal adaptive reflectance fusion model for complex heterogeneous regions. *Remote Sensing of Environment*, *114*(11), 2610-2623.
- Zhu, X., Helmer, E. H., Gao, F., Liu, D., Chen, J., & Lefsky, M. A. (2016). A flexible spatiotemporal method for fusing satellite images with different resolutions. *Remote Sensing of Environment*, *172*, 165-177.
- Zhuo, W., Fang, S., Gao, X., Wang, L., Wu, D., Fu, S., . . . Huang, J. (2022). Crop yield prediction using MODIS LAI, TIGGE weather forecasts and WOFOST model: A case study for winter wheat in Hebei, China during 2009–2013. *International Journal of Applied Earth Observation and Geoinformation*, *106*, 102668.
- Zhuo, W., Huang, J., Gao, X., Ma, H., Huang, H., Su, W., . . . Yin, D. (2020). Prediction of winter wheat maturity dates through assimilating remotely sensed leaf area index into crop growth model. *Remote Sensing*, *12*(18), 2896.
- Ziliani, M. G., Altaf, M. U., Aragon, B., Houborg, R., Franz, T. E., Lu, Y., . . . McCabe, M. F. (2022). Early season prediction of within-field crop yield variability by assimilating CubeSat data into a crop model. *Agricultural and Forest Meteorology*, *313*, 108736.

Acknowledgements

First and foremost, I would like to thank my first supervisor, Prof. Dr Tobias Ullmann, for his valuable guidance and unwavering support throughout this project. His expertise, encouragement, and patience have been instrumental in shaping this thesis. Prof. Dr Tobias Ullmann's astute observations and constructive criticism have enabled me to refine my research questions and approach, and his unwavering encouragement has been a constant source of motivation. His willingness to engage in thoughtful discussions and provide insightful feedback has been crucial in shaping the direction of this work.

I also extend my heartfelt thanks to my second supervisor, Prof. Dr Ingolf Steffan-Dewenter, for his innovative ideas and funding support that have helped me achieve my research goals. My deepest gratitude goes to my third and fourth supervisors, Prof. Dr Andrea Holzschuh and Prof. Dr Andreas Nüchter, for their intuitive advice and feedback in annual PhD meetings. I am immensely grateful to my mentor, Dr Thorsten Dahms, for his valuable support during my PhD.

I would also like to thank Prof. Dr Christopher Conrad and Dr Carina Kübert-Flock for selecting me as a PhD student in the Landklif project. I am grateful to the Department of Remote Sensing, University of Würzburg, for their full support and for allowing me to work independently. I want to thank Dr Martin Wegmann for securing contracts and Mr Simon Sebold's technical support, which helped me process satellite data faster. I thank all my colleagues at the Department of Remote Sensing, University of Würzburg, for their support.

I want to thank Dr Stephan Schröder-Köhne, from graduate school of science and technology (GSST), for his valuable support and guidance throughout my doctoral journey. His approach of asking critical questions helped me to frame my research questions and formulate a clear and concise methodology. His devotion and helping nature played an important role in completing this Doctorate.

I want to acknowledge the complete Landklif team, who helped me learn and understand the various streams where remote sensing data could be helpful. I am

Acknowledgements

deeply thankful to Dr Thomas Rummeler and Dr Joel Arnault for providing the relevant climate data for this project. I acknowledge the Professorship of Ecological Services, University of Bayreuth, for providing me with the updated Land Cover Map of Bavaria 2019. I am particularly thankful to Mrs Jie Zhang and Dr Sarah Redlich, both Department of Animal Ecology and Tropical Biology, University of Würzburg, for developing the initial concept and methodology for the Land Cover Map of Bavaria. With Ms Melissa Versluis, Ms Rebekka Riebl, Ms Maria Hänsel, Dr Bhumika Uniyal, and Prof. Dr Thomas Koellner (all Professorship of Ecological Services, University of Bayreuth), this concept and methodology were further developed. I am grateful to Ms Melissa Versluis (Professorship of Ecological Services, University of Bayreuth) for creating the Land Cover Map of 2019 based on the concluding methodology for the whole of Bavaria. I also acknowledge the data providers for the base layers ATKIS (Bayerische Vermessungsverwaltung), IACS (Bayerisches Staatsministerium für Ernährung, Landwirtschaft und Forsten), and Corine LC (European Environment Agency). I would also like to thank the National Aeronautics and Space Administration (NASA) Land Processed Distributed Active Archive Center (LP DAAC) for MODIS, the U.S. Geological Survey (USGS) Earth Resources Observation and Science (EROS) Center for Landsat, and the Copernicus Sentinel-2 mission for the Sentinel-2 data.

I am deeply grateful to Prof. Dr Tobias Ullmann, Mr Johannes Mast, Ms Emma Phelan, and Dr Darlene Murphy for their invaluable contribution to proofreading my thesis. Their keen attention to detail, expertise in language, and commitment to excellence have been instrumental in ensuring the accuracy and clarity of this thesis.

Thanks to my friends Sebastian Buchelt, Jakob Schwalb-Willmann, Johannes Mast, Itohan Osa-Abu, Lothar Helm, and Karin Druxes for unwavering support and encouragement throughout this journey. Lastly, I want to thank my parents for showing their confidence and morally and financially supporting me to study in Germany.

Affidavit

I hereby confirm that my thesis entitled, "**Potential of Remote Sensing in Modelling Long-Term Crop Yields**", is the result of my own work. I did not receive any help or support from commercial consultants. All sources and / or materials applied are listed and specified in the thesis.

Furthermore, I confirm that this thesis has not yet been submitted as part of another examination process neither in identical nor in similar form.

Würzburg, 06.04.2023

Place, Date

Signature

Eidesstattliche Erklärung

Hiermit erkläre ich an Eides statt, die Dissertation „**Potenzial der Fernerkundung für die Modellierung langfristiger Ernteerträge**“ eigenständig, d.h. insbesondere selbständig und ohne Hilfe eines kommerziellen Promotionsberaters, angefertigt und keine anderen als die von mir angegebenen Quellen und Hilfsmittel verwendet zu haben.

Ich erkläre außerdem, dass die Dissertation weder in gleicher noch in ähnlicher Form bereits in einem anderen Prüfungsverfahren vorgelegen hat.

Würzburg, 06.04.2023

Ort, Datum

Unterschrift

CV

Education

| Institution | Date | Course | Qualification |
|--|--------------|---------------------------|------------------------|
| University of Würzburg,
Germany | 2019-present | Crop Yield
Modelling | Doctor of Philosophy |
| University of Würzburg,
Germany | 2016-2019 | EAGLE* | Master of Science |
| Punjab Agricultural
University, India | 2013-2015 | Remote
Sensing | Master of Technology |
| Punjab Technical
University, India | 2009-2013 | Information
Technology | Bachelor of Technology |

* Applied Earth Observation and Geoanalysis of the Living Environment

Project Experience

| Project Name | Date | Title | Contribution |
|--------------|-----------------------|--------------------|---|
| ECOGLOB | 01.03.2022-Present | Research Associate | Using machine learning for flower cover mapping in Bavaria |
| InCubed | 01.04.2023-Present | Research Associate | Developing an automatic approach for pipeline monitoring |
| Landklif | 01.03.2019-30.09.2022 | PhD Student | Successfully generated synthetic remote sensing NDVI time series and modelled crop yields for Bavaria from 2001 to 2019 |
| JECAM | 01.15.2017-02.28.2019 | Research Assistant | Successfully validated crop biomass using five different crop growth models. |

Teaching Experience

| Course Name | Date | Organization | Contribution |
|-----------------------------------|---|------------------------|----------------|
| Scientific Writing | Winter semester 2022/23 | University of Würzburg | 2 SWS |
| Cloud computing in Remote Sensing | Winter semester 2022/23 | University of Würzburg | 2 SWS |
| Google Earth Engine Advances | Summer semester 2023 | University of Würzburg | 2 SWS |
| Applications of Earth Observation | Winter semester 2022/23, Winter semester 2021/22, and Winter semester 2020/21 | University of Würzburg | Guest lecturer |
| Advance Programming | Summer semester 2019 | University of Würzburg | 2 SWS |

Skills

- Advanced programmer in R, Google Earth Engine, Java script, C, and C++.
- Advanced knowledge of ArcGIS, QGIS, ENVI, ERDAS, and E-Cognition.
- Expertise in generating multisensory spatio-temporal remote sensing time series.
- Expertise in crop yield modelling.
- Experience in scientific writing.

Internships/Innovations/Workshops

- Attended Living Planet Symposium (LPA) organized by European Space Agency (ESA), Milan, Italy 11.05.2019-17.05.2019.
- Presented PhD research in 41st Canadian Symposium on Remote Sensing from 13.07.2020-17-07-2020.
- Attended a workshop "Supervising PhD Students" by Dr. Michael Decker organized by University of Würzburg on 01.05.2020.
- Attended a workshop on Young Entrepreneur in Science supported by Bundesministerium für Bildung und Forschung on 23.09.2020-24.09.2020.
- Attended a statistical analysis workshop organized in the Landklif project from 05.10.2020-06.10.2020.
- Attended an ESA conference "EO For Agriculture Under Pressure" 2021.
- Attended a Scientific writing workshop organized in the Landklif project from 22.02.2021-24.02.2021.
- Attended a Bayklif PhD Retreat in Tutzing from 28.09.2021-30.09.2021.
- Attended the ESA Living Planet Symposium at Bonn from 23.05.2022-27.05.2022.
- Presented on the use of google earth engine in earth observation in GeoSens EO4IntDev training Program 19.09.2022-23.09.2022.

Publications

- **Dhillon, M. S.**, Kübert-Flock, C., Dahms, T., Rummeler, T., Arnault, J., Steffan-Dewenter, I., & Ullmann, T. (2023). Evaluation of MODIS, Landsat 8 and Sentinel-2 Data for Accurate Crop Yield Predictions: A Case Study Using STARFM NDVI in Bavaria, Germany. *Remote Sensing*, 15(7), 1830. Retrieved from <https://www.mdpi.com/2072-4292/15/7/1830>.
- **Dhillon, M. S.**, Dahms, T., Kübert-Flock, C., Liepa, A., Rummeler, T., Arnault, J., . . . Ullmann, T. (2023). Impact of STARFM on Crop Yield Predictions: Fusing MODIS with Landsat 5, 7, and 8 NDVIs in Bavaria Germany. *Remote Sensing*, 15(6), 1651. Retrieved from <https://www.mdpi.com/2072-4292/15/6/1651>
- **Dhillon, M. S.**, Dahms, T., Kuebert-Flock, C., Rummeler, T., Arnault, J., Stefan-Dewenter, I., & Ullmann, T. (2023). Integrating random forest and crop modelling improves the crop yield prediction of winter wheat and oil seed rape. *Frontiers in Remote Sensing*, 3, 109.
- Benjamin, C. S., Uphus, L., Lüpke, M., Rojas-Botero, S., **Dhillon, M. S.**, Englmeier, J., . . . Redlich, S. (2022). Modelling the Relative Abundance of Roe Deer (*Capreolus capreolus* L.) along a Climate and Land-Use Gradient. *Animals*, 12(3), 222.
- **Dhillon, M. S.**, Dahms, T., Kübert-Flock, C., Steffan-Dewenter, I., Zhang, J., & Ullmann, T. (2022). Spatiotemporal Fusion Modelling Using STARFM: Examples of Landsat 8 and Sentinel-2 NDVI in Bavaria. *Remote Sensing*, 14(3), 677.
- Redlich, S., Zhang, J., Benjamin, C., **Dhillon, M. S.**, Englmeier, J., Ewald, J., . . . Hovestadt, T. (2022). Disentangling effects of climate and land use on biodiversity and ecosystem services—A multi-scale experimental design. *Methods in Ecology and Evolution*, 13(2), 514-527.
- **Dhillon, M. S.**, Kaur, S., Sidana, B. K., & Aggarwal, R. (2021). Groundwater irrigation and energy nexus in central Punjab-trends and analysis. *Journal of Agricultural Development and Policy*, 31(2), 222-227.
- Truckenbrodt, S., Ahmadian, N., Borg, E., Borrmann, P., Böttcher, F., Conrad, C., . . . Hüttich, C. (2021). Feldmessgeräte.
- **Dhillon, M. S.**, Dahms, T., Kuebert-Flock, C., Borg, E., Conrad, C., & Ullmann, T. (2020). Modelling Crop Biomass from Synthetic Remote Sensing Time Series: Example for the DEMMIN Test Site, Germany. *Remote Sensing*, 12(11), 1819.
- **Dhillon, M. S.**, Kaur, S., & Aggarwal, R. (2019). Delineation of critical regions for mitigation of carbon emissions due to groundwater pumping in central Punjab. *Groundwater for Sustainable Development*, 8, 302-308.
- **Singh Dhillon, M.**, Kaur, S., Sood, A., & Aggarwal, R. (2018). Estimation of carbon emissions from groundwater pumping in central Punjab. *Carbon Management*, 9(4), 425-435.

Würzburg, 06.04.2023

Place, Date

Signature